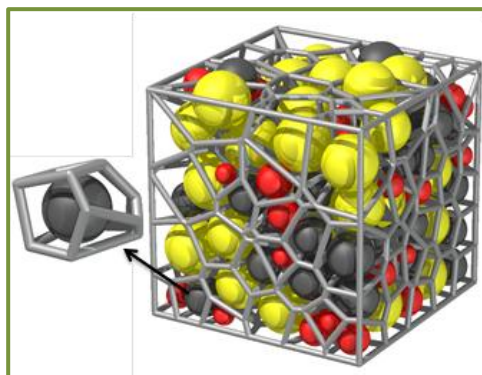
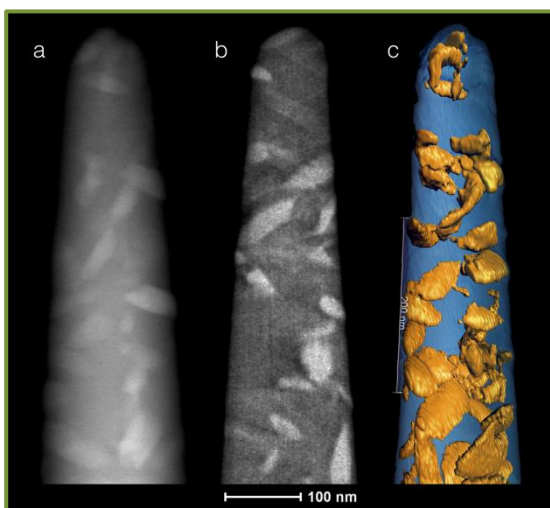
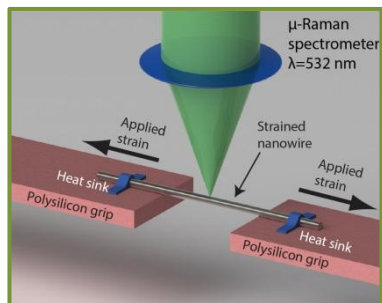
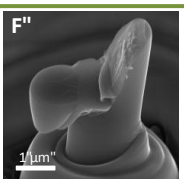
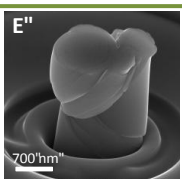
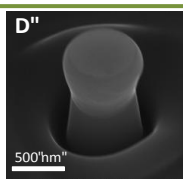
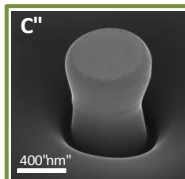
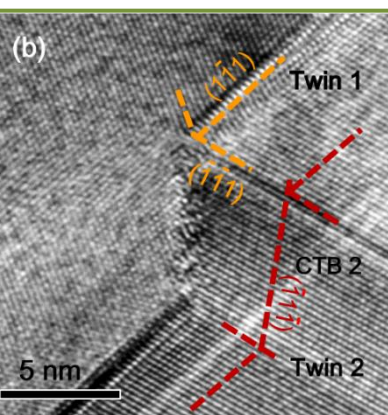
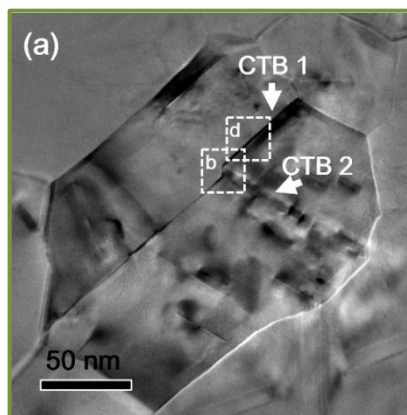
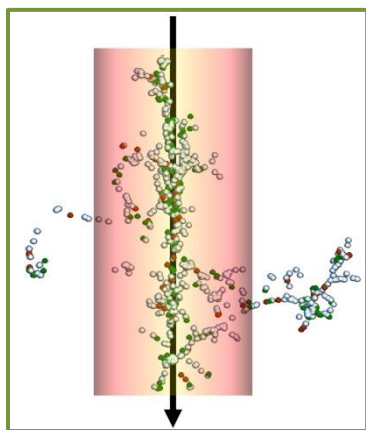


# Mechanical Behavior and Radiation Effects 2015 Principal Investigators' Meeting

September 14-16, 2015  
Gaithersburg Hilton, Gaithersburg, MD



U.S. DEPARTMENT OF  
**ENERGY**

Office of  
Science

Materials Sciences and Engineering Division  
Office of Basic Energy Sciences

## Cover

**Top Left:** Combined effects of energy loss to electrons and atomic nuclei by an ion. Electronic energy loss results in a concentric thermal spike along the ion path (depicted by arrow), while energy loss to atomic nuclei results in atomic collisions that displace atoms creating damage (Weber et al., ORNL)

**Top Right:** Microstructure of long coherent twin boundaries (CTB) in twinned Al films. (a) Low magnification TEM micrograph of the CTB multi-junction in Al film. (b) HRTEM micrograph showing the intersection of CTBs at the junctions. (Zhang et al., Texas A&M)

**Middle Left:** Uniaxial compression tests of Zr-Ni-Al metallic glass pillars showing a transition in response as size increases. Typical SEM images post compression shown for pillar diameters of (C) 492 nm, (D) 540 nm, (E) 1300 nm, and (F) 1560 nm (Greer et al., Cal Tech)

**Middle Right:** Schematic of experimental setup for *in situ* Raman piezothermography method applied to strained, suspended nanowires (Gianola et al., Penn)

**Bottom Left:** A needle fabricated from a  $\text{Ni}_{50.3}\text{Ti}_{29.7}\text{Hf}_{20}$  alloy, aged 315 hours at  $550^\circ\text{C}$ , used for H-phase volume fraction analysis. (a) An example of 1 of 180 HAADF STEM images used in creating the back-projection, a frame of which is shown in (b), which formed the building blocks for the 3D rendering shown in (c). (Mills et al., The Ohio State University)

**Bottom Right:** Voronoi tessellation for the structure of an ethane-bridged oxycarbosilane hybrid organosilicate glass. This is used to obtain the volume accessible to each atom via their corresponding simplex volumes. The free volume change between compressive and tensile loading is directly related to the change in the Voronoi cell volume since the atomic volume remains constant. (Dauskardt et al., Stanford)

---

This document was produced under contract number DE-AC05-06OR23100 between the U.S. Department of Energy and Oak Ridge Associated Universities.

The research grants and contracts described in this document are supported by the U.S. DOE Office of Science, Office of Basic Energy Sciences, Materials Sciences and Engineering Division.

## Foreword

This volume comprises the scientific content of the 2015 Mechanical Behavior and Radiation Effects Principal Investigators' (PI) Meeting sponsored by the Division of Materials Sciences and Engineering (DMS&E) in the Office of Basic Energy Sciences (BES) of the U. S. Department of Energy (DOE). The meeting, held on September 14–16 at the Gaithersburg Hilton, Gaithersburg, Maryland, is the fifth such meeting on this topic and is one among a series of research theme-based PI meetings being held by DMS&E. The meeting's focus is on research in mechanical behavior and radiation effects of materials, and it also features research that cuts across several other BES core research program areas and Energy Frontier Research Centers where appropriate and relevant.

The studies of mechanical behavior and radiation effects have a long and important history with respect to the generation, transmission, utilization and conservation of energy. It is a tribute to the researchers that they have continued to move the field forward into a number of important areas, as can be seen by the diversity of projects being presented at this meeting. Attendees will note a number of new projects and research directions since the previous meeting including one new recipient of an Early Career Research Program award. These new projects add to the exciting areas of research and cutting-edge techniques that are a hallmark of this program.

The purpose of the Mechanical Behavior and Radiation Effects PI Meeting is to bring together researchers funded by DMS&E in this important area of research on a periodic basis (approximately every two years) in order to facilitate the exchange of new results and research highlights, to nucleate new ideas and collaborations among the participants, and to identify needs of the research community. The meeting will also help DMS&E in assessing the state of the program, identifying new research directions and recognizing programmatic needs.

I would like to express my sincere thanks to all of the attendees for their active participation and for sharing their ideas and new research results. I would also like to express my sincere gratitude to Ms. Teresa Crockett in DMS&E, and Ms. Linda Severs (plus others) of the Oak Ridge Institute for Science and Education (ORISE) for their dedicated and outstanding work in taking care of all the logistical aspects of the meeting.

John Vetrano  
Program Manager  
Mechanical Behavior and Radiation Effects  
Division of Materials Sciences and Engineering  
Office of Basic Energy Sciences  
U.S. Department of Energy





# ***Agenda***



**Mechanical Behavior and Radiation Effects  
Principal Investigators' Meeting Agenda**

**Monday, September 14, 2015**

7:00 – 8:00 am **Breakfast**

8:00 – 8:15 am *Introductory Remarks*  
**John Vetrano and TS Byun**

**Session I** Chair: **Ivar Reimanis**, Colorado School of Mines

8:15 – 8:45 am **George Pharr**, Oak Ridge National Laboratory  
*Multiscale Mechanical Properties and Alloy Design*

8:45 – 9:15 am **Brian Sheldon**, Brown University  
*Understanding and Controlling Toughening Mechanisms in Nanotube Reinforced Ceramic Coatings*

9:15 – 9:45 am **Reinhold Dauskardt**, Stanford University  
*Mechanical and Fracture Behavior of Molecular-Reinforced Hybrid Glasses*

9:45 – 10:15 am **Break**

**Session II** Chair: **Stefanos Papanikolaou**, Johns Hopkins

10:15 – 10:45 am **John Allison**, University of Michigan  
*Software Center for Predictive Theory and Modeling*

10:45 – 11:15 am **Wei Cai**, Stanford University  
*Thermal Activation in Dislocation Dynamics of Face-Centered Cubic Metals*

11:15 – 11:45 am **Brad Boyce**, Sandia National Laboratory  
*Nanomechanics and Nanometallurgy of Boundaries*

11:45 – 12:15 pm **David Fullwood**, Brigham Young University  
*Grain Boundary-Dislocation Interactions in Polycrystals: Characterization and Simulation for the Effective Design of High-Strength, High-Ductility Structural Alloys*

12:15 – 1:45 pm **Working Lunch / Poster Introductions**

**Session III** Chair: **TS Byun**, Pacific Northwest National Laboratory

1:45 – 2:15 pm **Linda Horton**, BES, Director, Division of Materials Science and Engineering  
*Program Updates*

2:15 – 2:30 pm **John Vetrano**, BES  
*Program Overview*

- 2:30 – 3:00 pm **Yanwen Zhang**, Oak Ridge National Laboratory  
*Energy Dissipation to Defect Evolution: an Energy Frontier Research Center*
- 3:00 – 3:30 pm **Break**
- Session IV** Chair: **Tim Rupert**, University of California, Irvine
- 3:30 – 4:00 pm **Mitra Taheri**, Drexel University  
*Linking the Correlated Dependence of Grain Boundary Structure and Density to Defect Evolution Mechanisms during Radiation Damage*
- 4:00 – 4:30 pm **Pascal Bellon**, University of Illinois-UC  
*Materials for Extreme Irradiation Environments*
- 4:30 – 5:00 pm **Xinghang Zhang**, Texas A&M University  
*Deformation Mechanisms of Nanotwinned Al*
- 5:00 – 6:00 pm **Free Time**
- 6:00 – 7:00 pm **Dinner and Discussions**
- 7:00 – 9:30 pm **Poster Session I**

## Tuesday, September 15, 2015

- 7:00 – 8:30 am **Breakfast**
- Session V** Chair: **Gary Was**, University of Michigan
- 8:30 – 9:00 am **Karl Sieradzki**, Arizona State University  
*Dynamic Fracture in Dealloying Induced Stress Corrosion Cracking*
- 9:00 – 9:30 am **Steve Bruemmer**, Pacific Northwest National Laboratory  
*Crack-Tip Mechanisms Driving Environmental Degradation*
- 9:30 – 10:00 am **Ian Baker**, Dartmouth University  
*Structure/Property Relationships in Two-Phase f.c.c./B2 FeNiMnAl Alloys*
- 10:00 – 10:30 am **Break**
- Session VI** Chair: **Michael Demkowicz**, Massachusetts Institute of Technology
- 10:30 – 11:00 am **Dane Morgan and Izabela Szlufarska**, University of Wisconsin  
*Radiation Effects in Nanocrystalline Ceramics: Multi-Scale Model and Experiment*

- 11:00 – 11:30 am **Bill Weber**, Oak Ridge National Laboratory  
*Electronic and Atomic Response of Ceramic Structures to Irradiation*
- 11:30 – 12:00 am **Lin Shao**, Texas A&M University  
*Radiation Response of Low Dimensional Carbon Systems*
- 12:00 – 1:30 pm **Working Lunch / Poster Introductions**
- Session VII** Chair: **Rishi Raj**, University of Colorado
- 1:30pm – 2:00pm **Rob Ritchie**, Lawrence Berkeley National Laboratory  
*Damage Tolerant and Hierarchical Structural Materials*
- 2:00pm – 2:30pm **Daniel Gianola**, University of Pennsylvania  
*Modulating Thermal Transport Phenomena in Nanostructures via Elastic Strain at Extreme Limits of Strength*
- 2:30pm – 3:00pm **Elisa Riedo**, City University of New York  
*NanoMechanics: Elasticity and Friction in Nano-Objects*
- 3:00pm – 3:30pm **Break**
- Session VIII** Chair: **Sam Daly**, University of Michigan
- 3:30pm – 4:00pm **Cate Brinson**, Northwestern University  
*Granular Constraints and Size Effects in Polycrystalline Shape Memory Alloys*
- 4:00pm – 4:30pm **Mike Mills**, The Ohio State University  
*Transformation and Deformation Mechanisms in High-Temperatures Shape Memory Alloys with Nanoprecipitates*
- 4:30pm – 5:00pm **Alejandro Strachan**, Purdue University  
*Tunable Hetero-Epitaxial Shape Memory Alloys*
- 5:00pm – 6:00pm **Free Time**
- 6:00pm – 7:00pm **Dinner and Discussions**
- 7:00pm – 9:30pm **Poster Session II**

## Wednesday, September 16, 2015

7:00am – 8:30am **Breakfast**

**Session IX** Chair: **Mark Asta**, University of California, Berkeley

8:30am – 9:00am **Krystyn Van Vliet and Harry Tuller**, Massachusetts Institute of Technology  
*COFFEI: Chemomechanics of Far-From-Equilibrium Interfaces*

9:00am – 9:30am **Blas Uberuaga**, Los Alamos National Laboratory  
*Disorder and Diffusion in Complex Oxides: Towards Prediction and Control*

9:30am – 10:00am **Richard LeSar**, Ames Laboratory  
*Nanotwinned Materials for Energy Technology*

10:00am – 10:30am **Break**

**Session X** Chair: **Irene Beyerlein**, Los Alamos National Laboratory

10:30am – 11:00am **Maryam Ghazisaeidi**, The Ohio State University  
*Atomic Scale Computational and Experimental Investigation of Twinning Mechanisms in HCP Systems*

11:00am – 11:30am **Martin Crimp and Carl Boehlert**, Michigan State University  
*Characterization and Modeling of Deformation Induced Damage in Titanium Alloys*

11:30am – 12:00pm **Carlos Tomé**, Los Alamos National Laboratory  
*Multi-Scale Study of the Role of Microstructure in the Deformation Behavior of Hexagonal Materials*

12:00pm – 12:15pm **Closing Remarks by John Vetrano**

# ***Poster List***





# Mechanical Behavior and Radiation Effects Principal Investigators' Meeting

## POSTER SESSION I Monday, September 14, 2015

- 1) **COFFEI: Chemomechanics of Far-From-Equilibrium Interfaces**  
Jessica Swallow and Harry Tuller, Massachusetts Institute of Technology
- 2) **Stress-Coupled Grain Boundary Migration**  
Kevin Hemker, Johns Hopkins University
- 3) **Constructing Comprehensive Models of Hydrogen Behavior at Grain Boundaries using High-Throughput Experiments**  
Michael Demkowicz, MIT
- 4) **Nanomechanics and Nanometallurgy of Boundaries**  
Brad Boyce, SNL/NM
- 5) **Localized Deformation and Intergranular Fracture of Irradiated Alloys under Extreme Environmental Conditions**  
Gary Was, University of Michigan
- 6) **Investigation of Radiation Damage Tolerance in Interface-Containing Metallic Nanostructures**  
Julia Greer, California Institute of Technology
- 7) **Predictive Modeling of Synergistic Effects in Nanoscale Ion Track Formation**  
Eva Zarkadoula and Bill Weber, ORNL
- 8) **Stability of Nanoclusters in Metal Matrices under Extreme Environments**  
Chad Parish, ORNL
- 9) **Energetics of Radiation Tolerant Nanoceramics**  
Ricardo Castro, University of California-Davis
- 10) **Software Center for Predictive Theory and Modeling**  
John Allison, University of Michigan
- 11) **Deformation Mechanisms at Grain Boundaries in Polycrystals**  
Michael Sangid, Purdue University , Samantha Daly, University of Michigan
- 12) **Doping Metallic Grain Boundaries to Control Atomic Structure and Damage Tolerance**  
Tim Rupert, University of California – Irvine
- 13) **Granular Constraints and Size Effects in Polycrystalline Shape Memory Alloys**  
Partha Paul and Cate Brinson, Northwestern University

**POSTER SESSION II**  
**Tuesday, September 15, 2015**

- 1) **Mechanical Behavior in Ceramics with Unusual Thermal-Mechanical Properties**  
Ivar Reimanis, Colorado School of Mines
- 2) **Atomistic and Mesoscopic Study of Plastic Deformation of Alloys of Body Centered Cubic Transition Metals and Magnetic Iron**  
Vaclav Vitek, University of Pennsylvania
- 3) **Understanding Microplasticity Processes Related to Fatigue Damage Using High Energy X-Rays and a Crystal-Based Modeling Formulation**  
Matthew Miller, Cornell University
- 4) **Low Scale Characterization of Twins in HCP using Microscopy and Modeling**  
Yue Liu and Carlos Tomé, LANL
- 5) **Nanotwinned Materials for Energy Technology**  
Richard LeSar, Ames Laboratory
- 6) **Using Artificial Microstructures to Understand Microstructure Property Relationship-Toughening Mechanisms in Metallic Glass**  
Jan Schroers, Yale University
- 7) **Deformation and Failure Mechanisms of Shape Memory Alloys**  
Samantha Daly, University of Michigan
- 8) **Atomistic Simulations of Stability and Mechanical Behavior in Metallic Glasses**  
Mark Asta and Rob Ritchie, LBNL
- 9) **Deformation Physics of Ultrafine Scale Materials**  
Nate Mara and Jian Wang, LANL
- 10) **Multiscale Mechanical Properties and Alloy Design**  
Yanfei Gao, UT-Knoxville and George Pharr, ORNL
- 11) **Nanoindentation of Micrograins in Polycrystals Under Multiaxial Stress: Control of Abrupt & Stochastic Plastic Events**  
Stefanos Papanikolaou, JHU
- 12) **The Coupling Between Interfacial Charge and Mechanical Deformation at High Temperatures in Ceramics**  
Rishi Raj, University of Colorado
- 13) **Deformed Materials: Towards a Theory of Materials Morphology Dynamics**  
Jim Sethna, Cornell University
- 14) **Effect of Realistic 3D Microstructure in Crystal Plasticity Finite Element Analysis of Polycrystalline Ti-5Al-2.5Sn**  
Chen Zhang and Carl Boehlert, Michigan State University

# ***Table of Contents***



## Table of Contents

<b>Foreword</b> .....	i
<b>Agenda</b> .....	v
<b>Poster Sessions</b> .....	xi
 <b>Abstracts</b>	
<i>Invited Talk from an Energy Frontier Research Center: Influence of Chemical Disorder on Energy Dissipation and Defect Evolution in Advanced Alloys—Progress toward Structural Materials by Design</i>	
<b>Yanwen Zhang, Hongbin Bei, German D. Samolyuk, G. Malcolm Stocks, Roger E. Stoller, William J. Weber, Lumin Wang, Magdalena Caro, and Alfredo Caro</b> .....	3
<i>Center for PRedictive Integrated Structural Materials Science – PRISMS Center</i>	
<b>John Allison</b> .....	5
<i>Structure/Property Relationships in Two-Phase f.c.c./B2 FeNiMnAl Alloys</i>	
<b>Ian Baker</b> .....	10
<i>Materials for Extreme Irradiation Environments</i>	
<b>Pascal Bellon, Robert S. Averback, Shen J. Dillon, William P. King, and Dallas R. Trinkle</b> .....	14
<i>Characterization and Modeling of Deformation Induced Damage in Titanium Alloys</i>	
<b>Carl J. Boehlert, T. R. Bieler, M. A. Crimp, and P. Eisenlohr</b> .....	19
<i>Nanomechanics and Nanometallurgy of Boundaries</i>	
<b>Brad L. Boyce</b> .....	24
<i>Granular Constraints and Size Effects in Polycrystalline Shape Memory Alloys</i>	
<b>L. Catherine Brinson and D. C. Dunand</b> .....	30
<i>Crack Tip Mechanisms Driving Environmental Degradation</i>	
<b>S. M. Bruegger, D. K. Schreiber, C. Wang, M. J. Olszta, M. L. Sushko and K. M. Rosso</b> .....	34
<i>Thermal Activation in Dislocation Dynamics of Face-Centered Cubic Metals</i>	
<b>Wei Cai</b> .....	40
<i>Energetics of Radiation Tolerant Nanoceramics</i>	
<b>Ricardo Castro</b> .....	42

<i>Mechanical and Fracture Behavior of Molecular-Reinforced Hybrid Glasses</i> <b>Reinhold H. Dauskardt</b> .....	47
<i>High-Throughput Experiments on Grain Boundaries</i> <b>Michael J. Demkowicz</b> .....	51
<i>Grain Boundary – Dislocation Interactions in Polycrystals: Characterization and Simulation for the Effective Design of High-Strength, High-Ductility Structural Alloys</i> <b>David Fullwood, Eric Homer, and Robert Wagoner</b> .....	55
<i>Atomic Scale Computational and Experimental Investigation of Twinning Mechanisms in HCP Systems</i> <b>Maryam Ghazisaeidi, Michael J. Mills</b> .....	59
<i>Modulating Thermal Transport Phenomena in Nanostructures via Elastic Strain at Extreme Limits of Strength</i> <b>Daniel S. Gianola</b> .....	63
<i>Investigation of Radiation Damage Tolerance in Interface-Containing Metallic Nanostructures</i> <b>Julia R. Greer</b> .....	68
<i>Nanoscale Characterization of Intragranular and Intergranular Deformation Mechanisms</i> <b>Kevin Hemker</b> .....	81
<i>Nanotwinned Materials for Energy Technologies</i> <b>Richard LeSar, Peter Collins, Alex King, Mikhail Mendeleev, and Ryan Ott</b> .....	85
<i>Formation of Persistent Slip Networks during Low Cycle Fatigue</i> <b>Matthew Miller, Paul Dawson, and Jim Williams</b> .....	90
<i>Transformation and Deformation Mechanisms in High-Temperature Shape Memory Alloys with Nanoprecipitates</i> <b>Michael J. Mills, Peter M. Anderson, Yunzhi Wang</b> .....	95
<i>From Micro-pillar Uniaxial Compression to Micro-grain Nano-indentation under Multi-axial Stress: Control and Understanding of Abrupt and Stochastic Plastic Events</i> <b>S. Papanikolaou and K. Hemker</b> .....	101
<i>Stability of Nanoclusters in Metal Matrices under Extreme Environments</i> <b>Chad M. Parish, Michael K. Miller, German Samolyuk, Yury N. Osetskiy, Michael J. Mills, and Dong Ma</b> .....	105
<i>Multiscale Mechanical Properties and Alloy Design</i> <b>George M. Pharr, Yanfei Gao, Hongbin Bei, James R. Morris, and Yury Osetskiy</b> .....	111



<i>Electric Field and Temperature Induced Defect Catastrophe and Related Phenomena</i> <b>Rishi Raj</b> .....	118
<i>Mechanical Behavior in Ceramics with Unusual Thermal-Mechanical Properties</i> <b>Ivar Reimanis and Cristian Ciobanu</b> .....	123
<i>Nanomechanics: Elasticity and Friction in Nano-Objects</i> <b>Elisa Riedo</b> .....	129
<i>Damage-Tolerant Structural Materials</i> <b>Robert O. Ritchie, Mark Asta, and Antoni P. Tomsia</b> .....	133
<i>Doping Metallic Grain Boundaries to Control Atomic Structure and Damage Tolerance</i> <b>Timothy J. Rupert</b> .....	137
<i>Deformation Mechanisms at Grain Boundaries in Polycrystals</i> <b>Michael D. Sangid and Samantha Daly</b> .....	142
<i>Using Artificial Microstructures to Measure Fracture Toughness in Metallic Glasses and Their Cellular Structures and Composites</i> <b>Jan Schroers</b> .....	146
<i>Deformed Materials: Towards a Theory of Materials Morphology Dynamics</i> <b>James P. Sethna</b> .....	150
<i>Radiation Responses of Low Dimensional Carbon Systems</i> <b>Lin Shao</b> .....	152
<i>Understanding and Controlling Toughening Mechanisms in Nanotube Reinforced Ceramic Coatings</i> <b>Brian W. Sheldon, Nitin Padture, and Jun Lou</b> .....	156
<i>Dynamic Fracture in Dealloying Induced Stress Corrosion Cracking</i> <b>Karl Sieradzki</b> .....	161
<i>Understanding, Controlling and Creating Martensitic Phase Transformations in Nanostructured Polycrystals and Metamaterials</i> <b>Alejandro Strachan</b> .....	165
<i>Interfacial Effects in Radiation Phenomena of Ceramics</i> <b>Izabela Szlufarska, Dane Morgan, Paul Voyles</b> .....	170
<i>Linking the Correlated Dependence of Grain Boundary Structure and Density to Defect Evolution Mechanisms during Radiation Damage</i> <b>Mitra Taheri</b> .....	175

<i>Multi-Scale Study of the Role of Microstructure in the Deformation Behavior of Hexagonal Materials</i> <b>Carlos N. Tomé, Irene J. Beyerlein, Rodney M. McCabe, and Jian Wang</b> .....	180
<i>Chemomechanics of Far-From-Equilibrium Interfaces (COFFEI)</i> <b>Harry L. Tuller, Krystyn J. Van Vliet, W. Craig Carter, Yet-Ming Chiang, and Bilge Yildiz</b> .....	186
<i>Disorder and Diffusion in Complex Oxides: Towards Prediction and Control</i> <b>Blas Pedro Uberuaga</b> .....	193
<i>Atomistic and Mesoscopic Study of Plastic Deformation of Alloys of Body-Centered-Cubic Transition Metals and Magnetic Iron</i> <b>V. Vitek</b> .....	199
<i>Localized Deformation and Intergranular Fracture of Irradiated Alloys under Extreme Environmental Conditions</i> <b>Gary S. Was, Ian M. Robertson, and Diana Farkas</b> .....	204
<i>Electronic and Atomic Response of Ceramic Structures to Irradiation</i> <b>William J. Weber, Yanwen Zhang, and Matthew F. Chisholm</b> .....	209
<i>Deformation Mechanisms of Nanotwinned Al</i> <b>Xinghang Zhang</b> .....	216
<b>Author Index</b> .....	223
<b>Participant List</b> .....	227

# ***Abstracts***



## **Influence of chemical disorder on energy dissipation and defect evolution in advanced alloys - progress toward structural materials by design**

**Yanwen Zhang, Director, Oak Ridge National Laboratory**

**Hongbin Bei, German D. Samolyuk, G. Malcolm Stocks, Roger E. Stoller, and William J. Weber, PI, Oak Ridge National Laboratory**

**Lumin Wang, PI, University of Michigan**

**Magdalena Caro and Alfredo Caro, PI, Los Alamos National Laboratory**

The development of metallic alloys is arguably one of the oldest sciences, dating back at least 3,000 years. Most research and applications have been focused on alloys with one principal element, to which the addition of alloying elements in low concentrations leads to various performance improvements and changes in radiation resistance. In sharp contrast to traditional alloys, recent success in the synthesis of single-phase concentrated solid solution alloys (SP-CSAs) has opened up new frontiers in materials research. In these alloys, a random arrangement of multiple elemental species on a lattice (fcc or bcc) results in unique site-to-site lattice distortions and local disordered chemical environments.

Intense radiation in nuclear fission and fusion energy power systems, nuclear waste forms, high-energy accelerators and space exploration transfers energy to the electrons and atoms that make up the material, and thereby produces defects that ultimately compromise material strength and lifetime. A grand challenge in materials research is to understand complex electronic correlations and non-equilibrium atomic interactions, and how such intrinsic properties and dynamic processes affect energy transfer and defect evolution in irradiated materials. Since SP-CSAs possess unique links between intrinsic material properties (can be altered by alloy complexity), energy dissipation and various defect dynamic processes; they are ideal systems to fill knowledge gaps between electronic-/atomic-level interactions and radiation resistance mechanisms.

In our work, we show that chemical disorder and compositional complexity in SP-CSAs have an enormous impact on defect dynamics through substantial modification of energy dissipation pathways. Based on a closely integrated computational and experimental study using a novel set of Ni-based SP-CSAs, we have explicitly demonstrated that increasing chemical disorder can lead to a substantial reduction in the electron mean free path and electrical and thermal conductivity. These reductions have a significant impact on energy dissipation and consequentially on defect evolution during ion irradiation. Considerable enhancement in

radiation resistance with increasing chemical complexity from pure nickel to binary, and to more complex quaternary solid solutions, is observed under ion irradiation.

Contrary to conventional alloys with low solute concentration but multiple phases, energy dissipation and defect evolution at the level of electrons and atoms in SP-CSA systems with extreme compositional disorder is an unexplored frontier in materials science. The integrated experimental/modeling effort provides new insights into defect dynamics at the level of atoms and electrons, and an innovative path forward towards solving a long-standing challenge in structural materials. Understanding how material properties can be tailored by alloy complexity and their influence on defect dynamics may pave the way for new design principles of radiation-tolerant structural alloys for advanced energy systems, as well as for new defect engineering paradigms benefiting broader science and technology.

Work supported by the Energy Dissipation to Defect Evolution Center (EDDE), an Energy Frontier Research Center funded by the U.S. Department of Energy, Office of Science.

## Center for Predictive Integrated Structural Materials Science – PRISMS Center

**John Allison, Principal Investigator**

Department of Materials Science and Engineering  
University of Michigan (UM)  
Ann Arbor, MI

### **Program Scope**

The overarching goal of the PRISMS Center is to establish a unique scientific platform that will enable accelerated predictive materials science. The platform has three key components and associated objectives:

1. **PRISMS Integrated Computational Software:** Develop and establish PRISMS (PRedictive Integrated Structural Materials Science), a suite of integrated multi-scale computational tools for predicting the microstructural evolution and mechanical behavior of structural metals. This software suite will be open-source, efficient and extensible.
2. **PRISMS Integrated Science Use Cases:** Significantly advance the science of metals by integrating the use of PRISMS computational tools with advanced experimental methods focused on specific scientific challenges. The use cases demonstrate the application of the integrated PRISMS capability for making major advances in the quantitative and predictive understanding of microstructural evolution and mechanical behavior of magnesium alloys.
3. **The Materials Commons:** Develop and deploy “The Materials Commons,” a knowledge repository and virtual collaboration space for curating, archiving and disseminating information from experiments and computations. Materials Commons is a collaboration platform for the PRISMS community and, ultimately, the broader materials community.

The other faculty involved in the PRISMS Center are Samantha Daly, associate professor of mechanical engineering (UM); Krishna Garikipati, professor of mechanical engineering; (UM) Vikram Gavini, associate professor of mechanical engineering (UM); Margaret Hedstrom, professor School of Information (UM); H. V. Jagadish, professor of electrical engineering and computer science (UM); J. Wayne Jones, professor of materials science and engineering (UM); Emmanuelle Marquis, associate professor of materials science and engineering (UM); Amit Misra, chair and professor of materials science and engineering (UM), Veera Sundararaghavan, associate professor of aerospace engineering (UM); Katsuyo Thornton, professor of materials science and engineering (UM); and Anton Van der Ven, associate professor of materials (University of California-Santa Barbara). The PRISMS Center also has five full time staff and sixteen graduate students and post-doctoral fellows.

### **Recent Progress and Future Plans**

The PRISMS Center was established in September 2012. Substantial progress has been made in each of the three primary thrusts (Use Cases, PRISMS Software and Materials Commons) as described below. We have also established an annual workshop to develop our external PRISMS collaborative community and to train external users in use of PRISMS software tools and Materials Commons. Additional information can be found on the PRISMS Center website: <http://prisms-center.org>.

#### ***PRISMS Integrated Software***

The five major integrated open source codes described below will be developed and made available to the community. Initial versions of four of these (CASIM, PRISMS-PF, PRISMS-Plasticity and PRISMS-Integration Tools) are being released on September 1, 2015 and can be accessed via GitHub.



PRISMS-IntegrationTools: Integration of PRISMS codes and other software is being accomplished using the IntegrationTools package that includes an API for easily passing arbitrary functions and fields between different software programs.

CASM, a Clusters Approach to Statistical Mechanics: The initial release provides functionality for symmetry identification, enumeration of symmetrically unique supercells and configurations, use of automatically determined or custom reference states for formation energy calculation, and convex hull identification. Future planned releases include kinetic Monte Carlo calculations of non-dilute diffusion coefficients.

PRISMS-PF: The PRISMS Phase Field code uses the finite element (FE) method, and is a massively scalable numerical framework for implementing phase field models for the multiscale materials modeling effort of PRISMS. The PRISMS FE framework using the deal.ii open-source finite element library has been implemented.

PRISMS-Plasticity: The PRISMS-Plasticity code is a massively parallel numerical framework for implementing continuum and crystal plasticity finite element (CPFE) models using the deal.ii open source library. Various continuum plasticity and crystal plasticity material models have been developed. The ability to carry out computations of crack and shear band evolution is being developed using variational multiscale methods (VMM) and is planned for future release.

PRISMS-RSDFT: To enable an accurate electronic structure study of the energetics of defects in crystalline materials, real-space methods are being developed for simulation domains containing tens of thousands of atoms. This enables accurate capture of both the electronic-structure of dislocation cores and the long-range elastic fields. The initial PRISMS Real Space DFT code will be released in late 2016/early 2017.

### ***PRISMS Use Cases***

The PRISMS Use Cases serve as demonstrations and test beds for the development of the PRISMS framework and of our highly integrated and collaborative scientific workflows. Highlights from these four use cases are summarized below:

#### Precipitate Evolution Use Case

High strength in Mg alloys is achieved by a particular precipitation sequence exhibited by a variety of Mg-rare earth (RE) alloys. It involves the formation first of Guinier-Preston zones followed by the precipitation of nano-scale  $\beta'$  and  $\beta_1$  phases with optimal orientations for strengthening. Fundamental questions being addressed include how precipitation mechanisms can be described theoretically such that the evolution during aging heat treatments can be predicted and what, in particular, about the rare-earth elements causes this favorable precipitation morphology and orientation. Our initial demonstration of this integrated framework is on  $\beta'$  precipitate evolution in a Mg-Nd alloy. Using CASM, we formulated a phenomenological free energy that is capable of simultaneously describing the nucleation and growth of hcp based  $\beta'$  as well as the formation of the bcc based  $\beta_1$ . These results were combined with high resolution TEM results to identify critical new features of the Mg-RE phase diagram. Using the new PRISMS-PF code, a phase field model was developed to simulate the evolution of  $\beta'$  precipitates in Mg-RE alloys. The energetics of the system was parameterized for bulk thermodynamics, anisotropic interfacial energy, and strain energy due to the misfit of the precipitates relative to the lattice. Figure 1a shows the morphology of a single  $\beta'$  precipitate in a Mg-Nd alloys and Figure 1b shows the results of a large scale run with over 1000  $\beta'$  precipitates in a Mg-Gd alloy. The precipitation sequences and quantitative 3D precipitate characteristics are also being probed experimentally in several binary, ternary and higher Mg-RE alloys using a range of techniques

including high resolution transmission electron microscopy and atom probe tomography. Future plans include comprehensive experimental characterization and full parameterization of the PRISMS-PF simulation for precipitation in the Mg-Nd, Mg-Y and Mg-Nd-Y systems. We plan to incorporate a concurrent nucleation algorithm into the phase-field model to study the early stages of precipitate formation and evolution.

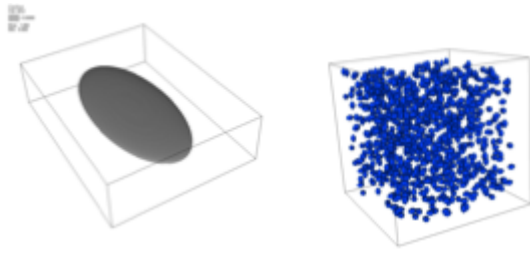


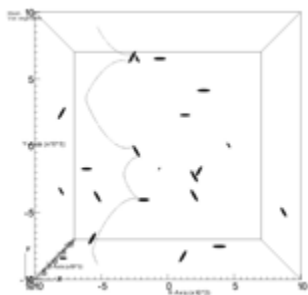
Figure 1. PRISMS-PF simulation of a) equilibrium shape of a  $\beta'$  precipitate in Mg-Nd (considering interfacial energy anisotropy only) and b) large scale simulation of  $\beta'$  precipitation in Mg-Gd.

### Recrystallization and Grain Growth Use Case

Grain size, grain size distribution and grain orientations have a well-documented influence on the mechanical properties of metal alloys. Thus developing methods for predicting these characteristics is an important PRISMS capability. We have developed and parameterized a research Phase Field Crystal (PFC) code. Using PFC, grain boundary energies are calculated over a range of grain misorientation angles. We have also completed recrystallization and grain growth experiments in pure Mg and Mg alloy WE43 for use in phase field model parameterization and validation.

### Tensile Behavior Use Case

An important and unique aspect of the PRISMS Center is the integration of detailed microstructural simulations with property models, and it is in this use case that this is being accomplished. The Tensile Behavior Use Case group is investigating and developing predictive capabilities for a wide range of complex phenomena including dislocation-precipitate and dislocation-dislocation interactions in this hcp system, prediction of alloying effects on solid solution strengthening, prediction and measurements of strain distributions and the propensity for cracking at grain and twin boundaries. We are using ParaDis as the primary dislocation dynamics code to be integrated into the PRISMS framework, in collaboration with LLNL. We have modified the code to incorporate the effects of precipitate strengthening as shown in Figure 2. Using experimentally-obtained microstructure images as input, the response of crystalline aggregates to mechanical loading has been computed using the PRISMS-Plasticity code. The single crystal response in this code is based on evolution laws for micro-scale state variables, namely, slip and twin system resistances. In addition, using variational multiscale method (VMM), the crystal plasticity computations were extended towards modeling 2D fracture under static and cyclic loading. Using *in-situ* distortion-corrected image correlation combined with scanning electron microscopy (SEM-DIC), full-field maps of deformation are captured on fields of view ranging from the length scale of capturing twinning inside a single grain to the statistical behavior of a collection of grains. Electron backscatter diffraction data of full-field crystallographic information are mapped into PRISMS-Plasticity, which allows the experimental deformation fields from SEM-DIC and predicted deformation fields from CPFE to be compared. Using this method, slip systems, twinning, macroscopic and microscopic strain localization and microstructural level strain gradients were clearly and quantitatively resolved. Advanced computational methods being developed for this use case include PRISMS-RSDFT and an advanced phase field technique for mechanically driven transformations such as twins. PRISMS-RSDFT has been used to conduct studies on the energetics of dislocations to determine the dislocation core-size and quantification of the dislocation core-energy in aluminum. This



study revealed that the electronic-structure perturbations arising from the edge-dislocation in aluminum are present up to  $10|b|$  from the dislocation line.

*Figure 2. ParaDis simulation of dislocation on basal plane interacting with gamma precipitates in a Mg-Al-Zn alloy. Precipitates were measured experimentally, stored in The Materials Commons and mapped to ParaDis.*

### Fatigue Behavior Use Case

The Fatigue Behavior Use Case group is developing capabilities for predicting the role of alloying and microstructure on the low cycle fatigue response and the growth of microstructurally small fatigue cracks in Mg alloys. Crack propagation under cyclic loading is modeled using the PRISMS-Plasticity code with the addition of cohesive elements. We are focused on predicting the propagation path (and ultimately propagation rates) of microstructurally and physically small cracks growing from micro-notches. Analytical methods were developed to directly calibrate cohesive parameters from targeted fatigue crack growth experiments. The model is used to identify microstructure-sensitive crack growth processes and to explore the role of grain size (hard/soft grains) and role of misorientations on crack propagation. The experimental program in fatigue integrates new fundamental observations of the earliest stages of fatigue crack initiation and propagation from notches with multiscale modeling efforts. We employ a unique ultrasonic fatigue capability that allows *in situ* observation of crack initiation and early crack propagation in a state-of-the-art SEM system, where high resolution observations of fatigue damage accumulation, crack initiation from notches, and the interaction of small fatigue cracks with microstructure can be studied (see Fig. 3).

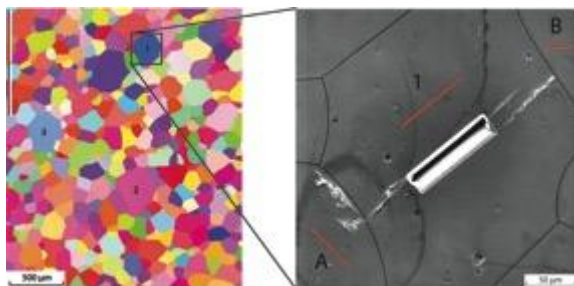


*Figure 3. (a) EBSD image of the sample microstructure with three grains identified for micronotches. (b) SEM image with crack propagation reorientation at boundary 1/A ( $85^\circ$  tilt and  $30^\circ$  twist) and arrest at boundary 1/B ( $43^\circ$  tilt and  $82^\circ$  twist). Grain boundaries are outlined in black and red lines indicate basal traces*

### ***The Materials Commons***

The Materials Commons is designed to be a general repository and collaboration platform for the metals community in the PRISMS technical emphasis areas (microstructural evolution and mechanical properties). We envision the Materials Commons becoming a continuous, seamless part of the scientific workflow. The Materials Commons has been under constant development since the program inception, and is now being used regularly by about 25 members of the PRISMS community. There are three main focus areas for Materials Commons: the data model for representing scientific data provenance, website design and usability, and development of secure and scalable storage and access. Materials Commons stores not only the data generated from experiments or simulations but also inter-relationships between these data and associated meta-data. In collaboration with students from the University of Michigan School of Information, we conducted multiple user reviews and applied standard heuristics to continuously measure and improve website usability. The Materials Commons backend is designed to provide data security along with performance. The entire code base has been open-sourced and progress can be tracked at <https://github.com/materials-commons>.

## Publications

1. S. Rudraraju, A. Van der Ven and K. Garikipati, "Three-dimensional iso-geometric solutions to general boundary value problems of Toupin's gradient elasticity theory at finite strains", *Comp. Meth. App. Mech. Engrg.* (2014)
2. P. Motamarri, V. Gavini, "A subquadratic-scaling subspace projection method for large-scale Kohn-Sham DFT calculations using spectral finite-element discretization", *Phys. Rev. B* 90 115127 (2014).
3. M. Iyer, B. Radhakrishnan, V. Gavini, "Electronic structure study of an edge dislocation in aluminum and the role of macroscopic deformations on its energetics", *J. Mech. Phys. Solids*, (2015).
4. V. Sundararaghavan, S. Sun, "Modeling crack propagation in polycrystalline alloys using a variational multiscale cohesive method," 2nd World Congress on Integrated Computational Materials Engineering (Edited by M. Li et. al.), Wiley, New York, p. 225-230 (2013).
5. S. Panwar, V. Sundararaghavan, "Modeling fatigue failure using variational multiscale method", *Computational mechanics* (2015).
6. S. Sun and V. Sundararaghavan, "Modeling crack propagation in polycrystalline microstructure using variational multi-scale method", *International Journal of Solids and Structures*, (2015).
7. E. Sitzmann and E. A. Marquis, Chemistry and morphology of  $\beta'$  precipitates in an aged Mg-Nd-Y-Zr alloy, *Philosophical Magazine Letters*, (2015).

## Structure/Property Relationships in Two-Phase f.c.c./B2 FeNiMnAl Alloys

Ian Baker

Thayer School of Engineering, Dartmouth College, Hanover, New Hampshire, 03755

[Ian.Baker@Dartmouth.edu](mailto:Ian.Baker@Dartmouth.edu)

### Program Scope

The aim of the work proposed here is to develop an understanding of the microstructural stability and deformation mechanisms that control the strength of these potentially-useful f.c.c./B2 FeNiMnAl alloys over a range of temperatures and strain rates. The work includes examining the effects of additional elemental additions and TEM *in-situ* straining studies.

### Recent Progress

As-cast  $\text{Fe}_{28}\text{Ni}_{18}\text{Mn}_{33}\text{Al}_{21}$ , which consists of aligned, 50 nm, (Ni, Al)-rich B2 and (Fe, Mn)-rich f.c.c. phases (see Figure 1a), was annealed at a variety of temperatures up to 1423 K for up to 250 h and the microstructures and mechanical properties were examined. It was shown that the as-cast microstructure arises from a eutectoid transformation at  $\sim 1300$  K. Annealing at temperatures  $\leq 1073$  K produces  $\beta$ -Mn-structured precipitates, while annealing at temperatures  $> 1073$  K leads to dramatic coarsening of the two-phase B2/f.c.c. microstructure, but does not produce  $\beta$ -Mn precipitation. Interestingly, annealing at temperatures  $> 1073$  K delays the onset of  $\beta$ -Mn precipitation during subsequent anneals at lower temperatures. Coarsening the B2/f.c.c. lamellar structure by annealing at higher temperatures softens it and leads to increases in ductility, from fracture before yield to  $\sim 8\%$  elongation: the presence of  $\beta$ -Mn precipitates makes the fine, brittle B2/f.c.c. microstructures even more brittle, but significant ductility is possible even with  $\beta$ -Mn precipitates present if the B2/f.c.c. matrix is coarse and more ductile.

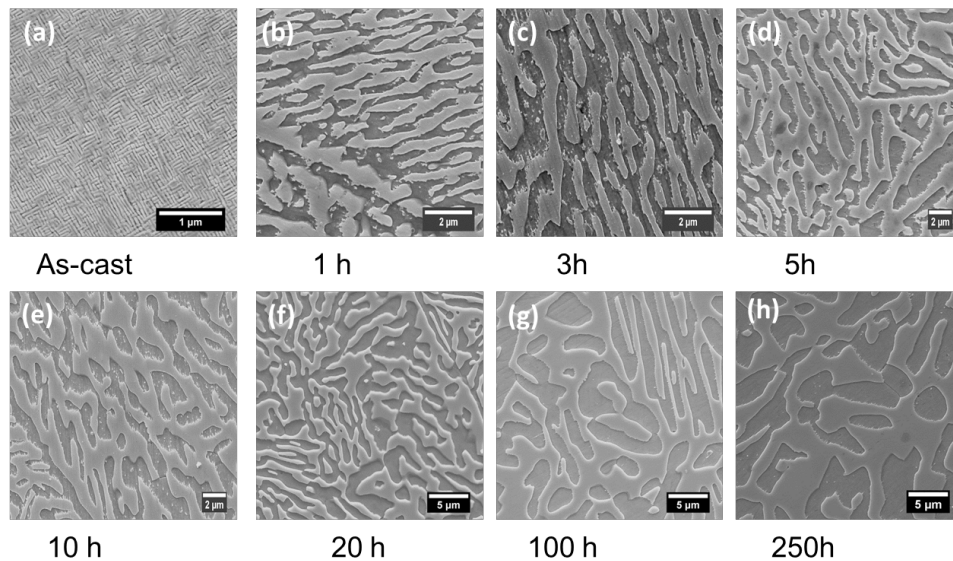


Figure 1. Secondary electron images of  $\text{Fe}_{28}\text{Ni}_{18}\text{Mn}_{33}\text{Al}_{21}$  annealed at 1173 K for different times.

Annealing at 1173 K for times up to 250 h was used to generate a wide range of phase widths (50 nm - 2.5  $\mu\text{m}$ ), see Figure 1, over which to quantify the effects of changing the phase width,  $\lambda$ , on the mechanical properties. The coarsening kinetics over this two orders of magnitude change could be described by  $r^2 - r_0^2 = kt$ , where  $r$  is the average of the B2 + f.c.c. phase widths

after time  $t$  at 1173 K,  $r_0$  is initial phase width, and  $k$  is a constant. It was found that the yield strength,  $\sigma_y$ , follows a Hall-Petch-type relationship, i.e.  $\sigma_y = \sigma_0 + k_y \lambda^{-1/2}$ , where  $\sigma_0$  is the strength for the single-phase material, and  $k_y$  is a constant. Interestingly, the work-hardening rate also followed a  $\lambda^{-1/2}$  relationship, while the elongation to failure increased as  $\lambda$  increased from failure before yielding in the as-cast material to  $\sim 7\%$  for the material with the largest  $\lambda$ , see Figure 2.

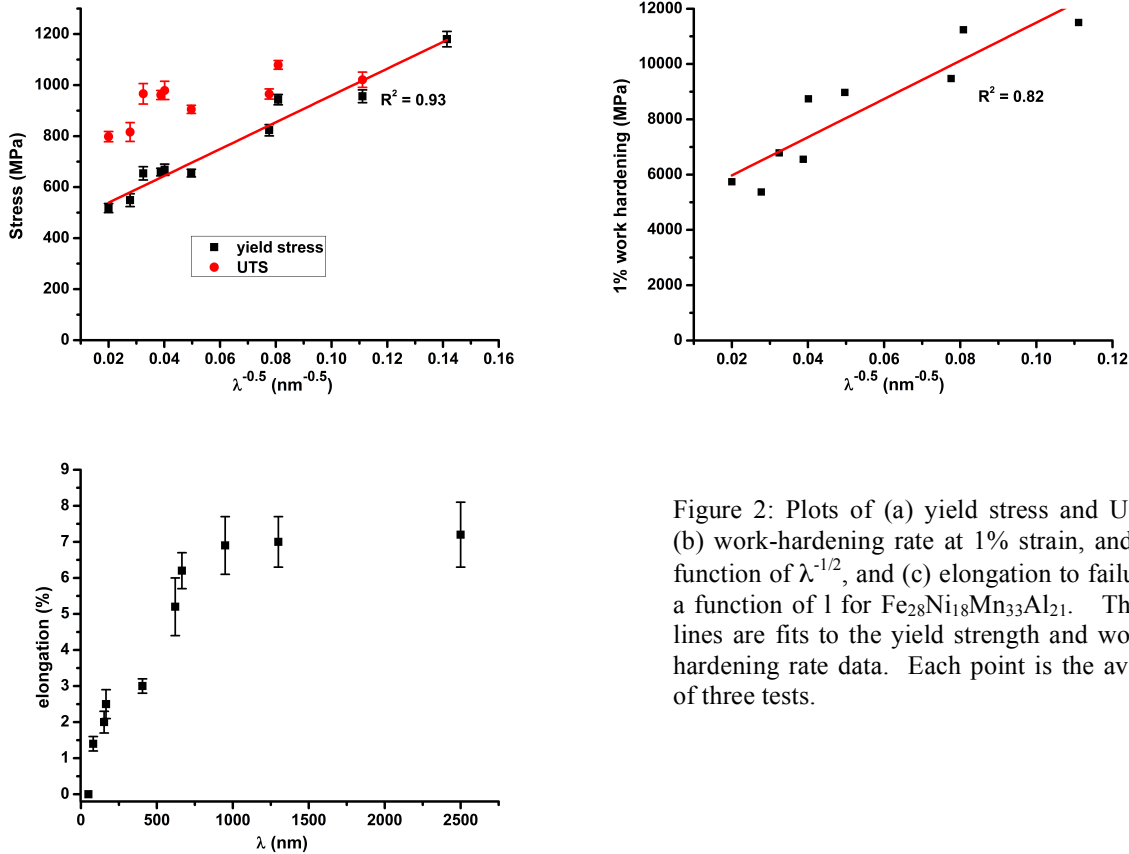


Figure 2: Plots of (a) yield stress and U.T.S., (b) work-hardening rate at 1% strain, and as a function of  $\lambda^{-1/2}$ , and (c) elongation to failure as a function of  $l$  for  $\text{Fe}_{28}\text{Ni}_{18}\text{Mn}_{33}\text{Al}_{21}$ . The red lines are fits to the yield strength and working hardening rate data. Each point is the average of three tests.

Cold rolling was performed on the as-cast, two-phase (f.c.c. + B2), lamellar-structured, high entropy alloy  $\text{Fe}_{28.2}\text{Ni}_{18.8}\text{Mn}_{32.9}\text{Al}_{14.1}\text{Cr}_6$  and a similarly-structured, four-component alloy  $\text{Fe}_{36}\text{Ni}_{18}\text{Mn}_{33}\text{Al}_{13}$ . After cold-rolling the alloys were annealed at temperatures from 973-1273 K, and the resulting microstructures were examined and the room temperature tensile properties were determined. Annealing led to recrystallization to an equi-axed, duplex, sub-micron grain structure consisting of discrete B2 and f.c.c. grains with small changes in the compositions of the phases, see Figure 3. Interestingly, the Cr addition led to an increase in the recrystallization kinetics. The recrystallized alloys both showed yield strengths of  $\sim 600$  MPa and elongations of  $\sim 20\%$ , which was only slightly different from the mechanical properties of the as-cast lamellar-structured alloys, a feature ascribed to the similarity in the scale of the microstructure in the two states. It was shown that while initial plastic strain occurs only in the softer f.c.c. phase, eventually plastic deformation takes place in both phases.

$\text{Fe}_{30}\text{Ni}_{20}\text{Mn}_{35}\text{Al}_{15}$ , which also consists of submicron scale alternating B2 and f.c.c. lamellae, can show a room temperature yield strength of 600 MPa and elongation of  $\sim 10\%$  at a strain rate of  $3 \times 10^{-3} \text{ s}^{-1}$ , but suffers from environmental embrittlement such that at slow strain rates ( $3 \times 10^{-6} \text{ s}^{-1}$ ) elongations of  $< 1\%$  are observed. It was found that the addition of Cr alleviates this



embrittlement and results in a change to a ductile, dimple-type fracture, see Figure 4. X-ray photoelectron spectroscopy showed that this was related to chromium oxide formation on the specimen surface.

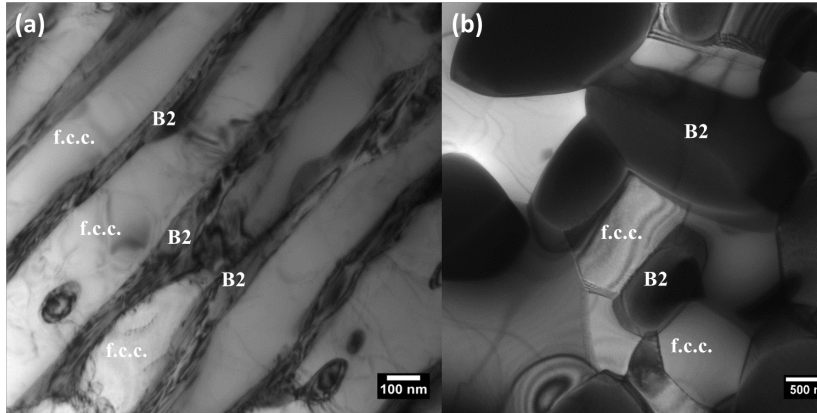


Figure 3. BF TEM images of  $\text{Fe}_{28.2}\text{Ni}_{18.8}\text{Mn}_{32.9}\text{Al}_{14.1}\text{Cr}_6$  in (a) the as-cast condition, and (b) after cold-rolling to a 60% thickness reduction and annealing at 1273 K for 1 h.

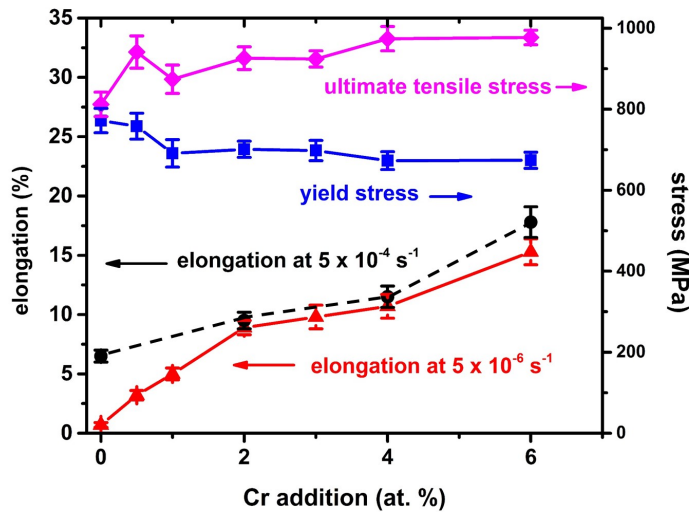


Figure 4. Room temperature elongation, yield stress and UTS as a function of at. % Cr added to  $\text{Fe}_{30}\text{Ni}_{20}\text{Mn}_{35}\text{Al}_{15}$  tested at a strain rate of  $5 \times 10^{-6} \text{ s}^{-1}$ . The elongation is shown for tests performed at  $5 \times 10^{-4} \text{ s}^{-1}$  when environmental embrittlement does not occur.

### Future Plans

We are examining the effects of both interstitials, and cold rolling and recrystallization on the microstructure and mechanical properties of both two-phase and single-phase FeNiMnAl alloys.

### Participants/Collaborators

Dr. F. Meng (*Ph.D. student/Postdoctoral Fellow*), Z. Wang (*Ph.D. student*), C. Cheng (*undergraduate*), R.A. Strain (*undergraduate*), S. Bauer (*undergraduate*), R. Harder (*undergraduate*), M.E. Schwalbe (*undergraduate*), Dartmouth College  
 P.-B. Nebel, A. Brandenburg (*undergraduate exchange students*), Helmut Schmidt Univ., Germany  
 M. Nagpal - *High school student, Los Angeles*  
 Prof. P.R. Munroe, *Dept. of Materials Science and Engineering, U. New South Wales, Australia*,  
 Dr. Z. Cai, Dr. S. Chen, *X-ray Science Division, Advanced Photon Source, ANL*.  
 Professor Y. Liu, Dr. J. Qiu (*exchange Ph.D. student*), *Central South Univ., Changsha, PRC*.  
 Dr. H. Bei, Dr. M.K. Miller, Dr. K. More, *Materials Science and Technology Division, ORNL*  
 Professor Yifeng Liao, *Northwestern University*



### Publications

1. Wu, X., I. Baker, H. Wu and P.R. Munroe, “Accelerated precipitation due to mechanical milling of two-phase B2/L2<sub>1</sub> Fe<sub>30</sub>Ni<sub>20</sub>Mn<sub>20</sub>Al<sub>30</sub>, J. Alloys and Compounds, 559 (2013) 97–100.
2. Wu, X., and I. Baker, “Dislocations in Nanostructured Two-Phase Fe<sub>30</sub>Ni<sub>20</sub>Mn<sub>20</sub>Al<sub>30</sub>“, *Microscopy Research and Technique*, 76 (2013) 263–267.
3. Wu, X., I. Baker, H. Wu. M. K. Miller, K. L. More, Z. Cai and S. Chen, “Microstructure and Mechanical Properties of Two-Phase Fe<sub>30</sub>Ni<sub>20</sub>Mn<sub>20</sub>Al<sub>30</sub> Alloy, Part I: Microstructure”, *J. Materials Science*, 48 (2013) 7435-7445.
4. Wu, X., I. Baker and H. Wu. “Microstructure and Mechanical Properties of Two-Phase Fe<sub>30</sub>Ni<sub>20</sub>Mn<sub>20</sub>Al<sub>30</sub> Alloy, Part II: Mechanical Properties”, *J. Materials Science*, 48 (2013) 6535–6541.
5. Qiu, J., I. Baker, Y. Liu and P.R. Munroe, “The effect of Stoichiometry on the Dry Sliding Wear of FeAl”, *Intermetallics*, 40 (2013) 19–27.
6. Wu, X., F. Meng, I. Baker and P.R. Munroe, “An Overview of Dry Sliding Wear of Two FeNiMnAl Alloys”, *MRS Proceedings*, **1516** (2013).
7. Wu, X., I. Baker, H Wu and P.R. Munroe, “The Mechanical Properties of Near-equiatomic B2/f.c.c. FeNiMnAl Alloys”, *MRS Proceedings*, **1516** (2013).
8. Baker, I., X. Wu, F. Meng and P.R. Munroe, “An Overview of the Microstructures and Mechanical Properties of FeNiMnAl Alloys” *Materials Science Forum*, **783-786** (2014) 2549-2554.
9. Qiu, J., Y. Liu, F. Meng, I. Baker, and P.R. Munroe, “Effects of environment on dry sliding wear of powder metallurgical Ti-47Al-2Cr-2Nb-0.2W”, *Intermetallics*, **63** (2014) 10-19.
10. Wu, X. and I. Baker, “Dislocations in B2/L2<sub>1</sub> Fe<sub>30</sub>Ni<sub>20</sub>Mn<sub>20</sub>Al<sub>30</sub> after High Temperature Deformation”, *Proceedings of Microscopy and Microanalysis*, Indianapolis, IN, 4-8<sup>th</sup>, 2013
11. Meng, F., S.F. Bauer, Y. Liao and I. Baker, “Concentration dependence of Cr for alleviating environmental embrittlement in Fe<sub>30</sub>Ni<sub>20</sub>Mn<sub>35</sub>Al<sub>15</sub>” *Intermetallics*, **56** (2015) 28-32.
12. Meng, F. and I. Baker, “Nitriding of a High Entropy FeNiMnAlCr Alloy”, *J. Alloys and Compounds*, **645** (2015) 376–381.
13. Baker, I. and F. Meng, “Lamellar Coarsening in Fe<sub>28</sub>Ni<sub>18</sub>Mn<sub>33</sub>Al<sub>21</sub> and its Influence on Room Temperature Tensile Behavior”, *Acta Materialia*, **95** (2015) 124–131.
14. Meng, F., J. Qiu, I. Baker and H. Bei, “The effects of annealing on the microstructure and mechanical properties of Fe<sub>28</sub>Ni<sub>18</sub>Mn<sub>33</sub>Al<sub>21</sub>”, *J. Materials Science*, in press.
15. Meng, F., I. Baker and A. Brandenburg, “The Effect of Recrystallization on the Microstructure and Mechanical Behavior of a Novel FeNiMnAlCr High Entropy Alloy”, submitted to the *J. Alloys and Compounds*.

### Patent Applications

- “Fe-Ni-Mn-Al-Cr alloys and Methods for Production Thereof” Ian Baker, Fanling Meng, Jingwen Qiu, Filed 3/21/2014
- “Nitriding to Harden the Surface of FeNiMnAlCr Eutectic Alloys”, Fanling Meng and Ian Baker, Filed 7/20/2014
- “Improving the Mechanical Properties of Eutectic Fe-Ni-Mn-Al Alloys by Cold Work and Annealing”, Ian Baker, Fanling Meng and André Brandenburg, Filed 11/10/2014.

## Materials for Extreme Irradiation Environments

Pascal Bellon<sup>1</sup>, Robert S. Averback<sup>1</sup>, Shen J. Dillon<sup>1</sup>, William P. King<sup>2</sup>, Dallas R. Trinkle<sup>1</sup>

<sup>1</sup> Department of Materials Science and Engineering, University of Illinois at Urbana-Champaign, Urbana, IL.

<sup>2</sup> Department of Mechanical Science and Engineering, University of Illinois at Urbana-Champaign, Urbana, IL.

### Program Scope

This program has been developing a new approach to the design of radiation resistant materials, based on concepts of nanostructuring and self-organization. While focus is on nuclear applications, we expect that the scientific advancements brought forth by this Cluster will have broad impact on materials needs for a number of other advanced energy technologies. The Cluster focuses on the fundamental processes controlling the formation of novel, self-organized, nanostructured materials, their long-term structural and dimensional stability, and the relationships between the nanoscale features and the macroscopic properties. The research combines irradiation experiments, *in situ* and *ex situ* characterization of microstructure and properties, and atomistic simulations and continuum modeling.

The program builds on our past work on self organization in binary alloys, extending the approach to ternary and quaternary alloy systems that form stable compounds, in particular silicides, e.g., Cu-Si-X (X=W, Mo, Nb) systems. While these systems add complexity, they offer new degrees of freedom, which greatly expand our control of the stability and properties of self-organized materials. The research additionally explores the roles of sinks and defect fluxes on phase stability and self-organization, using samples fabricated with nanometer precision and characterized by advanced transmission electron microscopy and atom probe tomography techniques. The cluster also evaluates the properties of these new materials: their mechanical strength and their resistance to thermal and irradiation-induced creep. A new apparatus for measuring *in situ* creep properties of highly miniaturized samples under elevated temperature irradiation is under advanced stages of development. This research integrates experiments with atomistic and continuum modeling for elucidating mechanisms, analyzing results and designing experiments. The modeling combines first principles calculations with atomistic and continuum modeling, emphasizing the coupling between point defects, solute atoms, defect sinks, and applied and internal stresses. We presently investigate non-equilibrium segregation to sinks and its effects on climb and creep rates model on Cu-Si alloys. The model will soon be extended to

Cu-Si alloys with nanoprecipitate defect sinks, and compared with our own experimental measurements on irradiation creep rate in nanostructured Cu-Si-X alloys.

## Recent Progress

**1. Compositional patterning in ternary alloys.** We have shown that nanostructuring by intracascade precipitation, which we originally observed in highly immiscible binary alloys such as Cu-W and Cu-Mo, can also be employed to induce the formation of high number density of nanoscale precipitates such as carbides, e.g., in Ni-W-C [1], and silicides, e.g., in Cu-Mo-Si [2]. These systems offer additional control of the size and stability of self-organized nanoprecipitates, as the free energy of formation of these compounds can be made very large, as illustrated in Fig. 1, where nanoprecipitates in  $\text{Cu}_{89}\text{Si}_{7.5}\text{Mo}_{3.5}$ , have been stabilized to 750 °C.

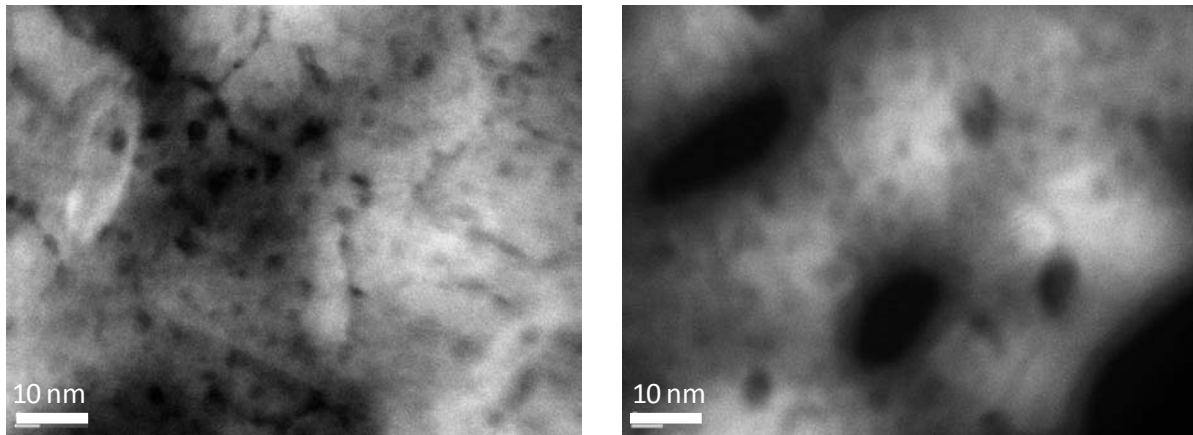


**Fig. 1.** Z-contrast STEM images from plane view samples of  $\text{Cu}_{89}\text{Si}_{7.5}\text{Mo}_{3.5}$  irradiated at RT with 1.8 MeV Kr ions to a dose of  $2 \times 10^{16}$  ions/cm<sup>2</sup> (left) and then annealed at 750 °C for 1 hour (right). The average size of the silicide precipitates (dark contrast) remains below 3 nm, despite the high temperature annealing.

**2. Direct measurement of interfacial sink strength.** The ability of sinks to absorb point defects, quantified by the sink strength, plays an important role in materials under irradiation but few (if any) direct measurements of sink strengths are available. We addressed this important problem by measuring local radiation-enhanced diffusion coefficients,  $D_{RED}^*$ , in Cu using Au tracer atoms [3]. Thin films with buried Au layers are irradiated at different temperatures with 1.8 MeV Kr ions and the diffusion coefficients measured. The success of this method relies on the ability to measure “buried” tracer profiles and associated diffusion coefficients over lengths scales less than 20 nm using energy dispersive spectroscopy in a high-resolution scanning transmission electron microscope. The experiments determined the shape of the vacancy concentration gradient near the interface, the thickness dependence of the excess vacancy concentration at the center of films, and the temperature dependence of the vacancy concentration in several model systems, Cu/Nb and Cu/V, which have a Kurdjumov-Sachs orientation relationship, and Cu/Ni, which is cube-on-cube. These data allow the sink efficiencies  $\eta = J_{meas}/J_{ideal}$ , of the different types of interfaces to be quantified via fitting the

experimental results to appropriate kinetic rate equations or KMC simulations. Good qualitative agreement is found for the sink efficiencies between these experiments and MD simulations.

**3. In-situ measurement of irradiation-induced creep.** A new creep apparatus was constructed to measure the creep response of miniaturized metal pillars during room temperature and elevated temperature ion irradiation. The sub - 1  $\mu\text{m}$  diameter pillars can be cut from either bulk samples or thin films using FIB. We used this method to perform a comparative experimental

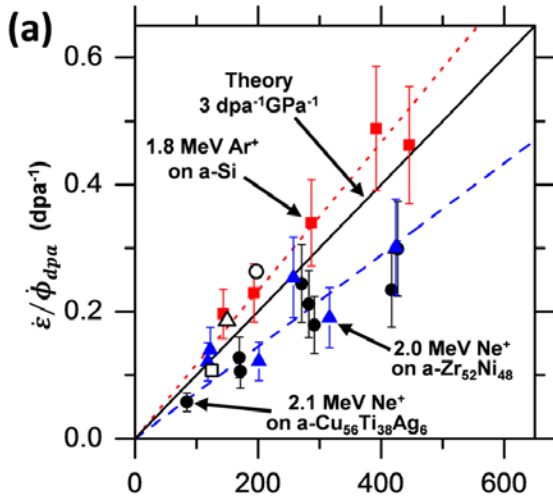


**Fig. 2.** Normalized strain rate as a function of the absolute value of micropillar stress, in Mpa. The filled symbols are the results from the present study and agree very well with the theoretical predictions (solid line).

mean-field (SCMF) kinetic approach offers a new and powerful computational framework for modeling alloy evolutions under irradiation. We selected the dilute  $\text{Ni-Si}$  alloy system as a test system since detailed experimental studies point to a strong drag of solute atoms by point defects fluxes under irradiation, leading to Si segregation and  $\text{Ni}_3\text{Si}$  precipitation even in *undersaturated* solid solutions [5, 6]. In collaboration with Dr. Maylise Nastar at CEA-Saclay, we have introduced several key developments to the SCMF method, allowing in particular for a general modeling of vacancy-driven solute drag in BCC alloys [7], FCC alloys [8], and FCC alloys under strain [9, 10]; we have also demonstrated that the effect of strain on transport coefficients can be directly predicted from atomistic calculations on unstrained cells using the elastic dipole model [11]. Our results on the effect of strain on diffusion have direct implications on the flow of solute in materials containing internal stresses, as illustrated in Figure 3 by the diffusion field near a dislocation core. These results are significant as they bear directly on the effect of alloying elements on irradiation creep, for which little is currently known.

analysis of irradiation-induced creep in a variety of amorphous materials with very different types of bonding, in order to elucidate the mechanisms responsible for creep in these materials [4]. The results show strong support for the point defect model of plastic flow in a- $\text{Cu}_{56}\text{Ti}_{38}\text{Ag}_6$ , a- $\text{Zr}_{52}\text{Ni}_{48}$ , and a-Si. The model also works well a- $\text{SiO}_2$  when electronic excitation is not too large (for example during 1.8 MeV Kr irradiation or fast neutron irradiation). In general, however, the electronic excitation in ion irradiated a- $\text{SiO}_2$  irradiation creates thermal spikes along the track substantially increasing the fluidity.

#### 4. Modeling of alloy kinetics in the presence of strain.

The self-consistent

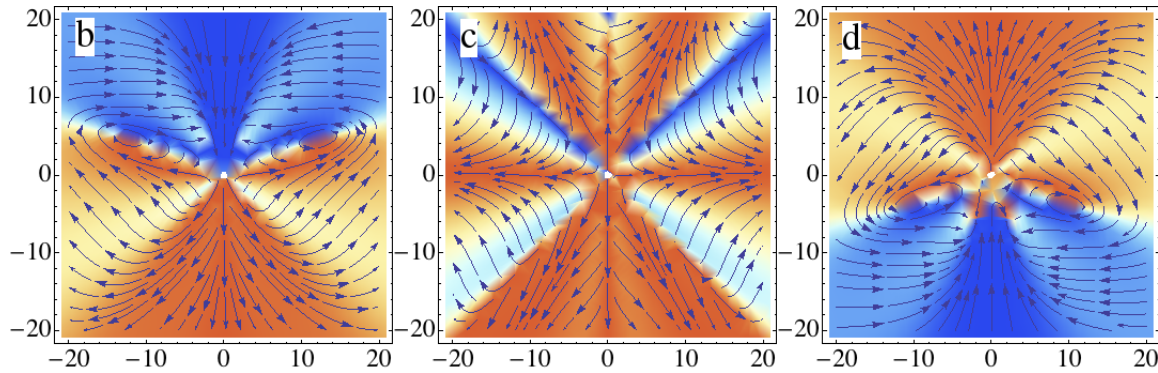


**Fig. 3.** Initial silicon flow due to vacancy flux induced by volumetric strain of an edge dislocation in Ni 50K below crossover, at crossover and 50K above crossover. The color indicates flow into (blue), away from (orange), or perpendicular to (white) the dislocation core. The anisotropy in mobility (Onsager) tensor, which is heterogeneous in space, leads to unusual flow patterns around the dislocation core, located in the center of each plot.

## Future Plans

The Cluster will continue to investigate irradiation-induced self-organization in complex ternary and quaternary alloys in order to improve the resistance of these nanostructures to elevated temperature irradiation and annealing. We will also investigate the possibility of synthesizing these structures by a different non-equilibrium process, this time relying on severe plastic deformation, such as ball milling and high-pressure torsion. In addition to the fundamental interest in understanding non-equilibrium self-organization, it can also offer synthesis approaches that overcome limitations encountered with using thin film deposition. We will extend our work on sink efficiencies from pure Cu to self-organized nanostructures. In particular we will study the effect of particle structure (elemental phase versus intermetallics), coherency (by varying its size), and core/shell structuring on sink strength. We will extend our in-situ irradiation creep experiments to elevated temperatures, in order to assess whether nanostructuring by precipitation and by grain boundary segregation can be used to suppress creep rates. Lastly, we will continue to develop the SCMF model and couple it to phase field modeling, so as to determine dislocation climb rate, and thus creep rates, in alloys with and without nanostructuring. These predictions will be compared to our experimental measurements.

## References

- [1] J. Lee, C. R. Lear, X. Zhang, P. Bellon, R. S. Averback, *Metall Mater Trans* **46a**, 1046 (2015).
- [2] J. Lee, J. Beach, X. Zhang, R. S. Averback, and P. Bellon, In preparation.
- [3] S. M. Mao, S. P. Shu, J. Zhou, R. S. Averback, and S. J. Dillon, *Acta Materialia* **82**, 328 (2015).
- [4] S. Özerinç, R. S. Averback, and W. P. King, *Journal of Nuclear Materials* **451**, 104 (2014).
- [5] A. Barbu and A. J. Ardell, *Scripta Metallurgica* **9**, 1233 (1975).
- [6] A. Barbu and G. Martin, *Scripta Metallurgica* **11**, 771 (1977).
- [7] T. Garnier, M. Nastar, P. Bellon, and D. R. Trinkle, *Phys Rev B* **88**, 134201 (2013).
- [8] T. Garnier, D. R. Trinkle, M. Nastar, and P. Bellon, *Phys Rev B* **89**, 144202 (2014).
- [9] T. Garnier, Z. B. Li, M. Nastar, P. Bellon, and D. R. Trinkle, *Phys Rev B* **90**, 184301 (2014).
- [10] T. Garnier, V. R. Manga, D. R. Trinkle, M. Nastar, and P. Bellon, *Phys Rev B* **88**, 134108 (2013).
- [11] T. Garnier, V. R. Manga, P. Bellon, and D. R. Trinkle, *Phys Rev B* **90**, 024306 (2014).

## Publications

1. Garnier, T., V.R. Manga, **D.R. Trinkle**, M. Nastar, and **P. Bellon**: Stress-induced anisotropic diffusion in alloys: Complex Si solute flow near a dislocation core in Ni. *Physical Review B* **88**, 134108:1-6 (2013).
2. Garnier, T., M. Nastar, **P. Bellon**, and **D.R. Trinkle**: Solute drag by vacancies in body-centered cubic alloys. *Physical Review B* **88**, 134201:1-16 (2013).
3. Özerinç, S., **R.S. Averback**, and **W.P. King**: In situ creep measurements on micropillar samples during heavy ion irradiation. *Journal of Nuclear Materials* **451**, 104-110 (2014).
4. Stumphy, B., S.W. Chee, N.Q. Vo, **R.S. Averback**, **P. Bellon**, and M. Ghafari: Irradiation-induced patterning in dilute Cu-Fe alloys. *Journal of Nuclear Materials* **453**, 66-74 (2014).
5. Garnier, T., V.R. Manga, **P. Bellon**, and **D.R. Trinkle**: Diffusion of Si impurities in Ni under stress: A first-principles study. *Physical Review B* **90**, 024306:1-9 (2014).
6. Mao, S., S. Özerinç, **W.P. King**, **R.S. Averback**, and **S.J. Dillon**: Effect of irradiation damage on the shear strength of Cu-Nb interfaces. *Scripta Materialia* **90-91**, 29-32 (2014).
7. Tai, K., **R.S. Averback**, **P. Bellon**, N.Q. Vo, Y. Ashkenazy, and **S. J. Dillon**: Orientation relationship formed during irradiation induced precipitation of W in Cu. *Journal of Nuclear Materials* **454**, 126-129 (2014).
8. Garnier, T., **D.R. Trinkle**, M. Nastar, and **P. Bellon**: Quantitative modeling of solute drag by vacancies in face-centered-cubic alloys. *Physical Review B* **89**, 144202:1-15 (2014).
9. Wang, M., N.Q. Vo, M. Champion, T.D. Nguyen, D. Setman, **S. Dillon**, **P. Bellon**, and **R.S. Averback**: Forced atomic mixing during severe plastic deformation: Chemical interactions and kinetically driven segregation. *Acta Materialia* **66**, 1-11 (2014).
10. Garnier, T., Z. Li, M. Nastar, **P. Bellon**, and **D.R. Trinkle**: Calculation of strain effects on vacancy-mediated diffusion of impurities in fcc structures: General approach and application to Ni<sub>1-x</sub>Si<sub>x</sub>. *Physical Review B* **90**, 184301:1-8 (2014).
11. Mao, S., S. Shu, J. Zhou, **R.S. Averback**, and **S. Dillon**: Quantitative comparison of sink efficiency of Cu-Nb, Cu-V, Cu-Ni interfaces for point defects. *Acta Materialia* **82**, 328 (2015).
12. Lee, J., C.R. Lear, X. Zhang, **P. Bellon**, and **R.S. Averback**: Irradiation-induced nanoprecipitation in Ni-W alloys. *Metallurgical and Materials Transactions A* **46A**, 1046-1061 (2015).
13. Stumphy, B., **R.S. Averback**, and **P. Bellon**: Novel nano-scale precipitate structures in ion-irradiated Cu<sub>1-x</sub>V<sub>x</sub> alloys: "Cherry-pit" formation. *Journal of Materials Research* **30**, 170-178 (2015).
14. Badillo, A., **P. Bellon**, and **R.S. Averback**: A phase field model for segregation and precipitation induced by irradiation in alloys. *Modelling and Simulation in Materials Science and Engineering* **23**, 035008:1-24 (2015).
15. Özerinç, S., **R.S. Averback**, and **W.P. King**: In situ measurements of irradiation-induced creep in amorphous Cu<sub>56</sub>Ti<sub>38</sub>Ag<sub>6</sub>, Si and SiO<sub>2</sub> micropillars. *Journal of Applied Physics* **117**, 024310 (2015).

# Characterization & Modeling of Deformation Induced Damage in Titanium Alloys

**Principal Investigators: C.J. Boehlert, T.R. Bieler, M.A. Crimp, and P. Eisenlohr**  
**Michigan State University, 428 S. Shaw Lane, Rm 2527, East Lansing, Michigan 48824**

## Program Scope

We are using a synergistic experimental and computational approach to identify and examine processes that cause damage nucleation at interfaces in two-phase  $\alpha+\beta$  titanium (Ti) alloys. We have systematically studied a near- $\alpha$  phase Ti alloy (Ti-5Al-2.5Sn(wt.%), henceforth referred to as Ti525) and compared the results with work on commercially pure (CP) Ti in order to determine how differences in composition and microstructure affect the processes that cause damage nucleation at interfaces at ambient and elevated temperature. We have characterized heterogeneous deformation behavior and slip system activity as a function of temperature using slip trace analysis, as well as instances of slip transfer and grain boundary deformation behavior of this alloy, and compared the results to single-phase  $\alpha$  CP Ti. Using this knowledge to examine the deformation behavior in more complex and commercially important two-phase  $\alpha+\beta$  Ti-alloy systems is an objective. Successful completion of this research program will establish a modeling paradigm in which the physical processes responsible for damage nucleation in polycrystals can be simulated.

## Recent Progress

A critical component in simulations is development of a constitutive model that activates the different slip systems accurately. We have developed a synergistic experimental and statistical approach to identify the relative slip activity in Ti alloys, and we are developing ways to install measured microstructures using Differential Aperture X-ray Microscopy (DAXM) into a computational crystal plasticity model. Using this approach we have systematically studied two near- $\alpha$  phase Ti alloys; Ti525 and Ti-8Al-1Mo-1V(wt.%) (Ti811), and two two-phase  $\alpha+\beta$  alloys; Ti-3Al-2.5V(wt.%) (Ti325) and Ti-6Al-4V(wt.%) (Ti64), compared the results with work on CP Ti, and simulated one particular microstructural patch in Ti525 to identify origins of unusual deformation modes [1]. More damage was observed in creep tests where grain boundary sliding led to cracking at grain boundaries and triple points. This will be the focus of future work. We have also identified what is needed to carry out credible simulation of microstructural patches, so that weak links in the microstructure can be predicted with confidence based on combining slip trace analysis, DAXM, and microstructure patch simulation. Thus, by continuing to develop modeling efforts to include grain boundary sliding, we anticipate being able to identify why some boundaries slide more than others, while others crack. The following summarizes our findings to date.

### 1. Grain Boundaries and Interfaces in Slip Transfer between the $\alpha$ and $\beta$ Phases

The mechanisms of slip transfer between the  $\alpha$  and  $\beta$  phases in lamellar Ti alloy microstructures have been examined systematically in Ti64 [2,3]. We performed a comparable study of how slip in the  $\alpha$  phase interacts with the  $\beta$  phase in Ti525, when the  $\beta$  phase is globular [4]. The minority  $\beta$  phase in Ti525 resides at  $\alpha$  grain boundaries and triple points as grains that are a few microns in diameter. The orientation relationships between these  $\beta$  grains and their  $\alpha$  neighbors were assessed using EBSD to determine if the Burgers relationship  $\{0001\}\alpha\parallel\{0\ 1\ -1\}\beta$  with  $\langle 1\ 1\ -2\ 0\rangle\alpha\parallel\langle 111\rangle\beta$  is present, as it is well known to exist in lamellar  $\alpha/\beta$  interfaces with the parent  $\beta$  grain. Only 16% of these boundaries were found to be close to this relationship. After deformation, slip trace analysis near about 100  $\alpha/\beta$  interfaces showed that only 38% had visible slip traces in the  $\alpha$  phase abutting the  $\beta$  phase. Less than half of these interfaces exhibited correlated slip transfer across the  $\alpha/\beta$  interface. All 15 of these indicated slip transfer by  $\langle a\rangle$  slip in  $\alpha$  into  $\beta$   $\langle 111\rangle$  slip. The slip



transfer parameter  $m'$  (see [5] for definition) from the 15 instances of slip transfer indicates that there is a 98% confidence that the slip plane alignment favors slip transfer, but only an 80% confidence that the slip direction is correlated. These observations suggested that slip bands in the  $\beta$  phase are stimulated by slip bands in  $\alpha$ . This suggests that the  $\beta$  phase accommodates stress concentrations, which precludes formation of slip bands. Combining the two into an  $m'$  assessment gave only a 30% confidence that the combination of the slip plane and the direction favors slip transfer. This low confidence in  $m'$  differs from other observations in CP Ti and TiAl grain boundaries where  $m'$  combined with a high Schmid factor is effective in predicting conditions that lead to slip transfer [2,3]. However, slip bands are not the only indication of slip activity, as slip can occur in less concentrated ways.

## 2. Comparison of the deformation behavior of CP Ti and Ti525 at ambient and elevated temperatures and different strain rates

The tension and tensile-creep deformation behavior of CP Ti and Ti525 deformed *in-situ* inside a SEM at 23°C and 455°C was compared [1,6]. The yield stress of CP Ti decreased dramatically with increasing temperature, but temperature had much smaller effect on Ti525. EBSD was performed both before and after deformation, and slip trace analysis was used to determine the active slip and twinning systems (Fig. 1), as well as the Schmid factors based on the global stress state. Prismatic slip was the most commonly observed slip system, and it was observed over the entire Schmid factor range, indicating that the local stress tensor varies significantly from the global stress state of uniaxial tension in some locations. Basal slip activity in Ti525 was observed in a larger fraction of grains than in CP Ti, similar to previous observations [7], whereas pyramidal  $\langle c+a \rangle$  slip was more prevalent in CP Ti. Although twinning was an active deformation mode in tension tests of the CP Ti, it was rare in Ti525. At 23°C, the fraction of grains exhibiting obvious slip traces was over 90%, whereas less than 10% of the grains exhibited surface slip traces during creep at 200-250MPa. Instead, grain boundary sliding became prevalent under creep conditions, and it was more apparent in Ti525 than CP Ti. A robust statistical analysis that compensates for the texture was carried out [8] to assess the significance of the comparative activity of the different slip systems under the variety of experimental conditions examined, so that ratios of the CRSS on different slip systems could be extracted.

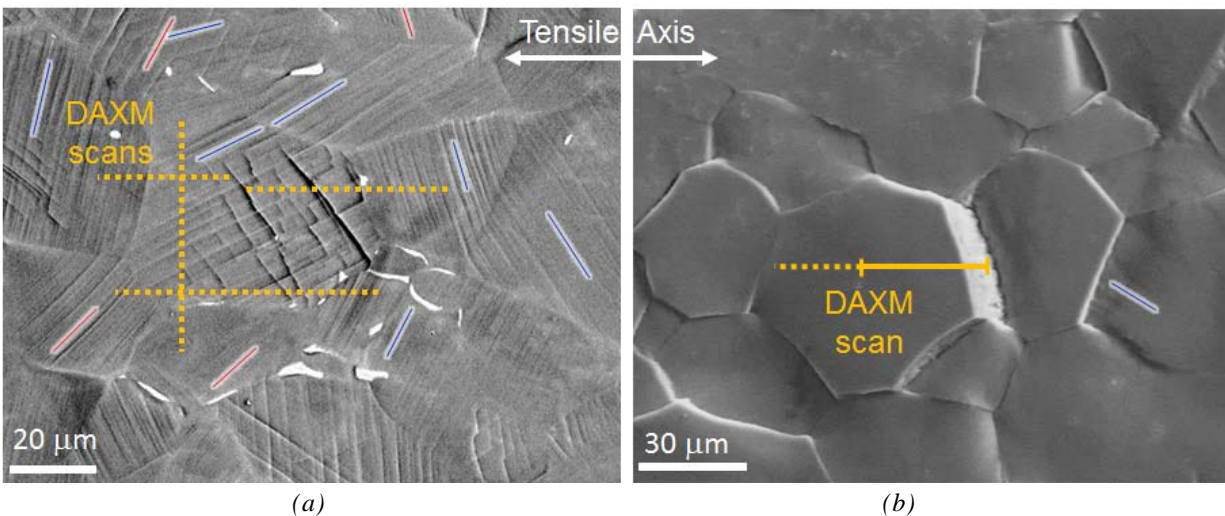


Figure 1. Secondary electron SEM images providing examples of a deformed Ti525 microstructures showing extensive slip bands (blue are basal, red are prism) after 4% tensile strain at 23 °C (a) and grain boundary sliding with few slip bands after 13% creep strain at 455 °C 250 MPa (b). Locations of DAXM scans are indicated. The loading direction was horizontal.



### 3. Heterogeneous strain and cracking in Ti525 and CP Ti

The micrographs in Fig. 1 illustrate extremes in deformation microstructures, with slip bands evident at RT and grain boundary sliding dominant in creep conditions. Grain boundary sliding can cause cracks or pores to develop, as illustrated in Fig. 2, which shows a region with a triple point crack and grain boundary crack. An orientation map is shown to illustrate that there are relatively hard orientations ( $\langle c \rangle$ -axis within  $30^\circ$  of the tensile axis) among at least one of the grains adjacent to each of the cracks. In hard-oriented grains the lack of more easily operated slip systems prevents hard orientations from accommodating shape changes that occur in neighboring grains.

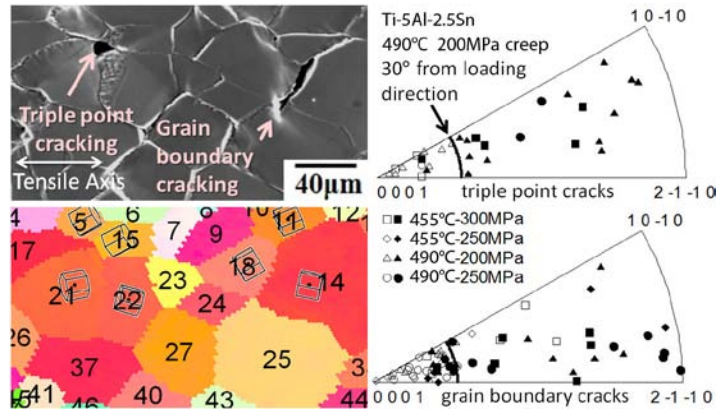


Figure 2. Upper left is a secondary electron SEM image of Ti525 after tensile creep deformation to  $\sim 16\%$  strain at  $490^\circ\text{C}$  and  $200\text{ MPa}$ . Lower left is the EBSD inverse pole figure map of the corresponding microstructural patch before deformation. The right hand side shows inverse pole figures highlighting the grain orientations associated with cracks; open symbols represent the hardest orientations of grain pairs or triples.

### 4. 3D Subsurface Microstructure Characterization and Simulation of dislocation slip

The microstructure surrounding the central grain with irregular edges in Fig. 1a was characterized with DAXM to obtain the subsurface geometry of grains. This information was converted into a 3D mesh and computationally deformed using the (CPFE) model as shown in Fig. 3. This patch was chosen because while fainter basal plane traces are evident, the irregular edges in the grain could not be identified using slip trace analysis, so the origin of these ledges was sought (similar features were observed in about 6 other grains in the neighborhood). The longest of these jagged traces appeared immediately upon yielding. Two meshes were generated, a quasi-3D columnar grain mesh from reconstructed boundary files obtained from EBSD data, and an approximation of the 3D grain shapes using four slices of DAXM data. Phenomenological constitutive model parameters were obtained by computationally deforming 2000 orientations measured by EBSD with an optimization scheme to obtain the measured stress-strain curve. The model 3D grain geometry matched the experimentally-measured orientation changes more accurately [9]. This implies that the grain geometry needs to be accurately represented before details of heterogeneous strain (and damage nucleation mechanisms) can be assessed computationally. This outcome is important because it indicates that using experimental measurements to assess the capability of a simulation model requires a reasonably accurate representation of the grain geometry, so that the more fundamental mechanistic constitutive model features can be properly identified and installed [9].

The model 3D grain geometry matched the experimentally-measured orientation changes more accurately [9]. This implies that the grain geometry needs to be accurately represented before details of heterogeneous strain (and damage nucleation mechanisms) can be assessed computationally. This outcome is important because it indicates that using experimental measurements to assess the capability of a simulation model requires a reasonably accurate representation of the grain geometry, so that the more fundamental mechanistic constitutive model features can be properly identified and installed [9].

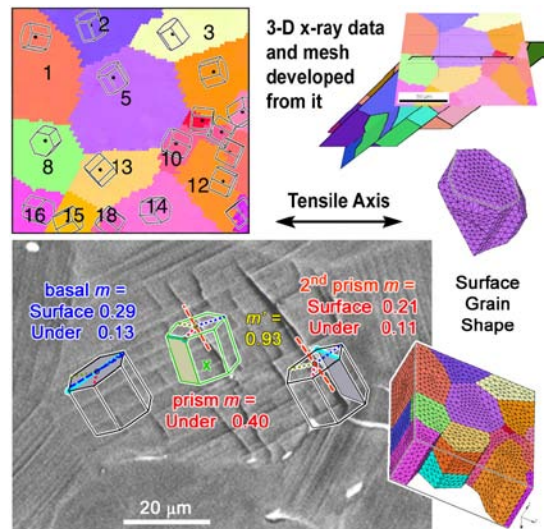


Figure 3. EBSD and 3D orientation data of Ti525 patch with CPFE mesh. The grain below the surface purple grain had highly activated prism slip that forced slip or shear cracking on a second order prism plane in the surface grain.

Given the mesh geometry and constitutive model, it was possible to examine what caused the dramatic

ledges to form. The grain beneath the surface grain in Fig. 3 has an orientation for which the Schmid factor for prism slip is high (green prism). This system has a high degree of geometrical alignment with a second order prism slip system in the surface grain#5, which matched the traces of the ledges. As this is not a commonly observed slip system, either slip or shear cracking occurred due to slip transfer across the subsurface boundary. This indicates that this alloy system may enable modes of deformation not normally observed [5].

### 5. Electron Channeling Contrast Imaging (ECCI) of Dislocations Across Grain Boundaries

An ECC image of dislocations piled up at an R9 incoherent  $\Sigma 3$  twin boundary in polycrystalline Ni is shown in figure 4 (top). TEM style contrast Burgers and line analysis of the dislocations on both sides of the boundary (not shown) indicate that the dislocations on both sides of the boundary have the same Burgers vector and slip plane. This suggests that while the boundary resists the motion of the dislocations, slip transfer across the boundary occurs without the need for complex dislocation reactions. Analysis of a variety of other high angle boundaries, including a coherent  $\Sigma 3$  boundary (Fig. 4 bottom) and a  $\Sigma 9$  boundary, reveal dislocations with different Burgers vectors and slip planes on either side of the boundaries. In these cases, significant strain contrast is observed at the boundaries, consistent with the accumulation of dislocations at the boundaries. This suggests that strain transfer across high angle boundaries, including many “special boundaries”, is difficult and results in localized strain accumulation, which may precede damage nucleation.

### 6. Future Plans

We have developed an integrated experimental measurement and modeling approach that can provide information to assist interpretation of detailed mechanisms of deformation at the mesoscale. Now that this infrastructure is in place, it will be possible to identify discrepancies between mathematical models and experimental observations with a degree of confidence not achieved in the past, focusing on Ti alloys and slip/grain boundary sliding mechanisms. From discrepancies between observations and models, new insights about deformation modes are possible. These insights can be used to more rapidly explore the physical reality that occurs in heterogeneous deformation and damage nucleation processes.

### References

1. H. Li *et al.*, *Phil. Mag.* 92(23), (2012) 2923-2946.
2. M.F. Savage *et al.*, *Phil. Mag.* 84(11), (2004) 1127-1154.
3. M.F. Savage *et al.*, *Mat. Sci. Eng. A*, A319, (2001) 398-403.
4. J.R. Seal *et al.*, *Mat. Sci. Eng. A*, 552, (2012) 61-68.
5. T.R. Bieler *et al.*, *Curr. Opin. Sol. State Mater. Sci.* 18(4), (2014) 212-226.
6. H. Li *et al.*, *Phil. Mag.*, 93(21), (2013) 2875-2895.
7. J.C. Williams *et al.*, *Metall. Mater. Trans.* 33A, (2002) 837-850.
8. H. Li *et al.*, *Acta Materialia* 61, (2013) 7555-7567.
9. C. Zhang *et al.*, *Intern. Jour. of Plasticity*, 69, (2015) 21-35.

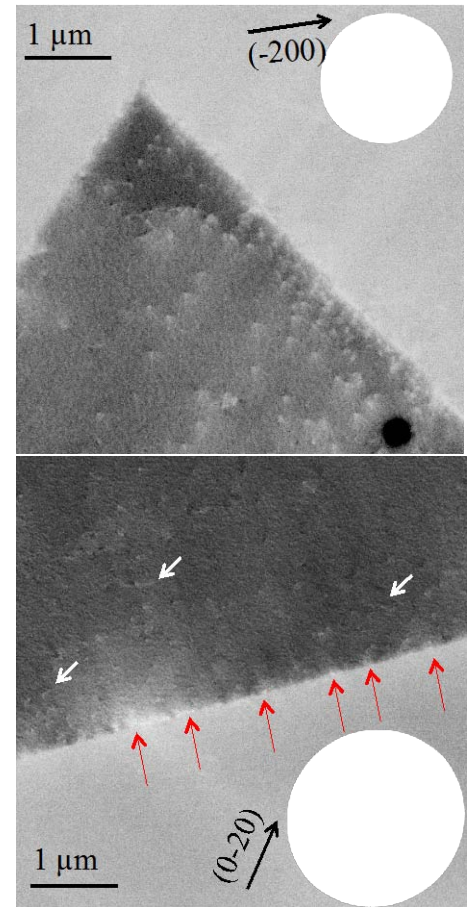


Figure 4. (top) ECC image of dislocations interacting with an R9 incoherent twin boundary in Ni indicates resistance to slip across the boundary but no evidence of dislocation reactions. (bottom) Image of dislocations interacting with coherent  $\Sigma 3$  boundary reveals extensive strain contrast at the boundary, consistent with the accumulation of dislocations during slip transfer.

## Publications (2013-2015)

I.G. Dastidar, A.L. Pilchak, T.R. Bieler, V. Khademi, M.A. Crimp, and C.J. Boehlert, "The Tensile and Tensile-Creep Deformation Behavior of Ti-8Al-1Mo-1V(wt.%)", Materials Science and Engineering A, Vol. 636 (2015) 289-300. doi: 10.1016/j.msea.2015.03.059

H. Li, C.J. Boehlert, T.R. Bieler, and M.A. Crimp, "Analysis of the Deformation Behavior in Tension and Tension-Creep of Ti-6Al-4V(wt.%) at 298K and 728K Using *In-Situ* SEM Experiments", Phil Mag, Vol. 95 no. 7 (2015) 691-729. <http://dx.doi.org/10.1080/14786435.2014.1001459>

C. Zhang, H. Li, P. Eisenlohr, W. Liu, C.J. Boehlert, M.A. Crimp, T.R. Bieler, "Effect of Realistic 3D Microstructure in Crystal Plasticity Finite Element Analysis of Polycrystalline Ti-5Al-2.5Sn", International Journal of Plasticity, Vol. 69 (2015) 21-35. <http://dx.doi.org/10.1016/j.ijplas.2015.01.003>

H. Li, D.E. Mason, T.R. Bieler, C.J. Boehlert, and M.A. Crimp, "Methodology for Estimating the Critical Resolved Shear Stress Ratios of  $\alpha$ -Phase Ti Using EBSD Based Trace Analysis", Acta Materialia, Vol. 61 (2013) 7555-7567. <http://dx.doi.org/10.1016/j.actamet.2013.08.04>

H. Li, C.J. Boehlert, T.R. Bieler, and M.A. Crimp, "Analysis of the Deformation Behavior in Tension and Tension-Creep of Ti-3Al-2.5V(wt.%) at 298K and 728K Using *In-Situ* SEM Experiments", Metallurgical Transactions A, Vol. 45A (2014) 6053-6066. DOI: 10.1007/s11661-014-2576-7

H. Li, D.E. Mason, Y. Yang, T.R. Bieler, M.A. Crimp, and C.J. Boehlert, "Comparison of the Deformation Behavior of Commercially Pure Titanium and Ti-5Al-2.5Sn(wt.%) at 296K and 728K", Philosophical Magazine, Vol. 93 No. 21 (2013) 2875-2895. <http://dx.doi.org/10.1080/14786435.2013.791752>.

T.R. Bieler; P. Eisenlohr; C. Zhang; H.J. Phukan; M.A. Crimp, "Grain boundaries and interfaces in slip transfer", Current Opinion in Solid State and Materials Science, Vol. 18 no. 4 (2014) 212-226.

## **Nanomechanics and Nanometallurgy of Boundaries**

**Brad L. Boyce, Sandia National Laboratories**

### **Program Scope**

Nanostructured metallic alloys have revealed intriguing scientific phenomena such as Hall-Petch breakdown and stress-induced grain growth, yet this class of metals is often plagued by grain structure instability, limited ductility, and a lack of available bulk processing routes. This program fosters a better understanding of grain boundary motion and grain growth as it relates to the unusual mechanical properties of nanostructured metals. While grain instability was once viewed as a detrimental attribute that was difficult to control and predict, our improved understanding of this phenomenon offers the opportunity to tailor stability for particular thermomechanical environments. The driving hypothesis for the current program is that grain instability as manifest in mechanically-induced grain boundary motion can dissipate mechanical energy as a means to enhance the ductility, toughness, fatigue, and wear in nanocrystalline metals. To explore this hypothesis, we are exploring three grain boundary stabilization scenarios: (1) impurity pinning to reduce boundary mobility, (2) solute boundary segregation to reduce the free energy penalty of the boundary, and (3) boundary relaxation to reduce local free volume and entropy. In-situ aberration-corrected TEM will reveal the nature of the defect interactions with grain boundaries and the role of local chemical and structural configurations; cryogenic and high temperature indentation/tension testing will reveal the coupled thermomechanical dependency of boundary processes and quantify the resulting effects on mechanical properties; and high-throughput molecular dynamics modeling will shed light on the unit mechanisms responsible for the experimentally observed behavior.

### **Recent Progress**

In the current year, we continue to examine grain boundary instability of nanostructured metals and the impact of boundary instability on mechanical performance. For this purpose, we rely on (1) thin film processing methods including pulsed laser deposition and magnetron sputtering to produce pure metals and binary nanostructured alloys of varying degrees of thermodynamically predicted stability, (2) in situ deformation, heating, and ion-irradiation of these films in the TEM and synchrotron, and (3) ex situ characterization before and after various mechanical environments (tension, shear, indentation, fatigue, wear).

The presentation will focus on the role of stress-concentrating notches on fatigue behavior of nanocrystalline metals. Recent studies have shown the potential for nanocrystalline metals to possess excellent fatigue resistance compared to ultrafine and coarse grained counterparts (e.g. [1, 2]). Although the mechanical properties of nanocrystalline metals are

believed to be particularly susceptible to material flaws, recent reports suggest that nanocrystalline metals are unexpectedly impervious to stress concentrations, attributed to “extreme stress homogenization” [3, 4]. In the present work, nanocrystalline NiFe samples containing micro-sized notches were tested in tension-tension fatigue. In all notched specimens, dramatic reductions in the fatigue lives were observed (Fig. 1), which correspond to relatively high fatigue stress concentrations and notch sensitivities in the nanocrystalline materials. The apparent contradiction between this result and prior publications can be explained in terms of differences in the ratio of notch size to microstructure size. Furthermore, the notch fatigue study provided additional confirmation of the role of abnormal grain growth on fatigue crack initiation. Microstructural analysis under the fractured notched regions revealed cyclically-induced abnormal grain growth (AGG) as a predominant deformation and crack initiation mechanism during high-cycle fatigue.

The thin film notch fatigue method provides a pathway to drive fatigue-driven microstructural evolution in a spatially localized region. This offers an excellent opportunity to develop new detection techniques to rapidly detect the onset of AGG associated with the emergence of rare, abnormally large grains. Bimodal grain structures are common in many alloys, arising from a number of different causes including incomplete recrystallization and abnormal grain growth. These bimodal grain structures have important technological implications, such as the well-known Goss texture [5] which is now a cornerstone for electrical steels. Yet our ability to detect bimodal grain distributions is largely confined to brute force cross-sectional metallography. We have developed a new method for rapid detection of unusually large grains embedded in a sea of much finer grains. Traditional x-ray diffraction based grain size measurement techniques such as Scherrer, Williamson-Hall [6], or Warren-Averbach [7] rely on peak breadth and shape to extract information regarding the average crystallite size. However, these line broadening techniques are not well suited to identify a very small fraction of abnormally large grains. The present method utilizes statistically anomalous intensity spikes in the Bragg peak to identify regions where abnormally large grains are contributing to diffraction (Fig. 2). This needle-in-a-haystack technique is demonstrated on a nanocrystalline Ni-Fe alloy which has undergone

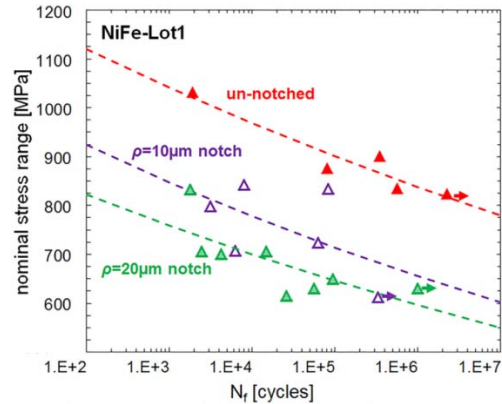


**Figure 1.** Notch-fatigue of nanocrystalline Ni-Fe showing clear stress concentration effect.

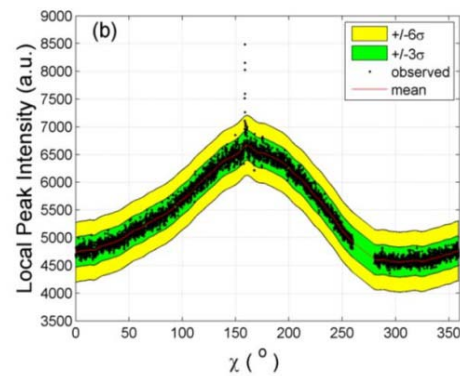


**Figure 2.** A caked (111) diffraction ring with an intensity spike caused by abnormal grain growth.



fatigue-induced abnormal grain growth. In this demonstration, the technique readily identifies a few large grains that occupy less than 0.00001% of the interrogation volume. While the technique is demonstrated in the current study on nanocrystalline metal, it would likely apply to any bimodal polycrystal including ultrafine grained and fine microcrystalline materials with sufficiently distinct bimodal grain statistics.

## **Future Plans**

Moving forward, the focus of the project expands towards binary nanocrystalline alloys with solutes that are chosen to segregate to the grain boundary and lower or eliminate the thermodynamic driving force for grain boundary motion. A key question is whether these thermally stabilized grain boundaries are also stable against mechanical stimuli such as fatigue or wear. To this end, we are developing a phase field model for binary alloy segregation and boundary stabilization. This diffuse-interface model of GB segregation in binary metallic alloys is capable of accounting for bulk thermodynamics, interfacial energies, and the interaction of alloying elements with GBs. In addition, the model will extend current treatments by independently treating solute-solute interactions within both the bulk grain and GB regions, allowing for deviations from dilute and ideal systems and the ability to account for phase separation processes occurring in conjunction with grain growth. This baseline model can be compared against existing observations of thermal stability, but more importantly the model will be modified to include a representation of stress-driven boundary motion.

In addition to the mesoscale phase field model, we will be using molecular dynamics (MD) to examine the atomic-scale unit processes associated with grain boundary motion. Our previous high-throughput MD model indicated that a significant fraction of grain boundary types have a mobility that surprisingly increases or stays constant with decreasing temperature [8]. With that result, we are now selectively comparing specific anti-thermal boundaries to boundaries that are structurally similar but obey conventional Arrhenius kinetics. Specifically we are expecting to determine if the atomic shuffling process for boundary motion is different for the anti-thermal grain boundaries compared to their conventional counterparts.

To complement the modeling results, we will continue to rely on thin film deposition by electroplating, magnetron sputtering, or pulsed laser deposition and thermomechanical testing including indentation, monotonic tension, fatigue, and wear behavior. Specifically, we are investigating more carefully the time-dependent plasticity of nanocrystalline metals. While nanocrystalline metals have long been known to have a high strain-rate sensitivity (SRS), we are examining the interconnections between the SRS, low-temperature primary creep behavior, and stress relaxation behavior. A key question is the relative role of grain boundary motion and stress-induced grain growth on these viscoplastic phenomena. To augment quantitative ex-situ studies that rely on post-mortem TEM and XRD, we also continue to engage in-situ methods for observing microstructural evolution under various driving forces. Specifically in that regard, we are adopting an in-situ MEMS based test platform for stress relaxation studies, and a proprietary technique for in-situ fatigue studies.

Finally, we are proposing to expand our core program to potentially strengthen a focus on the use of in-situ ion irradiation to dynamically alter the local atomic configuration of the grain boundary during thermally- or mechanically-driven grain growth. While the thermodynamic models for binary alloy stabilization predict that certain boundary chemistries will stabilize the microstructure, we hypothesize that grain growth only stops for some grain boundaries – the prior theories treat all grain boundaries equally, yet realistic solute segregation is heterogeneous [9] and different boundary types will have widely varying energetic response [8, 10]. In addition, our prior modeling work demonstrated that a small population of stationary boundaries stops overall grain growth [11]. Sandia’s recently commissioned In situ Ion Irradiation TEM (I<sup>3</sup>TEM) opens up the possibility to directly observe the stabilizing effects of modified grain boundary structure and chemistry during microstructural evolution [12]. The I<sup>3</sup>TEM can dynamically introduce irradiation damage, implant self-ions, or implant alloying species. A potentially definitive set of experiments would be to trigger boundary motion through thermal or mechanical stimulus, accelerate that motion through self-ion knock-on damage, decelerate motion through implantation of a drag species, and finally to stop motion entirely through implantation of a thermodynamic stabilization species. This initial effort focuses primarily on elucidating the effects of self-ion damage on boundary mobility, with anticipated follow-on work in the latter two areas. Atomistic modeling will complement experiments by isolating effects that are difficult to separate experimentally, such as the relative importance of displacement damage and thermal components, the constraining effect of grain ensembles and triple junctions in polycrystals on overall growth behavior, and the effect of grain boundary grooving effect on boundary mobility in electron transparent thin films.

## References

- [1] B. L. Boyce and H. A. Padilla, *Metallurgical and Materials Transactions A*, 2011, vol. 42A
- [2] T. Hanlon, Y. N. Kwon, and S. Suresh, *Scripta Materialia*, 2003, vol. 49, no. 7, pp. 675-680.
- [3] S. Kumar, M. A. Haque, and H. Gao, *Applied Physics Letters*, 2009, vol. 94, no. 25, p. 253104.
- [4] S. Kumar, X. Li, A. Haque, and H. Gao, *Nano Letters*, 2011, vol. 11, no. 6, pp. 2510-2516.
- [5] N. P. Goss, *Transactions of the American Society for Metals*, 1935, vol. 23, no. pp. 511-544.
- [6] G. K. Williamson and W. H. Hall, *Acta Metallurgica*, 1953, vol. 1, no. 1, pp. 22-31.
- [7] B. E. Warren, *Progress in Metal Physics*, 1959, vol. 8, no. pp. 147-202.
- [8] E. R. Homer, E. A. Holm, S. M. Foiles, and D. L. Olmsted, *Jom*, 2014, vol. 66, no. 1, pp. 114-120.
- [9] T. Chookajorn, H. A. Murdoch, and C. A. Schuh, *Science*, 2012, vol. 337, no. 6097, pp. 951-954.
- [10] D. L. Olmsted, E. A. Holm, and S. M. Foiles, "Survey of grain boundary energies in four elemental metals," in *Recrystallization and Grain Growth Iv*. vol. 715-716, E. J. Palmiere and B. P. Wynne, Eds., ed Stafa-Zurich: Trans Tech Publications Ltd, 2012, pp. 179-179.
- [11] E. A. Holm and S. M. Foiles, *Science*, 2010, vol. 328, no. 5982, pp. 1138-1141.
- [12] D. C. Bufford and K. Hattar, *Journal of Materials Research*, 2014, vol. 29, no. 20, pp. 2387-2397.

## Publications

1. X. Zhao, D.J. Strickland, P.M. Derlet, M.-r. He, Y.-J. Cheng, J. Pu, K. Hattar and D.S. Gianola: In situ measurements of a homogeneous to heterogeneous transition in the plastic response of ion-irradiated  $\langle 111 \rangle$  Ni microspecimens *Acta Materialia*. **88**, 121 (2015).
2. X. Yi, M.L. Jenkins, K. Hattar, P.D. Edmondson and S.G. Roberts: Characterisation of radiation damage in W and W-based alloys from 20 MeV self-ion near-bulk implantations *Acta Materialia*. **92(0)**, 163 (2015).
3. F. Ulomek, C.J.O. O'Brien, S.M. Foiles and V. Mohles: Energy conserving orientational force for determining grain boundary mobility *Modelling and Simulation in Materials Science and Engineering*. **23**, 025007 (2015).
4. G.J. Tucker and S.M. Foiles: Quantifying the influence of twin boundaries on the deformation of nanocrystalline copper using atomistic simulations *International Journal of Plasticity*. **65(0)**, 191 (2015).
5. C. Sun, M. Kirk, M. Li, K. Hattar, Y. Wang, O. Anderoglu, J. Valdez, B.P. Uberuaga, R. Dickerson and S.A. Maloy: Microstructure, chemistry and mechanical properties of Ni-based superalloy Rene N4 under irradiation at room temperature *Acta Materialia*. **95(0)**, 357 (2015).
6. J.E. Mogonye, K. Hattar, P.G. Kotula, T.W. Scharf and S.V. Prasad: He implantation for improved tribological performance in Au electrical contacts *Journal of Materials Science*. **50(1)**, 382 (2015).
7. M.T. Janish, P.G. Kotula, B.L. Boyce and C.B. Carter: Observations of fcc and hcp tantalum *Journal of Materials Science*. **50(10)**, 3706 (2015).
8. O. El-Atwani, K. Hattar, J.A. Hinks, G. Greaves, S.S. Harilal and A. Hassanein: Helium bubble formation in ultrafine and nanocrystalline tungsten under different extreme conditions *Journal of Nuclear Materials*. **458**, 216 (2015).
9. O. El-Atwani, S. Gonderman, S. Suslov, M. Efe, G. De Temmerman, T. Morgan, K. Bystrov, K. Hattar and J.P. Allain: Early stage damage of ultrafine-grained tungsten materials exposed to low energy helium ion irradiation *Fusion Engineering and Design*. **93**, 9 (2015).
10. S.W. Chee, S.H. Pratt, K. Hattar, D. Duquette, F.M. Ross and R. Hull: Studying localized corrosion using liquid cell transmission electron microscopy *Chemical communications (Cambridge, England)*. **51(1)**, 168 (2015).
11. B.L. Boyce, T.A. Furnish, H.A. Padilla, D. Van Campen and A. Mehta: Detecting rare, abnormally large grains by x-ray diffraction *Journal of Materials Science*. accepted for publication, (2015).
12. C.M. Barr, L. Barnard, J.E. Nathaniel, K. Hattar, K.A. Unocic, I. Szlurfarska, D. Morgan and M.L. Taheri: Grain boundary character dependence of radiation-induced segregation in a model Ni-Cr alloy *Journal of Materials Research*. **30(09)**, 1290 (2015).
13. J. Sharon, K. Hattar, B. Boyce and L. Brewer: Compressive Properties of  $\langle 110 \rangle$  Cu Micro-Pillars after High-Dose Self-Ion Irradiation *Materials Research Letters*. **2(2)**, 57 (2014).
14. E.R. Homer, E.A. Holm, S.M. Foiles and D.L. Olmsted: Trends in Grain Boundary Mobility: Survey of Motion Mechanisms *JOM*. **66(1)**, 114 (2014).



15. K. Hattar, D.C. Bufford and D.L. Buller: Concurrent in situ ion irradiation transmission electron microscope *Nuclear Instruments and Methods in Physics Research Section B: Beam Interactions with Materials and Atoms*. **338**, 56 (2014).
16. O. El-Atwani, A. Suslova, T. Novakowski, K. Hattar, M. Efe, S. Harilal and A. Hassanein: In-situ TEM/heavy ion irradiation on ultrafine-and nanocrystalline-grained tungsten: effect of 3MeV Si, Cu and W ions *Materials Characterization*. (2014).
17. S.P. Coleman, D.E. Spearot and S.M. Foiles: The effect of synthetic driving force on the atomic mechanisms associated with grain boundary motion below the interface roughening temperature *Computational Materials Science*. **86**, 38 (2014).
18. C. Chisholm, K. Hattar and A.M. Minor: In Situ TEM Concurrent and Successive Au Self-Ion Irradiation and He Implantation *Materials Transactions*. **55**(3), 418 (2014).
19. D.C. Bufford and K. Hattar: Physical response of gold nanoparticles to single self-ion bombardment *Journal of Materials Research*. **29**(20), 2387 (2014).
20. D. Bufford, S.H. Pratt, T.J. Boyle and K. Hattar: In situ TEM ion irradiation and implantation effects on Au nanoparticle morphologies *Chemical Communications*. (2014).
21. J. Brons, J. Hardwick, H. Padilla II, K. Hattar, G. Thompson and B. Boyce: The role of copper twin boundaries in cryogenic indentation-induced grain growth *Materials Science and Engineering: A*. **592**, 182 (2014).
22. C.M. Barr, G.A. Vetterick, K.A. Unocic, K. Hattar, X.-M. Bai and M.L. Taheri: Anisotropic radiation-induced segregation in 316L austenitic stainless steel with grain boundary character *Acta Materialia*. **67**, 145 (2014).

### **Acknowledgment**

Sandia is a multiprogram laboratory operated by Sandia Corporation, a Lockheed Martin Company, for the United States Department of Energy's National Nuclear Security Administration under Contract No. DE-AC04-94AL85000.

## **Granular Constraints and Size Effects in Polycrystalline Shape Memory Alloys**

**Prof. L. Catherine Brinson<sup>1</sup>, Prof. David C. Dunand<sup>1</sup>**

<sup>1</sup>Northwestern University

### **Program Scope**

Shape Memory Alloys (SMAs) have found wide commercial applications due to the remarkable properties of shape memory effect and superelasticity exhibited by them. A diffusionless phase transformation between a high symmetry austenite phase and a low symmetry martensite phase is the cause behind these properties. Thermal cycling or an external stress can activate this transformation. The microstructure formed during the phase transformation shows a hierarchical nature. It consists of symmetry related variants of martensite, which in turn form twins with each other. At a higher length scale of polycrystals, the nature of the microstructure formed in a grain is strongly influenced by its neighborhood. An understanding of this interaction is key to the development of optimized textures for SMA assemblies. Additionally the granular constraints and surface effects are amplified in thin films, porous materials and oligocrystalline materials. In this project, we intend to quantify the effect of granular constraints and relaxation at the sample surface on the progress of phase transformation.

We have developed a three-pronged approach to characterize the granular constraint. At the macro scale we have employed a phenomenological modeling framework to simulate the macroscopic response of NiTi SMA specimen with micron-scale features. This is complimented by tension testing and local strain measurement using digital image correlation (DIC). At the meso-scale, we have employed electron backscatter diffraction (EBSD) to characterize the crystallographic and morphological features of the microstructure. Comparison of the grain orientations obtained from EBSD and local strain data from DIC allows us to determine if local transformation strain deviates from the predicted value due to granular constraints. At the micro-scale, we have employed synchrotron X-ray diffraction to obtain a grain-level picture of the progress of phase transformation [1]. These approaches together track the phase transformation from micron to macro scale and allow answering two key questions.

First, at what length scale a micromechanical model for SMA behavior is more appropriate compared to a macro-scale model? As the specimen size relative to the grain size decreases, a point is reached when factors like the local crystal orientation and texture become important in determining the local transformation strain. If we intend to predict the SMA response at such a small length scale, it is key to choose an appropriate modeling framework. This question is addressed using DIC based experiments and macro-scale modeling.

Second, what is the nature of phase transformation progress at the grain scale in a polycrystalline SMA? What are the specific effects of granular constraints and surface effects? We address this issue using a synchrotron X-ray diffraction based microstructure reconstruction technique. This technique allows us to track the phase, volume and strain in the individual grains in a polycrystalline aggregate [1, 2].

### Recent Progress

When the grain size ( $\sim 100 \mu\text{m}$ ) approaches the feature size in the SMA specimen, deviation from the strain predicted by macroscopic models is observed. This result is obtained by measuring the local strain distribution around microscopic features using DIC and comparing that with macro model prediction. We prepared three plane-stress dog-bone tension specimens from equiatomic NiTi. One of the specimens was monolithic (MONO). The second had 125  $\mu\text{m}$  holes machined along the centerline with 125  $\mu\text{m}$  separation between them along the loading direction (CP125). The third sample had 500  $\mu\text{m}$  holes separated by 500  $\mu\text{m}$  (CP500). **Figure 1a** shows the predicted strain distribution at the peak stress in the CP125 specimen using the macroscopic phenomenological model of Panico and Brinson [3, 4]. A local strain minimum is predicted between the holes. **Figure 1b** shows the strain measured using DIC at a macro stress of 300 MPa. There is a strain maximum between the holes. **Figure 1c** shows the EBSD scan on the sample. There is a grain with

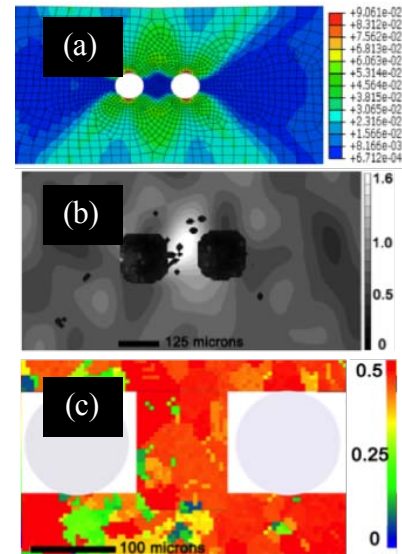


Figure 1 (a) Strain predicted by macro model. (b) DIC measurement. (c) EBSD grain orientation.

large schmid factor for transformation situated between the holes. The local strain maximum due to a favorably oriented grain is not captured by the macroscopic model. This underscores the need to transition to a microstructure-aware micromechanical model for predicting deformation at smaller length scales.

Cubic austenite to monoclinic martensite transformation is observed in a bulk single crystal of equiatomic NiTi with potential formation of a single martensite plate with type II twinning. This result was obtained from synchrotron x-ray diffraction data using a grain reconstruction technique [1, 2]. The single crystal specimen was loaded to 900 MPa and unloaded. **Figure 2a** shows the stress-strain curve with three regimes- an initial elastic, an intermediate phase transformation and potentially a final slip regime. **Figure 2b** shows occurrence of a phase change characterized by appearance of new spots in the area diffraction pattern. **Figure 2c** shows DIC measurements of the strain along loading direction at the peak load (similar to Figure 1b). We can observe bands of larger strain alternating with bands of lower strain. Potential interfaces between austenite and martensite can be determined using crystallographic theory of martensite transformation [5]. After calculating the orientations of 192

possible A-M interfaces and 124 possible M-M twin interfaces for the NiTi system, a type II twin involving variants 1 and 4 is identified as a potential candidate that matches the observed strain distribution. The potential interface is shown in **Figure 2d**.

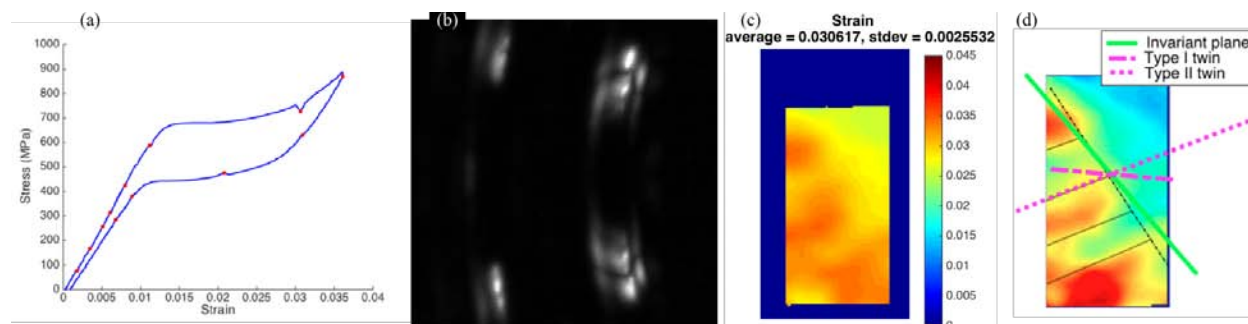


Figure 2 (a) Stress-strain curve for NiTi single crystal tension test. (b) Area diffraction pattern showing austenite (bright) and martensite (weaker) spots. (c) Local strain distribution at peak load showing bands (d) Potential A-M and M-M interfaces predicted from crystallography.

## Future Plans

Building on the length scale study described above and the single crystal diffraction experiments, we are currently preparing to characterize the effect of neighborhoods in polycrystalline NiTi. We are characterizing and processing the material so that we are able to obtain high fidelity results from synchrotron x-ray based grain reconstruction studies this Autumn. The diffraction based study focuses on comparing the progression of phase transformation in the surface grains vs. grains in the bulk. In preparation of the polycrystalline NiTi study, we have recently reconstructed the grain-level microstructure in NiTi comprising of ~10 000 grains and in steels comprising of ~1000 grains.

Two additional exercises for the near future include preparing a manuscript to describe the size effect study and performing a micromechanics based modeling study to verify if such a model is able to reproduce the observed strain distribution in the samples with micro-holes.

## References

- [1] Bernier, J. V., N. R. Barton, U. Lienert, and M. P. Miller. 2011. *The Journal of Strain Analysis for Engineering Design*. doi:10.1177/0309324711405761.
- [2] Advanced Photon Source (MIDAS grain reconstruction software) <https://www1.aps.anl.gov/Science/Scientific-Software/MIDAS> . Accessed on Aug 19, 2015.
- [3] Panico, M., and L. C. Brinson. 2007. "A Three-Dimensional Phenomenological Model for Martensite Reorientation in Shape Memory Alloys." *Journal of the Mechanics and Physics of Solids* 55 (11): 2491–2511. doi:10.1016/j.jmps.2007.03.010.

[4] Zhu, Pingping, Aaron P. Stebner, and L. Catherine Brinson. 2013. “A Numerical Study of the Coupling of Elastic and Transformation Fields in Pore Arrays in Shape Memory Alloy Plates to Advance Porous Structure Design and Optimization.” *Smart Materials and Structures* 22 (9). doi:10.1088/0964-1726/22/9/094009.

## **Publications**

1. Stebner, Aaron P., Harshad M. Paranjape, Bjørn Clausen, L. Catherine Brinson, and Alan R. Pelton. 2015. “In Situ Neutron Diffraction Studies of Large Monotonic Deformations of Superelastic Nitinol.” *Shape Memory and Superelasticity*, May, 1–16. doi:10.1007/s40830-015-0015-2.
2. Paul, P., Paranjape, H. M., Stebner, A.P., Brinson, L.C., Dunand D. “Size Effects in Superelastic Shape Memory Alloys”, in-preparation for journal submission.

## Crack Tip Mechanisms Driving Environmental Degradation

S.M. Bruemmer, D.K. Schreiber, C. Wang, M.J. Olszta, M.L. Sushko and K.M. Rosso  
Pacific Northwest National Laboratory

### Program Scope

Revolutionary advancements in site-specific sample preparation, in-situ experimental methods and atomically-resolved 3D analytical tomography are being leveraged to develop a seminal understanding of underpinning mechanisms at the atomic scale that control the cracking response in high-temperature gaseous to lower-temperature aqueous environments. Definitive empirical observations are correlated with innovative multiscale simulation tools to evaluate specific mechanisms that control, limit or facilitate degradation phenomena. Observations to date have revealed dramatic compositional and microstructural changes that accompany grain boundary selective oxidation. The rapid development of these features requires accelerated interfacial diffusion that can only be explained by oxidation-induced vacancy injection. Observed compositional redistributions ahead of oxidation fronts are consistent with predicted vacancy-mediated, grain boundary diffusivities for those elements calculated at the quantum mechanical level. Intergranular degradation is found to advance in many corrosion-resistant alloys by selective grain-boundary oxidation even at low temperatures. Collectively, these measurements and observations are generally inconsistent with continuum mechanics and electrochemical models of environmental degradation underscoring the critical need for fundamental understanding at the atomic and molecular level. This program will discover and define the mechanisms controlling environmental degradation through cutting-edge empirical observations and original modeling of grain boundary reaction processes that bridge from atomistic to macroscopic length scales.

### Recent Progress

Research progress has focused on evaluating three fundamental premises that we believe collectively control intergranular (IG) corrosion/oxidation and stress corrosion cracking (SCC) in high-temperature hydrogenated water environments: *(1) that grain boundary selective oxidation is required for degradation and cracking, (2) that O diffusion into Ni metal grain boundaries can and does occur at these low temperatures consistent with the model for internal oxidation, and (3) that vacancy formation and injection during oxidation accelerates diffusion and degradation kinetics.* The relative importance of these aspects has been shown to change with material (e.g. alloying species and concentration) and environment (e.g. electrochemical potential and temperature). Recent results have demonstrated that selective oxidation at grain boundaries controls IG corrosion and SCC response [1] for high-purity Ni-Cr and Ni-Al binary alloys, but not for pure Ni, Ni-5Cu or Ni-5Fe alloys. Mechanisms of IG degradation were different for Ni-5Cr [2] where a continuous oxidation front without O ingress was found versus that for Ni-4Al [3] where internal oxidation was discovered as illustrated in Figure 1. Selective oxidation clearly produced vacancy injection and accelerated local diffusion (particularly for Ni-Cr alloys) that

accompany the IG degradation process even in the absence of externally applied stress. A multiscale, first principles-based model of reactive diffusion processes has been developed to gain insights into the processes controlling this grain boundary oxidation [4]. It combines activation energies for elementary diffusion processes calculated quantum mechanically [5] with collective atomistic dynamics reaching into the mesoscale domain of experimental observations. Simulations (Figure 2) reveal that grain boundary oxidation of Ni-5Cr alloy proceeds through the rapid diffusion and selective oxidation of Cr, creating a continuous plate-like oxide ( $\text{Cr}_2\text{O}_3$ ) in tandem with a monotonic Cr vacancy distribution in Ni-rich metal ahead of the reaction front. In contrast, Ni and Al are both oxidized in a Ni-4Al alloy forming an IG  $\text{NiAl}_2\text{O}_4$  film. Results suggest that the similarity of Al and Ni diffusivity, in comparison to much more rapid Cr grain boundary transport, partially explains the differences in O ingress into the metal and the tendency of Ni-4Al to form a mixed oxide. All of these predicted grain boundary oxidation characteristics are consistent with experimental observations on corroded Ni-5Cr [2] and Ni-4Al [3] alloys by high-resolution transmission electron microscopy (TEM) and atom probe tomography (APT).

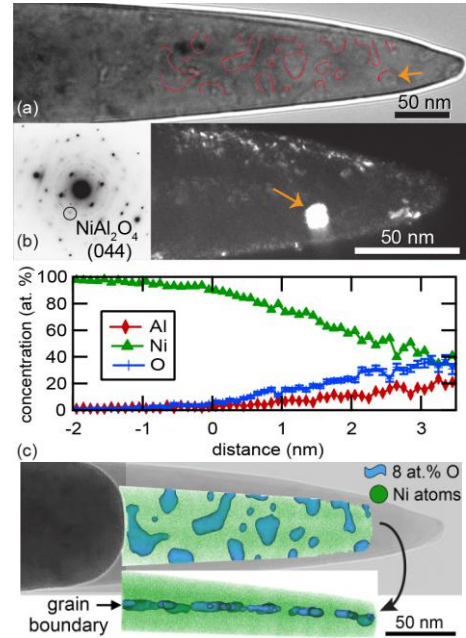


Figure 1. Combined TEM (a,b) and APT (c,d) of grain boundary tip illustrating internal Ni-Al oxides and interfacial compositions in Ni-4Al binary alloy exposed to hydrogenated water [3].

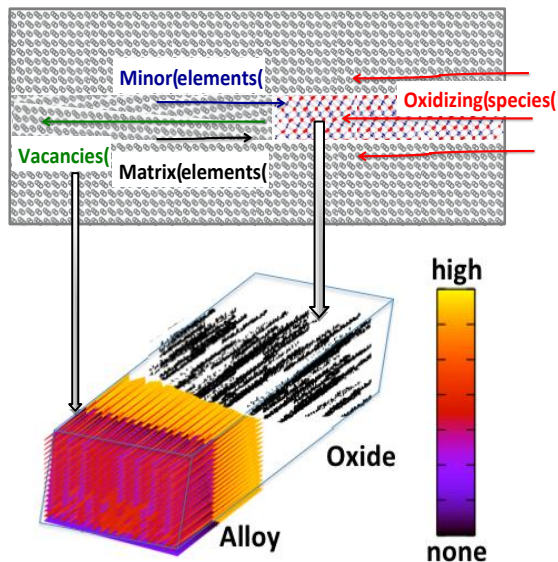


Figure 2. Schematics of predicted oxidation at Ni-5Cr grain boundaries showing oxide porosity (black) and the distribution of vacancies (scale) in the metal ahead of the oxidation front [4].

Corrosion and crack growth tests have also evaluated the influence of bulk Cr concentration on IG degradation of Ni alloys in high temperature hydrogenated water [6]. SCC growth rates sharply increased with bulk Cr concentration from 5 to 20 at% primarily due to changes in matrix strength and crack-tip deformation combined with similar grain boundary corrosion/oxidation behavior (based on crack-tip characterizations). Propagation rates decreased for a Ni-30Cr alloy consistent with the rapid formation of a protective film at grain boundaries. Collectively these discoveries have redefined our fundamental understanding of environmental degradation and generated results that prompt new questions and avenues of research. Substantial effort continued on the development of unique experimental and modeling capabilities.

These have included the construction of dedicated microautoclaves that enable rapid quenching of high-temperature corrosion microstructures, establishment of novel site-specific sample preparation methods for TEM and APT observations, further development of APT directed at oxides and corrosion structures [7-10], design and development of unique in-situ TEM oxidation experiments [11,12], and the development and testing of theoretical models [4,5,13] designed by expanding, creating and applying innovative modeling strategies for computational kinetics simulations of selective IG oxidation from atomic to mesoscopic scales. Our new insights into environmental degradation mechanisms would have been unobtainable without these critical technique developments.

## **Future Plans**

*The driving hypothesis for future research is that common underpinning mechanisms at the atomic scale control grain boundary oxidation and IG cracking in both high-temperature gaseous and low-temperature aqueous environments. These processes involve selective oxidation, vacancy injection and local composition changes along grain boundaries that cannot be adequately explained by existing theories of environmental degradation.* Experimental and modeling results highlighted in the Recent Progress have refined our key issues to be pursued. Paramount among these are the discoveries that O can enter the metallic grain boundary and promote classical internal oxidation during IG attack in hydrogenated water and that seemingly different grain boundary oxidation mechanisms occur for Ni-Cr and Ni-Al alloys. At the same time, new issues were identified requiring the influence of electrochemical potential and bulk Cr composition on grain boundary oxidation and IGSCC to be addressed. Critical focus areas for proposed experimental and modeling research therefore include: (1) *establishing grain boundary oxidation and cracking mechanisms in gaseous versus aqueous environments including the role of hydrogen;* (2) *elucidating the influence of selective oxidation phases and their properties (e.g. porosity, solubility and stability) on interfacial reaction processes, grain boundary changes and IG degradation;* and (3) *isolating early stages of grain boundary oxidation occurring during IG crack growth.* The more complex aspects of crack-tip selective oxidation and crack advance (e.g., effects of stress and localized deformation) are also critical for future research, but it is essential that basic grain boundary oxidation processes are first defined and modeled.

Complementing aqueous experiments with controlled gaseous tests at identical Ni/NiO stability will enable the delineation of *oxidation from corrosion mechanisms* and indicate H effects unique to the aqueous environment and simultaneously facilitate a closer linkage with in-situ TEM and modeling activities. The gaseous environment will be established maintaining the same bias toward selective oxidation processes. Comparisons will elucidate, for example, whether the porous oxide morphology observed in Ni-Cr alloys is the result of an aqueous corrosion process or a solid-state oxidation front that might also form in the absence of corrosion. Similarly, in-situ TEM experiments in gaseous and aqueous environments will reveal dynamic processes that dominate in both environments and their respective differences. In particular, novel in-situ observations of *grain boundary oxidation and corrosion will resolve reaction kinetics, elemental*



*diffusion pathways and vacancy effects.* Together these experiments will guide the development of mechanistic models to include reactions at gas/solid, liquid/solid and solid/solid interfaces. The maturation of these modeling techniques will then direct further experiments by identifying key nanostructural features (e.g. porosity development, specific phase formation, vacancy supersaturation and grain boundary composition changes) that can be pursued experimentally to resolve atomistic processes controlling IG degradation.

The early stages of oxidation strongly influence material degradation, but are notoriously difficult to capture and differentiate from steady-state oxidation structures. Our experimental and theoretical approaches provide an avenue to pursue the dynamic processes during oxidation and associated compositional redistributions. Mechanistic models that combine quantum mechanical calculations with bridging mesoscopic simulations will play a critical role in evaluating experimental observations and the competition between thermodynamics and kinetics in oxidation and nanostructural material changes. In-situ oxidation experiments, leveraging both developed and new TEM methods and a newly designed in-situ APT reaction chamber, will be used to explore initial and partially developed oxidation structures for linkage to mechanistic models. Comparisons with more developed microstructures will also indicate key aspects controlling both *initial and steady state grain boundary oxidation processes.*

A critical aspect will continue to be the development and application of cutting-edge SCC testing capabilities, high-resolution analytical microscopy techniques, in-situ and operando experiments and original approaches to fundamental modeling methods to generate unique insights into materials degradation phenomena. Specific goals for the next 3 years include the development of quantitative crack-growth testing in gaseous environments, in-situ APT oxidation experiments, in-situ TEM corrosion/oxidation experiments of grain boundaries and a mesoscopic simulation tool that bridges from fundamental atomistic DFT calculations to mesoscopic oxidation processes along grain boundaries.

## References

1. S.M. Bruemmer, M.J. Olszta, D.K. Schreiber and M.B. Toloczko, "Grain boundary corrosion and stress corrosion crack growth of high-purity nickel binary alloys in high temperature hydrogenated water," *Corros.*, (2015) submitted for publication.
2. D.K. Schreiber, M.J. Olszta and S.M. Bruemmer, "Grain boundary depletion and migration during selective oxidation of Cr in a Ni-5Cr binary alloy exposed to high-temperature hydrogenated water," *Scripta Mater.*, 89 (2014) 41.
3. D.K. Schreiber, M.J. Olszta and S.M. Bruemmer, "Directly correlated transmission electron microscopy and atom probe tomography of grain boundary oxidation in a Ni-Al binary alloy exposed to high-temperature water," *Scripta Mater.*, 69 (2013) 509.
4. M.L. Sushko, V. Alexandrov, D.K. Schreiber, K.M. Rosso, and S.M. Bruemmer, "Multiscale model of metal alloy oxidation at grain boundaries," *J. Chem. Phys.* 142-21, (2015), Article # 214114.
5. V.Y. Alexandrov, M.L. Sushko and K.M. Rosso, " Ab initio modeling of bulk and intragranular diffusion in Ni alloys," *J Phys Chem Letters* 6-9 (2015) 1618.

6. S.M. Bruemmer, M.J. Olszta, D.K. Schreiber and M.B. Toloczko, "Influence of bulk Cr concentration on IGSCC growth rates of nickel binary alloys in hydrogenated water," *International Cooperative Group Meeting on Environment-Assisted Cracking*, Ann Arbor, MI, May 2015.
7. D.K. Schreiber, M.J. Olszta and S.M. Bruemmer, "Complementary atom probe tomography and electron microscopy of oxidation of Ni-base alloys in high-temperature water environments," *Microsc. Microanal.*, 19 (2013) 970.
8. S. Gin, J.V. Ryan, D.K. Schreiber, J. Neeway and M. Cabie, "Contribution of atom-probe tomography to a better understanding of glass alteration mechanisms: Application to a nuclear glass specimen altered in a granitic environment," *Chem. Geol.*, 349 (2013) 99.
9. D. Santhanagopalan, D.K. Schreiber, D.E. Perea, R.L. Martens, Y. Janssen, P. Khalifah and Y.S. Meng, "Effects of laser energy and wavelength on the analysis of LiFePO<sub>4</sub> using laser assisted atom probe tomography," *Ultramicrosc.*, 148 (2015) 57.
10. D.K. Schreiber, A.N. Chiaramonti, L.M. Gordon and K. Kruska, "Applicability of post-ionization theory to laser-assisted field evaporation of magnetite," *Appl. Phys. Lett.*, 105, (24) 5. 10.1063/1.4904802
11. C.-M. Wang, A. Genc, H. Cheng, L. Pullan, D.R. Baer and S.M. Bruemmer, "In-Situ TEM visualization of vacancy injection and chemical partition during oxidation of Ni-Cr nanoparticles," *Sci. Rep.*, 4 (2014) 3683.
12. Wang, C., Schreiber D. K., Olszta M. J., Baer, D. R., and Bruemmer S. M., (2015) Direct in-situ TEM observation of oxidation by the injected vacancies for Ni-4Al alloy using a microfabricated nanopost. *ACS Journal of Applied Materials & Interfaces*, in press.
13. Z. Xu, D. Li, K.M. Rosso, D.K. Schreiber and S.M. Bruemmer, "Modeling selective intergranular oxidation of binary alloys," *J. Chem. Phys.*, 142-1 (2014) 9.

### **Publications (Late 2013 – Present)**

- Alexandrov V., Sushko M. L., Schreiber D. K., Bruemmer S. M., and Rosso K. M. (2015) Ab initio modeling of bulk and intragranular diffusion in Ni alloys. *Journal of Physical Chemistry Letters* 6, (9) 1618-1623. 10.1021/acs.jpcllett.5b00177
- Santhanagopalan D., Schreiber D. K., Perea D. E., Martens R. L., Janssen Y., Khalifah P., and Meng Y. S. (2015) Effects of laser energy and wavelength on the analysis of LiFePO<sub>4</sub> using laser assisted atom probe tomography. *Ultramicroscopy* 148, 57-66. 10.1016/j.ultramic.2014.09.004
- Sushko M. L., Alexandrov V., Schreiber D. K., Rosso K. M., and Bruemmer S. M. (2015) Multiscale model of metal alloy oxidation at grain boundaries. *Journal of Chemical Physics* 142, (21) Article # 214114. 10.1063/1.4921940
- Wang, C., Schreiber D. K., Olszta M. J., Baer, D. R., and Bruemmer S. M., (2015) Direct in-situ TEM observation of oxidation by the injected vacancies for Ni-4Al alloy using a microfabricated nanopost. *ACS Journal of Applied Materials & Interfaces*, published online DOI: 10.1021/acsami.5b04341
- Xu Z., Li D., Schreiber D. K., Rosso K. M., and Bruemmer S. M. (2015) Modeling selective intergranular oxidation of binary alloys. *Journal of Chemical Physics* 142, (1) 9. 10.1063/1.4905226
- Zhai, Z., Olszta M. J., Toloczko M. B. and Bruemmer S. M. (2015) Precursor corrosion damage and stress corrosion crack initiation in alloy 600 during exposure to PWR primary water.

- 17th International Conference on Environmental Degradation of Materials in Nuclear Power Systems – Water Reactors*, Canadian Nuclear Society, Ottawa, Ontario, Canada.
- Bruemmer S. M., Olszta M. J., Overman N. R., and Toloczko M. B. (2015) Cold work effects on stress corrosion crack growth in alloy 690 tubing and plate materials. *17th International Conference on Environmental Degradation of Materials in Nuclear Power Systems – Water Reactors*, Canadian Nuclear Society, Ottawa, Ontario, Canada.
- Olszta M. J., Schreiber D. K., and Bruemmer S. M. (2014) High-resolution characterizations of film formation and localized corrosion in alloy 690 exposed to PWR primary water. *Corrosion 2014*, NACE International, San Antonio, TX.
- Schreiber D. K., Chiaramonti A. N., Gordon L. M., and Kruska K. (2014) Applicability of post-ionization theory to laser-assisted field evaporation of magnetite. *Applied Physics Letters* 105, (24) 5. 10.1063/1.4904802
- Schreiber D. K., Olszta M. J., and Bruemmer S. M. (2014) Grain boundary depletion and migration during selective oxidation of Cr in a Ni-5Cr binary alloy exposed to high-temperature hydrogenated water. *Scripta Materialia* 89, 41-44. 10.1016/j.scriptamat.2014.06.022
- Wang C. M., Genc A., Cheng H. K., Pullan L., Baer D. R., and Bruemmer S. M. (2014) In-Situ TEM visualization of vacancy injection and chemical partition during oxidation of Ni-Cr nanoparticles. *Scientific Reports* 4, 6. 10.1038/srep03683
- Schreiber D. K., Olszta M. J., and Bruemmer S. M. (2013) Directly correlated transmission electron microscopy and atom probe tomography of grain boundary oxidation in a Ni-Al binary alloy exposed to high-temperature water. *Scripta Materialia* 69, (7) 509-512. 10.1016/j.scriptamat.2013.06.008
- Schreiber D. K., Olszta M. J., Saxey D. W., Kruska K., Moore K. L., Lozano-Perez S., and Bruemmer S. M. (2013) Examinations of oxidation and sulfidation of grain boundaries in alloy 600 exposed to simulated pressurized water reactor primary water. *Microscopy and Microanalysis* 19, (3) 676-687. 10.1017/s1431927613000421
- Bruemmer S. M., Olszta M. J., Toloczko M. B., and Thomas L. E. (2013) Linking grain boundary microstructure to stress corrosion cracking of cold-rolled alloy 690 in pressurized water reactor primary water. *Corrosion* 69, (10) 11. 10.5006/0808
- Bruemmer S. M., Olszta M. J., Overman N. R., and Toloczko M. B. (2013) Microstructural effects on stress corrosion crack growth in cold-worked alloy 690 tubing and plate materials. *16th International Conference on Environmental Degradation of Materials in Nuclear Power Systems – Water Reactors*, NACE International, Asheville, NC.
- Olszta M. J., Schreiber D. K., Toloczko M. B., and Bruemmer S. M. (2013) Alloy 690 surface nanostructures during exposure to PWR primary water and potential influence on stress corrosion crack initiation. *16th International Conference on Environmental Degradation of Materials in Nuclear Power Systems – Water Reactors*, NACE International, Asheville, NC.
- Schreiber D. K., Olszta M. J., L. E. Thomas, and Bruemmer S. M. (2013) Grain boundary characterization of alloy 600 prior to and after corrosion by atom probe tomography and transmission electron microscopy. *16th Int. Conf. Environmental Degradation of Materials in Nuclear Power Systems*, NACE International, Asheville, NC.

# Thermal Activation in Dislocation Dynamics of Face-Centered Cubic Metals

PI: Wei Cai, Stanford University

## Program Scope

This proposed research project will use state-of-the-art atomistic and dislocation dynamics simulations to answer the following fundamental questions about the thermally activated dislocation processes (cross slip and forest cutting) in pure face-centered-cubic metals. How does the mechanism of homogeneous cross slip depend on various stress components? What is the dominant mechanism of cross slip in a realistic dislocation microstructure? How does the interaction between a gliding and forest dislocation influence the mechanism and activation volume of forest cutting? Is dynamic recovery controlled by cross slip of dislocations to avoid strong barriers or by thermally assisted removal of the Lomer-Cottrell locks?

## Recent Progress

We successfully computed the energy barrier for the homogeneous cross slip of a screw dislocation in FCC Ni as a function of three different stress components acting simultaneously using the atomistic model. We have found that hundreds of data points for the cross slip energy barrier can be well described by defining a “effective stress”  $\tau^* = C_e^g \tau_e^g + C_e^c \tau_e^c + (D_s^c \tau_s^c)^2$  and let the energy barrier be a function of  $\tau^*$ ,  $E_b(\tau^*) = E_0 \left[1 - \left(\frac{\tau^*}{\tau_0}\right)^p\right]^q$ . These results also allow us to delineate the stress domain in which the Friedel-Escaig mechanism and the Fleischer mechanism dominate, respectively.

Given the energy barrier function, the cross slip rate can be computed from  $k = v_0 \frac{l}{l_0} \exp\left(-\frac{E_b(\tau^*)}{k_B T}\right)$ , where  $v_0 \frac{l}{l_0}$  is the rate prefactor, which is usually assumed to be several orders lower than the Debye frequency. We performed MD simulations to directly determine the cross slip rate and hence the rate prefactor. We found that the rate prefactor is many orders of magnitude higher than previous expected, indicating a large activation entropy of cross slip. This is similar to the situation we discovered for dislocation nucleation [1].

We have incorporated the cross slip rate function predicted by atomistic simulations into our dislocation dynamics (DD) simulation program. We have significantly improved the time-integration efficiency of our DD simulation by developing a new (force-based) subcycling integration scheme. This allows us to exceed 1% of strain in a day, while the previous algorithm can only reach 0.15% strain in the same computation time.

## Future Plans

We will determine the origin of the anomalously large rate prefactor (which increases the predicted cross slip rate by many orders of magnitude). We will extend our findings for FCC Ni to predict cross slip rates of other FCC metals (such as Al and Cu), without having to repeat the same amount of atomistic simulations.


We will use the cross-slip rate function and the more efficient time-integration algorithm to perform DD simulations for the Bonneville-Escaig experiments, in which a metal is first deformed in one orientation and then in a different orientation to maximize the probability of cross slip. Our goal is to predict the temperature effect on the stress-strain curve of FCC metals and compare with experiments.

We also plan to investigate other thermally activated processes such as dislocation-precipitate interactions and dislocation intersections by atomistic and DD simulations.

## References

[1] S. Ryu, K. Kang, W. Cai, “Entropic Effect on the Rate of Dislocation Nucleation”, *Proc. Natl. Acad. Sci. USA*, 108, 5174 (2011).

## Publications

1. K. Kang, J. Yin and W. Cai, “Stress Dependence of Cross Slip Energy Barrier for Face-Centered Cubic Nickel”, *J. Mech. Phys. Solids*, 62, 181 (2014).
2. R. B. Sills and Wei Cai, “Efficient Time Integrators for Dislocation Dynamics Simulations”, *Model. Simul. Mater. Sci. Eng.*, 24, 025003 (2014).
3. W. Cai, R. B. Sills, D. M. Barnett, and W. D. Nix, “Modeling a Distribution of Point Defects as Misfitting Inclusions in Stressed Solids”, *J. Mech. Phys. Solids*, 66, 154 (2014).
4. E. J. L. Borda, W. Cai, and M. de Koning, “Ideal Shear Strength of a Quantum Crystal”, *Phys. Rev. Lett.*, 112, 155303 (2014). Paper selected as PRL Editor’s suggestion .
5. R. A. Bernal, A. Aghaei, S. Lee, S. Ryu, K. Sohn, J. Huang, W. Cai, and H. Espinosa, “Intrinsic Bauschinger Effect and Recoverable Plasticity in Pentatwinned Silver Nanowires Tested in Tension”, *Nano Letters*, 15, 139 (2015).

## **Energetics of Radiation Tolerant Nanoceramics**

**Ricardo Castro, University of California-Davis**

### **Program Scope**

Nanomaterials were initially expected to show generally enhanced radiation resistance attributed to the increased interface areas. Interfaces would act as effective sinks for radiation-induced defects, ultimately maintaining the integrity of these materials under long exposures to radiation. However, some nanocrystalline compositions have shown a decreased tolerance to radiation when compared to the parent bulk material. The thermodynamic hypothesis was then formulated that the phase-transition resistance in nanocrystalline materials is dependent on both grain boundary energy/area and irradiation-induced point defect free energy contributions. To show a significant enhanced radiation resistance, the sum of these contributions must be smaller than the Gibbs free energy barrier for the phase-transition, usually from crystalline to amorphous. Therefore, depending on size, interface energy, and transition energy, a particular system would have different radiation tolerance at the nanoscale.

The lack of reliable experimental data on the interface energies of many ceramic materials makes it extremely difficult to prove this concept and enable the prediction and tuning of nanoceramics performance as radiation shields to exploit their full potential. In this project, we systematically evaluate this concept by measuring the interface energies of series of ceramics with potential interest for nuclear components, and attempt to establish the relationship between composition (and distribution of components), interface energies, and radiation resistance, aiming to enable a fine selection of nanomaterials with enhanced performance.

### **Recent Progress**

Several works have been reported on ion irradiation of fully stabilized zirconia (YSZ) and an impressive radiation tolerance is consistently observed, making it clearly a candidate for applications in high radiation environments. For instance, no amorphization was observed in zirconia to levels of irradiation of at least 100 dpa which is enough to cause amorphization of other ceramic materials already considered to show high radiation resistance, such as  $\text{MgAl}_2\text{O}_4$ , at similar irradiation spectrum. Damage accumulation is however clearly observed for irradiation using Xe ions. As the fluence increases, three stages of damage accumulation could be identified in zirconia: the first involving the formation of isolated defect clusters; a second intermediate stage where damage increases rapidly; and a third stage where accumulation is retarded due to the overlapping of dislocations and lattice defects [1].

Here we show that nanocrystalline YSZ shows lesser amount of defects as compared to the bulk counterpart. To prove this, nanograined YSZ samples were prepared using high pressure assisted Spark Plasma

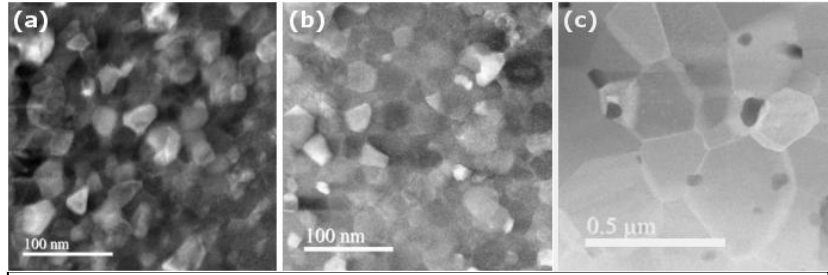


Figure 1. Nanograined YSZ with 25, 38 and 220 nm.

Sintering. Nanocrystalline samples with 3 different sizes 25nm, 38nm and 220nm (bulk) were irradiated using  $Kr^+$  irradiation at 400keV. Figure 1 shows the non-irradiated samples prepared by using 600 MPa, 950°C for 5 min to reduce grain coarsening and allow densification.

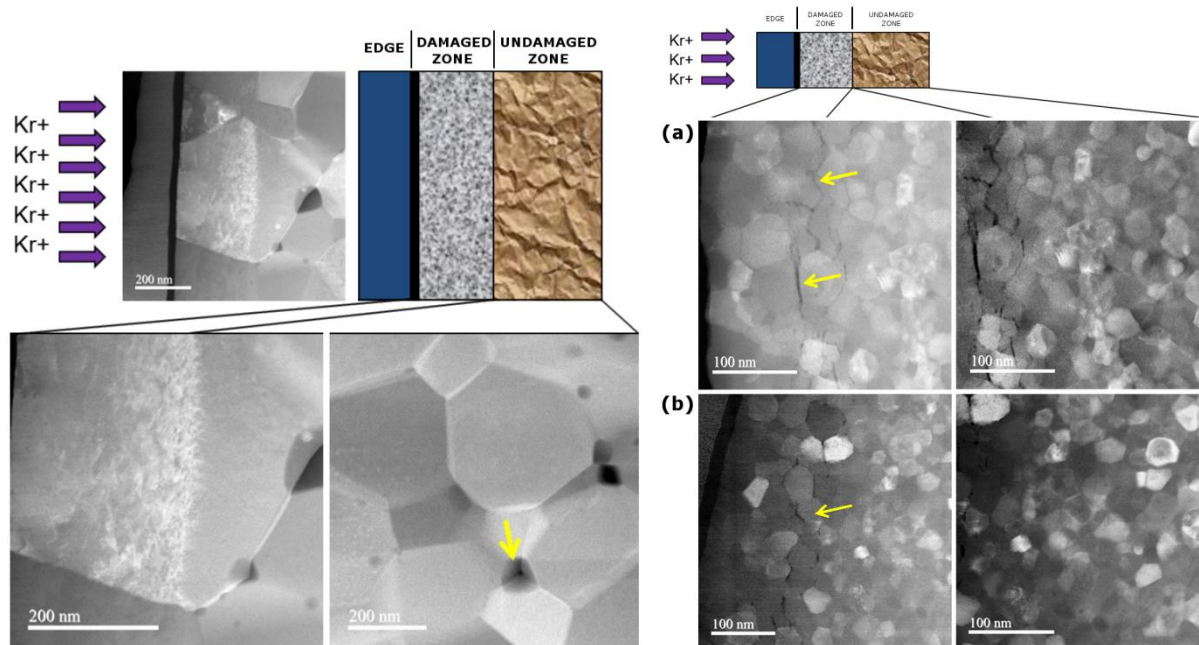


Figure 2. (left) Bulk sample after  $Kr^+$  irradiation and (right) nanograined sample after the same radiation dose.

Figure 2 shows the microstructure by transmission electron microscopy of the sample with 220 nm (left) and 38nm (right) revealing the damage profile caused by irradiation. In both cases, a fairly narrow radiation damaged zone is observed, which is consistent with simulations of the radiation depth. On the other hand, the sample with 220 nm shows considerably more damage as compared to the nanograined one, as noticed from the contrasts in the micrograph on the size exposed to the radiation. The nanograins remain quite smooth, showing only few signs of damage. In order to quantify the defects, higher magnifications were used, as shown in Figure 3.

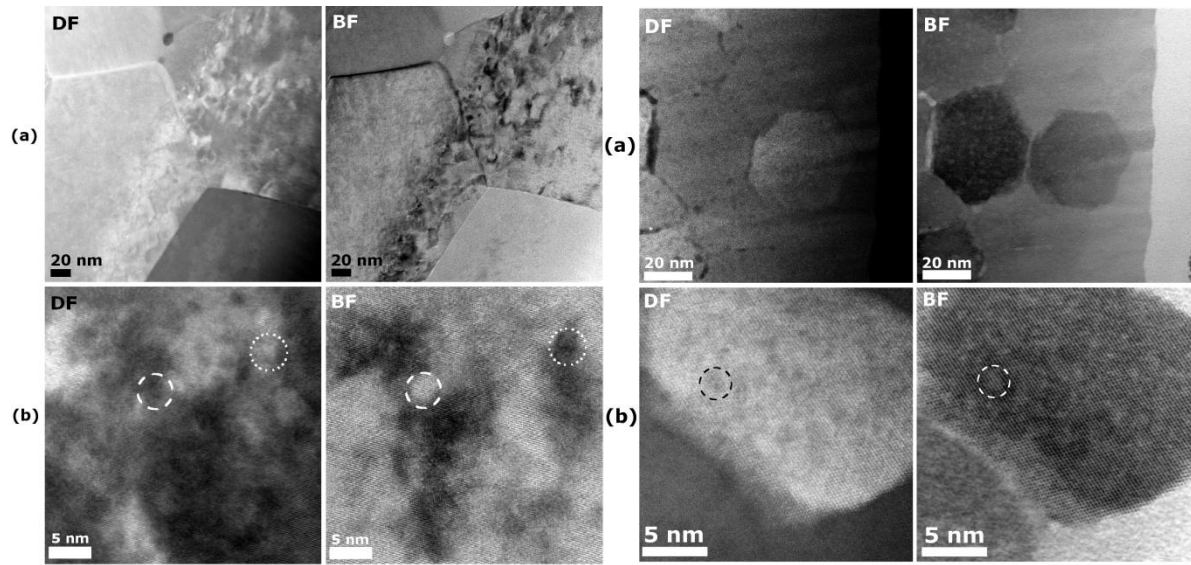


Figure 3. (left group of 4) Bulk sample after Kr<sup>+</sup> irradiation and (right group) nanogained sample after the same

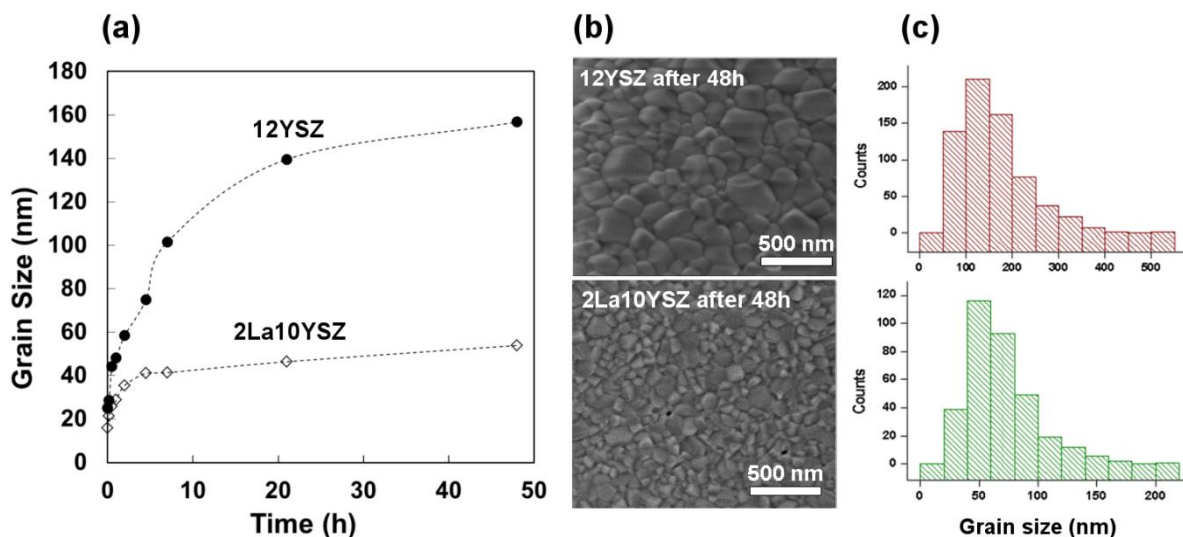
Figure 3 not only shows the amount of defects is smaller for the nanogained samples, but also shows that the type of defect differs. That is, in the large grained sample, two kinds of defects can be seen as bright contrast and dark contrast in the dark field (DF) image, and reversed in the bright field image (BF). These are likely vacancy clusters (or voids) and accumulations of atoms as interstitials, respectively. These are defects created during the cascade that move around but are not eliminated since the irradiation is done at room temperature where diffusion is very small in YSZ. The nanogained samples, however, only show the vacancy clusters, with no interstitials present (no bright spots in the DF image). This indicates that the defects are somehow being absorbed by the microstructure, likely in the high density of grain boundaries present there.

Another observation on these samples was that the nanogained ones suffered significant radiation induced grain growth. This is a result of the accumulation of defects of interstitials (O and Zr) to the boundaries, causing a net movement resulting in grain enlargement [2].

As grain growth is a practical problem for the usage of nanogained materials, we have tested another sample of YSZ doped with lanthanum. While thermally activated grain growth can be virtually stopped by using this dopant that decreases the grain boundary energy, as proven elsewhere [3], as shown in Figure 4, our results on irradiation showed no significant difference as compared to undoped YSZ. This suggests that the coarsening is indeed induced by the defects accumulating at the boundaries rather than a thermal activation.



Figure 4. (a) Grain growth at 1100°C for doped and undoped YSZ; (b and c) grain sizes of coarsed samples.



## Future Plans

CeO<sub>2</sub> nanograined samples have been already irradiated and are being studied in terms of defect concentrations in a similar manner. Mn doped CeO<sub>2</sub> is also being studied to evaluate the role of chemistry in increasing or not the overall radiation tolerance.

The concept of nanostability at high temperature (against coarsening instead of radiation) is also being explored in MgAl<sub>2</sub>O<sub>4</sub> samples using dopants, given the promising data presented in Figure 4 that shows that thermodynamics can indeed be used to create stable nanocrystals. Other systems have also been studied considering this idea but studying nanoparticles instead.

Since thermodynamic data is being generated to evaluate the thermodynamics of radiation damage, the data naturally gives out phase stability diagrams, being the most remarkable YSZ polymorphism as a function of grain size and Y content [4]. We are also building a device capable of producing samples with grain sizes below 10nm.

## References

- [1] Sickafus, K. E. et al. Radiation damage effects in zirconia. *J. Nucl. Mater.* 274, 66-77 (1999).
- [2] Dey, S. et al. Radiation Tolerance of Nanocrystalline Ceramics: Insights from Ytria Stabilized Zirconia. *Sci. Rep.* 5, 7746 (2015)
- [3] Dey, S. et al. Grain Growth Resistant Nanocrystalline Zirconia by Targeting Zero Grain Boundary Energies. *J. Mater. Res.* (Accepted)
- [4] Drazin, J. and Castro, R.H.R. Phase Stability in Nanocrystals: A Predictive Diagram for Ytria–Zirconia. *J. Am. Ceram. Soc.*, 98 [4] 1377–1384 (2015)

## Publications

1. Dey, S. et al. Radiation Tolerance of Nanocrystalline Ceramics: Insights from Yttria Stabilized Zirconia, *Scientific Reports*, 5, 7746 (2015).
2. Drazin, J.W. and Castro, R.H.R. Phase Stability in Nanocrystals: A Predictive Diagram for Yttria–Zirconia, *Journal of the American Ceramic Society*, 98, 1377 (2015).
3. Chang, C-H. et al. Energetics of Oriented Attachment of Mn-doped SnO<sub>2</sub> Nanoparticles, *Journal of Physical Chemistry C*, Accepted.
4. Hasan, Md. et al. Synthesis of stoichiometric nickel aluminate spinel nanoparticles, *American Mineralogist*, 100, 652 (2015).
5. Dholabhai, P. et al., Structure and Segregation of Dopant-defect Complexes at Grain Boundaries in Nanocrystalline Doped Ceria, *Physical Chemistry Chemical Physics*, 17, 15375-15385 (2015).
6. Rufner, J. et al. Synthesis and Sintering Behavior of Ultrafine (<10 nm) Magnesium Aluminate Spinel Nanoparticles, *Journal of the American Ceramic Society*, 96, 2077-2085 (2014).
7. Rufner, J. et al. Mechanical properties of individual MgAl<sub>2</sub>O<sub>4</sub> agglomerates and their effects on densification, *Acta Materialia*, 69, 187-195, 2014.
8. Drazin, J.W. and Castro, R.H.R. Water Adsorption Microcalorimetry Model: Deciphering Surface Energies and Water Chemical Potentials of Nanocrystalline Oxides, *Journal of Physical Chemistry C*, 118 (19), pp 10131–10142 (2014)
9. Quach, D. et al, Water adsorption and interface energetics of zinc aluminate spinel nanoparticles: Insights on humidity effects on nanopowder processing and catalysis *Journal of Materials Research*, 28, 2004-2011, 2013.
10. Castro, R.H.R. On the thermodynamic stability of nanocrystalline ceramics, *Materials Letters*, 96, 45-56, 2013.

## Mechanical and Fracture Behavior of Molecular-Reinforced Hybrid Glasses

Professor Reinhold H. Dauskardt

Department of Materials Science and Engineering, Stanford University

Email: dauskardt@stanford.edu

### Program Scope

Our research is focused on fundamental studies related to the molecular design, synthesis, characterization and modeling of molecular-reinforced hybrid glass films for superior mechanical and fracture properties. Molecular-reinforced hybrid glass films exhibit unique electro-optical properties while maintaining excellent thermal stability. They have important technological application for emerging nanoscience and energy technologies including anti-reflective and ultra-barrier layers in photovoltaics and display technologies. However, they are often inherently brittle in nature, do not adhere well to adjacent substrates, and exhibit poor mechanical properties. Our research brings together a unique combination of internationally recognized thin-film processing and mechanical characterization capabilities coupled with computational modeling that we have pioneered to study hybrid films.

We have recently focused on the development of atmospheric plasma deposition techniques to not only inexpensively deposit hybrid films but also control their molecular structure and connectivity. Composition and molecular structure are characterized using high resolution X-ray, electron, optical and nuclear spectroscopy. Mechanical properties are studied using acoustic, nanoindentation, force modulated AFM, and thin-film adhesion and cohesion techniques we have pioneered for thin-film structures. Furthermore, we leverage computational modeling capabilities that have allowed us to understand the complex molecular structure, free volume, cohesive and elastic properties of hybrid molecular materials. This has enabled the molecular design, synthesis, characterization and modeling of hybrid films for superior mechanical and fracture properties in hostile chemical and UV radiation environments.

### Recent Progress

**Atmospheric Plasma Deposition of Hybrid Films:** The ability to deposit and control hybrid composition and molecular structure is central to optimizing mechanical properties. In recent work, we demonstrate a dual organic and inorganic precursor method to deposit hybrid transparent organosilicate protective bilayers on poly methyl methacrylate (PMMA) substrates with atmospheric plasma deposition in lab ambient air. The bottom layer was a hybrid organosilicate adhesive layer deposited with dual organic 1, 5-cyclooctadiene (CYC) and widely used inorganic tetraethoxysilane (TEOS)

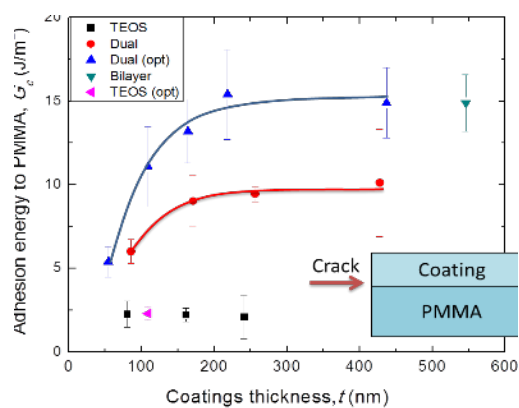


**Figure 1:** Adhesion energy,  $G_c$ , of deposited coatings to PMMA as a function of coating thickness.

precursors. The selection of the organic CYC precursor allowed incorporation of carbon chain in the organosilicate hybrid layer, which resulted in improved adhesion. The top layer was a dense silica coating with high Young's modulus and hardness deposited with TEOS. The deposited bilayer structure showed ~100% transparency in the visible light wavelength region, twice the adhesion energy and five times the Young's modulus of commercial polysiloxane sol-gel coatings (**Fig. 1**).

We can control the hybrid molecular network structure by using organic and inorganic precursors with different carbon chain lengths. The layer was a hybrid organosilicate adhesive layer deposited by the dual precursors of 1,5-cyclooctadiene (CYC) accompanied with bis(triethoxysilyl) methane (BTESM), bis(triethoxysilyl) ethane (BTESE), and bis(trimethoxysilyl) hexane (BTMSH), respectively. Corresponding top layer was a dense silica coating with high Young's modulus and hardness deposited with single precursor (BTESM, BTESE, and BTMSH). Besides distinct enhancement of the adhesion energy with PMMA substrates compared to commercial polysiloxane sol-gel coatings, we demonstrate the improvement of mechanical properties and their relationship to the carbon bridge length of the precursor (**Fig. 2**).

**Computational Modeling of Hybrid Glasses:** We have developed computational tools to generate highly accurate molecular models of hybrid organosilicate glasses. In this work, we model an ethane-bridged oxycarbosilane (Et-OCS). With NPT molecular dynamic simulations, we use simulated annealing to obtain a low energy structure and then simulated the bulk modulus under both compressive and tensile hydrostatic pressure. We also developed a novel approach for exploring free volume. Using the Voronoi network of the simulation space (**Fig. 3a**), we can obtain the volume accessible to each atom via their corresponding simplex volumes. The free volume change between compressive and tensile loading is directly related to the change in the Voronoi cell volume since the atomic volume remains constant.

A particularly interesting question in our recent

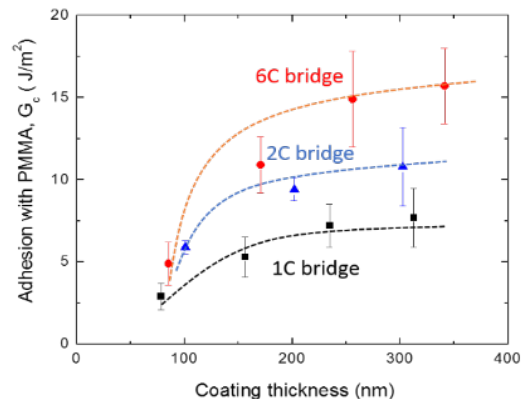


**Figure 2:** Adhesion energy,  $G_c$ , of deposited coatings to PMMA as a function of coating thickness.

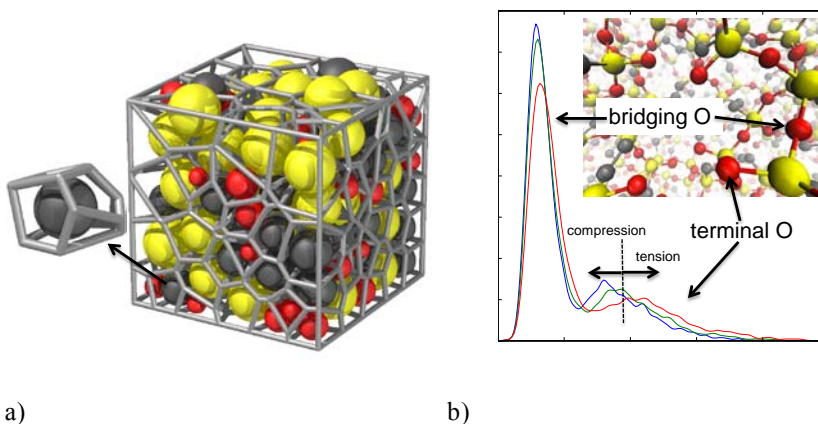
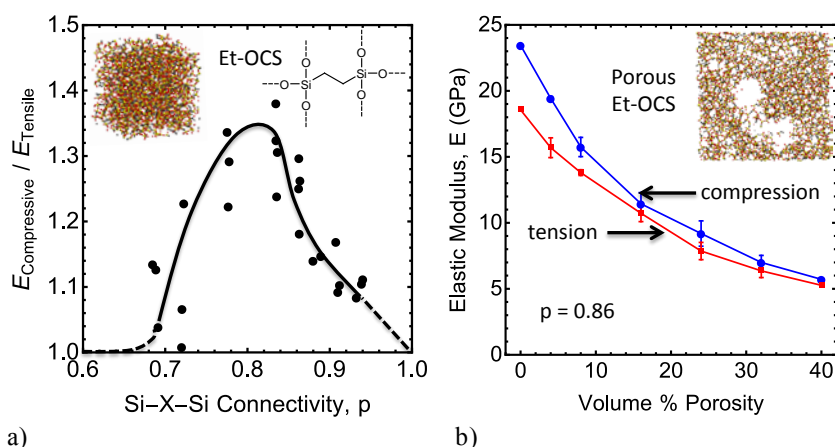


**Figure 3:** (a) Voronoi tessellation of the structure and (b) the distribution of the bridging and terminal O Voronoi simplicies (atomic + free volume) under compressive (blue), equilibrium (green), and tensile (red) stress states.

research has been the possibility of the existence of asymmetrical elastic behavior of hybrid organic-inorganic glasses which would have significant effects on thermomechanical stresses and thermal expansion behavior. We report the first indication that organosilicate glasses display asymmetric elastic behavior, a rare phenomenon for dense molecular materials (**Fig. 4a**). As the network percolates (Si-X-Si connectivity,  $p \sim 0.6$ ), the degree of asymmetry quickly increases to about 35% and then steadily decreases as network becomes more connected.

We argue that the fundamental mechanism behind this elastic asymmetry is the existence of terminal groups that limit network connectivity and effectively bridge the network in compression, while in tension, the terminal groups disconnect the molecular network and explore considerably more volume under elastic deformation. This gives rise to the unexpected asymmetric modulus. We show the difference in accessible volume for terminal O under compressive and tensile loading using our free volume methods (**Fig 3b**). Nanoporous hybrids are of interest in a number of applications since they possess a tunable molecular structure, corresponding to a range of optical and dielectric properties. It is well known that nanoporosity degrades the mechanical

properties of these materials. However, we show that increasing volume % porosity decreases the degree of elastic asymmetry between the compressive and tensile moduli (**Fig. 4b**). Porosity increases the distance between terminal O and thus less leads to less effective bridging in compression, which reduces the amount of elastic asymmetry.



a) **Figure 4:** (a) Ratio of the compressive modulus to the tensile modulus of Et-OCS as a function of network connectivity and (b) the elastic modulus of nanoporous Et-OCS as a function volume % porosity.

## Future Plans

In support of our program objectives, we will continue our research to develop hybrid films with improved mechanical and fracture properties. Specifically, we will continue to pioneer the use of atmospheric plasma deposition of a range of hybrid materials where we will exploit our ability to deposit and react higher boiling point precursors to form multi-functional films with enhanced mechanical and adhesive properties. Furthermore, we will leverage our computational tools to develop molecular models capable of probing the elastic and thermal properties of hybrid molecular materials that have otherwise been difficult to be studied experimentally in addition to predicting hybrid materials with enhanced mechanical and fracture properties derived from novel precursors.

## Publications

To be submitted:

1. J.A. Burg, R.H. Dauskardt, "The Origins of Elastic and Thermal Expansion Asymmetry in Dense Molecular Materials," **Nat. Mat.**, 2015
2. M. Oliver, J.A. Burg, T. Frot, G. Dubois, M.H. Sherwood, R.H. Dauskardt, "Hyperconnected Organosilicate Glass networks," **Adv. Mat.**, 2015
3. S. Dong, J. Han, Z. Zhao, R.H. Dauskardt, "Atmospheric Plasma Deposition of Transparent Bilayer Protective Coatings on Plastics Using Different Carbon Bridge Precursors" **ACS Appl. Mat. Int.**, 2015

Published:

4. S. Dong, Z. Zhao, R.H. Dauskardt, "Dual Precursor Atmospheric Plasma Deposition of Transparent Bilayer Protective Coatings on Plastics," **ACS Appl. Mat. Int.**, 7 (32), pp 17929-17934, 2015.
5. L. Cui, K. Lioni, A. N. Ranade, K. Larson-Smith, G. Dubois, R. H. Dauskardt, "Highly Transparent Multi-Functional Bilayer Coatings on Polymers Using Low Temperature Atmospheric Plasma Deposition", **ACS Nano**, 8, 7186-7191, 2014.
6. S. Dong, M. Watanabe, "Conductive Transparent TiNx/TiO2 Hybrid Films Deposited on Plastics in Air Using Atmospheric Plasma Processing." **Adv. Funct. Mat.**, 24, 3075-3081, 2014.
7. Y. Matsuda, I. Ryu, S.W. King, J. Bielefeld, R.H. Dauskardt, "Toughening Thin-Film Structures with Ceramic-Like Amorphous Silicon Carbide Films," **Small**, 10, 253-257, 2014.
8. M. Watanabe, L. Cui, R. H. Dauskardt, "Atmospheric Plasma Deposition of Transparent Semi-Conductive ZnO Films on Plastics in Ambient Air", **Organic Electronics**, 15, 775-784, 2014.
9. Y. Matsuda, N. Kim, S.W. King, J. Bielefeld, J.F. Stebbins, R.H. Dauskardt, 5, "Tunable Plasticity in Amorphous Silicon Carbide Films," **ACS Appl. Mat. Int.**, 7950-7955, 2013.
10. Y. Matsuda, S.W. King, R.H. Dauskardt, "Tailored Amorphous Silicon Carbide Barrier Dielectrics by Nitrogen and Oxygen Doping," **Thin Solid Films**, 531, 552-558, 2013.
11. Y. Matsuda, S.W. King, M. Oliver, R.H. Dauskardt, "Moisture-Assisted Cracking and Atomistic Crack Path Meandering in Oxidized Hydrogenated Amorphous Silicon Carbide Films," **J. Applied Physics**, 113, 2013.
12. M. Giachino, G. Dubois, R.H. Dauskardt, "Heterogeneous Solution Deposition of High-Performance Adhesive Hybrid Films." **ACS Appl. Mat. Int.**, 5, 9891-9895 2013.
13. L. Cui, A. N. Ranade, M. A. Matos, G. Dubois, R. H. Dauskardt, "Improved Adhesion of Dense Silica Coatings on Polymers by Atmospheric Plasma Pretreatment", **ACS Appl. Mat. Int.**, 5, 8495-8504, 2013.

## **High-throughput experiments on grain boundaries**

**Michael J. Demkowicz**

**Department of Materials Science and Engineering, Massachusetts Institute of Technology,  
Cambridge, MA 02139**

### **Program Scope**

The goal of this project is to rapidly construct, analyze, and model experimental databases containing the complete crystallographies and selected physical properties of thousands of individual grain boundaries (GBs), providing substantial coverage of the complete, five-dimensional space of GB crystallographies. These databases will be analyzed rapidly using automated image-processing methods. Constitutive laws describing the physical properties of GBs as a function of their crystallography will be constructed based on this analysis.

In the current project, we will apply these high-throughput experiments on GBs to study hydrogen (H) solubility and diffusivity at thousands of individual grain boundaries (GBs) in nickel (Ni) and to determine how local GB plasticity affects these properties. The outcome of this work will be the most comprehensive description ever assembled of H behavior at individual GBs, spanning over a wide range of GB crystallographies and GB states: from well-annealed to highly deformed. This work will lead to improved predictions of H transport through polycrystalline Ni-base alloys: a phenomenon of central importance to H embrittlement (HE). It will also guide the development of microstructures with tailored H transport, e.g. ones that minimize uptake of H from the environment. Finally, it will demonstrate the rapid extraction of detailed GB crystallography-processing-property relations from high-throughput experiments using limited computational resources. Many of the methods used to accomplish these goals are transferrable and may be applied to study GB-related behaviors in other settings, such as Li transport through battery electrodes or oxidation of GBs in steels.

### **Recent Progress**

Describing the crystallography of a GB requires five parameters. Electron backscatter diffraction (EBSD) measures four of these parameters for each of GB on the surface of the sample: three for the misorientation between the neighboring grains and one for the trace of the GB plane on the surface. However, EBSD does not determine the inclination of the GB plane with respect to the surface. We developed a method to determine GB plane inclinations in foils with through-thickness grains (Fig. 1A). By extracting the complete crystallography of thousands of individual



GBs in a single specimen, this method enables the construction of large experimental databases of GB crystallographies and properties.

The method images both sides of a sample using an optical stereo-microscope under different illumination conditions (Fig. 1B). The collected images are post-processed in MATLAB, first to locate GB traces and then to register the images taken from both sides of the sample (Fig. 1D). The registration of the top- and back-side images is performed using pre-made notches on the sample edges (visible along the edges of Fig. 1B and 1C). The inclination of each GB plane is computed from the average distance between top-surface and back-surface traces (Fig. 4E) and the sample thickness. The samples in Fig. 1 are Al sheets produced by the group of Dr. J. Erlebacher at Johns Hopkins University.

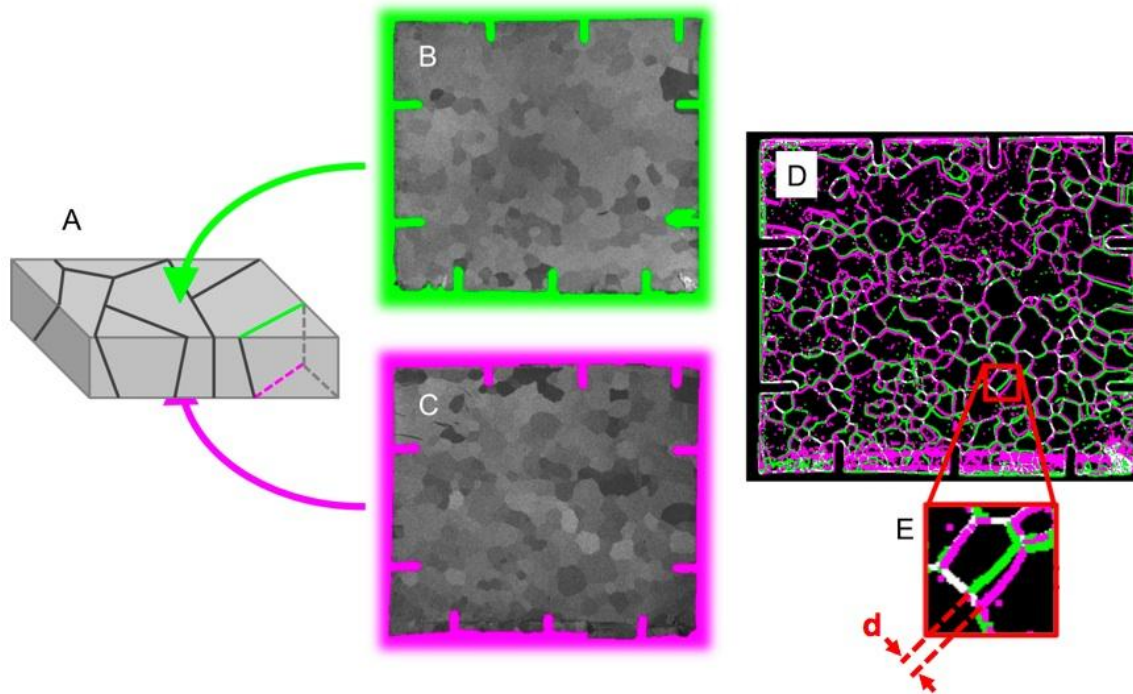


**Fig. 1:** Measuring GB plane inclinations: (A) schematic representation of a sample with through-thickness grains; (B) and (C) are optical stereo-micrographs from both surfaces of the sample showing the grain structure; (D) overlapped images of GB traces from the top- and back-surfaces; (E) detail of the overlapped GB traces showing a clear shift between top- and back-traces of the same GB.

An important unanticipated finding of the previous award period is that nonlinear dimensionality reduction methods originally developed for computer vision applications are extremely effective tools for analyzing large databases of GB information. We will use these algorithms to analyze the large, experimental databases of GB properties acquired in this project. As a demonstration, we have applied these methods to analyze a large database of GB corrosion susceptibilities in Al. They enabled us to find groupings of GBs that are especially susceptible to corrosion as well as ones that exhibit corrosion resistance.



## Future Plans

We will use engineered foils with through-thickness grains, such as those described above, to investigate H solubility and diffusivity at GBs in Ni. Local H concentrations are difficult to measure because H interacts weakly with photons and electrons: the workhorses of optical, x-ray, and electron microscopy. This difficulty has been a major obstacle to understanding H interactions with specific microstructural features, such as individual GBs. We have designed a novel experiment, illustrated in Fig. 2, to perform quantitative measurements of H concentration at individual GBs using neutron radiography (NR). NR determines the composition of a target by measuring the attenuation of a beam of neutrons passing through it. It is analogous to x-ray radiography (as in medical x-rays), except it uses a beam of neutrons, rather than x-rays.

Compared to other elements, naturally abundant  $^1\text{H}$  has a very high cross section for scattering and absorbing thermal neutrons (approximately four times higher than Ni). Thus, it is readily detectable using NR. We will use NR to make 2-D images of H concentration in H-charged Ni foils with through-thickness grains. The resolution of this technique is sufficient to measure H concentrations at individual GBs. By analyzing these images, we will determine the heats of solution and diffusivities of H at individual GBs. To study the effect of plasticity on GB H behavior, samples will be deformed and local plastic strains found using digital image correlation (DIC). We will use NR capabilities at the BT2 thermal imaging instrument, operated as a user facility by the Radiation Physics Division of the Physical Measurement Laboratory at NIST.

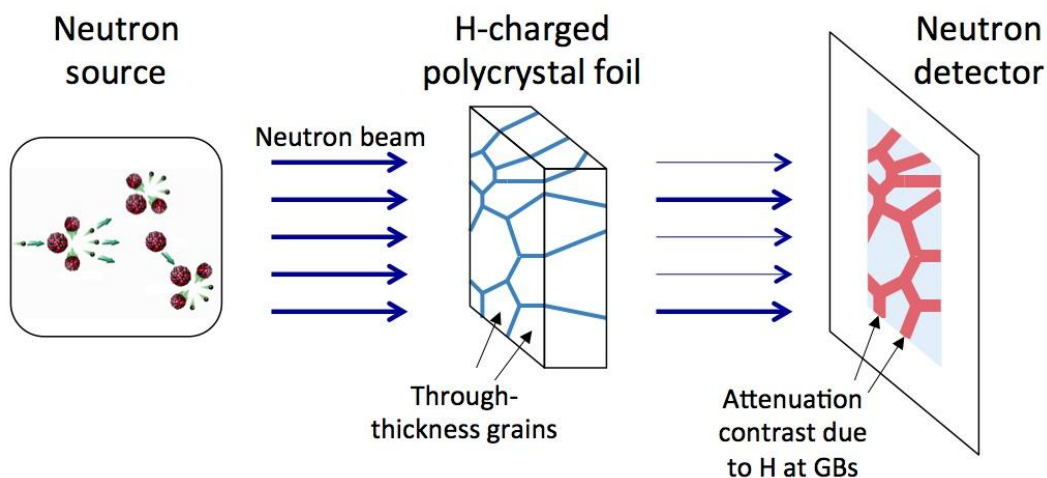


**Fig. 2:** Schematic illustration of the proposed experiment. By analyzing the acquired image (far right), H concentrations at individual grain boundaries may be obtained.

Once we have collected H solubility and diffusivity data for a large number of individual GBs, we will formulate GB constitutive models that express these properties as functions of GB crystallography, i.e. the misorientation  $g$  and the GB plane normal,  $\hat{n}$ :  $E_H = \Phi(g, \hat{n})$  for the GB

H solution energy and  $D_H = \Psi(g, \hat{n})$  for GB H diffusivity. We will use nonlinear dimensionality reduction to determine whether our experimental data spans the full 5-D space of GB crystallographies. If it does not, we will restrict our constitutive laws to the submanifold within this space one which our data lie. To interpret trends in GB H solubility and diffusivity in terms of atomic scale mechanisms, we will also perform atomistic simulations on selected GBs. We will investigate whether H behavior correlates to other GB properties, such as GB energy, specific free volume, or defect content. These simulations will help to identify the physical mechanisms responsible for differences in H behavior at different GBs.

## Publications

1. O. K. Johnson and C. A. Schuh, *The uncorrelated triple junction distribution function: Towards grain boundary network design*, Acta Materialia **61**, 2863 (2013).
2. K. C. Alexander and C. A. Schuh, *Exploring grain boundary energy landscapes with the activation-relaxation technique*, Scripta Materialia **68**, 937 (2013).
3. J. K. Mason and O. K. Johnson, *Convergence of the hyperspherical harmonic expansion for crystallographic texture*, Journal of Applied Crystallography **46**, 1722 (2013).
4. O. K. Johnson and C. A. Schuh, *The triple junction hull: Tools for grain boundary network design*, Journal of the Mechanics and Physics of Solids **69**, 2 (2014).
5. R. Aggarwal, M. J. Demkowicz, Y. M. Marzouk, *Bayesian inference of substrate properties from film behavior*, Modelling and Simulation in Materials Science and Engineering **23**, 015009 (2015).
6. O. K. Johnson, L. Li, M. J. Demkowicz, C. A. Schuh, *Inferring grain boundary structure–property relations from effective property measurements*, Journal of Materials Science **50**, 6907 (2015).
7. R. Aggarwal, M. J. Demkowicz, Y. M. Marzouk, *Information-driven experimental design in materials science*, in Information-driven Approaches to Materials Discovery and Design, T. Lookman, F. Alexander, K. Rajan eds. (Springer, 2015); **submitted**.

# Grain Boundary – Dislocation Interactions in Polycrystals: Characterization and Simulation for the Effective Design of High-Strength, High-Ductility Structural Alloys

David Fullwood, Eric Homer, Brigham Young University  
Robert Wagoner, Ohio State University

## Program Scope

This project aims to develop and verify a breakthrough capability to effectively treat large dislocation populations ( $\sim 10^{14}/\text{m}^2$ ) and their interactions, particularly with grain boundaries (GBs). Local and meso-scale dislocation activity, tensor populations, and activation stresses will be determined in the neighborhood of GBs through novel experiments, analysis, and simulation for a wide range of boundaries for two crystal structures: FCC/Ni and BCC/Ta. The results will be incorporated in a super-dislocation (SD) model.

Three enabling technologies will be created and used to accomplish the objectives:

- 1) At the meso scale, “meso-dislocation microscopy” based upon high-resolution EBSD will measure critical meso-scale quantities: GND densities and tensor character, and meso-scale obstacle stress.
- 2) At the atomistic level, “high-throughput molecular dynamics” will be constructed to simulate the equivalent local unitary (non-meso) dislocation-GB interactions and local obstacle stresses for a wide range of GB types.
- 3) At the macro scale, but linking all three scales, a “superdislocation model” based on finite element modeling (FEM) will analyze deforming multi-crystals using initial and evolving populations of dislocations consistent with crystal plasticity and GB obstacle stresses. These technologies will be applied to, and proven using, a *critical experiment* to track dislocation activity in the vicinity of selected GBs of Ni and Ta during controlled *in-situ* deformation. Careful comparative analysis of the three sets of results to reveal the fundamental mechanisms and linkages among the scales that control the properties of polycrystalline alloys based on grain and GB structure.

## Recent Progress

**Dislocation microscopy:** Four journal papers are in-press that cover critical areas of progress in the use of the cross correlation EBSD for dislocation measurement. These address topics such as the effect of step size on measured GND content, and the resolution of GND density onto individual slip systems. Fig. 1 illustrates the partial validation of the methodology for resolving GND content in a Ni sample that has been subject to wedge indentation.

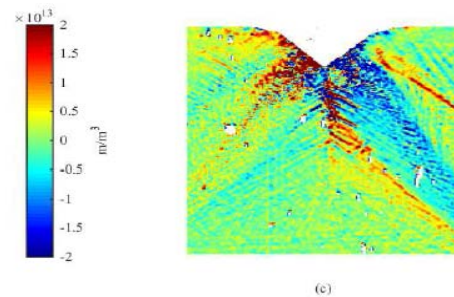


Figure 1: Dislocation density map for combined  $(1\bar{1}1)[\bar{1}01]$  and  $(1\bar{1}1)[011]$  edge dislocation types, around an indented nickel single crystal. The results are almost identical to values calculated using detailed plasticity calculations for the highly constrained system (see Ruggles IJP paper in ‘Publications’)

## Atomistic Modeling:

### **GB Dislocation Nucleation:**

Present simulations examine dislocation nucleation at the GB under varying triaxial stress states. The focus is the development of a model that properly accounts for and ultimately predicts the slip system and stress for nucleation under an arbitrary stress state.

Schmid's law by itself does not match the simulation results well as can be seen in Figure 2. A normal stress-dependent modification to Schmid's law, similar to Ref. [1], can improve the match for some boundaries, but is still inadequate. Current efforts are

focused on understanding why specific slip systems are preferred for nucleation besides having a lower shear stress based on Schmid's law. An adapted model is being developed to account for incentivized slip systems and the reasons behind their preference. Ultimately, this new model for dislocation nucleation can be incorporated in the super dislocation model to and will provide new functionality that accounts for both the structure and stress state in GB-dislocation interactions.

**Construction algorithm for GBs in FCC and BCC materials:** A series of scripts has been developed to construct atomistic GBs with arbitrary misorientations and boundary plane orientations in FCC metals. This is included in a published conference proceedings. Efforts are beginning for the creation of BCC Ta GBs to match the Ta GBs examined in experiments.

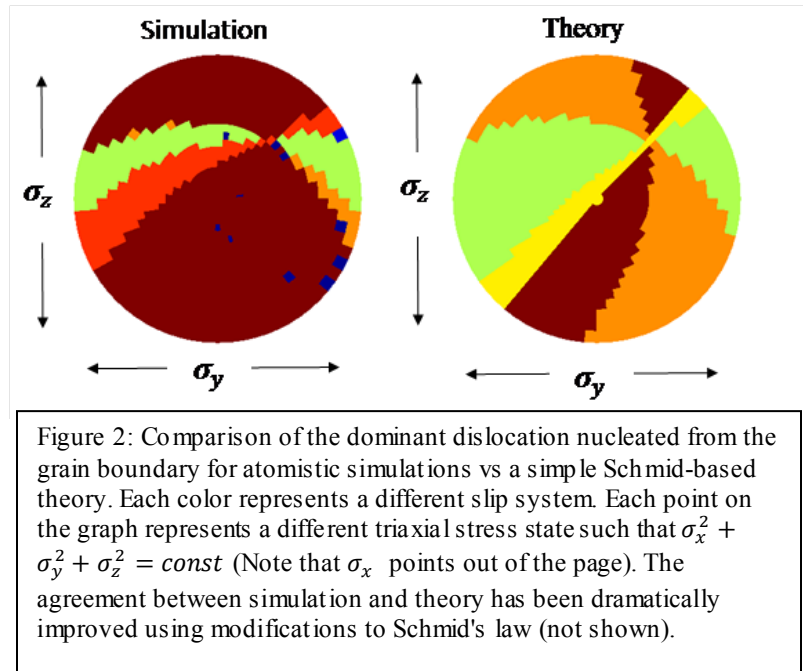
**Fundamental zones (FZs) for boundary plane orientation:** Recent advances have been implemented to introduce FZs for boundary plane orientation. Remarkable structure-property relationships of GB energy, mobility and excess free volume emerge from these FZs. A publication on this work is under review at Scientific Reports.

## Super Dislocation Model:

**UMAT development:** Various logistical and unification challenges have been overcome to arrive at a robust UMAT for the SD model, and three resultant core subroutines have been rigorously checked on minimum alloy steel:

- HARDENING: calculate slip resistance in each slip system
- GAMMADOT: calculate shear rate in each slip system
- REDIST: distribute SDs after grain scale simulation and calculate back stress by grain/grain boundary (GB) interaction)

**Ta constitutive parameter identification:** Material constitutive parameters for Ta were identified using stress-strain response and crystallographic orientation data of a Ta oligocrystal supplied by Sandia National Lab (SNL) [2]. Using the data, the constitutive parameters were calibrated for



SD model by inverse (and iterative) FE analysis. Determined parameters were used for simulations of Ta tensile and shear samples.

**Sample design for Critical Experiment:** The critical experiment requires a pure shear deformation along slip systems that impinge on a grain boundary of interest. The SD model and conventional continuum simulations were used to optimize the sample geometry and shear direction, starting from the work of Gao et al. [3]. The resultant specimen design is illustrated in Fig. 3. The specimens are currently being cut ready for investigations of dislocation interactions, pile-up and obstacle stress at the grain boundary.

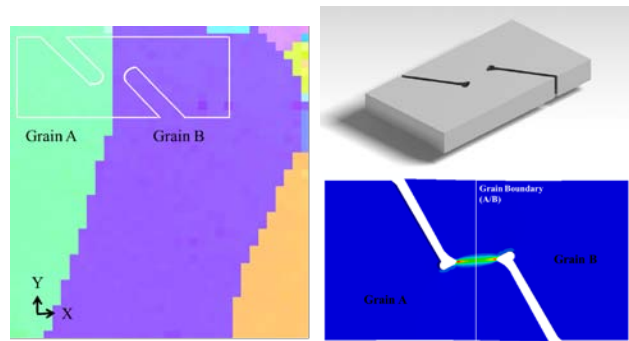


Figure 3: Overlay of shear sample schematic over large Ta grain (IPF map; left). CAD drawing of final sample design, and FEA model of stressed sample.

### Critical Experiment:

The SD model was used to simulate lattice curvature of a Ta oligocrystal (prepared by SNL) due to geometrically necessary dislocation evolution, based on Nye's tensor [4]. This was compared directly with EBSD data (see Fig. 4). Dislocation build-up at various grain boundaries, and several shear bands are successfully predicted by the model.

### Future Plans

#### Dislocation Microcopy:

Current progress will be incorporated into an open-source EBSD analysis tool (OpenXY) developed by the team. Validation will be further enhanced with transmission EBSD.

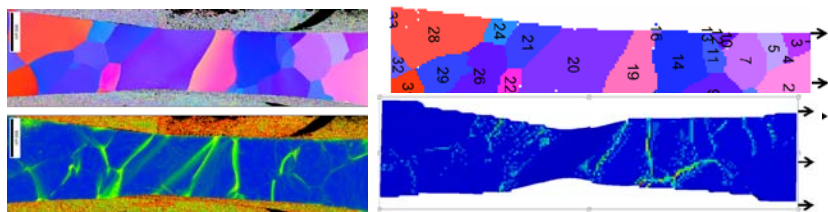


Figure 4: Inverse pole figure (IPF) map of Ta oligocrystal grain orientations above kernel-average-misorientation (KAM) map (left), and the related input and output (lattice curvature) from the SD model (right)

#### Atomistics:

**Training models:** Although our models are physically motivated, they currently have to be calibrated to simulated data. Work is underway to calculate the fitting parameters without having to run the entire simulation.

**Simulating grain boundary dislocation interactions:** Nucleation simulations will be followed by interaction simulations to determine the obstacle stress a dislocation encounters when it impinges on a grain boundary using atomistic simulations.

#### SD Model:

Based upon the results of the Ta oligocrystal and bicrystals, the underlying SD model assumptions, such as slip transmission criteria, dislocation interaction, etc., will be revisited. New mechanisms will be incorporated into the model, and current parameters will be tuned and calibrated.

### **Critical Experiment:**

Tantalum shear bicrystal specimens are currently being cut for polishing and testing. The final geometry and orientation will be input to the SD model for predicting the dislocation evolution with the currently assumed obstacle stress. Multiple bicrystals will then be prepared for sampling the space of potential grain boundaries.

Large-grained nickel material is also being annealed for an equivalent set of tests on FCC material.

### **References**

1. Douglas E. Spearot, Mark A. Tschopp, Karl I. Jacob, David L. McDowell, Tensile strength of  $\langle 100 \rangle$  and  $\langle 110 \rangle$  tilt bicrystal copper interfaces, *Acta Materialia*, 55(2) (2007), 705-714.
2. H. Lim, J. D. Carroll, C. C. Battaile, T. E. Buchheit, B. L. Boyce, and C. R. Weinberger, *International Journal of Plasticity*, 60 (2014) 60, 1-18.
3. F. Gao & L. Gui & Z. Fan, Experimental and Numerical Analysis of an In-Plane Shear Specimen Designed for Ductile Fracture Studies, *Exp. Mech.*, 51 (2011), 891-901.
4. J. F. Nye, *Acta Metallurgica*, 1(2) (1953), 153-162.

### **Publications**

1. Ali Khosravani, David Fullwood, B.L. Adams, T. Rampton, Michael Miles, Raj Mishra, Nucleation and propagation of 1012 twins in AZ31 magnesium alloy, *Acta Materialia*, in press
2. T.J. Ruggles, D.T. Fullwood, J. Kysar, Resolving geometrically necessary dislocation density onto individual dislocation types using EBSD-based continuum dislocation microscopy, *International Journal of Plasticity*, in press
3. David Fullwood, Mark Vaudin, Craig Daniels, Timothy Ruggles, and Stuart I. Wright, Validation of Kinematically Simulated Pattern HR-EBSD for Measuring Absolute Strains and Lattice Tetragonality, *Materials Characterization*, in press
4. Thomas J. Hardin, Timothy J. Ruggles, Daniel P. Koch, Stephen R. Niezgoda, David T. Fullwood, Eric R. Homer, Analysis of Traction-Free Assumption in High-Resolution EBSD Measurements, *Journal of Microscopy*, in press
5. Homer ER. Investigating the mechanisms of grain boundary migration in annealing processes using molecular dynamics. 36th Risø International Symposium Proceedings (Invited), IOP Conference Series MSE, vol 89 <http://dx.doi.org/10.1088/1757-899X/89/1/012006>
6. T.J. Ruggles, T.M. Rampton, A. Khosravani, D.T. Fullwood, The effect of length scale on the determination of geometrically necessary dislocations via EBSD continuum dislocation microscopy, *Ultramicroscopy*, Under Review (submitted May 2015)
7. E.R. Homer, S. Patala, J. Priedeman, Grain Boundary Plane Orientation Fundamental Zones and Structure-Property Relationships, *Scientific Reports*, Under Review (submitted Jun 2015)

# Atomic Scale Computational and Experimental Investigation of Twinning Mechanisms in HCP Systems

Maryam Ghazisaeidi, Assistant professor, Materials Science and Engineering, Ohio State University (Co-PI: Michael J. Mills, Ohio State University)

## Program Scope

The overarching goal of this project is to understand the fundamental reasons underlying different twinning behavior of various hcp metals by comparing twin nucleation and growth mechanisms in these systems. Of particular interest is the effect of alloying on twin nucleation and growth in Ti alloys. This project has three major thrusts: (1) studying twin nucleation as a result of slip transfer at the grain boundaries, using molecular dynamics/statics calculations, (2) quantifying the effect of Al on twin growth in Ti alloys, using *ab initio* calculations and experiments and (3) quantifying oxygen effects on twinning behavior of Ti through *ab initio* calculations and experiments. In this presentation we will only focus on computational aspects of objective (2). We use density functional theory (DFT) to study the structure of the Ti (10-12) twin boundary, the corresponding twinning dislocation, and the twin–solute interaction energies for Al. Next, we will examine the solute strengthening of twinning mode using a new Labusch-type weak pinning model.

## Recent Progress

We start with the coherent twin boundary structure and compute the stable structure. The interaction energies of Al solutes with the (10-12) twin boundary are calculated using density functional theory (DFT). Fig. 1 shows the twin/solute interaction energy map. Possible independent solute sites are identified and numbered based on their distance from the twin boundary as shown in Fig.1. Interaction energies at all the unnumbered sites are obtained from mirror symmetry with respect to the twin boundary and translational invariance along the boundary plane. Note that the strongest interaction occurs at the twin boundary showing an oscillating repulsion/attraction behavior. Bulk geometry is retrieved and the twin/solute interaction energy quickly fades for sites away from the twin boundary. The reference energy configuration is taken to be a system with a solute atom at a bulk-equivalent site -far from the twin boundary.

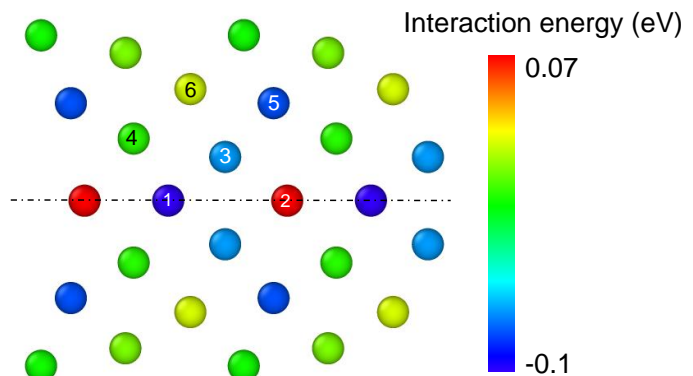


Figure 1 Interaction energy map between Ti twin boundary and Al solutes



A twinning dislocation (disconnection) is a line defect with both dislocation and step characters [1-2]. In the case of (10-12) twin, the twinning dislocation step involves two atomic planes. As the twinning dislocation glides on the twin plane, it transforms the crystal structure on one side to the corresponding mirror structure, advancing the twin boundary by the step height. The Burger's vector character of the twinning dislocation is geometrically related to the twinning shear and is defined as a fraction of the perfect lattice vector along the twinning shear direction as  $\vec{b}_t = s[10\bar{1}\bar{1}]$  where  $s = 0.087$  is determined by the shear necessary to create a two-layer-thick twin lamella and is computed using the DFT-computed  $c/a$  ratio of 1.587 for Ti. As a first step, we approximate the disconnection with two coherent twin boundaries separated by a two atomic-layer step as shown in Fig.2.

Previous calculations of the same twinning dislocation in Mg have shown that the dominant interactions occur at the twin boundaries rather than the defect core [3]. Therefore, this is a reasonable approximation. We will directly compute the structure of this defect and interactions with solutes in the future.

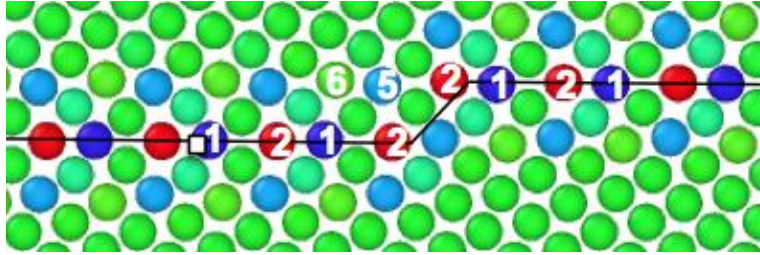


Figure 2 Twinning dislocation (disconnection) approximated with two twin boundaries separated by a step. The interaction energy map is obtained by juxtaposing the map in Fig.1

Next, using the above interaction energies, we calculate the stress and energy barrier required to move the twinning dislocation caused by the presence of solutes via a new Labusch-type weak pinning model [4]. This model is based on the collective effect of solutes; a straight dislocation bows out in the glide plane towards favorable solute environments to minimize its potential energy. However, bowing has a cost in elastic energy. Therefore, the favorable configuration of a dislocation is that which minimizes the total energy as a function of the dislocation bowing segments of length  $\zeta$  and the amplitude of the bowing  $w$ . The total energy as a function of roughening amplitude  $w$  and segment length  $\zeta$  is given by

$$E_{tot}(\zeta, w) = \left[ \left( \Gamma \frac{w^2}{2\zeta} \right) - \left( \frac{c\zeta}{a_0} \right)^{1/2} \Delta\tilde{E}_p(w) \right] \frac{L}{2\zeta}$$

Where  $L$  and  $a_0$  are line length and periodicity along the line direction (lattice parameter), respectively,  $\Gamma$  is the dislocation line tension and  $c$  is the solute concentration. The quantity  $\Delta\tilde{E}_p(w)$  is given by

$$\Delta\tilde{E}_p(w) = \left[ \sum_{ij} (U(x_i, y_j) - U(x_i - w, y_j))^2 \right]^{1/2}$$



with  $U(x_i, y_j)$  being the solute–dislocation interaction energy for a solute at position  $(x_i, y_j)$  in the plane perpendicular to the dislocation line and relative to a dislocation at the origin  $(x=0, y=0)$ . Minimizing the total energy with respect to  $\zeta$  gives a characteristic segment length  $\zeta_c$  as a function of  $w$  and the total energy at this characteristic as a function of  $w$  only. The characteristic roughening  $w_c$  is then obtained by numerical minimization of  $E_{tot}/L$ . The energy barrier and the zero temperature yield stress, controlling the motion of segments of length  $\zeta_c$  can be obtained from this minimum energy. Thermal activation theory is then used to obtain the yield stress at a given temperature  $T$  and strain rate  $\dot{\epsilon}$ . Fig.3 shows the total energy per unit length as a function of  $w$ . Unlike previous applications of the model to slip modes in Al and Mg [4,5], a clear minimum in the total energy does not emerge from the analysis; this is unique to the twin and is consistent with previous studies in Mg alloys. The existence of multiple roughening amplitudes implies that for fixed values of temperature, concentration, and strain rate, there are now many configurations available for the twinning dislocation to optimize its energy. Among all of these configurations, the one requiring the highest stress to achieve the desired strain rate at any given temperature is the configuration that controls the strengthening.

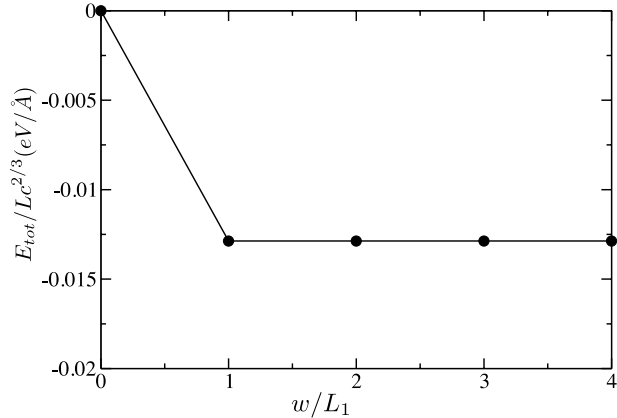


Figure 3 Normalized energy per unit length vs. roughening amplitude normalized by the periodicity of the coherent twin boundary  $L_1 = 6.92$  Å for Al interacting with the twinning dislocation in Ti.

Thus, a prediction of the yield stress versus temperature and concentration requires computing the strength for all possible roughening amplitudes and then determining the maximum among all these strength values. The strength versus temperature at a given  $c$  is then constructed as the “envelope” of the strength vs.  $T$  curves for each  $w$ . We derive an

$$\tau_y(T, \dot{\epsilon}) = \frac{2\pi(33 - 8\sqrt{2})}{25\sqrt{5}b} \frac{[-E_{tot}/Lc^{2/3}]^{3/2} \sqrt{\Gamma} c}{k_B T \ln \dot{\epsilon}_0/\dot{\epsilon}}$$

analytical form for this stress envelope, given by

where  $b$  is the Burgers vector magnitude, and  $\dot{\epsilon}_0$  is a reference strain rate [3]. The numerical prefactors are determined by the crystallographic orientation of the defect. We present results for the stress required to move the twinning dislocation in a random field of Al solutes as a function of temperature and solute concentration and compare the strengthening effect of Al on the twinning mode in Ti vs. Mg.

## Future Plans

First, we will compute the twinning dislocation geometry and interaction energy with Al solutes directly from DFT. The approximate energies above are reliable only if the defect

core remains compact, but to date, a direct DFT based calculation of the twinning disconnection in Ti does not exist. The next step is to analyze the effect of Al on a new twin thickening mechanism proposed for Mg alloys [6]. This model presents a thermally activated, stress-driven mechanism for the growth of twin boundaries by forming islands on existing boundaries. Fluctuations in the local concentration of solutes drastically affect the stressed required for activation of this mechanism. This analysis completes the study of solid solution effects on (10-12) twinning mode in Ti. Comparing the results, with available data for Mg-Al alloys can shed light on differences in ways Al solutes affect twinning in Ti vs. Mg alloys. Furthermore, the possibility of short-range order (SRO) formation in Ti-Al alloys and the interactions of these SROs with the twinning mode will be studied. On the experimental side, Microtensile testing of single crystal Ti-Al alloys in  $\langle c \rangle$  orientation will be performed to investigate twinning in single crystal mode for more direct comparison with computational predictions.

## References

1. Serra A, Bacon DJ, Pond RC. Acta Metall 1988;36:3183–203.
2. Serra A, Bacon DJ, Pond RC. Acta Metall 1999;47:1425–39.
3. M. Ghazisaeidi, L. G. Hector Jr and W. A. Curtin, Acta Mater, 2014; 80: 278-287.
4. Leyson GPM, Hector Jr LG, Curtin WA, Woodward CF. Nat Mater 2010;9:750–5.
5. Leyson GPM, Hector Jr LG, Curtin WA. Acta Mater 2012;60:5197–203.
6. A. Luque, M. Ghazisaeidi and W. A. Curtin, Acta Mater , 2014;81:442-456.

## Publications

“The Effects of Short-Range Ordering and Texture on Twinning in an  $\alpha$ -Ti-6 wt% Al Alloy”, M. C. Brandes, Gopal Viswanathan, W. Morgan, N. Thirumalai, M. Ghazisaeidi and M. J. Mills, *to be submitted to Acta Mater*

# **Modulating Thermal Transport Phenomena in Nanostructures via Elastic Strain at Extreme Limits of Strength**

**Daniel S. Gianola**

*Department of Materials Science and Engineering  
University of Pennsylvania, Philadelphia, PA 19104*

## **Program Scope**

Nanoscale materials fabricated with nearly pristine crystal structure are often endowed with ultra-strength behavior, where material failure occurs at a significant fraction of its ideal limit. The thermal conductivity exhibited by such materials is also uniquely affected by the high surface-to-volume ratio at the nanoscale. The juxtaposition of the vastly increased dynamic range of elastic strain available in ultra-strength nanomaterials and altered thermal transport shows promise for tunable thermal properties. This project aims to exploit these properties of high-strength nanostructures to elucidate the coupling between large mechanical strains and thermal conductivity (both electron and phonon) leading to better understanding and control of the thermal performance in these materials. Unique fabrication methods to produce nanosized quasi-defect free single crystals and modern nanomechanical testing will be used to identify the size-dependent dynamic range of elastic strain and understand deformation mechanisms near the ideal limit. Identifying and quantifying thermal transport phenomena as a function of mechanical strain in these nanostructures will open the door to using elastic strain engineering in high-strength nanomaterials to tune thermal transport. The results of these investigations will be used to improve the performance, efficiency, and versatility of advanced thermal management and energy conversion devices with tunable response.

## **Recent Progress**

Results from our work supported by this DOE program have demonstrated the influence of strain, resulting both from externally applied mechanical loading as well as the introduction of core defects possessing a self-stress, on the lattice thermal conductivity of Si nanowires. These results were obtained using *in situ* Raman piezothermography, a novel experimental approach developed under this DOE program at Penn (Fig. 1). Our results show that, whereas phononic transport in undoped Si nanowires is only marginally affected by uniform elastic tensile strain, point defects introduced via ion bombardment that disrupt the pristine lattice reduces the thermal conductivity by over 80%.

The implications of our work on Si nanowires are two-fold. First, our results glean insight on a current debate as to whether surface- or core-governed pathways predominate in controlling lattice thermal conductivity in Si nanostructures. We show that bulk phenomena governed by core defects have a large effect even at the nanoscale, where surface effects are expected to dominate. This suggests a new avenue of controlling thermal transport in nanostructures beyond surface modification, namely via defect engineering. This is particularly important as current strategies for roughening nanowires are known to introduce porosity in the interior of the structure, and our results strongly imply that these core defects could be responsible for the majority of the reduction in thermal conductivity in reports of rough

nanowires. Indeed, our findings confirm recent theoretical work showing that phonon scattering from core defects dominates over scattering from rough surfaces in nanowires.

Second, our results strongly indicate that spatially varying (inhomogeneous) elastic strain fields are much more potent at reducing lattice thermal conductivity than uniform strain (e.g. uniaxial tension). Since specific heat capacity, phonon group velocities, and phonon scattering times govern the lattice thermal conductivity, our findings suggest that uniform strains affect only phonon frequencies, and thus heat capacity and group velocity, whereas nonuniformity in strain affects phonon scattering times. Guided by these experiments, we further hypothesize that enhancing anharmonicity by way of inhomogeneity in strain could be a powerful means to engineering thermal conductivity.

Inspired by the dominant role of spatially heterogeneous strain in controlling thermal transport, we developed fabrication schemes for rationally introducing nonuniform strain fields in Si thin films via nanomesh geometries. We term these *metadefect* structures, which are tunable by virtue of the engineered elastic strain gradients around ordered features in the nanomesh, patterned with length scales larger than the underlying atomic structure. In analogy to atomic-level defects in crystalline materials that introduce heterogeneous and long-range elastic strain fields owing to perturbations of the otherwise perfect crystalline lattice, we exploit strain amplification around patterned features to tune global thermal transport behavior. This year, we began batch fabrication of freestanding nanomesh films from silicon-on-insulator wafers and preliminary thermal testing of these Si nanomeshes.

We also extended this general concept of heterogeneous elastic strain engineering to modeling of tunable electrical conductivity and Seebeck coefficients in strained silicon nanomeshes with architected porosity. In conjunction with thermal conductivity, these three functional properties comprise the thermoelectric figure of merit. We combined analytical models for electron mobility in uniformly stressed silicon with finite element analysis of strained silicon nanomeshes to guide experimental design. Our results show that the nonuniform and multiaxial strain fields defined by the nanomesh geometry give rise to spatially varying electronic structure band shifts and warping, which in aggregate accelerate electron transport along directions of high stress. This allows for global electrical conductivity and Seebeck enhancements beyond those of homogeneous samples under equivalent far-field stresses, ultimately increasing thermoelectric power factor over unstrained samples.

Our previous finding that uniform strain affects thermal conductivity only weakly, whereas defects have a strong effect, motivates the need for a means of tunably applying heterogeneous states of strain in order to understand the effect of gradients on phonon scattering.

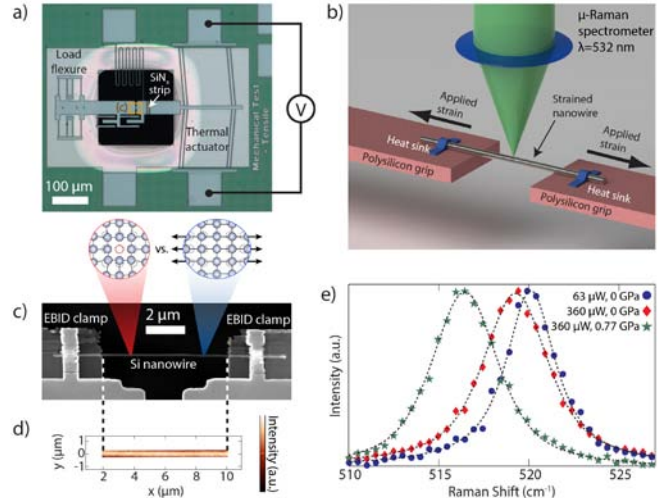


Figure 1: *In situ* Raman piezothermography method applied to strained, suspended nanowires. a) MEMS tensile testing device. b) Schematic of experimental setup. c) SEM image of a  $\langle 111 \rangle$  Si nanowire clamped to the MEMS device. d) A to-scale map of Raman peak intensities. e) Sample spectra collected at low ( $63 \mu\text{W}$ ) and high ( $360 \mu\text{W}$ ) applied laser powers and at 0 and 0.77 GPa.

It would furthermore be useful to find ways of isolating the strain gradient effect since the relative weights of the mechanisms behind phonon scattering from defects (strain gradients, mass-difference, changes in interatomic potential, interfaces, etc.) are not well studied in real systems. There are several means by which heterogeneous strain may be reversibly applied to a nanostructure, including bending or indenting within the elastic regime or straining a kinked nanowire or a micromesh. The last of these is attractive since we may draw parallels between a micromesh -- a thin film containing pores which extend through the thickness -- and a defected system. Pores may be considered similar to vacancy clusters in that they are essentially missing atoms; however, the spatial extent of strain gradients near these pores would be relatively low compared to the size of the pores. This is in contrast to a vacancy cluster, where the volume of the distorted lattice is on the order of the volume of missing atoms. Applying a far-field load to a micromesh creates a heterogeneous state of strain, with varying strain states and magnitudes within the same structure, with the largest gradients near the holes, analogous to systems containing high vacancy concentrations. Although this analogy is imperfect, measurements of micromesh thermal conductivity both with and without strain may shed light on the relative importance of the mechanisms behind vacancy scattering as well as provide another means of engineering materials thermal conductivity.

Free-standing Si tensile bars were fabricated in the device layer of commercially available (100) silicon-on-insulator (SOI) wafers with the axis along the  $\langle 110 \rangle$  direction. We found an unstrained, fully dense tensile bar of thickness  $1.65 \pm 0.01 \mu\text{m}$  to have room temperature thermal conductivity nearly identical to that of bulk Si, as would be expected for a sample of this size. Up to 1% tensile strain was applied to the tensile bar, and up to 8% decrease in thermal conductivity was observed. We applied the piezothermography method used for fully dense Si to two nominally-identical micromesh structures and measured thermal conductivity as a function of far-field strain. Unstrained micromeshes exhibited thermal conductivities of  $20\text{--}21 \text{ W m}^{-1} \text{ K}^{-1}$ . This is approximately half what we'd expect by comparison with mesh structures of roughly similar dimensions ( $4.5 \mu\text{m}$  thickness with  $2.3 \mu\text{m}$ -diameter pores and  $4 \mu\text{m}$  spacing, fabricated by Song and Chen using deep reactive ion etching), and we attribute the difference to our use of the FIB to fabricate the pores.

We observed measurably nonuniform strains within the mesh region for far-field strains above 0.08% and up to 0.32%, after which the tensile bars fractured. The strain patterns were self-similar at all strains (Fig. 2 a,b). We observed decreasing thermal conductivity in the two nominally identical Si micromeshes with increasing far-field strain -- equivalently, increasing strain gradients within the mesh -- far beyond what we measured for uniformly strained Si (Fig. 2c). The linear fit to these data suggests a 48% decrease in thermal conductivity for every 1% applied far-field strain. The maximum

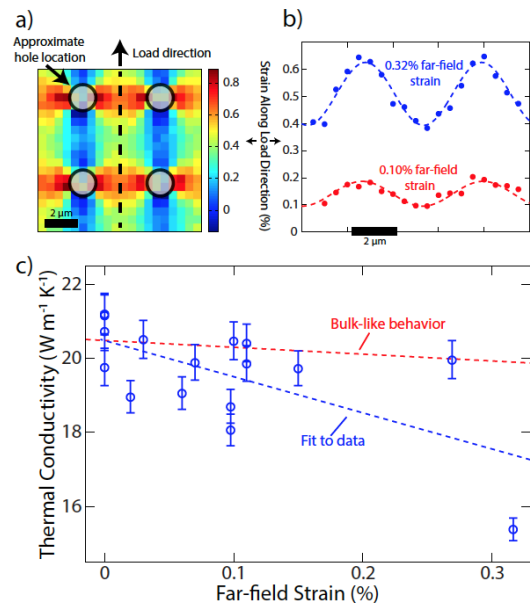


Figure 2: Preliminary thermal conductivity of strained Si micromeshes. (a) Experimentally measured nonuniform strains in a mesh with far-field strain of 0.32% as determined by Raman spectroscopy. (b) Strain profiles along path shown in (a) for two applied strain levels showing sinusoidal strain gradients. (c) Thermal conductivity of Si micromesh, indicating a stronger dependence on strain relative to the fully dense (bulk-like) films.

strain in the mesh, at the edges of the pores, is about 3x the far-field strain, so this is equivalent to a 16% decrease in thermal conductivity for every 1% increase in the maximum strain in the mesh. In contrast, for the fully dense tensile bars (uniform strain), we observed just 8% decrease for every 1% applied strain, a far smaller change than what we measure in the meshes. We confirmed that no permanent deformation such as defects or microcracks was responsible for the decrease in thermal conductivity at least up to 0.15% far-field strain, since thermal conductivity recovered upon unloading (we were unable to perform unloading tests beyond 0.15% due to sample failure). These results therefore show that heterogeneous strain is a far more effective modifier of thermal conductivity than uniaxial strain, since the changes in thermal conductivity in strained meshes outpace the changes in thermal conductivity for uniaxially strained systems.

Thorough simulations will need to be performed in order to fully understand these results, and to our knowledge strain fields which vary over such long distances or do not arise from some defect have not been studied. In general, it has been known since the 1950s that the decrease in thermal conductivity in defected systems (e.g. vacancies, dislocations, grain boundaries) arises in part from the introduction of structural disorder and subsequent breaking of lattice symmetry, as well as spatially-varying interatomic force constants. These increase vibrational anharmonicity and hence phonon scattering, reducing the phonon scattering time. More recently, simulations by Meng et al. demonstrated that the magnitude and spatial extent of the interfacial strain field between two different crystals partly determines the scattering rate with a strong dependence on phonon wavelength -- phonons with wavelength shorter than the thickness of the strained region are more likely to scatter. This may help explain why we observe decreases in thermal conductivity without introducing smaller length scales. A similar study incorporating the full strain tensor and phonon dispersion could shed light on our findings as well as allow for an optimization of the mesh pattern for tuning thermal conductivity.

## Future Plans

Our results clearly underscore the importance of not only elastic strain, but also spatially varying strain gradients, in controlling both thermal and electrical transport in Si micro- and nanostructures. This concept is encapsulated in the term *metadefect* that we have coined, which represents a strategy for engineering such gradients in a tunable fashion. We believe this approach is a new and potent strategy for tuning function properties, and will thus be the focus of our efforts in the next funding cycle. Three specific strategies will be targeted over the next reporting period: (1) a systematic study of thermal conductivity in the Si micromeshes to complement our preliminary results, (2) the development of a nanomesh fabrication route entirely based on patterning and Si etching without the use of the damaging FIB, and (3) rational patterning of mesh geometries to elicit large changes in thermal and charge transport with remotely applied elastic strains. The last target will consider the intrinsic length scales with phonon physics and target strain gradient length scales that match phonon mean free paths in Si and other semiconductor materials. Furthermore, phonon mean free paths represent a distribution of length scales at finite temperature, and these experimentally measured statistics can be used to introduce disorder in the mesh geometry to match distribution of such length scales. This can be achieved by designing the mesh lattice and its accompanying disorder in Fourier space (spatial frequencies), and then transforming this to real space in the form of pore spatial positions. These designed geometries can directly input into the experimental patterning process during fabrication.

**Publications** (from previous 2 years of DOE project)

- K.F. Murphy, L.Y. Chen, D.S. Gianola, “Effect of organometallic clamp properties on the apparent diversity of tensile response of nanowires,” *Nanotechnology*, **24** (2013) 235704.
- K.F. Murphy, B. Piccione, M.B. Zanjani, J.R. Lukes, D.S. Gianola, “Strain- and Defect-Mediated Thermal Conductivity in Silicon Nanowires,” *Nano Letters* 14 (2014) 3785.
- B. Piccione, D.S. Gianola, “Tunable Thermoelectric Transport in Nanomeshes via Elastic Strain Engineering,” *Applied Physics Letters* 106 (2015) 113101.
- E.A. Flores-Johnson, T.J. Rupert, K.J. Hemker, D.S. Gianola, Y. Gan, “Modelling wrinkling interactions produced by patterned defects in metal thin films,” *Extreme Mechanics Letters* (2015) available online, <http://dx.doi.org/10.1016/j.eml.2015.07.002>.

# Investigation of radiation damage tolerance in interface-containing metallic nano structures.

Julia R. Greer

California Institute of Technology (Caltech) Pasadena, CA 91125

## Program Scope

The proposed work seeks to conduct a basic study by applying experimental and computational methods to obtain quantitative influence of helium sink strength and proximity on He bubble nucleation and growth in He-irradiated nano-scale metallic structures, and the ensuing deformation mechanisms and mechanical properties. The proposed work utilizes a combination of **nano-scale *in-situ* tension and compression** experiments on low-energy He-irradiated samples combined with site-specific **microstructural characterization** and **modeling efforts**. This systematic approach will provide us with critical information for identifying key factors that govern He bubble nucleation and growth upon irradiation as a function of both *sink strength and sink proximity* through an experimentally-confirmed physical understanding. So far, the attention has been focused on studying individual bcc/fcc interfaces within a single nano structure: a single **Fe (bcc)-Cu (fcc)** boundary per pillar oriented perpendicular to the pillar axes, as well as pure bcc and fcc nano structures. Additional interfaces of interest include bcc/bcc and metal/metallic glass all within a single nano-structure volume. The model material systems are: (1) pure single crystalline **Fe and Cu**, (2) a single **Fe (bcc)-Cu (fcc)** boundary per nano structure (3) a single **metal-metallic glass**, all oriented non-parallel to the loading direction so that their fracture strength can be tested.

A nano-fabrication approach, which involves e-beam lithography and templated electroplating, is utilized, which enables precise control of the initial microstructure control. Experimentally determined stress-strain relationships are enhanced by *in-situ* SEM observations coupled with TEM microstructural characterization of the same samples before and after deformation (irradiated and as-fabricated) and atomistic (MD) modeling. A comprehensive suite of experiments is being conducted to quantitatively assess the key parameters for He bubble nucleation and growth by independently varying the sink strength, sink proximity, and He implantation temperature and dose. The implantations have been conducted at Sandia and Los Alamos National Labs. Nano structures containing He-enriched interfaces are tested under *uniaxial tension* to assess embrittlement, resulting boundary strength, and deformation mechanisms. Successful execution of this work will help identify which types of interfaces are particularly resilient against radiation damage.



## Recent Progress

Our current progress is summarized in this table:

Goal	Accomplishment
Developed methodology to Al-Ni-Zr metallic glasses in compression and tension configurations, as well as in nano-architected meta-materials. <u>Personnel:</u> R. Liontas	Compressive and tensile specimens shaped as cylinders with “hats” for gripping have been fabricated from a sputtered Ni-Al-Zr metallic glass film. Conditions for sputtering were optimized to unambiguously produce metallic glass (amorphous) confirmed by TEM.
Conducted in-situ nano-mechanical experiments on Ni-Al-Zr nano-glasses and discovered ductility in excess of 100% at unusually large dimensions of ~250nm. <u>Personnel:</u> R. Liontas and D. Chen (not supported by this grant)	Nano-mechanical experiments were performed in custom-made in-situ nanomechanical instrument comprised of PI-85 Hysitron device inside of a DualBeam Versa FIB (FEI).
Characterization and annealing of sputtered nano-metallic glasses to quantify free volume <u>Personnel:</u> R. Liontas, and D. Chen	Samples for TEM analysis and simultaneous in-situ tensile experiments were prepared via site-specific FIB/Omniprobe lift-out. Microstructural TEM analysis was carried out on all samples to ensure amorphous nature of metallic glasses for each fabrication method.
Atomistic simulations <u>Personnel:</u> Mehdi Zadeh (not supported by this grant)	Close collaboration with the Institute for High Performance Computing to simulate the same Ni-Al-Zr glass to help quantify the amount and distribution of free volume, as well as the physics of shear band initiation.

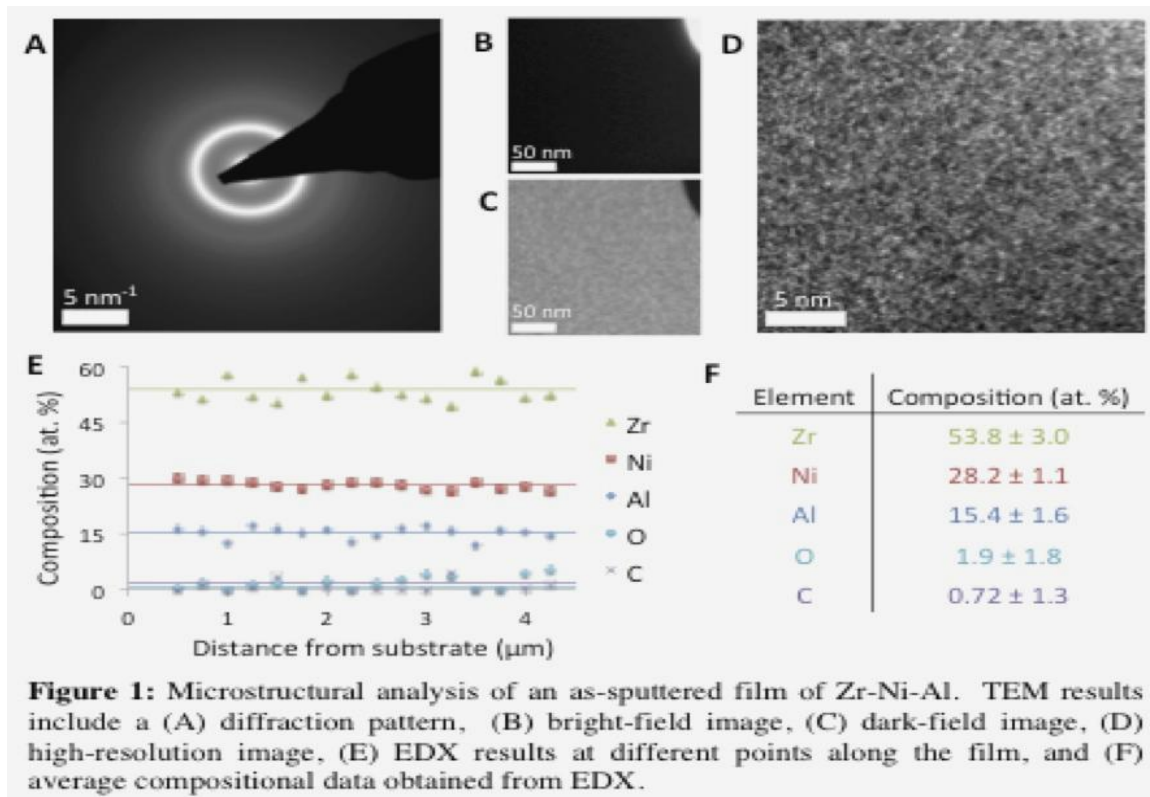
## In the last 2 years we focused on the effects of irradiation on nano-structured metallic glasses.

Building upon our previous work, which showed an improvement in the tensile properties of Ni-P metallic glass nanopillars upon helium irradiation, we are studying the use of nano-structured metallic glass as a new class of radiation-damage tolerant materials. By nano-structuring the metallic glass we are able to proliferate both “smaller is more ductile” size effects and radiation-induced improvements in ductility to a larger scale material. We nano-structure the metallic glass through the use of nanolattices, which are fabricated by utilizing two-photon direct laser writing lithography to create a three-dimensional polymer skeleton and then sputtering the metallic glass directly onto that polymer skeleton.

We have selected Zr-Ni-Al as the metallic glass for this study. This metallic glass was chosen for its oxidation resistance and high glass transition temperature, which will allow study of irradiation at elevated temperatures without crystallization or oxidation. Additionally, the chosen system contains only metallic atoms and is thus a true *metallic* glass with metallic as opposed to covalent bonding. We create this metallic glass by sputtering a  $Zr_{56}Ni_{22}Al_{22}$  alloyed

target at 100 W under 3 mTorr Ar. The deposition rate under these conditions is  $\sim 4 \text{ nm min}^{-1}$  and thus by sputtering for various times we can create nanolattices with various metallic glass wall thicknesses.

As this sputtered Zr-Ni-Al metallic glass has not been studied previously, we first undertook a fundamental study of its microstructure and mechanical properties. The microstructure was examined by transmission electron microscopy (TEM) of a film that had been sputtered for  $\sim 20$  hours to a thickness of  $\sim 4.5 \mu\text{m}$ . These TEM results are shown in Figure 1. As can be observed in Figure 1, the sample is confirmed amorphous by the presence of diffuse rings in its diffraction pattern (Figure 1A), uniform contrast bright-field (Figure 1B) and dark-field (Figure 1C) images, as well as the lack of any observable ordering in the high resolution TEM image (Figure 1D). Energy-dispersive x-ray spectroscopy (EDX) was also conducted on the film at various distances from the substrate in order to determine if there were any variations in chemical composition with sputtering time. The resultant quantification of the chemical composition from the EDX data is plotted in Figure 1E as a function of distance from the substrate and shows no significant variation in the chemical composition of the film as a function of distance from the substrate and hence this sputtering process does not vary over time. The horizontal lines shown in Figure 1E are plotted at the average composition for each element and Figure 1F displays these average composition values. Figure 1F indicates there is very little carbon or oxygen present in the sample with less than 2 at. % of each, and the stoichiometry of Zr/Ni/Al corresponds to  $\text{Zr}_{55}\text{Ni}_{29}\text{Al}_{16}$ .



We examined the mechanical properties of the Zr-Ni-Al metallic glass via uniaxial compression tests on nano-pillars. Cylindrical samples were fabricated by focused-ion beam (FIB) from the same  $\sim 4.5 \mu\text{m}$  thick sputtered film shown in Figure 1. These nano-pillars had diameters ranging from 225 nm to  $1.56 \mu\text{m}$ , and corresponding heights such that the aspect ratio was 1:3. The pillars were compressed at a strain rate of  $1 \times 10^{-3} \text{ s}^{-1}$  in a special *in-situ* nanomechanical instrument that is comprised of a Hysitron PI-85 nanoindenter inside the Versa 3D DualBeam. The resultant compression data is displayed in Figure 2. These pillars exhibited two very distinct regimes of mechanical behavior depending on their size: ductile behavior and homogeneous flow was observed for “small” pillars with initial diameters  $\leq 555 \text{ nm}$ , while shear banding and localized failure was observed for “large” pillars with initial diameters  $\geq 890 \text{ nm}$ . These differences in mechanical response are apparent from the stress-strain curves, which show

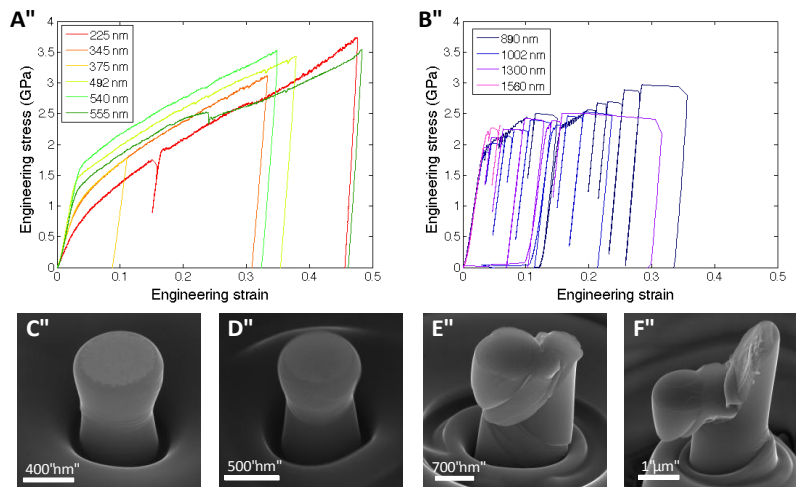


**Figure 2:** Uniaxial compression tests on FIB-milled Zr-Ni-Al pillars. Engineering stress-strain data for (A) “small” pillars with diameters ranging 225-555 nm and (B) “large” pillars with diameters ranging 890-1560 nm. Typical SEM images of the pillars post-compression are shown for pillars with initial diameters of (C) 492 nm, (D) 540 nm, (E) 1300 nm, and (F) 1560 nm.

uniform plastic loading for the “small” pillars (Figure 2A), and many strain bursts from the catastrophic shear banding events for the “large” pillars (Figure 2B). The post-compression images of the pillars also illustrate the differences in mechanical response with the “small” pillars exhibiting homogeneous deformation near the top of the pillars (Figure 2C-D) and the “large” pillars exhibiting clear shear bands (Figure 2E-F). Overall,

the compression data indicates a transition from homogeneous flow to shear banding at a pillar diameter of 555 nm, which is larger than any previous reports of observed ductility in metallic glass.

Building on these unexpected compression results, we fabricated additional samples for uniaxial tension tests. A thin metallic glass film was first deposited directly XeF<sub>2</sub> etch of the underlying Si substrate. Tensile samples were then FIB-milled directly onto the TEM grid, which facilitated ease of TEM analysis after mechanical testing. Pillars were fabricated with widths ranging from 85 – 215 nm and heights correspond to an aspect ratio of  $\sim 1:10$ . Tensile tests were performed at a strain rate of  $1 \times 10^{-3} \text{ s}^{-1}$  using the Hysitron PI-85 nanomechanical testing instrument *in-situ* in the Versa 3D SEM using custom-milled diamond tension grips. The resultant data is shown in Figure 3 and grouped by pillar width: (A-C) sub-100 nm, (D-F)  $\sim 100 \text{ nm}$ , (G-I)  $\sim 150 \text{ nm}$ , (J-L)  $\sim 200 \text{ nm}$ . As with the compression pillars (Figure 2), the tensile pillars exhibit two distinct regimes of mechanical behavior: “small” pillars widths  $\leq 153 \text{ nm}$  fail by extremely noticeable necking and reach true strains  $\sim 150\%$  while “large” pillars widths  $\geq 199 \text{ nm}$  fail by shear

banding and only a small amount of ductility in the stress-strain curves. The extreme ductility in the “small” metallic glass pillars, as evidenced by the value of ~150% true strain, is exceptionally large and indicates the as-sputtered Zr-Ni-Al metallic glass is in a very unrelaxed state with a large amount of free volume present.

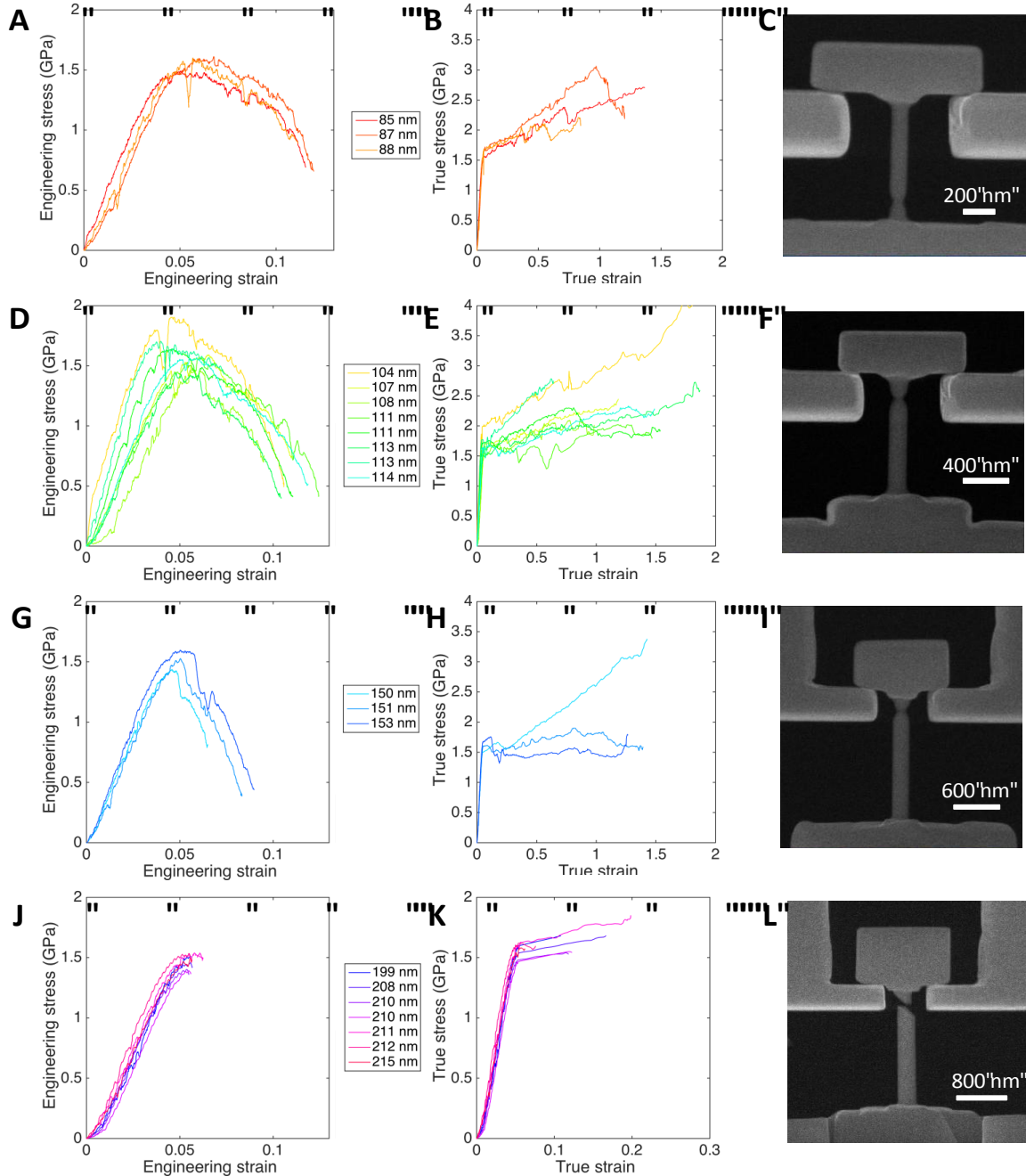


**Figure 3:** Uniaxial tensile tests on FIB-milled Zr-Ni-Al pillars for: (A-C) sub-100 nm pillar widths, (D-F) ~100 nm pillar widths, (G-I) ~150 nm pillar widths, and (J-L) ~200 nm pillar widths. Engineering stress-strain data is shown in (A, D, G, J), true stress-strain data is shown in (B, E, H, K), and SEM images of the pillars around the time of fracture are shown for pillar widths of (C) 85 nm, (F) 111 nm, (I) 151 nm, and (L) 210 nm.

The as-sputtered metallic glass had remarkably enhanced ductility often in excess of 100%, which is consistent with a high fraction of free volume in the sputtered glass. Efforts are underway to quantify the amount of relaxation and free volume in this metallic glass and relate it to ductility. We are currently studying the same metallic glass in a more relaxed state with lower free volume to test whether the ductility would be suppressed. Towards this aim, subsequent to sputtering the Zr-Ni-Al metallic glass directly on the TEM grid, we annealed the sample in an Ar environment for 24 hours at a temperature of 625 K ( $\sim 0.85T_g$ ). The as-sputtered metallic glass contains an excess of free volume, in a non-equilibrium state, frozen in the material from the sputtering deposition process. Annealing the metallic glass increases the mobility of the atoms, allowing a relaxation process with structural rearrangement that reduces the amount of excess free volume. Following this annealing step, tensile pillars were fabricated following an identical FIB-milling process as the as-sputtered film with pillar widths in the same range as those previously tested, 79 – 209 nm. As with the as-sputtered pillars, tensile tests were performed at a strain rate of  $1 \times 10^{-3} \text{ s}^{-1}$  using the Hysitron PI-85 nanomechanical testing instrument in-situ in the Versa SEM. After annealing, the sample's microstructure was analyzed by TEM to ensure that crystallization and oxidation had not occurred, these TEM results are shown in Figure 4 with an image of the entire pillar analyzed shown in (Figure 4A). The sample maintained an amorphous microstructure upon annealing, as evidenced by the diffuse ring in the diffraction pattern (Figure 4C) and the uniform contrast bright-field (Figure 4D) and dark-field (Figure 4E) images. The EDX results (Figure 4B) indicate an increase in the amount of carbon and oxygen present from the as-sputtered sample (Figure 1F) but the amounts are  $\leq 10 \text{ at. \%}$  and still not significant enough to warrant concern. Oxidation was prevented in this sample by annealing in an Ar environment. Furthermore, the process of FIB-milling the nano-pillars from a larger film of Zr-Ni-Al metallic glass provides substantial oxidation protection, as the annealing is conducted prior to FIB-milling the pillars. Therefore any surface oxides layers resulting from annealing are removed by the FIB-fabrication process and the actual pillar test-section is more than  $1 \mu\text{m}$  from the film surface exposed to the annealing environment.

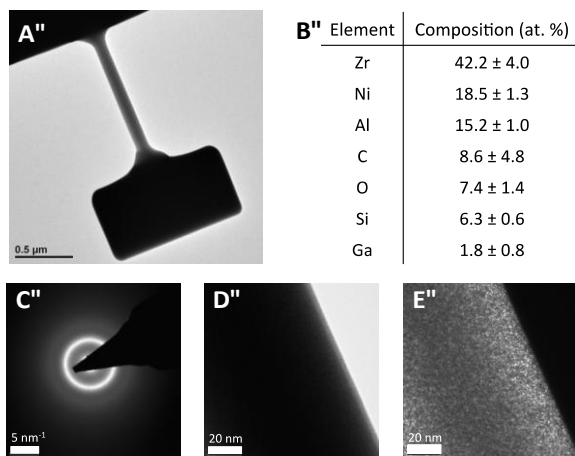


Figure 4: Microstructural analysis of a tensile pillar FIB-milled from a sputtered film of Zr-Ni-Al metallic glass after annealing at 625 K for 24 hours. TEM results include (A) TEM image of the whole pillar (B) chemical composition data obtained from EDX, (C) diffraction pattern, (D) bright-field image, and (E) dark-field image.

The mechanical data for the annealed pillars is shown in Figure 5. The data is grouped by pillar width, with (A-C) sub-100 nm, (D-F)  $\sim 100 \text{ nm}$  pillar widths, (G-I)  $\sim 150 \text{ nm}$ , and (J-L)  $\sim 200 \text{ nm}$  pillar widths. Engineering stress-strain data is shown in (A, D, G, J), true stress-strain data is shown in (B, E, H, K), and SEM images of the pillars around the time of fracture are shown in (C, F, I, L). As with the as-sputtered compressive (Figure 2), and tensile (Figure 3) pillars, these annealed pillars show two distinct regimes of mechanical behavior: “small” pillar widths

$\leq 93$  nm fail by noticeable necking and reach true strains above 100%, while “large” pillar widths  $\geq 105$  nm fail by shear banding with only a small amount of ductility in the stress-strain curves. The main difference between the as-sputtered and annealed pillars is not the presence of these two regimes of mechanical behavior, but the critical pillar width at which the mechanical behavior switch from homogeneous flow with significant necking to shear banding. For the as-sputtered pillars this transition occurred somewhere between 150 and 200 nm, and for the annealed pillars this transition occurs around 100 nm. Therefore, as expected we do see a loss in ductility and thus free volume upon annealing.

Beyond these two regimes of mechanical behavior (necking versus shear banding) there are also observable differences within each regime of mechanical behavior as a function of pillar width. For example, while annealed pillars  $\geq 105$  nm all fail by shear banding there is a loss of ductility as the pillar width gets even larger: the  $\sim 100$  nm annealed pillars (Figure 5D-F) exhibit more plasticity than the  $\sim 150$  nm annealed pillars (Figure 5G-I), which exhibit more plasticity than the  $\sim 200$  nm annealed pillars (Figure J-L). The shear-banding mechanism is not suppressed in pillar widths above the critical dimension ( $\sim 100$  nm for annealed pillars) but it may require higher forces to initiate at pillar widths closer to the critical dimension. A similar trend is observed in the necking regime for as-sputtered pillars: all as-sputtered pillars  $\leq 153$  nm failed by necking (Figure 3A-I), however smaller pillars exhibit more plasticity, for example compare  $\sim 150$  nm pillars (Figure 3G) with  $\sim 100$  nm pillars (Figure 3D).

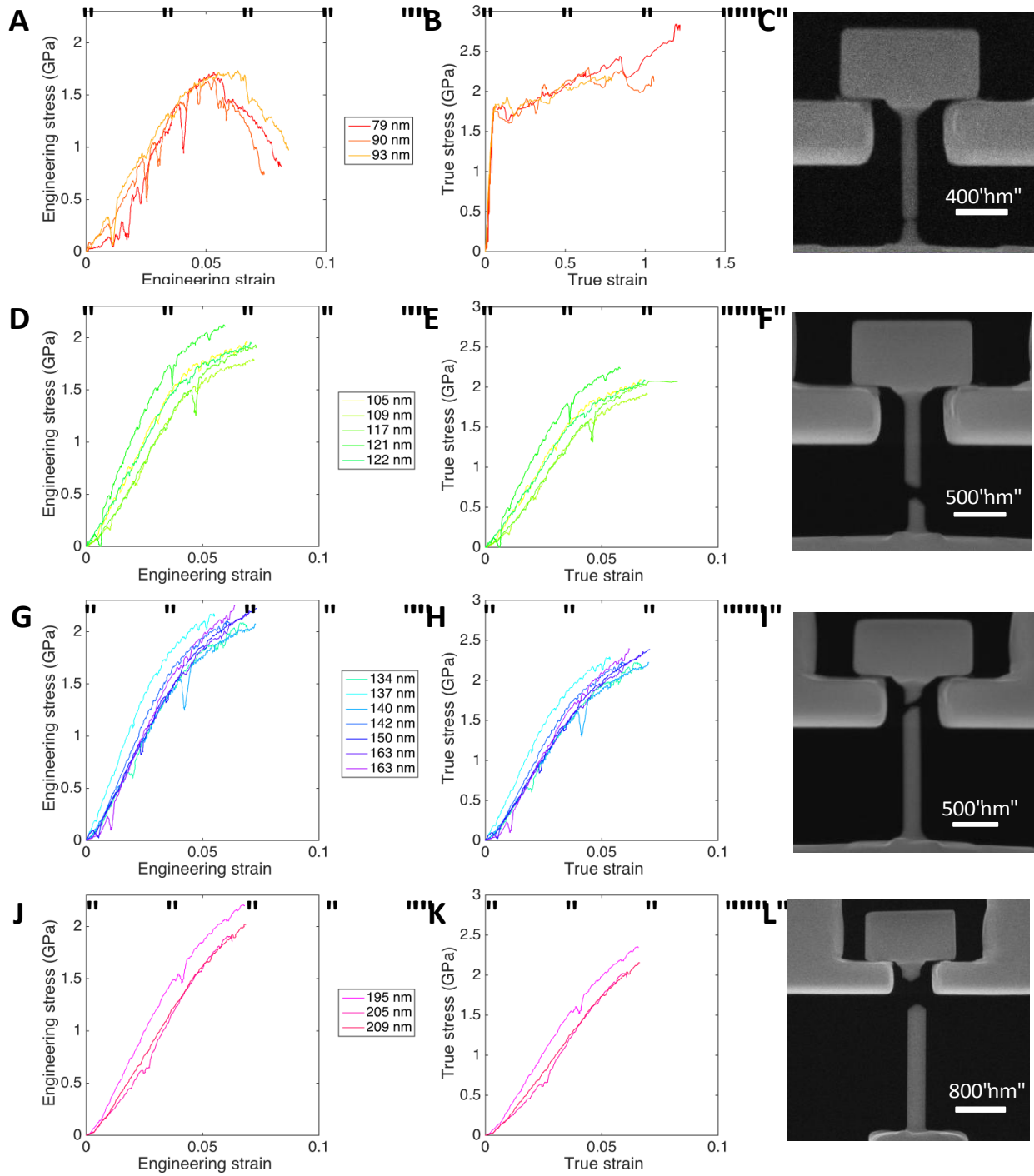


Figure 5: Uniaxial tensile tests on pillars FIB-milled from a sputter Zr-Ni-Al film after annealing at 625 K. (A-C) sub-100 nm pillar widths, (D-F) ~100 nm pillar widths, (G-I) ~150 nm pillar widths, and (J-L) ~200 nm pillar widths. Engineering stress-strain data is shown in (A, D, G, J), true stress-strain data is shown in (B, E, H, K), and SEM images of the pillars around the time of fracture are shown for pillar widths of (C) 93 nm, (F) 105 nm, (I) 137 nm, (L) 195 nm.

The mechanical properties from the data shown in Figures 3 and 5 can be extracted to provide a more quantitative comparison of mechanical response between pillars of different dimensions and state of relaxation. A summary of these mechanical properties is shown in Figure 6. The mechanical property that changes most significantly as a function of pillar dimension and relaxations state is plastic strain, defined as the total strain at fracture less the strain at the yield point. Figure 6 includes both the true plastic strain (Figure 6A) and the engineering plastic strain (Figure 6B). The true strain is calculated by utilizing the cross-sectional area of the pillar as it is tested, thus it accounts for the significant reduction in cross-sectional area upon necking, while the engineering strain is calculated by utilizing the initial cross-sectional area of the pillar. If there is no necking then the engineering strain is nearly identical to the true strain. For this reason, we see that large differences in the true plastic strain is a good metric for whether the mechanical behavior is in the necking (as opposed to shear banding) regime. As can be observed in Figure 6A, annealed pillars with sub-100 nm dimension and as-sputtered pillars with dimension of sub-100 nm, ~100 nm, and ~150 nm all exhibit true plastic strains in excess of ~100% and these large true strain values come about from the necking behavior. In contrast, as-sputtered pillars with ~200 nm dimension and annealed pillars with dimensions of ~100 nm, ~150 nm, and ~200 nm all exhibit true plastic strain < 10% due to the lack of substantial necking behavior. The engineering plastic strain is normalized to the initial cross-sectional area and is thus not as sensitive to strains resulting from necking phenomena. As Figure 6B shows, both the as-sputtered and annealed pillars exhibit an increase in engineering plastic strain as the pillar width is reduced. The annealed pillars also exhibit less engineering plastic strain than the as-sputtered pillars due to the loss in free volume upon annealing. For comparison, the engineering plastic strain from other studies on similarly sized metallic glass in various relaxation states are also plotted in Figure 6B. Particularly noteworthy is the huge difference in the plastic engineering strain from these previously studies [Chen 2013], [Liontas 2014] on other metallic glasses and the metallic glass in the current work: these previous studies show engineering plastic strains  $\leq$  ~2%, while in the current study similarly sized annealed pillars show engineering plastic strains ~5% and similarly sized as-sputtered pillars show engineering plastic strain ~8% (over a factor of 4 increase from previously reported “ductile” metallic glass!).

The large difference in plasticity between the current study and previous studies may be due to the sputtering process used to deposit the Zr-Ni-Al metallic glass of the current study. The reference studies of Figure 6B were conducted on an electrodeposited metallic glass and other studies reporting ductility in nano-sized metallic glass have utilized FIB-milling of a bulk metallic glass formed by quenching<sup>1</sup>. The only other report of a sputtered metallic glass made into nano-pillars was conducted on a Pd<sub>77</sub>Si<sub>23</sub> metallic glass, which due to the presence of Si does not have true metallic bonding, and this study only focused on compression, not tension<sup>2</sup>. Nonetheless, ductility was observed in this compressive study for pillar diameters up to 400 nm, which is quite large and comparable to the compressive ductility observed in the current work for pillar diameters up to 555 nm. Therefore, sputtering may be a method of metallic glass



fabrication to create ductile metallic glass of a variety of chemical compositions. Further study of other sputtered metallic glass systems is necessary to verify this hypothesis.

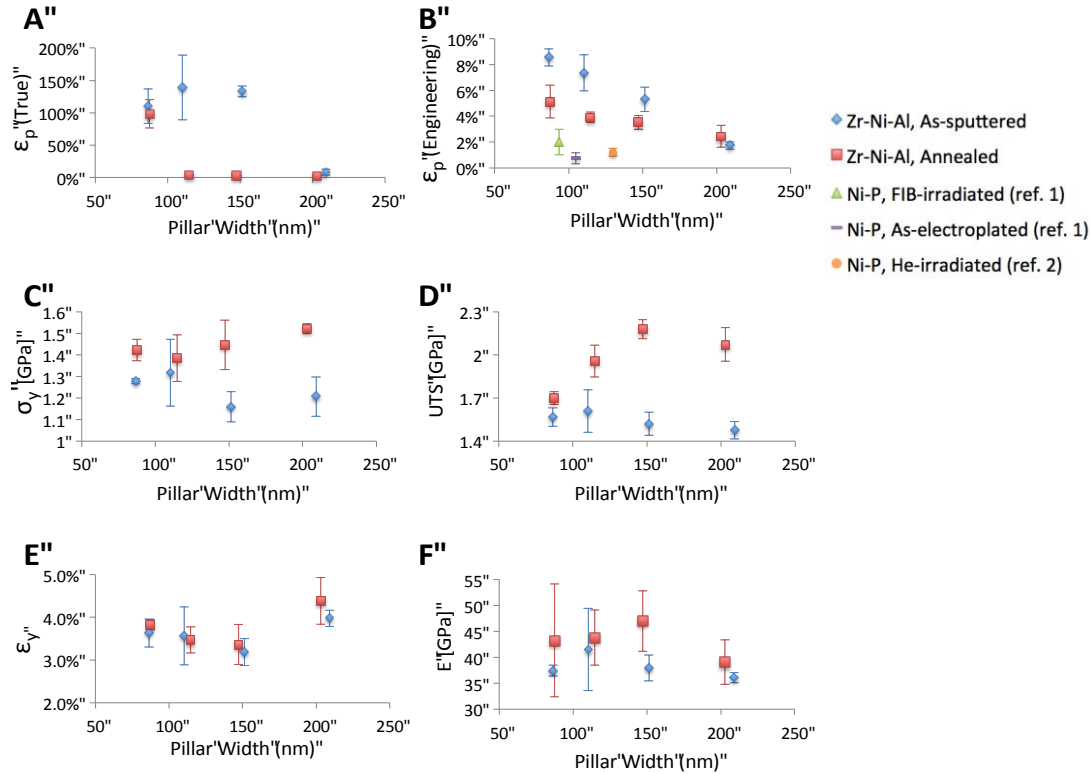


Figure 6: Mechanical properties obtained from the tensile data of as-sputtered Zr-Ni-Al shown in Figures 3 and annealed Zr-Ni-Al shown in Figure 5. Properties include: (A) true plastic strain, (B) engineering plastic strain, (C) yield strength, (D) ultimate tensile strength, (E) yield strain, and (F) elastic modulus. All properties are obtained from the engineering stress-strain data except for the true plastic strain shown in (A), which is obtained from the true stress-strain data. In (B), the engineering plastic strain is compared with reports of other plastic strain values from literature<sup>3, 4</sup>

Other mechanical properties of interest in Figure 6 are the strength, yield strain, and elastic modulus. Both the yield strength (Figure 6C) and ultimate tensile strength (Figure 6D) were higher for the annealed sample than the as-fabricated sample. This is expected as annealing is a structural relaxation process, which reduces free volume and hence increases density. Upon annealing, there appears to be a larger increase in the ultimate tensile strength than the yield strength. However, this apparent discrepancy arises because both these strength values are from engineering stress, which is normalized by the initial cross-sectional area of the pillar and thus underestimates the stress if necking occurs. Necking occurs after yielding so only the ultimate tensile strength (not yield strength) of pillars that undergo necking is reduced. Furthermore, both samples yield at approximately the same yield strain (Figure 6E) defined as the strain at yielding, when the data first deviates from linear elastic loading. Both sputter and as-annealed samples

also have similar values of elastic modulus (Figure 6F) with the annealed samples having a slightly larger elastic modulus. However, uniaxial tension experiments at the nanoscale often have significant variability in measured moduli data especially when the moduli are measured from the loading portions of the nanomechanical data as has been done here.

With this fundamental understanding of the microstructure and mechanical properties of this sputtered Zr-Ni-Al metallic glass, we then began applying this material to nanolattices. The fabrication process for the nanolattices involved using two-photon direct laser writing lithography to create a 3-dimensional polymer skeleton, which we could then sputter the metallic glass onto. The nanolattices were composed of a 15- $\mu\text{m}$  octahedron unit cell and each nanolattice was 5 cells wide x 5 cells long x 5 cells tall. Thus each nanolattice was a cube with side dimension  $\sim 75 \mu\text{m}$ . The metallic glass was sputtered using the same conditions described previously for the pillars (100 W, in 3 mTorr Ar environment) and the sputtering time was varied to result in different thicknesses of metallic glass coatings. With a measured deposition rate of  $4 \text{ nm min}^{-1}$ , the sputtering times used of 30 minutes, 60 minutes, 120 minutes, and 240 minutes correspond to metallic glass coatings of  $\sim 60 \text{ nm}$ ,  $\sim 120 \text{ nm}$ ,  $\sim 240 \text{ nm}$ , and  $\sim 480 \text{ nm}$ . Compression tests were conducted on and these nanolattices containing a polymer core with various wall thicknesses of Zr-Ni-Al metallic glass, and also on nanolattices made of polymer-only with no metallic glass. The compression tests were conducted in-situ in the SEMentor, which is a nanoindenter arm inside of an SEM to allow visualization of the test. The strain rate was  $1 \times 10^{-3} \text{ s}^{-1}$ .

In summary, we have found that for this sputtered Zr-Ni-Al metallic glass, smaller is more ductile. The amount of ductility observed is unprecedented with true strains exceed 150% in some cases and the critical dimension for ductility being much larger than reported previously for other metallic glasses. These large critical dimensions are stated in Table 1 for all the mechanical tests on the Zr-Ni-Al metallic glass pillars of the current work.

Table 1: Summary of Pillar Mechanical Tests

State	Deformation	Pillar dimension for homogeneous flow	Pillar dimension for shear banding
As-sputtered	Uniaxial compression	$\leq 550 \text{ nm}$	$\geq 890 \text{ nm}$
As-sputtered	Uniaxial tension	$\leq 153 \text{ nm}$	$\geq 199 \text{ nm}$
Annealed	Uniaxial tension	$\leq 93 \text{ nm}$	$\geq 105 \text{ nm}$

The reason for this extreme ductility is likely due to the sputtering method of depositing the metallic glass, which leave the metallic glass with lots of excess free volume. Annealing the Zr-Ni-Al metallic glass at 625 K, which is below its glass transition temperature, allowed us to

annihilate excess free volume and thus tune the mechanical properties to be stronger but less ductile, while still maintaining the material's amorphous microstructure. Exhibiting a similar trend to the smaller is more ductile size effect in this metallic glass, polymer nanolattices coated with a thin ~60 nm layer of this metallic glass exhibited polymer-like ductility with enhanced strength from the metallic glass. However when the metallic glass coating thickness was increased too much  $\geq \sim 120$  nm, the nanolattices reached higher strengths but failed catastrophically.

## Future Plans

The next steps in this study are to investigate the effects of irradiation on the Zr-Ni-Al metallic glass nanolattices. As we have observed, Zr-Ni-Al metallic glass is sputtered in a form that already contains a large excess of free volume as evidenced by the large amount of observed ductility. Thus, it would be interesting to observe whether irradiation increases the free volume further or if there is some limit to how much free volume can be present. We plan to quantify the amount of free volume through differential scanning calorimetry (DSC) by monitoring the enthalpy change, which has been shown to correlate with the change in free volume<sup>5</sup>. The irradiation of the nanotrusses will be performed at Ion Beam Materials Laboratory of Los Alamos National Laboratory. We will be irradiating with Ni ions (self-ions for Zr-Ni-Al metallic glass) using the Tandem accelerator, which can irradiate with Ni ions at energies up to 12 MeV, which will be more than adequate to allow complete penetration of the nanolattices by the irradiating ions. We are excited to observe how this inherently ductile metallic glass will respond to large level of irradiation.

We also started collaborating with Wendy Mao's group at Stanford University to conduct in-situ X-ray Tomography and Diffraction experiments (at APS) to reveal the radial distribution functions in metallic glasses as a function of fabrication method – sputtered vs. annealed vs. electroplated, etc. These results will help gain insight into the free volume content and distribution in metallic glasses and their susceptibility to radiation damage.

## References

- (1) Jang, D. and Greer, J. R. *Nature materials*. **2010**, *9*, 215-219.
- (2) Volkert, C. A.; Donohue, A.; and Spaepen, F. *Journal of Applied Physics*. **2008**, *103*, 083539-083539.
- (3) Chen, D. Z.; Jang, D.; Guan, K. M.; An, Q.; Goddard, W. A.; and Greer, J. R. *Nano Lett.* **2013**, *13*, 4462-8.
- (4) Lontas, R.; Gu, X. W.; Fu, E.; Wang, Y.; Li, N.; Mara, N.; and Greer, J. R. *Nano Lett.* **2014**, *14*, 5176-83.
- (5) Slipenyuk, A. and Eckert, J. *Scripta materialia*. **2004**, *50*, 39-44.

## Publications

- ⇒ R. Lontas, X.W. Gu, E. Fu, Y. Wang, N. Li, N.A. Mara, and J.R. Greer “Effects of helium implantation on the tensile properties and microstructure of Ni<sub>73</sub>P<sub>27</sub> metallic glass nanostructures” *Nano Letters* **14**(9) 5176–5183 (2014)
- ⇒ D.Z. Chen, X.W. Gu, Q.An, W.A. Goddard III, and J.R. Greer “Ductility and work hardening in nano-sized metallic glasses” *Appl Phys Lett* **106**, 061903 (2015)
- ⇒ S.-W. Lee, M. J. Zadeh, D. Z. Chen, Y.-W. Zhang, J. R. Greer “Transitions of Deformation Mode in Hollow Cu<sub>60</sub>Zr<sub>40</sub> Metallic Glass Nanolattices” *Nano Letters* DOI: 10.1021/acs.nanolett.5b01034 (2015)
- ⇒ R. Lontas, et al “Free Volume Drives >100% Tensile Deformability in Nano-Metallic Glasses” (in preparation, 2015).

# Nanoscale characterization of intragranular and intergranular deformation mechanisms

**Kevin Hemker**

[hemker@jhu.edu](mailto:hemker@jhu.edu)

223 Latrobe Hall, Johns Hopkins University, 3400 N Charles St., Baltimore MD 21218

## PROGRAM SCOPE

Nanocrystalline (nc) metals have unique mechanical properties, resulting from the deformation mechanisms that govern their behavior. The mechanical behavior of conventional materials is governed largely by dislocation motion, but for nanocrystalline metals other mechanisms can be active that will also affect the constitutive behavior of the material. We have employed *in situ* straining combined with TEM-based automated crystal orientation mapping to characterize the microstructure of nanocrystalline metals as they deform. This allows us to observe which deformation mechanisms are active as well as understanding how these mechanisms operate. Having developed the tools necessary to characterize stress-assisted grain growth in nanocrystalline metals, we are using those tools to quantify, locally and at the nanoscale, the influence that stress concentrations and microstructural details have on the deformation behavior of polycrystalline metals and alloys. This work uses the TEM-based elastic strain measurement capabilities of the Topspin system recently developed by NanoMEGAS/Appfive together with the orientation mapping from ASTAR. This analysis system offers a minimum detectable strain of  $2 \times 10^{-4}$  with a spatial resolution of 2.5 nm and can be employed to perform *in situ* and post mortem characterization of coarse-grained polycrystalline metals at various levels of plastic deformation. Active deformation mechanisms have been identified and local measures of structure, orientation, and stress are being collected and used to elucidate nanoscale details such as: the role of local stress concentrations in nascent twin formation in polycrystalline Mg and Zr; the redistribution of local stress during grain boundary migration, twinning, and dislocation pileups; and the storage of geometrically necessary dislocations during plasticity.

## RECENT PROGRESS

Recent efforts have focused on performing *in situ* straining experiments to observe the deformation mechanisms operative in nanocrystalline films. These experiments utilize the fabrication procedure developed at JHU that allows for films to be deposited and easily made freestanding, a Gatan single-tilt straining holder provided by Marc Legros (CEMES-CNRS), and the ASTAR system developed by NanoMEGAS. These experiments allow for a large area to be characterized throughout deformation; any change in the grain size, grain boundary character, or migration of boundaries can be observed and analyzed. Figure 1 shows a series of orientation maps taken of a Cu sample as it was progressively strained. The figure shows a  $0.8 \times 1.2 \mu\text{m}$  area (step size: 1.5 nm). These scans contain many grains that can be observed and tracked throughout the scans to observe and analyze any changes resulting from the imposed strain.

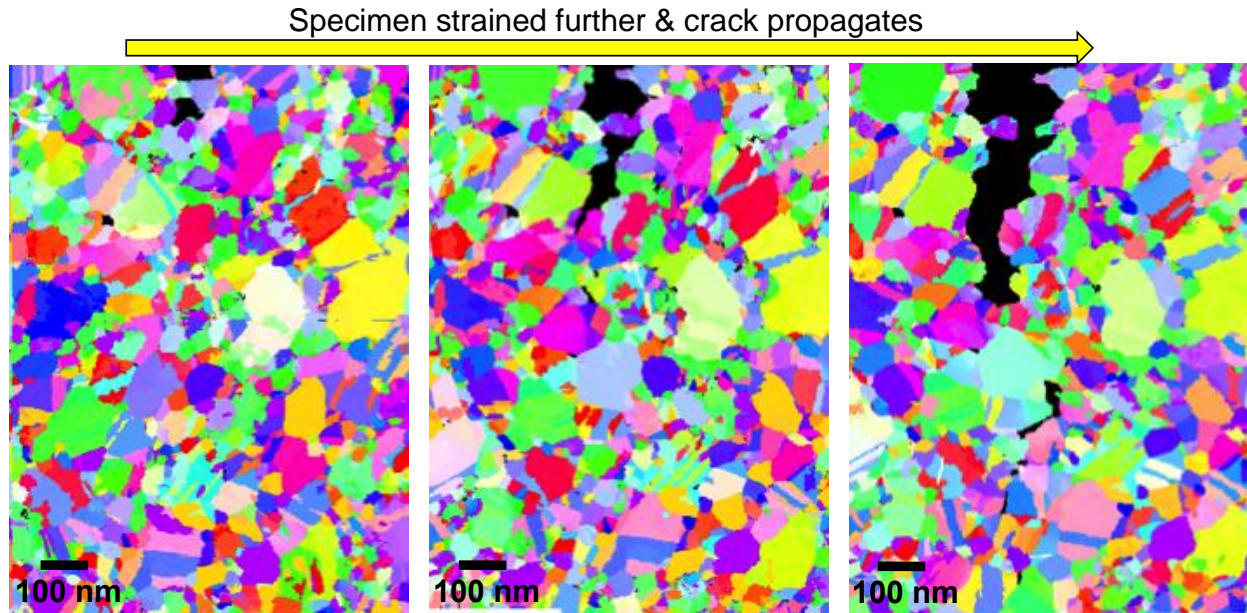


**Figure 1:** Consecutive orientation maps taken from an area in a Cu film as a crack propagates through it; specimen is strained further from left to right. Each pixel is colored according to orientation. Individual grains can be observed and characterized across scans to determine active deformation mechanisms.

Our studies focused primarily on stress-driven grain boundary migration and twin nucleation and growth. We also studied the fracture behavior of these films by analyzing the grain boundary character of the crack path. Through collaboration with the Taheri research group (Drexel), we also used the orientation maps to quantify dislocation density in grains over the course of deformation.

Figure 2 shows an example of stress-driven grain boundary migration in the Cu films. In the figure each point is colored according to its orientation and the boundaries are colored according to the misorientation between two grains with  $\Sigma 3$  boundaries in red. The top and bottom maps were taken before and after straining, respectively. Boundaries that migrated substantially are marked in the top scan with black arrows. This specific grain grew in all directions, but the growth is most pronounced from left to right. The boundaries that were mobile were of varying character. Low-angle ( $24^\circ$ ), high-angle ( $54^\circ$ ), and incoherent  $\Sigma 3$  boundaries all migrated in response to the applied strain. Furthermore, the misorientation between the grain that grew and those surrounding it remained constant within the error of the measurements, indicating that the grain boundary migration was not accompanied by a corresponding grain rotation.

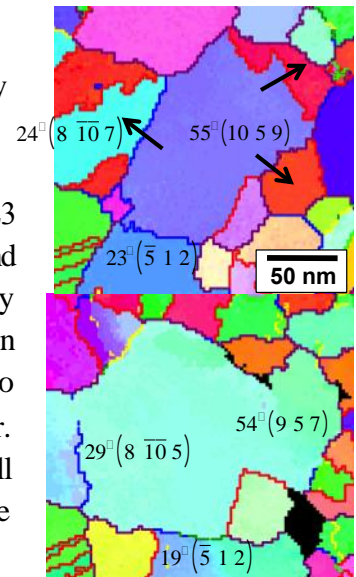


**Figure 2.** Example of stress-driven GB migration from an *in situ* experiment



20 nm



In addition to grain boundary migration, substantial twin nucleation and twin boundary migration was also observed in the Cu films. Figure 3 shows an example of twin nucleation. The scans were taken as the specimen was strained further going from the top to bottom scan. Initially, only one twin boundary was present—separating the pink from the blue twin variant in the grain. Upon further straining, an 8 nm thick twin nucleated on the left side of the grain. With an additional strain increment the twin propagated fully across the grain. Twin nucleation, propagation, and growth were prevalent in all Cu samples tested. In fact, twinning was much more prevalent than stress-driven migration of grain boundaries.

The *in situ* straining experiments on nanocrystalline copper show that both grain boundary migration and twinning are active deformation mechanisms that work in concert. Through collaboration with Asher Leff in the Taheri research group (Drexel) we have estimated geometrically necessary dislocation (GND) density from the orientation maps and have found that there are changes in the amounts of dislocation in grains during straining. This suggests that dislocation glide is also active in these films. Moreover, through analysis of the crack path, it was determined that cracks progress along grain boundaries the majority of the time and always avoids twin boundaries. Taken in whole, the results of the *in situ* experiments show that twin boundaries are very important to the

**Figure 3.** Example of twin nucleation in an *in situ* experiment.

Moving forward the focus of our research will be on using TEM-based local strain mapping to study deformation mechanisms within individual grains. To begin with, we have used commercially produced hot-pressed boron carbide to test the capabilities of the Topspin system. This boron carbide sample was selected, because it contains a number of defects of interest: grain boundaries, twin boundaries, coherent and incoherent precipitates, and dislocations. Figure 4 shows strain scans taken at a boron carbide grain boundary. There are three facets to this grain boundary, and the two upper facets have very little strain near the boundary. By contrast, the lower facet

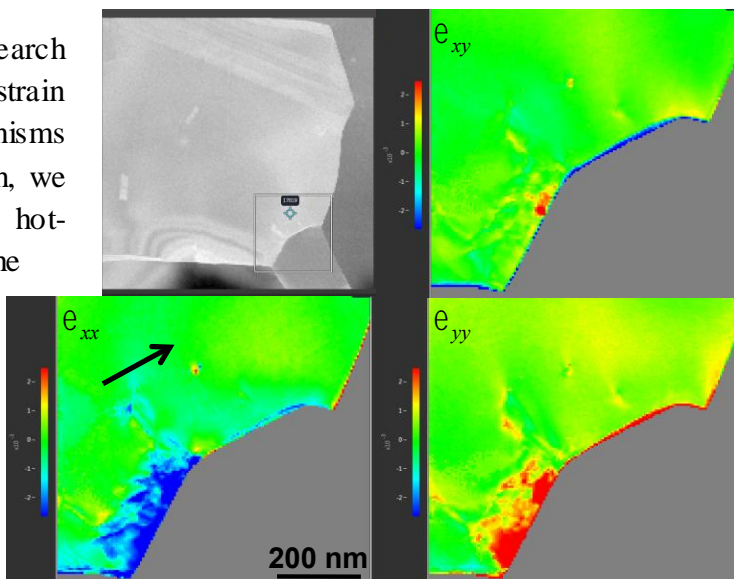


**Figure 4.** Strain maps taken at a grain boundary in boron carbide. Virtual STEM image in top left shows location of scan within the grain. In other images, strain maps correspond to the [100] direction in grain (black arrow, x direction).

has substantial elastic strain. In the x-direction, which is the [100] direction in the grain, there is compressive strain up to  $3 \times 10^{-3}$  with a tensile strain of the same magnitude perpendicular to it. There is very little shear strain in the region. The analysis done on boron carbide highlights the spatial resolution and overall capabilities of the Topspin system, and we will employ this technique to study other materials as well as study GND populations within grains.

## **FUTURE PLANS**

We plan to continue to use the Topspin strain analysis system to study deformation mechanisms such as twinning and dislocation mobility and storage. We will perform these experiments on coarse-grained Mg and Zr and two-phase composites. We plan to characterize these materials at varying levels of deformation and to utilize Topspin to measure elastic strains resulting from dislocation structures formed during deformation.

## **LIST OF PAPERS SUPPORTED BY THIS WORK**

- JA Sharon, P-C Su, FB Prinz, KJ Hemker, Stress Driven Grain Growth in Nanocrystalline Pt Thin Films, *Scripta Materialia*, **64** (2011) 25–28.
- HH Liu, S Schmidt, HF Poulsen, A Godfrey, ZQ Liu, JA Sharon, X Huang, Three dimensional orientation mapping in the transmission electron microscope, *Science*, **332** (2011) 833-834.
- F Momprou, M Legros, T Radetic, U Dahmen, DS Gianola, KJ Hemker, “In situ TEM observation of grain annihilation in tri-crystalline aluminum films, *Acta Materialia*, **60** (2012) 2209–2218.
- Y Zhang, JA Sharon, GL Hu, KT Ramesh, and KJ Hemker, Stress-driven grain growth in ultrafine-grained Mg thin film, *Scripta Materialia*, **68** (2013) 424-427.

## **PERSONNEL SUPPORTED BY THIS PROJECT**

Professor Kevin Hemker (PI), Mr. Paul Rottmann (PhD student stipend), Dr. Marc Legros (visiting scientist support).



# Nanotwinned Materials for Energy Technologies

Peter Collins, Alex King, Richard LeSar (Lead), Mikhail Mendeleev and Ryan Ott  
Ames Laboratory

## Program Scope

Nanotwinned metals and alloys are emerging as a particular form of nanoscaled material that can exhibit high strength coupled with improved thermal stability, both of which are yet completely understood. We have developed an integrated experimental, modeling and simulation program to examine the underlying mechanisms of plasticity in nanotwinned samples. We employ a range of methods to create systems with differing twin morphologies and microstructures and characterize their structures using a range of techniques, from electron microscopy to synchrotron scattering to the use of an atom probe. Mechanical testing of these samples is carried out in a novel tensile strain stage that enables accurate measurements of stress-strain behavior with concurrent *in situ* transmission electron microscopy (TEM) observations of evolving microstructures. We use a temperature-controlled nanoindenter to characterize the thermal dependence of the mechanical properties. The experiments are coupled with a modeling and simulation program that includes atomistics and discrete dislocation simulations. The experiments provide both realistic validation of models and a deeper understanding of fundamental mechanisms, enhancing the development of new understandings of deformation in nanotwinned materials. This program will not only shed new light on plasticity in nanotwinned materials by bridging the current gap between the experiments and modeling, but it will also greatly enhance our overall understanding of many collective and cooperative mechanisms of plasticity in these materials.

## Recent Progress

In our studies of nt-Ag, the TB spacing is essentially independent of the processing conditions, but the twin density, grain size and grain orientations can be readily controlled [1]. The texture, and thus the TB orientations relative to the tensile axis, is strongly dependent on the deposition rate as are the yield strength and tensile ductility. Fig. 1 shows the tensile yield stress as a function of the texture parameter,  $\Gamma$ , which is a measurement of the in-plane  $\{110\}$  and out-of-plane  $\{111\}$  texturing. TEM results have shown that the more randomly oriented films have lower

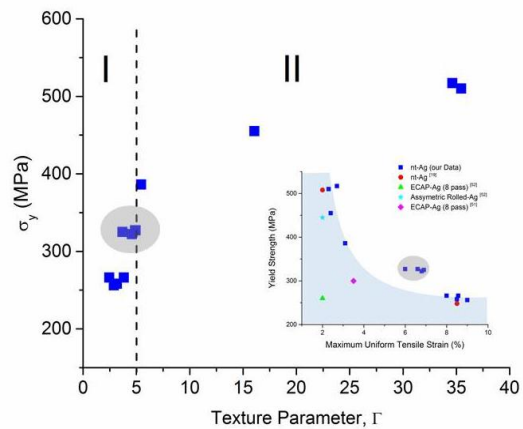


Figure 1. Measured yield stress as a function of texture parameter (defined in text) for nanotwinned Ag. Yield behavior falls into two types, as discussed in text.

twin densities than columnar-grained films that are strongly  $\{111\}$  textured (high  $\Gamma$  value). The mechanical behavior of the softer films can be associated with two different types of microstructure: (1) untwinned randomly oriented grains and (2) nanotwinned grains that are poorly oriented along the  $\langle 111 \rangle$  film normal. The former allows for easy slip compared to twinned grains, and thus decreased strength, while the latter is softer than nanotwinned grains that are strongly oriented along the film normal. Structures consisting of ultrafine-grains containing nanotwins with average twin boundary spacings of 8-12 nm dispersed in untwinned grains provide for the best combination of strength and tensile ductility (see inset in Fig. 1).

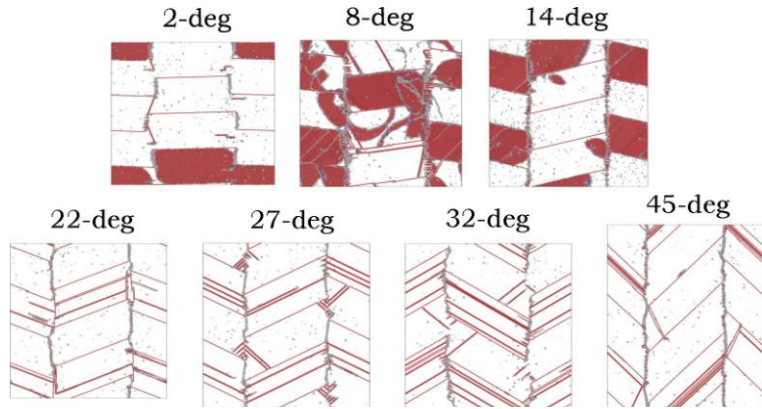


Figure 2. The MD snapshots corresponding to the beginning of the plastic deformations in pure Ag. Perfect bulk atoms (fcc) are not shown. Different dislocation types provides plasticity in low angle and high angle cases.

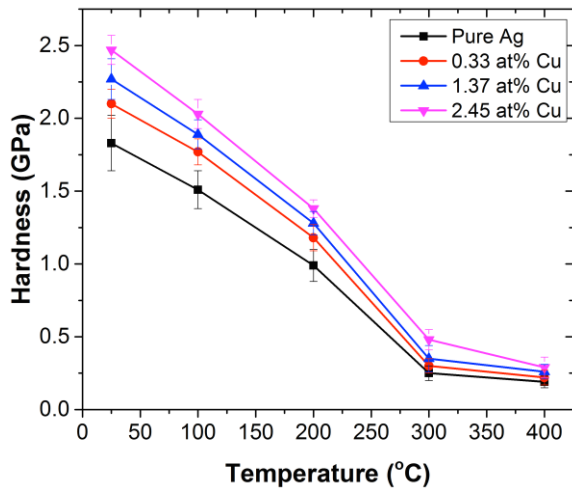


Figure 3. Effects of copper additions and temperature on the hardness of nanotwinned sliver for samples with low texture as determined with nanoindentation.

applied stress (see Fig. 2). The MD results suggest that in highly textured materials (small angle), the deformation is dominated by partial dislocation nucleation at the boundaries.

Nanoindentation experiments at temperatures up to 400 °C reveal two distinct thermal regimes of the mechanical behavior in pure silver nanotwinned materials, from which we can determine the activation energies of the deformation processes. At low temperatures (ambient to about 200 °C) the activation energy is consistent with dislocation nucleation being the rate-determining step of deformation while at higher temperatures (300-400 °C) it is more consistent with diffusion-based

mechanisms. The mechanisms identified by these experiments are consistent with the molecular dynamics simulations described above.

Stacking fault energy links mechanical properties to length scales through the stacking fault width, but often in obscure ways. To clarify these issues, we systematically investigated the role of the stacking fault energy (SFE) in the deformation properties of fcc metals using MD simulations based on embedded-atom model potentials in which the SFE was varied while other calculated properties were effectively constant [3]. The results indicate that properties such as yield strength and microstructural stability do not vary systematically with SFE, but rather fall into two distinct cases corresponding to “low” and “high” stacking fault energies. The first case is characterized by slip propagation by partial dislocations and lack of CTB migration while the second case is characterized by with effective slip propagation by complete dislocations and active CTB migration. However, the definition of “low” and “high” SFE appears to depend on the relative sizes of the stacking fault width and the nanotwin width, so the effect is determined by interplay between length scales.

#### *Effects of solutes on properties of nanotwinned systems*

Increasing concentration of Cu additions from 0 to 2.45 at.% in nt-Ag films continuously increases the hardness at room temperature (Fig. 3). The activation energies for deformation in the alloyed films show the same distinct temperature regimes as for pure nanotwinned silver.

Twin boundary migration behavior is well-matched between experiments and MD simulations,

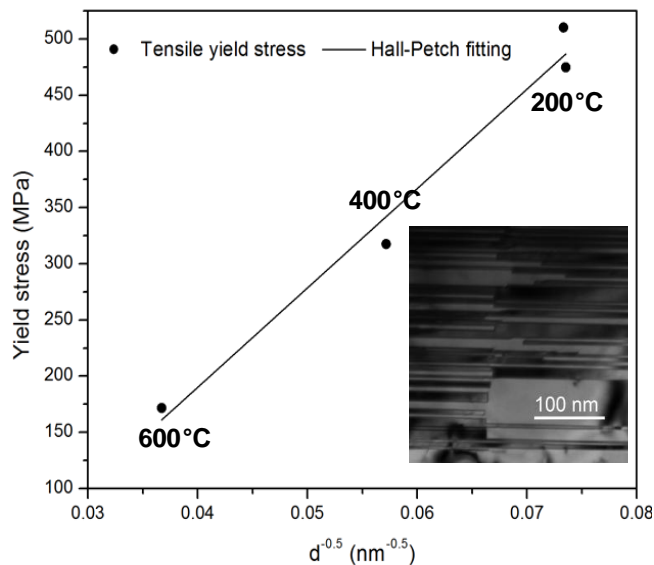


Figure 4. Hall Petch relationship for the thermally annealed nanotwinned Ag. Inset is from the *in-situ*TEM after 80 min of annealing ~200 °C. The dashed line is the approximate position of the prior grain boundary.

which have been conducted at the same length-scales. Twin shrinkage occurs via the motion of incoherent twin boundaries (ITBs) while the coherent twin boundaries (CTBs) are immobile. MD results show that even a small addition of Ag atoms stabilizes nanotwinned microstructures in Cu very significantly. The mechanism of the solute drag effect on the TB migration is associated with changing of the ITB shape or position to accommodate as many solutes as possible rather than solute segregation at the location of the ITB. The solutes do not migrate with ITB. Since we have no quantitative theory describing the drag from immobile solutes on the TB migration at this point, it is not

straightforward to predict what kind of solutes will act as the best stabilizer of the nanotwinned structure. In the simplest model proposed in [4], solute drag is proportional to the value of the

heat of segregation. Therefore, a solute that is most strongly attracted to the ITB will be the best dopant to stabilize the TB structure. Further work is necessary to clarify this question.

### *Thermal stability of nanotwinned silver*

Between 200 °C and 600 °C, the primary mechanism of grain growth for strongly {111} textured Ag, is found to be grain rotation.[5] Through this mechanism, slightly misoriented twin variants of the same sense were observed to merge across a grain boundary at ~180 °C while twins with opposing senses were locked, forming ITBs (Fig. 4). A small change in yield stress (475 MPa) was observed after annealing at 200 °C, consistent with an observed decrease in dislocation density. The yield stress then decreased by 38% and 66% at 400 and 600 °C, respectively. The effect on the tensile yield stress of annealing at these temperatures matches the effect on the nanoindentation hardness and correlates with the grain size [6].

### **Future Plans**

In an integrated, systematic program of experiments and modeling, we will control mesostructures and their associated length scales to isolate differing deformation mechanisms. Our immediate plans are to continue our work studying the effects of solutes on deformation mechanisms in NT-Ag materials. Preliminary work has shown that while the addition of small amounts of copper have a large effect on twin-boundary spacing and grain size, other, as yet unidentified, solute effects have an even larger effect on the strengthening of these materials.

We will employ a combination of experimental characterization tools (including ChemiSTEM and atom probe tomography) to determine the distribution of solute atoms between the twins, the grain boundaries and the regions between the twins and will compare those results to Monte Carlo simulations. Mechanical property tests at room and high temperatures will be used to map out the mechanical behavior. Precession electron diffraction (PED) will be employed to determine local misorientations and dislocation densities, which will be compared to discrete dislocation simulations. Our goal is to identify the roles that solute additions have on the physical mechanisms that control deformation in these materials.

### **References**

1. R.T. Ott, J. Geng, M.F. Besser, M. J. Kramer, Y. M. Wang, E. S. Park, R. LeSar and A. H. King, *Acta Mater.* 96, 378-389 (2015).
2. V. Borovikov, M. I. Mendeleev, A. H. King and R. LeSar, *J. Appl. Phys.* 117, 085302 (2015).
3. V. Borovikov, M. I. Mendeleev, A. H. King and R. LeSar, *Model. Simul. Mater. Sci. Engin.* 23, 055003 (2015).
4. M. I. Mendeleev and D .J. Srolovitz, *Phil. Mag. A* 81, 2243 (2001).
5. H. Zhang, J. Geng, R. T. Ott, M. F. Besser, and M. J. Kramer, *Metal. Mater. Trans. A* 46, 4078 (2015).
6. D. Bufford, H. Wang, and X. Zhang, *J. Mater. Res.* 28, 1729 (2013).

## Publications

- A. Bryden, S. Broderick, S. K. Suram, K. Kaluskar, R. LeSar, and K. Rajan, "Interactive Visualization of Apt Data at Full Fidelity," *Ultramicroscopy*, **132**, 129-135 (2013).
- Y. M. Wang, F. Sansoz, T. LaGrange, R. T. Ott, J. Marian, T. W. Barbee, and A. V. Hamza, "Defective Twin Boundaries in Nanotwinned Metals," *Nature Materials*, **12**, 697-702 (2013).
- T. M. Pollock and R. LeSar, "The Feedback Loop between Theory, Simulation and Experiment for Plasticity and Property Modeling," *Current Opinion in Solid State and Material Sciences*, **17**, 10-18 (2013). 10.1016/j.cossms.2013.03.003
- M. I. Mendeleev, C. Deng, C. A. Schuh, and D. J. Srolovitz, "Comparison of Molecular Dynamics Simulation Methods for the Study of Grain Boundary Migration," *Modelling and Simulation in Materials Science and Engineering*, **21**, 045017 (2013).
- M. I. Mendeleev and A. H. King, "The Interactions of Self-Interstitials with Twin Boundaries," *Philosophical Magazine*, **93**, 1268-1278 (2013). 10.1080/14786435.2012.747012
- Chernatynskiy, S. R. Phillpot, and R. LeSar, "Uncertainty Quantification in Multiscale Simulation of Materials: A Prospective," *Annual Review of Materials Research*, **43**, 157-182 (2013).
- M. H. Lee, B. S. Kim, D. H. Kim, R. T. Ott, F. Sansoz, and J. Eckert, "Effect of Geometrical Constraint Condition on the Formation of Nanoscale Twins in the Ni-based Metallic Glass Composite," *Philosophical Magazine Letters*, **94**, 351 (2014).
- R. LeSar, "Simulations of Dislocation Structure and Response," *Annual Review of Condensed Matter Physics*, **5**, 375-407 (2014).
- V. Borovikov, M. I. Mendeleev, and A. H. King, "Effects of Solutes on the Thermal Stability of Nanotwinned Materials," *Philosophical Magazine*, **94**, 2875-2885 (2014).
- V. Borovikov, M. I. Mendeleev, A. H. King and R. LeSar, "Effects of Schmid Factor and Slip Nucleation on Deformation Mechanisms in Columnar-grained Nanotwinned Ag and Cu," *Journal of Applied Physics*, **117**, 085302 (2015).
- R.T. Ott, J. Geng, M.F. Besser, M. J. Kramer, Y. M. Wang, E. S. Park, R. LeSar and A. H. King, "Optimization of strength and ductility in nanotwinned ultra-fine grained Ag: twin density and grain orientations," *Acta Materialia* **96**, 378-389 (2015).
- V. Borovikov, M. I. Mendeleev, A. H. King and R. LeSar, "Effect of stacking fault energy on mechanisms of plastic deformation in nanotwinned fcc metals," *Modeling and Simulation in Materials Science and Engineering* **23**, 055003 (2015).
- H. Zhang, J. Geng, R. T. Ott, M. F. Besser, and M. J. Kramer, "Effect of Temperature on the Nano/Microstructure and Mechanical Behavior of Nanotwinned Ag Films," *Metallurgical and Materials Transactions A* **46**, 4078 (2015).

## **Formation of Persistent Slip Networks During Low Cycle Fatigue**

**Matthew Miller<sup>1</sup>, Paul Dawson<sup>1</sup>, Ulrich Lienert<sup>2</sup>, Jim Williams<sup>3</sup>, Mark Obstalecki<sup>1</sup> and Robert Carson<sup>1</sup>**

<sup>1</sup>Sibley School of Mechanical and Aerospace Engineering, Cornell University, Ithaca, NY

<sup>2</sup>Deutsches Elektronen-Synchrotron, Hamburg, Germany

<sup>3</sup>Materials Science Department, The Ohio State University, Columbus, OH

### **Program Scope**

This project focuses on understanding crack initiation in ductile polycrystals during low cycle fatigue conditions. We have created a combined experiment/ simulation methodology for tracking heterogeneous cyclic plasticity at the size scale of individual grains. Similar to microcrack initiation that accompanies persistent slip bands (PSBs) within deforming single crystals aligned for single slip [1-3], we hypothesize that fatigue cracks form in polycrystals from regions of heterogeneous cyclic slip. During cyclic loading in ductile metals, plasticity eventually localizes – forming a persistent slip network (PSN) that encompasses groups of grains. We believe that the formation and character of this network during cyclic plasticity leads to the initiation of fatigue cracks in ductile metals like copper; the plastic strain amplitude initially being carried by the entire aggregate is eventually focused into localized regions - probably linking together to form a PSN. The highly concentrated, reversed movement of dislocations within this network could eventually lead to a critically damaged state at one or more locations. Unlike PSBs in single slip specimens, however, the PSNs won't necessarily be easily observable in a polycrystal / polyslip specimen. To characterize the PSNs, it is necessary to “watch” plastic strain heterogeneity on multiple size scales. We propose that understanding where and why a crack initiates involves understanding aspects of the way the entire polycrystalline aggregate evolves during cyclic plasticity. Details of the subgrain response such as the stress, lattice orientation and plastic strain rate distributions must be understood along with the “system” response of the aggregate.

The goal of this project is to investigate the PSN hypothesis by studying the evolving mechanical state of every crystal within a cyclically-deforming aggregate with high energy x-ray diffraction (HEXD) using x-rays produced at a synchrotron source. The evolving single crystal diffraction patterns (spots) reflect the elastic-plastic deformation being experienced by the crystal but inverting those patterns directly for a “picture” of the straining heterogeneity is not possible. Instead, we construct a virtual replica of the test specimen using crystal-based finite elements. The model produces an approximation of the spatial distribution of stress, lattice orientation and inelastic straining at every point during the deformation. We refine the finite element model by comparing the experimental diffraction patterns to results from virtual diffraction experiments on the synthetic specimen. During the first funding cycle, we developed the experimental and modeling tools during the first funding cycle, examining a copper alloy (OMC copper) and oxygen free high conductivity (OFHC) copper [4-6].

## Recent Progress

In our previous work, we examined the evolution of diffracted x-ray intensity during monotonic and cyclic loading of OMC copper. X-ray diffraction spots are sharp and nominally circular in an annealed material. As the deformation proceeds, the spots shift; during plastic deformation, the spots begin to spread. Using a virtual sample generated using finite elements, we correlated spreading in the azimuthal direction (Full Width at Half Maximum, FWHM) of the Debye-Scherrer ring with an increase in the distribution of lattice orientations within a grain subjected to monotonic [4] and cyclic [5,6] loading. During cyclic loading, we saw smaller FWHM in tension compared to compression. We are currently examining the detailed changes in FWHM during the entire hysteresis loop. Figure 1 depicts the macroscopic stress-strain curves for the *in situ* cyclic experiment on an OMC copper specimen. The points where HEXD experiments were conducted are labeled. We show results for one particular crystal as an example. We measured the azimuthal spread for each of the 28 peaks associated with the crystal, then computed a normalized change from point A in the loop, i.e.  $\Delta FWHM_{norm}^i = (FWHM^i - FWHM^i(A)) / FWHM^i(A)$ , where  $FWHM^i$  is the azimuthal full width at half maximum for the  $i^{th}$  peak, and  $FWHM^i(A)$  is the value at point A in the hysteresis loop. Figure 1(b) depicts the average and standard deviation of  $\Delta FWHM_{norm}^i$  for the diffraction experiment points on the 0.5% hysteresis loop. A number of interesting features can be seen. We see that the average  $\Delta FWHM_{norm}^i$  drops to a minimum at position E. However, the standard deviation actually increases slightly. Between position E and position F there is a significant change in the average. Since there were no measurements taken between positions E and F, it is not clear that E represents the minimum nor whether F represents the maximum of the average value. The macroscopic reverse yield point occurs somewhere between points D and E, so it would seem reasonable that all grains would reach a state of fully-developed plasticity between points E and F. The spread in  $\Delta FWHM_{norm}^i$  is also significantly increased at position F. Neither the average nor the standard deviation changes appreciably between positions F and G and both have reduced some by point H. This region is largely macroscopically elastic similar to the transition region between points A and E. If more HEXD experiments were conducted (like they were between A and D) it is likely that the average might evolve slowly here similar to what it did from A to E, all the while maintaining the large standard deviation. Finally, at position I, the average returns to a value very similar to that seen at A, with a slightly larger standard deviation.

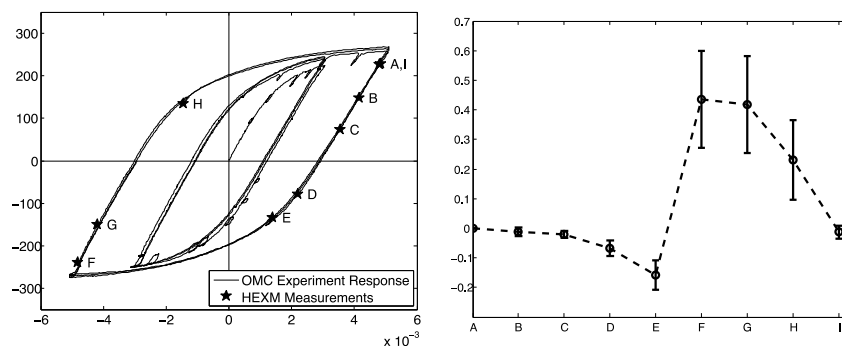


Figure 1. (Left) Experimental stress strain curve with HEXD positions labeled around the first cycle at 0.5% strain amplitude. (Right) Change in the average value of  $\Delta FWHM_{norm}^i$  during the loading cycle. The bars indicate the standard deviation of  $\Delta FWHM_{norm}^i$  for all peaks. The dashed lines are not data. They are presented to help guide the eye.

We built a virtual OMC copper polycrystal and simulated the cyclic experiments on the OMC copper. Figure 2(a) depicts the simulated 0.3% stress-strain curve. As mentioned, the distribution of intragrain misorientations correlates well with  $FWHM_{AZ}$ . Figure 2(b) depicts the evolution of the intragrain misorientation spread for 57 grains within the virtual OMC polycrystal. We use  $\Theta^m$ , the first invariant of the misorientation tensor  $\mathbf{A}$  as defined in [6], as a measure of misorientation spread.

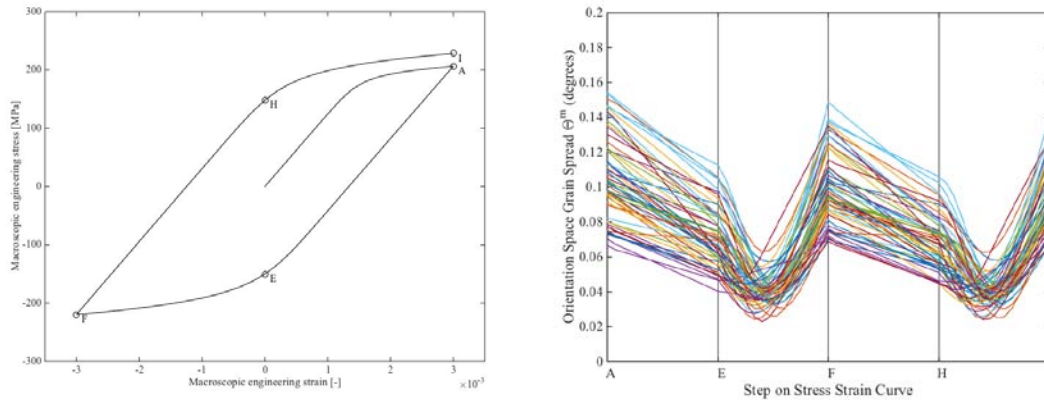


Figure 2. (Left) Simulation OMC copper stress-strain curve with various positions labeled around a 0.3% strain amplitude. (Right). Orientation space grain spread ( $\Theta^m$ ) history for 57 grains within the interior of the virtual OMC polycrystal.

Similarities and differences between Figures 1(b) and 2(b) can be noted. The extreme values of  $\Theta^m$  are seen at the tensile and compressive hysteresis loop tips with the smallest values and spread occurring in the elastic-plastic transition on both the compressive and tensile – going legs of the loop. The transition from smallest to largest  $\Theta^m$  occurs rapidly – as the material enters fully developed plastic straining – similar to the compressive going leg of the experimental data. It should also be noted that this expansion and contraction of the misorientation grain spread occurred in all 57 grains, which helps reinforce the decrease and increase of  $FWHM_{AZ}$  trend observed in Figure 1(b) from the one grain from the experiment. The tension-compression symmetry seen in the simulation data is not seen in the experiment however, the compressive value of the spreading is larger than the tensile value. To address this difference, we replaced the isotropic hardening formulation in the model with a latent hardening model employing a latent hardening ratio of 1.4. These results are shown in Figure 3. The compressive values of  $\Theta^m$  are now larger than the tension values of  $\Theta^m$  for a large subset of internal grains. We are continuing to explore other model changes including different ways of building the virtual polycrystal.

## Future Plans

The next important steps are to connect the diffracted intensity distributions and simulation quantities like intragrain misorientation to the PSN – a spatial distribution of heterogeneous cyclic straining. We need to understand what the PSN looks like in the model and to connect it with a diffraction “signature” in the HEXD data. We are implementing data



reduction schemes to more efficiently reduce the diffraction data for EVERY crystal within the aggregate. We have also transitioned from the OMC material to the OFHC copper; we already see large differences in the FWHM data.

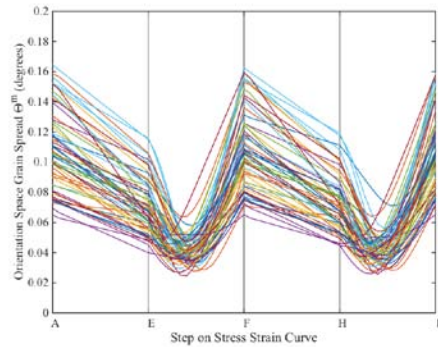


Figure 3. Orientation space grain spread,  $\Theta^m$ , history for 57 grains interior of the virtual OMC polycrystal employing latent hardening with a latent hardening ratio of 1.4

## References

1. N. Thompson, N. Wadsworth, and N. Louat, "Origin of fatigue fracture in copper," *Philosophical Magazine Series* **8**, 1(2):113–126, 1956
2. W.A Wood, S.McK Cousland, and K.R Sargant, "Systematic microstructural changes peculiar to fatigue deformation", *Acta Metallurgica*, **11**(7):643 – 652, 1963
3. H Mughrabi, *The Cyclic Hardening and Saturation Behaviour of Copper Single Crystals*. *Mater.Sci.Eng.* **33**(2):207–223, 1978
4. S.L. Wong, J-S. Park, M.P. Miller, and P.R. Dawson, "A Framework for Generating Synthetic Diffraction Images from Deforming Polycrystals Using Crystal-Based Finite Element Formulations," *Computational Materials Science*, **77**, 456-466, 2013
5. M.O. Obstalecki, S.L.Wong,P.R. Dawson, and M.P. Miller, "Quantitative analysis of crystal scale deformation heterogeneity during cyclic plasticity using high energy x-ray diffraction and finite element simulation," *Acta Materialia*, **75**, 259-272, 2014
6. S.L.Wong, M.O. Obstalecki, M.P. Miller, and P.R. Dawson, "Stress and deformation heterogeneity in individual grains within polycrystals subjected to fully reversed cyclic loading," *Journal of the Mechanics and Physics of Solids*, **79**, 157-185, 2015

## **2 Year Publications**

Obstalecki, M.O., Wong, S.-L., Dawson, P.R. and Miller, M.P. “Quantitative analysis of crystal scale deformation heterogeneity during cyclic plasticity using high energy x-ray diffraction and finite element simulation,” *Acta Materialia*, **75**, 259-272, 2014.

Wong, S.-L., Obstalecki, M.O., Miller, M.P. and Dawson, P.R. “Stress and deformation heterogeneity in individual grains within polycrystals subjected to fully reversed cyclic loading,” *Journal of the Mechanics and Physics of Solids*, **79**, 157-185, 2014.

## **Transformation and Deformation Mechanisms in High-Temperatures Shape Memory Alloys with Nano-precipitates**

**Principal Investigators: Profs. Michael J. Mills, Peter M. Anderson, and Yunzhi Wang.  
The Ohio State University, Department of Materials Science and Engineering**

### **Program Scope**

The focus of this program is on an emerging class of high temperature shape memory alloys (HTSMAs) that are exciting candidates for actuators and adaptive components in a wide range of energy and transportation applications. These HTSMAs offer the possibility of high reliability, lighter weight and increased capability while lowering space and power consumption. However, at present there is only elementary understanding of the important microstructure-property relationships. The goals of this effort therefore are to (1) develop a fundamental understanding of the inherent microstructure-property behavior of high temperature shape memory alloys and (2) develop computational models that capture these structure-property relationships and provide novel insights into the important transformation and plasticity mechanisms that govern their behavior.

Two HTSMA alloy systems are at the core of the effort: Ni(Ti,Hf) and (Ni,Au)Ti alloys can exhibit high transformation temperatures, large transformation strain and small permanent strain. These beneficial properties can be strongly influenced by the formation of nanoscale precipitates. Spearheaded by advanced characterization techniques, and aided by insights from first principles modeling, the unusual and novel atomic structure and composition of these precipitates is being determined, along with their coherency with the matrix. Interaction of precipitates with martensite at lower temperature and dislocation activity at higher temperature are key mechanistic insights being sought through in situ electron microscopy studies, and being understood through new phase field modeling approaches to particle/defect interactions. These insights are being incorporated into a microstructural finite element framework in order to capture how phase transformations, crystal plasticity, and time-dependent creep interact to determine the response.

### **Recent Progress**

Aging has an extraordinarily potent effect on mechanical behavior in Ni-rich Ni(Ti,Hf) alloy systems, due to the formation of H-phase precipitates. Recent work has focused on obtaining reliable volume fraction measurements of the H-phase precipitates. This is an important input to the modeling efforts. Nanoscale FIB fabricated needles of NiTiHf were analyzed by combining HAADF STEM imaging with computational 3D tomographic reconstructions. The precipitate volume fraction was calculated to be 14.3%. Similar efforts are planned for shorter aging conditions with smaller precipitates, where alternative techniques have proved inadequate.

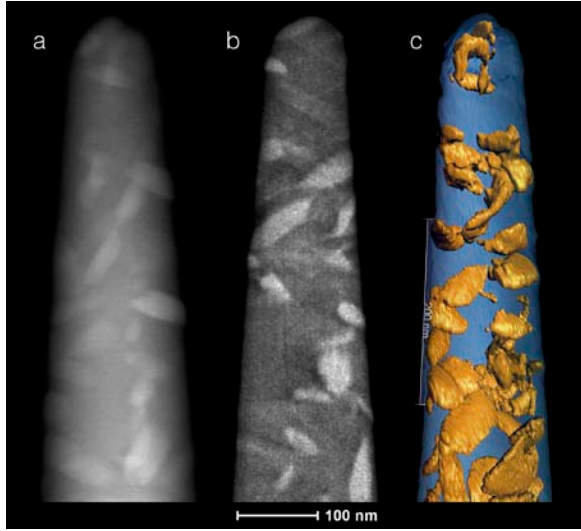


Figure 1: A needle fabricated from a  $\text{Ni}_{50.3}\text{Ti}_{29.7}\text{Hf}_{20}$  alloy, aged 315 hours at  $550^\circ\text{C}$ , used for H-phase volume fraction analysis. (a) An example of 1 of 180 HAADF STEM images used in creating the back-projection, a frame of which is shown in (b), which formed the building blocks for the 3D rendering shown in (c).

Microstructural characterization work has also continued in the NiTiAu system. Four alloy compositions containing 40at.% Au are currently being investigated: Ni-40Au-49Ti, Ni-40Au-49.7Ti, Ni-40Au-50Ti, and Ni-40Au-51Ti. Each of these alloys have very high transformation temperatures between  $400^\circ\text{C}$  and  $500^\circ\text{C}$  in the as-extruded condition, characterized by both differential scanning calorimetry (DSC) and differential thermal analysis (DTA) methods. Thus, these NiTiAu alloys have the highest transformation temperatures with attractive work output behavior. Remarkable with this system is also that, the variation in transformation and mechanical behavior with composition is small compared with the NiTiHf alloys. Thus, detailed microstructure analysis is necessary to understand the reason for these unusual and attractive behaviors.

Microstructural finite element (MFE) simulations have been developed to quantitatively study the dramatic and complex effect of aging (H-phase precipitates) in the NiTiHf alloys on the martensitic transformation (MT) process. A key hypothesis is that the process of martensite growth is fundamentally different in the presence of nanoscale precipitates when compared with large-scale particles. The orthorhombic structure of H-phase established in previous studies (Han et al. 1997, Yang et al., 2013) implies the existence of 6 H-phase variants in B2. The effect of multiple precipitate variants in close spatial proximity was recently combined with the HAADF STEM observed precipitate shape to investigate the influence of H-phase cluster on martensitic transformation (MT). Figure 2 shows the model RVE (2a), the initial nucleation of martensite (2b), and the simulated DSC for cooling (2c). All 24 CVPs are active in this simulation, which resembles an over-aged sample ( $\sim 100\text{nm}$  precipitate size). In contrast to the pronounced particle-particle interaction documented for the optimal-aging case (Chen, OSU Dissertation 2015), MT appears unaffected by the existence of the precipitate cluster. This is in agreement with the self-accommodating nature of the multi-CVP martensite at the precipitate scale, and also supports the earlier single-precipitate simulation results. Simulations similar to that shown in Figure 2 will be extended to other aging cases and by incorporating the latest precipitate morphology data as shown in Figure 1.

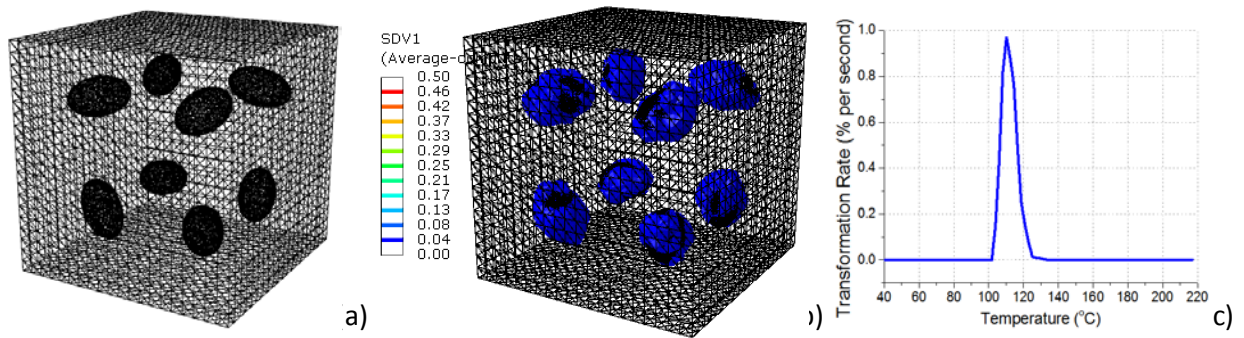


Figure 2. (a) MFE model with oblate-spheroid shaped precipitates. Major axis of each precipitate points to a  $(311)_{B2}$  orientation; (b) Initial nucleation of martensite on the surface of precipitates; (c) Simulated DSC for cooling from  $220^{\circ}\text{C}$  to  $0^{\circ}\text{C}$ . All 24 martensite CVPs are active in this simulation.

These simulations can reproduce the remarkable attribute of martensite plates to spanning over many variants of precipitates. By incorporating the latest precipitate morphology data as shown in Figure 1, the dependence of precipitate size on this effect is presently being explored in an effort to develop a more fundamental and general understanding of nanoscale precipitates on the martensitic transformation.

As discovered in previous research, functional fatigue in shape memory alloys originates from the existence of high symmetry “ghost structure” as well as symmetry-dictated non-phase-transformation pathways (SDNPTPs), which leads to the generation of crystalline defects during transformation cycling. In Ni-Ti system, it has been reported that the  $B19'$  structure is both geometrically and energetically close to a base-centered orthorhombic (BCO) structure, which has relatively high symmetry in its vicinity and can be regarded as the “ghost structure” (Figure 3). In order to further validate the existence of the SDNPTP, possible defect structures generated along this pathway are predicted through crystallography theory and compared with experimental observations.

As shown in Figure 3a, if the  $\{011\}$  cross-section of a B2 structure is considered, a simple rectangle structure in 2D can be found (Figure 3b, where atoms on only one sublattice, the blue ones, are shown for simplicity). Considering a transformation cycle from B2 to  $B19'$  and back to B2, a new B2 state could be reached if the SDNPTP between two  $B19'$  states is activated. By considering the deformation path between the two B2 structural states (including three pathway segments: two phase transition pathways between B2 and  $B19'$ , one SDNPTP between two  $B19'$  states), crystalline defects generated during the transformation cycle can be

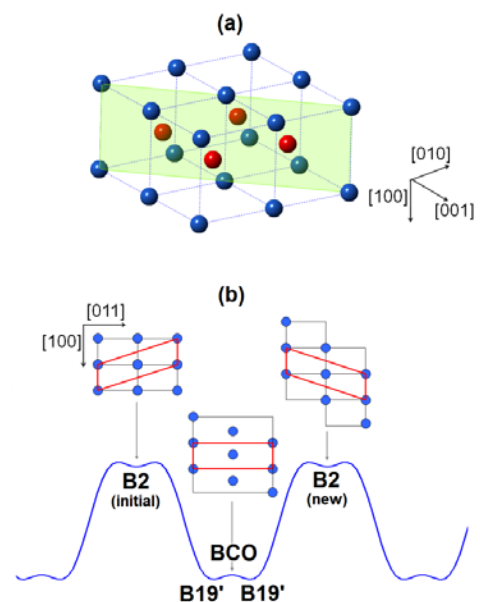


Figure 3: (a) B2 structure in Ni-Ti; (b) schematic drawing of global energy landscape in Ni-Ti (the lattice correspondence during the deformation are shown with the red boxes).

determined by applying the invariant plane strain condition, which yields two solutions. The first solution describes the [100] (011) type of dislocation, while the second solution suggests a  $\Sigma 9$  boundary in BCC structures, which is the characteristic defect of the SDNPTP. Similar calculations can be applied to determine defect structures after multiple transformation cycling. For example, it is found that  $\Sigma 3$ ,  $\Sigma 5$ ,  $\Sigma 7$ ,  $\Sigma 9$  and  $\Sigma 13$  boundaries can be generated after one cycle, while higher order special grain boundaries such as  $\Sigma 11$ ,  $\Sigma 15$ ,  $\Sigma 17$ , . . . ,  $\Sigma 37$ ,  $\Sigma 39$ , . . . can be generated after two cycles, etc. The types of defect structures predicted through crystallographic analysis agree well with experimental observations.

## **Future Plans**

In addition to further characterization of the new NiTiAu alloy system, plans are also in place to explore the effect of Hf composition on the site occupancy and intrinsic strength, using new capabilities in atomic-scale chemical analysis (EDS), atom probe tomography at EMSL, and micromechanical testing. This effort will also explore the fundamental mechanisms of defect production and functionality degeneration in SMAs during load-biased, thermal cycling—a key deformation mode for actuation. We will explore whether the remarkable observation of austenite grain refinement into the nanoscale range we have observed in binary NiTi also occurs in the NiTiHf alloys. These hypotheses will be critically examined both experimentally and by computer simulations at the defect level.

The effects of precipitates on the formation mechanism of multi-variant martensitic domains structures will be further investigated through a combination of experimental, theoretical and phase field simulation study. Crystallographic analysis will be carried out to predict the orientation relationship among austenite, martensite and H-phase precipitates and habit plane orientations, which can be validated by experimental characterizations. The self-accommodation of martensitic variants under the influence of precipitates, including the size and the spatial configuration of martensite domains, will also be investigated through phase field simulations, by which a fundamental understanding of precipitate-martensitic correlation will be established. Finally, we will uncover the fundamental principles by which nano-precipitates can impart extraordinary resistance to strain accumulation in HTSMA without deleteriously affecting work output and transformation strain. The approach will leverage advanced electron microscopy, novel phase field and microstructure-sensitive finite element modeling, and experimental validation using single crystal micropillar experiments under isothermal and load biased thermal cycling conditions.

## **References**

Han X, Wang R, Zhang Z, Yang D. *Acta Mater* 1997;46:273.

Yang F. PhD Thesis. The Ohio State University. 2013.

Chen X. PhD Thesis. The Ohio State University. 2015.

## Publications

1. F. Yang, L. Kovarik, P.J. Phillips, R.D. Noebe, M.J. Mills, "Characterization of Precipitate Phases in a Ti-Ni-Pd alloy," *Scripta Mater.* 67 (2012) 145-148.
2. Y. Gao, N. Zhou, F. Yang, Y. Cui, L. Kovarik, N. Hatcher, R. Noebe, M.J. Mills, Y. Wang, "P-phase precipitation and its effect on martensitic transformation in (Ni,Pt)Ti shape memory alloys," *Acta Mater.* 60 (2012) 1514-1527.
3. Y. Gao, H. Liu, R. Shi, N. Zhou, Z. Xu, J. Nie and Y. Wang, "Simulation Study of Precipitation in an Mg-Y-Nd Alloy" *Acta Mater.* 60 (2012) 4819-4832.
4. H. Liu, Y. Gao, J.Z. Liu, Y.M. Zhu, Y. Wang and J. F. Nie, "A Simulation Study of the Shape of  $\beta'$  Precipitates in Mg-Y and Mg-Gd Alloys," *Acta Mater.* 61 (2013) 453-466.
5. F. Yang, R.D. Noebe, M.J. Mills, "Precipitates in a Near-equiatomic (Ni + Pt)-rich TiNiPt alloy," *Scripta Mater.* 69 (2013) 713-715.
6. E. Acar, H.E. Karaca, B. Basaran, F. Yang, M.J. Mills, R.D. Noebe, Y.I. Chumlyakov, "Role of aging time on the microstructure and shape memory properties of NiTiHfPd single crystals," *Mater. Sci. Eng. A*, 573 (2013) 161–165.
7. F. Yang, D.R. Coughlin, P.J. Phillips, L. Yang, A. Devaraj, L. Kovarik, R.D. Noebe and M.J. Mills, "Structure analysis of a precipitate phase in an Ni-rich high-temperature NiTiHf shape memory alloy," *Acta Materialia*, 61(2013)3335-3346.
8. Y. Gao, N. Zhou, D. Wang and Y. Wang, "Pattern formation during cubic to orthorhombic martensitic transformations in shape memory alloys," *Acta Mater.* 68(2014) 93-105.
9. D. Wang, SenHou, Yu Wang, X.D. Ding, S.A. Ren, X.B. Ren and Y. Wang, "Superelasticity of Slim Hysteresis over a Wide Temperature Range by Nano Domains of Martensite," *Acta Mater.* 66(2014) 349-359.
10. C. Shen, J. Li and Y. Wang, "Predicting Structure and Energy of Dislocations and Grain Boundaries," *Acta Mater.* 74 (2014) 125-131.
11. D.R. Coughlin, F. Yang, R.D. Noebe, M.J. Mills, "Characterization of a High Strength 51Ni-29Ti-20Hf Shape Memory Alloy," *J. Mater. Sci.*, in minor revision.
12. L.X. Zhang, D. Wang, X.B. Ren and Y. Wang, "A new mechanism for low and temperature-independent elastic modulus," *Scientific Report* (2015 – in review (minor revision submitted)).
13. L. Nguyen, D. Wang, Y. Wang and M. De Graf, "Quantifying the abnormal strain state in ferroelastic materials: a moment invariant approach," *Acta Mater.* (accepted, April 2015).
14. H. Liu, Y. Gao, Y.M. Zhu, Y. Wang, J.F. Nie. "A simulation study of  $\beta_1$  precipitation on dislocations in an Mg-rare earth alloy." *Acta Mater.* 77(2014), 133-150.
15. H. Liu, Y. Gao, L. Qi, Y. Wang, J.F. Nie. "Phase-field simulation of Orowan strengthening by coherent precipitate plates in an aluminum alloy." *Metall Mater Trans* (accepted, April 2015).

16. M.L. Bowers, Y. Gao, L. Yang, D.J. Gaydos, M. De Graef, R.D. Noebe, Y. Wang, M.J. Mills. "Austenite grain refinement during load-biased thermal cycling of a Ni-Ti shape memory alloy." *Acta Mater* 91 (2015), 318-329.
17. X. Chen, A. Hehr, M.J. Dapino and P.M. Anderson (2015) "Deformation Mechanisms in a NiTi-Al Composite Fabricated Through Ultrasonic Additive Manufacturing". *Shape Memory and Superelasticity*. under review.
18. A. Hehr, X. Chen, J. Pritchard, M.J. Dapino and P.M. Anderson (2015). "Al-NiTi Metal Matrix Composites for Zero CTE Materials: Fabrication, Design, and Modeling", *Advanced Composites for Aerospace, Marine, and Land Applications II*, 13-28.



## From micro-pillar uniaxial compression to micro-grain nano-indentation under multi-axial stress: Control and understanding of abrupt and stochastic plastic events.

S. Papanikolaou (Lead PI), K. Hemker (co-PI)

Department of Mechanical Engineering

Hopkins Extreme Materials Institute

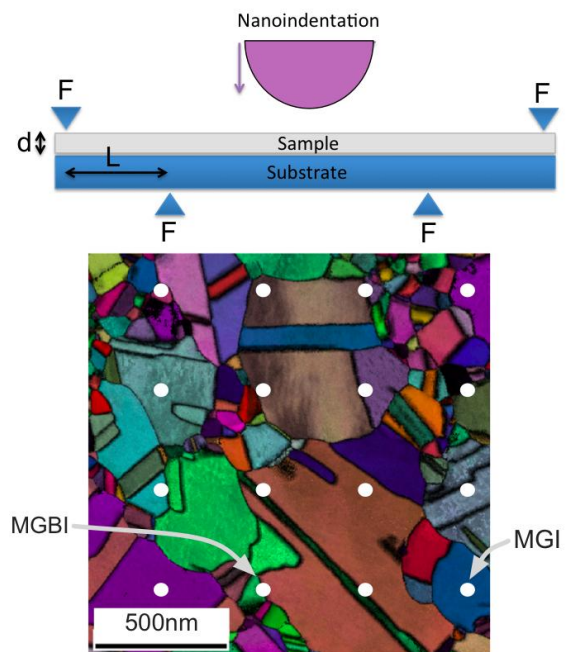
The Johns Hopkins University

### Program Scope

Over the last decade, it has become clear that the application of stress on micron-sized objects, such as micropillars,[1] leads to abrupt and stochastic plastic events that do not satisfy Weibull statistics (as expected for uncorrelated defect yielding) but instead seem to follow highly wide, power-law distributions, pointing towards co-operative multiscale dislocation plasticity mechanisms.[2,3] Are power-law distributed plastic events the rule or the exception in crystals? If the rule, can we design protocols to control and suppress them in order to achieve deterministic and smooth microforming processes?

Research efforts, to date, in small scale plasticity have mostly concentrated on nominally homogeneous deformation of micron-sized pillar samples, most prominently uniaxial compression and to a much smaller degree uniaxial tensile testing. Micropillar compression testing is surface dominated and moreover, surfaces are commonly atypical in being produced by focused ion beam milling. Nanoindentation provides a way of locally probing the plastic response of grains surrounded by other grains, and therefore a more typical picture of plasticity in small scales should be expected. We aim at utilizing nanoindentation for probing small scale plasticity on a large scale by obtaining statistically relevant information on the plastic behavior in polycrystals with grain sizes in the micro-meter regime and also combining with superposed in-plane stresses. Our proposed research aims at advancing our basic knowledge on small scale plasticity[4] and shed light on the question why the processes we know to be highly jerky and avalanche-like in small scales give the impression of a smooth deformation behavior in macro-scale dimensions.

Theoretical research to date on the jerkiness of nanopillar plasticity has been under development in two parallel functioning communities: In mechanical engineering studies, there have been extensive simulations of detailed, realistic materials and geometries in order to carefully quantify and constitutively model the phenomenon of nanopillar strengthening in FCC and BCC crystalline pillar experiments. In contrast, statistical physics studies have been focused in overly



#### Proposed Nanoindentation Set-up.

Top: Proposed nanoindentation of a thin film under in-plane stress. Bottom: Grain structure and orientation in a sample super-alloy polycrystal. The pre-defined grid of white disks signifies locations where we will perform nanoindentation.

simplified models of microscale crystal plasticity dynamics to quantify the statistical character of the post-yield plastic flow, and carefully quantify the range of qualitative dynamic behaviors or phases, as material and loading parameters are altered. The two communities have only recently been linked in a work by the lead-PI (SP) and collaborators where an explicit dislocation model has been built that can predict both strengthening and plastic flow character in a coherent connection with experimental evidence.[5]

In the current study, we aim at combining experiments and theory to unravel the mysteries of abrupt microplastic deformation in a natural dislocation environment: micron-sized grains (“micrograins”) of polycrystals. A novel experimental design will be used, that utilizes nanoindentation and 4-point bending techniques on the substrate of polycrystalline thin films of typical FCC metals (Al and Cu). The efforts in this realistic environment will be guided by concrete theoretical conjectures, based on intuition built from previous theoretical and experimental efforts on crystalline micropillar compression and nanoindentation.

Two distinct hypotheses will be tested in both theory and experiments:

*First, crystal plasticity of micron-sized grains during indentation has micropillar-like stochastic features: power-law plastic events at stresses above the macroscale yield strength, and strong size and rate effects.*

*Second, the application of uniform in-plane stress on thin films below the yield point can smoothen the abrupt micrograin plastic response during nanoindentation. On a technological level, indentation-induced localization (sink-in) can be, in principle, diminished in micro-grained polycrystals by the application of concurrent in-plane stresses.*

The first hypothesis has supporting evidence from nanoindentation near grain-boundaries[6] and interesting analogies with analogous behaviors in amorphous metals [7]. The second hypothesis can be justified by sensible generalizations of effective plasticity modeling[2]: the principal idea is that thermally activated processes may be enabled by the superposed stress contributing to a more homogeneous deformation behavior.

While the first hypothesis can be thought of fundamental importance, the second has a true technological one: mechanical forming procedures have clear economic effect in macroscopic shaping operations of metals and they are continuously minimized to enable small to medium lot size production of small components. The stochastic nature of plasticity in small scales has led researchers to the suspicion that there might be fundamental size-limits to smooth forming processes.[4] The second hypothesis targets at pushing this limit further down by performing deformations subject to superposed stress states.

Nanoindentation will be performed in sequential steps on a blind grid pattern of indent locations across the surface of large polycrystalline thin films of Cu and Al, being typical FCC crystals with large disparity in stacking fault energy. Thin films will remain under a homogeneous in-plane stress state during nanoindentation, implemented by 4-point bending. Nanoindentation curves will be gathered and statistically analyzed as function of average grain-grain misorientation, grain size and in-plane externally-imposed stress levels. Nanoindentation data will be correlated to direct observations of induced surface dislocation microstructures. A large

database of polycrystal individual-grain classification will be constructed and become freely accessible for future research efforts.

The guidance for experimental efforts will be driven by extensive simulations of models at complementary length-scales: a coarse-grained mesoscale theory of plasticity and theory of discrete dislocation plasticity in two dimensions with three dimensional effective mechanisms (2.5DDP). Simulations will be inspired by analogous studies of micropillar plasticity, but extended to model nanoindentation with multiple slip systems and on the surface of a bicrystal with microhard grain-boundaries. The envisaged 2.5DDP is for practical reasons a well suited instrument to enable direct comparison of nanoindentation data with a well established method of discrete dislocation dynamics previously used successfully for simulating micro-compression tests. This method shall also be further advanced by a stochastic implementation of grain boundary characteristics between the extreme cases of blocking all dislocations (micro-hard) or total deformability (micro-free), and a likewise stochastic implementation of thermally activated double cross slip. In addition, we will use non-local continuum models to rationalize the stochastic properties found in nanoindentation experiments. These kind of methods are successfully used in modeling various strongly stochastically dominated physical phenomena.

## **Recent Progress**

The proposed project has just started on Aug.1<sup>st</sup>, 2015. Thus, all efforts have focused on recruitment purposes. We have initiated a search for postdoctoral candidates that may have a background in either theory or experiments. It appears that we would need at least a few more months to settle to a properly skilled and talented candidate. Fortunately, a JHU undergraduate student will be making and testing Cu, Al samples for this projects next month. In this way, we will be making some progress in the next short period.

## **Future 12-month Plans**

During the coming year, we aim at build our experiment and also provide preliminary theoretical simulations for the stochastic nanoindentation behavior. In particular:

09/2015–12/2015 Experiment: We target at hiring a talented postdoctoral associate (or two postdocs partially supported by this project) to perform experiments and simulations of nanoindentation. During the first year, the work in the project will be fully experimental.

Theory/Simulation: We will generalize DDP codes (in collaboration with E. Van der Giessen), in order to accommodate the bicrystalline and circular indentation boundary conditions, as well as carefully implement double-cross-slip-assisted glide and nucleation-multiplication.

12/2015–08/2016 Experiment: We will initiate circular nanoindentation experiments for Al and Cu polycrystalline films, build films and attempt initial nanoindentations. Identify visualization tools and build software library for processing and visualizing the flow stress and avalanche data, as they get experimentally produced. We will use python-based tracking software of all changes

in data and software for providing full access to other researchers.

## References

Put the list of references here using this font (Times New Roman 12 pt).

- [1] D. M. Dimiduk, C. Woodward, R. LeSar and M. D. Uchic, Scale-free intermittent flow in crystal plasticity, *Science* 312 (2006) p.1188.
- [2] S. Papanikolaou, D. M. Dimiduk, W. Choi, J. P. Sethna, M. D. Uchic, C. F. Woodward, and S. Zapperi, Quasi-periodic events in crystal plasticity and the self-organized avalanche oscillator, *Nature* 490, (2012) p. 517.
- [3] S. Papanikolaou, F. Bohn, G. Durin, R. L. Sommer, S. Zapperi, and J. P. Sethna, Universality beyond power laws and the average avalanche shape, arXiv:0911.2291, *Nature Physics* 7, (2011) p. 316.
- [4] W. Wang, Y. Zhong, K. Lu, L. Lu, D. L. McDowell, T. Zhu, Size effects and strength fluctuation in nanoscale plasticity, *Acta Materialia* 60 (2012) p.3302.
- [5] K.J. Hemker and W.D. Nix, Nanoscale deformation: seeing is believing, *Nat. Mater.* 7 (2008) p.97.
- [6] W.A. Soer, J.T.M. De Hosson, Detection of grain-boundary resistance to slip transfer using nanoindentation *Mater. Lett.*, 59 (2005), p. 3192.
- [7] C. A. Schuh, A. S. Argon, T. G. Nieh, J. Wadsworth, The transition from localized to homogeneous plasticity during nanoindentation of an amorphous metal, *Philos. Mag.* 83 (2003) p. 2585.

## Publications

N/A

## Stability of Nanoclusters in Metal Matrices under Extreme Environments

Michael K Miller (ORNL, retired), Chad M. Parish (ORNL), German Samolyuk (ORNL), Yury N. Osetskiy (ORNL), Michael J. Mills (OSU), and Dong Ma (ORNL)

### Program Scope

This project explores the formation and stability of nanoclusters in far-from-equilibrium metallic matrices. The goal of this proposed research is to attain a fundamental mechanistic understanding of the formation and stability of nanoclusters in structural materials under extreme conditions. Extreme conditions include structural materials exposed to extremely high dose irradiation at elevated temperatures, as well as materials exposed to extreme temperatures under stress. This also includes materials that are far from equilibrium, such as those produced by mechanical alloying and friction stir methods in which excess vacancies and highly supersaturated solutes are present in solid solution.

### Recent Progress

Lately, we emphasize exploring how the nanoclusters (NCs) in the metallic matrices interact with externally applied stimuli, such as radiation, high temperature, strain, or severe deformation, combined with theoretical approaches to address NC stability at the basic level, to explain the fundamental behavior of NCs under extreme environments. The overarching goal is to understand the stability of NCs, both from their intrinsic thermodynamics and under extreme environments (creep, deformation, radiation). A subset of recent work is summarized below.

#### *A thermodynamic approach to stability of oxides in a metallic matrix*

A fundamental understanding of oxide NCs in metallic matrices requires a predictive capability. The most accurate theoretical approaches are based on density functional theory (DFT), which is limited to  $\sim 10^2$  atoms. Multi-scale approaches, e.g. DFT + Monte Carlo, are often used to model oxide metal systems at the atomic level. These approaches can qualitatively describe the kinetics of some processes but not the overall stability of individual phases. We propose [1] a new thermodynamic approach to study equilibrium in multi-phase systems, which can be sequentially enhanced by considering different defects and microstructures. We estimate the thermodynamic equilibrium by minimization of the free energy of the whole multi-phase system using a limited set of defects and microstructural objects for which the properties are calculated by DFT. The output of these calculations is the thermal equilibrium concentration of all the defects for a particular temperature and composition. Results confirmed the high temperature stability of yttria in iron. Our main development beyond previous single-phase approaches is the inclusion of the defect exchange between different phases controlled by the equivalence of chemical potentials of the same species of atoms in all phases. This model

enables calculation of the equilibrium concentrations of defects in all phases. Needed input parameters for the thermodynamic description are obtained from DFT calculations. We considered an example of yttria in bcc iron matrix as a two-phase three-component compound  $(Y_{2/5}O_{3/5})_x (bcc Fe)_{1-x}$ , where  $x$  is the atomic fraction of yttria in the pseudo-binary alloy. The equilibrium concentrations of point defects i.e. vacancies in both the  $Y_2O_3$  and bcc Fe phases, Y substitutions and O interstitials in Fe, Fe impurities, and antisite defects in  $Y_2O_3$  were estimated as a function of temperature and the fraction of yttria. We demonstrated that the main defects in the system correspond to thermal vacancies in bcc Fe ( $\sim 10^{-5}$ ), which was expected for the temperature 2000 K. In  $Y_2O_3$  particles, the main defects correspond to oxygen sublattice vacancies with an atomic concentration of  $\sim 10^{-9}$  and oxygen interstitial atoms in the octahedral interstitial positions in Fe-matrix. The concentration of the rest of the defects is less than  $10^{-12}$ . Such a small concentration of defects in the  $Y_2O_3$  particles demonstrates high thermal stability of yttria in iron that is consistent with the experimental data. The model suggested here has a number of obvious advantages over many currently used approaches. Compared to both the lattice and object KMC approach, the proposed model provides a possibility to include the global equilibrium in multi-phase systems. The advantage over the models based on a lattice approach or empirical potentials (this includes lattice KMC, phase field, and classical atomic scale modeling) is in more accurate defect energetics, used as input parameters, and calculated within the DFT technique.

#### *Influence of extreme temperature and strain on NCs*

Currently, a fundamental understanding of how friction stir welding (FSW) influences the nature and distribution of NCs in NFAs is lacking. Before this fundamental research on NFAs can be translated into practical applications such as in fission or fossil energy, reliable and robust methods to join (weld) NFAs are needed [2]. Traditional fusion welding is unsuitable for NFAs, because NCs are lost during melting. Here, we have explored FSW processing and post-weld heat-treatment (PWHT) influence the size, density, and chemistry of NFA 14YWT. FSW is a complex non-equilibrium process that involves very high temperature ( $>1000$  K) and large plastic strain levels, applied in very short times.

We collaborated with the ORNL welding group to analyze FSW-joined and as-FSW plus PWHT specimens of 14YWT. It was found that the base metal (BM), thermomechanically-affected zone (TMAZ), and stir-zone (SZ), of the FSW all contained high density Ti-Y-O NCs; the FSW process had not dissolved or otherwise removed the NCs, maintaining the NFA identity, unlike fusion (liquid-state) processing [3]; Figure 1. Interestingly, the density of NCs is not significantly changed by FSW (BM vs. TMAZ vs. SZ), but the PWHT resulted in increases in NC oxygen content, and especially number density (Figure 2, Table I). The exact cause of the increased number density is unknown, but we speculate that the FSW process drives some Y and Ti into solution, and the short (2 min, 1123 K) PWHT process allows a dense array of new NCs to nucleate from the vacancy- and solute-rich matrix. These results indicate that FSW has potential to allow this basic NFA research to eventually progress to application, and also indicates that the

fundamental understanding of the microstructural processes under FSW conditions is insufficient to allow for predictive models, and further explorations are needed.

### Exploring vacancy content of NCs

Previous work has disagreed on the nature of the NCs: are they stoichiometric  $Y_2Ti_2O_7$  and  $Y_2TiO_5$  oxides [4], or are they vacancy-rich non-equilibrium, non-stoichiometric suboxides [5]? Given their small size, and because they are embedded into metallic matrices which makes unambiguous TEM or APT chemical analysis impossible, this question is difficult to answer. Our recent experiments [6], however, combining APT and small-angle neutron scattering (SANS) have helped resolve this question, and showed that the NCs are very vacancy rich (~10-15%), and the vacancy content evolves with thermal treatment from the as-mechanically-alloyed state. APT measures the chemistry, size and density of NCs as a function of annealing time at 500°C (Figure 3); using this information to inform SANS data analysis, the NC vacancy content (which is inaccessible to TEM, APT, etc.) can be derived, Figure 4.

### NC / dislocation interactions during plastic deformation

Understanding the plastic deformation mechanisms of polycrystalline alloys has been a long-standing challenge for diffraction-based experiments. The main difficulty lies in the determination of dislocation density and character from diffraction peak profiles collected in laboratory accessible time and length scales. In this study, we established a novel diffraction profile analysis approach, and used in situ neutron diffraction to characterize the evolution of dislocation density and character in a14Y WT when subjected to tensile loading at various temperatures. We revealed a strong grain-

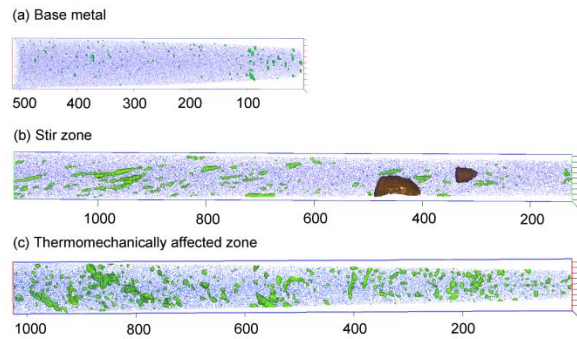


Figure 1: As-FSW sample: 5% Ti concentration isosurfaces of (a) BM, (b) SZ, and (c) TMAZ and showing the distribution of the Fe atoms (blue), Ti-Y-O-enriched NCs (green isosurface) and the Ti(O,C,N) precipitates (brown isosurface).

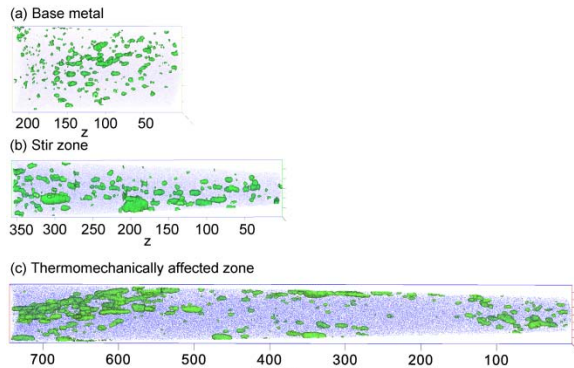


Figure 2: FSW and post weld heat treated sample: 3 % Ti concentration isosurfaces of (a) BM, (b) SZ, and (c) TMAZ showing the distribution of the Fe atoms (blue) and Ti-Y-O NCs and prescipitates (green isosurface).

Zone	Number density ( $\times 10^{22} m^{-3}$ )		NC size (nm)	
	As-FSW	PWHT	As-FSW	PWHT
BM	$5 \pm 2$	$5 \pm 2$	$1.9 \pm 0.6$	$1.6 \pm 0.8$
SZ	$2 \pm 2$	$20 \pm 10$	$2.8 \pm 1.6$	$2.0 \pm 1.1$
TMAZ	$6 \pm 3$	$9 \pm 3$	$2.9 \pm 1.4$	$2.3 \pm 1.5$

Table I: Estimates of the size and number density of the precipitates in the BM, SZ and TMAZ regions in the 14YWT NFA for both the as-FSW and after the PWHT conditions.

orientation dependent yielding and subsequent strain-hardening behavior, which is attributed to a dislocation avalanche followed by a steady-state dislocation accumulation. We showed a distinct hysteresis loop of dislocation density during unloading and reloading, manifesting a reversible rearrangement of dislocations and the strong hindrance to dislocation motions by the nanoclusters. We also presented a temperature and grain-orientation dependent dynamic recovery, which is signified by lattice softening and paradoxical concurrent dislocation accumulation at sufficiently large straining.

## Future Plans

The ongoing development of the thermodynamic approach to NC stability shows

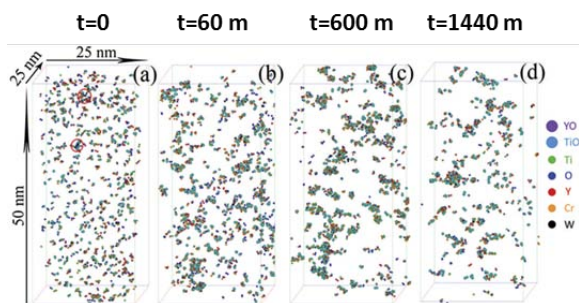


Figure 3: Atom probe tomography of as-milled powder annealed at 500°C shows the changes in NC density, size, and chemical composition with time.

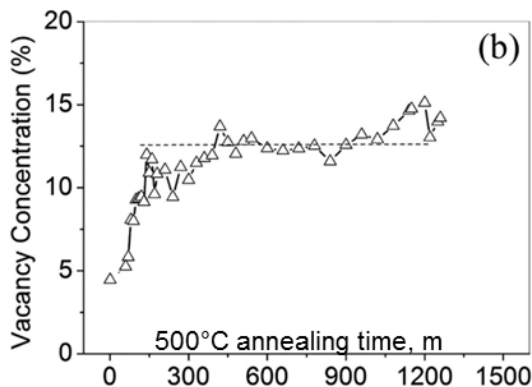


Figure 4: SANS-derived NC vacancy content as a function of in situ annealing time (min).

significant promise for elucidating NC behavior, as the model is expanded to more complex materials systems. This model will be developed further for a wide range of defect information such as NC-mobile defects interaction, NC-matrix interface properties, and defect sinks in the material that compete with NCs. These properties in application to irradiation and high-temperature conditions will be studied employing extensively *ab initio*, atomistic and mesoscale models. We will use neutron diffraction profile analysis to study *in situ* the interactions between NCs and dislocations during creep at various temperatures, and continue to develop APT and TEM-based methods to complement the theory and neutron work.

*Research supported by DOE Office of Science, Basic Energy Sciences, Materials Sciences and Engineering Division.*

## References

- [1] G. Samolyuk, Y. Osetsky, *Journal of Physics: Condensed Matter*, 27 (2015) 305001.
- [2] X. Yu, et al., *Science and Technology of Welding and Joining*, 20 (2015) 236-241.
- [3] B. Mazumder, et al., *Journal of Nuclear Materials*, 465 (2015) 204-211.
- [4] D. Bhattacharyya, et al., *Philosophical Magazine*, 92 (2012) 2089-2107.
- [5] M.K. Miller, et al., *Materials Science and Technology*, 29 (2013) 1174-1178.
- [6] Z. Zhang, et al., *Scientific Reports*, 5 (2015).



## **Publications**

### **January-August 2015**

Mazumder, B., M. Bannister, et al. (2015). "Helium trapping in carbide precipitates in a tempered F82H ferritic–martensitic steel." Nuclear Materials and Energy **1**: 8-12.

Miao, Y., K. Mo, et al. (2015). "In situ synchrotron tensile investigations on the phase responses within an oxide dispersion-strengthened (ODS) 304 steel." Materials Science and Engineering: A **625**: 146-152.

Parish, C. M. (2015). "When will Low-Contrast Features be Visible in a STEM X-Ray Spectrum Image?" Microscopy and Microanalysis: 1-19.

Parish, C. M., K. G. Field, et al. (2015). "Application of STEM characterization for investigating radiation effects in BCC Fe-based alloys." Journal of Materials Research **30**(09): 1275-1289.

Samolyuk, G. and Y. Osetsky (2015). "Thermodynamic approach to the stability of multi-phase systems: application to the Y<sub>2</sub>O<sub>3</sub>–Fe system." Journal of Physics: Condensed Matter **27**(30): 305001.

Yu, X., B. Mazumder, et al. (2015). "Stability of Y-Ti-O precipitates in friction stir welded nanostructured ferritic alloys." Science and Technology of Welding and Joining **20**(3): 236-241.

Zhang, Z., L. Yao, et al. (2015). "Vacancy-controlled ultrastable nanoclusters in nanostructured ferritic alloys." Scientific Reports **5**.

### **2014**

Edmondson, P., C. Parish, et al. (2014). "Thermal stability of nanoscale helium bubbles in a 14YWT nanostructured ferritic alloy." Journal of Nuclear Materials **445**(1): 84-90.

Li, Q., C. M. Parish, et al. (2014). "Helium solubility and bubble formation in a nanostructured ferritic alloy." Journal of Nuclear Materials **445**(1): 165-174.

Miller, M., C. Parish, et al. (2014). "Controlling diffusion for a self-healing radiation tolerant nanostructured ferritic alloy." Journal of Nuclear Materials.

Miller, M., D. Reinhard, et al. (2014). "Detection and quantification of solute clusters in a nanostructured ferritic alloy." Journal of Nuclear Materials.

Miller, M. K. and R. G. Forbes (2014). Atom-Probe Tomography: The Local Electrode Atom Probe, Springer.

Miller, M. K., Q. Li, et al. (2014). "Light Element Quantification in Irradiated Nanostructured Ferritic Alloys." Microscopy and Microanalysis **20**(S3): 1814-1815.

Parish, C. M. and M. K. Miller (2014). "Aberration-corrected X-ray spectrum imaging and Fresnel contrast to differentiate nanoclusters and cavities in helium-irradiated alloy 14YWT." Microscopy and Microanalysis **20**(02): 613-626.

Parish, C. M. and M. K. Miller (2014). "A review of advantages of high-efficiency X-ray spectrum imaging for analysis of nanostructured ferritic alloys." Journal of Nuclear Materials.

Parish, C. M., R. M. White, et al. (2014). "Response of nanostructured ferritic alloys to high-dose heavy ion irradiation." Journal of Nuclear Materials **445**(1): 251-260.

Stoica, G. M., A. D. Stoica, et al. (2014). "Temperature-dependent elastic anisotropy and mesoscale deformation in a nanostructured ferritic alloy." Nature communications **5**.

Yao, L. and M. K. Miller (2014). A new approach to atomic level characterization of grain boundaries by atom probe tomography. MRS Proceedings, Cambridge Univ Press.

### **August-December 2013**

Miller, M. K., C.-L. Fu, et al. (2013). "Stability of Oxygen-Enriched Nanoclusters and Helium Bubbles in Fe-Based Alloys under Extreme Conditions." Microscopy and Microanalysis **19**(S2): 1006-1007.

Miller, M. K., C. M. Parish, et al. (2013). "Advanced oxide dispersion strengthened and nanostructured ferritic alloys." Materials Science and Technology **29**(10): 1174-1178.

Miller, M. K., C. M. Parish, et al. (2013). "A Correlated APT and TEM Approach to Understand Nanostructured Ferritic Alloys." Microscopy and Microanalysis **19**(S2): 972-973.

Miller, M. K. and L. Yao (2013). "The Effects of Detector Efficiency on Distinguishing Solute Atoms in Random Solid Solution and Solute Clusters." Microscopy and Microanalysis **19**(S2): 988-989.

Miller, M. K. and L. Yao (2013). "Limits of detectability for clusters and solute segregation to grain boundaries." Current Opinion in Solid State and Materials Science **17**(5): 203-210.

Serizawa, A. and M. K. Miller (2013). "Radius dependence of solute concentration estimates of simulated ultrafine precipitates." Microscopy research and technique **76**(11): 1196-1203.

Yao, L. and M. Miller (2013). "Direct Experimental Measurement of Grain Boundary's Five-Parameters and Solute Segregations at Atomic Level." Microscopy and Microanalysis **19**(S2): 938-939.

Yao, L., S. Ringer, et al. (2013). "The anatomy of grain boundaries: Their structure and atomic-level solute distribution." Scripta Materialia **69**(8): 622-625.

## Multiscale Mechanical Properties and Alloy Design

George M. Pharr<sup>2,1</sup>, Yanfei Gao<sup>2,1</sup>, Hongbin Bei<sup>1</sup>, James R. Morris<sup>1,2</sup>, and Yuri Osetskiy<sup>1</sup>

<sup>1</sup>Oak Ridge National Laboratory, Materials Science and Technology Division, Oak Ridge, TN 37830; <sup>2</sup>University of Tennessee, Department of Materials Science and Engineering, Knoxville, TN 37996-2100

### Program Scope

The overarching goal of this program is to elucidate the mechanisms that control the deformation and phase stability of a unique new class of metallic alloys - *high entropy and equi-atomic single-phase solid solutions*. These alloys exhibit unusual but highly desirable mechanical properties including high strength and a breakdown of the traditional inverse relationship between strength and ductility at low temperatures. Highly coordinated experimental and theoretical efforts are being used to establish the importance of specific alloying elements on the mechanical properties of the alloys and model the unique deformation mechanisms that control their strength, ductility and toughness. The studies focus primarily on a family of equi-atomic alloys based on the quinary FeNiCoCrMn high entropy alloy and its quaternary, ternary, and binary single-phase subsets. Because some of the simpler alloys in this family exhibit many of the same unique mechanical properties as FeNiCoCrMn but are more amenable to theoretical examination, studying them will help to elucidate the controlling mechanisms and processes. State-of-the-art mechanical testing techniques and micro-analytical tools including advanced electron microscopy, x-ray and neutron diffraction, and atom probe tomography are being used to characterize the microstructure and mechanical behavior of the alloys before and after deformation. Modeling and simulation work based on molecular dynamics, *ab initio* calculations, and traditional micro-mechanics modeling are being employed to develop new theories and mechanistic descriptions of the behavior. The understanding gained will contribute to the development of broad scientific principles for the design of an important new class of structural materials for use in energy-related applications.

### Recent Progress

Both experimental and modeling efforts were undertaken to begin to understand the mechanical behavior and phase stability of high entropy and equi-atomic alloys. This report focuses on the mechanical behavior. Early on in the program, we realized that a better understanding of the mechanical properties might be achieved by experimentally examining the behavior of the less complicated but more theoretically tractable systems comprised of the equi-atomic binary, ternary, and quaternary alloy subsets of the FeNiCoCrMn quinary system. To this

end, a systematic study was undertaken to identify all the single-phase FCC subsets of the quinary alloy. In some cases, the phase stability was known through well-established binary and ternary phase diagrams, but in others, no phase diagrams were available. In this case, alloys were prepared by arc melting and drop casting followed by homogenization by annealing at an appropriate high temperature for 24 hrs [1].

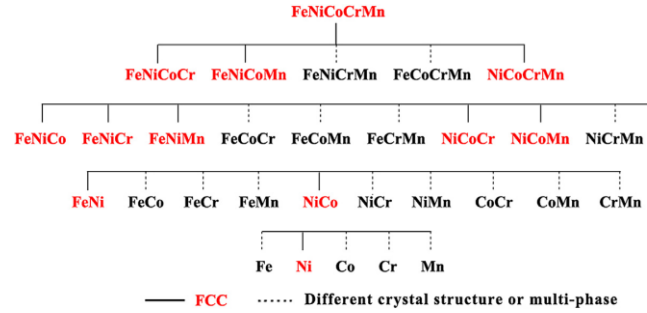


**Fig. 1.** Subsets of the FeNiCoCrMn quinary system that are single phase FCC (in red) [1].

Results of the study are shown in Fig. 1, in which the alloys that exist as single-phase FCC alloys are identified in red. The alloys in black are either multi-phase or exhibit a different crystal structure. The figure shows that 3 quaternary, 5 ternary, and 2 binary systems are single-phase FCC. These alloys, along with pure FCC Ni and the quinary FeNiCoCrMn alloy, were later used for basic studies of the effects of alloying elements on the mechanical behavior.

Close examination of the FeNiCoCrMn quinary system [2] revealed that its mechanical properties exhibit an especially interesting dependence on temperature. As shown in Fig. 2, the yield strength and ultimate tensile strength of the alloy increase as the temperature is decreased from room temperature to liquid nitrogen temperature, which is more typical of BCC rather than in FCC metals [2]. However, even more interesting is the fact that there is a significant increase in ductility with decreasing temperature, as evidenced by the increased elongations to failure. In addition, the material maintains an extraordinary fracture toughness of about  $220 \text{ MPa}\cdot\text{m}^{1/2}$  all the way down to 77 K [4]. This very unusual but highly desirable combination of properties, along with strengths of  $\sim 1 \text{ GPa}$ , make the alloy very attractive for cryogenic structural applications. It also raises the important fundamental scientific question of what the basic mechanisms are that produce this remarkable combination of properties.

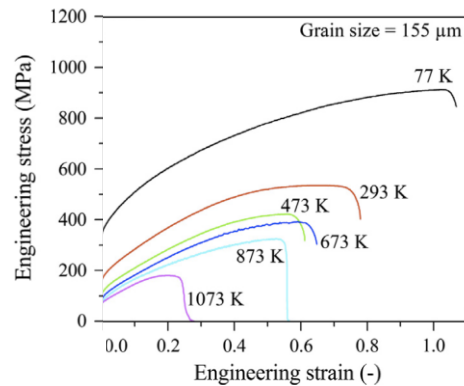


**Fig. 2.** Stress-strain curves for the FeNiCoCrMn high entropy alloy [2].

Although we are a long way from fully understanding the behavior, a TEM study of microstructures before and after deformation revealed several important clues, as shown in Fig. 3 [3]. At room temperature, the alloy deforms by dislocation glide on the normal FCC slip systems, i.e.,  $\frac{1}{2}\langle 110 \rangle$  type dislocations on  $\{111\}$  planes. The dislocation slip is very planar and associated with the development of planar arrays of dislocations (Fig. 3b) that often form when the inherent lattice resistance is high [5]. This is in sharp contrast to the normal behavior for elemental FCC materials like Cu or Ni, in which the lattice resistance is very small, and the strength is predominantly determined by other dislocation obstacles, such as solute atoms, precipitates, and

grain boundaries. Understanding the origin of this inherently large lattice resistance and how it is influenced by complexities in dislocation core structure that limit mobility and/or increase the Peierls stress is thus of paramount importance. One can certainly imagine that the core structure of a random solid solution containing five or more elemental species is exceedingly complex, as would be the local atomic motion and rearrangement processes that allow a dislocation to move. A high friction stress overcome by stress-assisted thermal activation could explain the strong increase in strength at reduced temperatures and the associated transition from athermal to thermally activated flow, in a manner similar to a BCC metal [3].

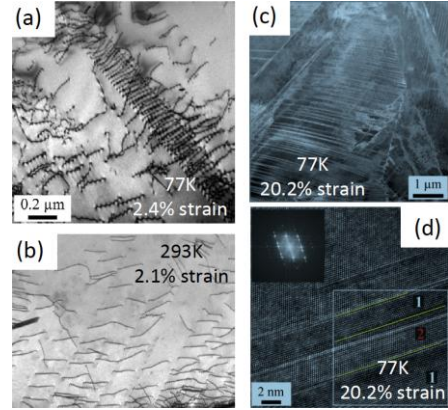


**Fig. 3.** TEM micrographs of interrupted tensile tests of the FeNiCoCrMn alloy.

Another important microstructural observation is the appearance of large number of very small deformation twins when the material is deformed to strains in excess of a few percent at liquid nitrogen temperatures (Fig. 3c,d) [2]. Such nano-twins are known to provide significant strengthening in thin films of copper and some steels [6-8], presumably by increasing the number of internal crystalline interfaces that hinder dislocation motion. Why twinning becomes prevalent at the lower temperatures is not well understood but is possibly related to a significant increase in lattice friction that diminishes dislocation mobility at low temperatures, thereby promoting other deformation mechanisms that require higher stresses to operate. The enhancement of nano-twinning processes at low temperatures may also increase the work hardening rate, which in turn would produce enhanced ductility in the way it postpones necking to higher strains.

We experimentally established the temperature dependence of the stress-strain behavior of all the single-phase binary, ternary and quaternary subsets of the FeNiCoCrMn quinary high entropy alloy [9]. The tests were conducted from 77K (liquid nitrogen temperature) to 673K. Of the numerous interesting observations made in the study, one of the most significant is that the combined increase in strength and ductility observed in the 5 element alloy is also observed in some of the 2, 3, and 4 element alloys. In fact, as shown in Fig. 4, the NiCoCr ternary alloy has the highest strength and ductility under all conditions of the 10 alloys investigated. It is also notable that even the FeNi and NiCo binaries show a significant increase in strength and ductility with decreasing temperature, albeit to a lesser degree than the other alloys. The importance of these observations is that the mechanical behavior of

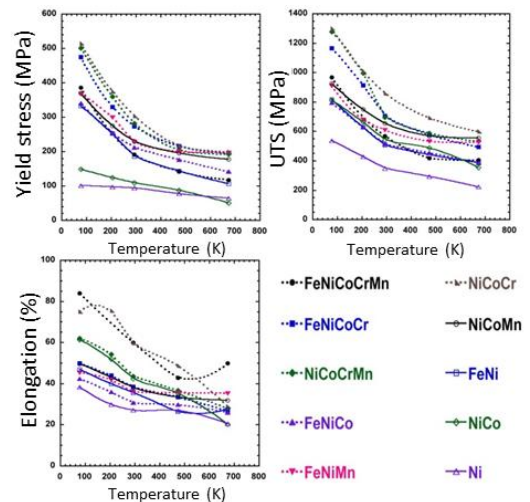


**Fig. 4.** The strength and ductility (elongation) of the single-phase equi-atomic alloys [9].

great scientific interest in the 5-element alloy is also observed in the ternary alloys, and to a lesser extent in the binaries. As we move forward, we thus plan to focus more attention on the binaries and ternaries, where modeling and simulation might help to more easily unravel the relevant mechanisms.

Finally, we recently completed a study of statistical correlations between the mechanical properties of the FCC equi-atomic alloys (see Fig. 1) and a number of material parameters that may be important in understanding them [10]. The analysis showed that both the strength and ductility are highly correlated with the annealing twin density. In addition, although the strength mildly correlates with the number of alloying elements, it appears that the specific nature of the alloying elements is more important than the number. Chromium, in particular, provides significant strengthening. These observations will be the subject of further scrutiny as we move forward.

### Future Plans

We plan to develop new ways to model and describe strengthening in solid solution alloys in order to address the unique issues encountered when the chemical species are in near equi-atomic proportions and the classical dilute limit theories for solid solution strengthening no longer apply. Specific questions to be answered are: (1) What governs the temperature dependence of the mechanical properties? (2) Why does the ductility increase hand-in-hand with strength? (3) What roles do short-range lattice distortion and long-range elastic interactions play, separately or synergistically? Answers to these questions will be obtained by atomistic modeling of dislocation core structures and mobility, understanding the temperature dependence produced by short-range and/or long-range interactions, and modeling the strain rate dependence and the role of twinning. The new models will be carefully guided by new experimental results. A primary hypothesis to be tested is that the dislocation core structure of an equi-atomic alloy and its mobility are determined by lattice distortion and atomic-level stress heterogeneity [9,11].

### References

- [1] Wu Z, Bei H, Otto F, Pharr GM, George EP, *Intermetallics* **46**, 131 (2014).
- [2] Otto F, Dlouhý A, Somsen C, Bei H, Eggeler G, George EP, *Acta Mater.* **61**, 5743 (2013).
- [3] Dieter G, *Mechanical Metallurgy*, McGraw-Hill, third edition (1986).
- [4] Gludovatz B, Hohenwarter A, Catoor D, Chang EH, George EP, Ritchie RO, *Science* **345**, 1153 (2014).
- [5] Mills M, private communication (2014).
- [6] Grassel O, Kruger L, Frommeyer G, Meyer LW, *Int. J. Plasticity* **16**, 1391 (2000).
- [7] Lu L, Chen X, Huang X, Lu K, *Science* **323**, 607 (2009)
- [8] Shen YF, Lu L, Lu QH, Jin ZH, Lu K, *Scripta Mater.* **52**, 989 (2005).
- [9] Wu Z, Bei H, Pharr GM, George EP, *Acta Mater.* **81**, 428 (2014).
- [10] Wu Z, Bei H, Pharr GM, George EP, in preparation (2015).
- [11] Zou Y, Maiti S, Steurer W, Spolenak R, *Acta Mater.* **65**, 85 (2014).

## Publications

### 2013

Y. Fan, Y. N. Osetskiy, S. Yip, and B. Yildiz, “Mapping strain rate dependence of dislocation-defect interactions by atomistic simulations,” *Proc. Nat. Acad. Sci.* **110**, 17756–17761 (2013).

A. Gali and E. P. George, “Tensile properties of high- and medium-entropy alloys,” *Intermetallics* **39**, 74–78 (2013).

W. Li, H. Bei, J. Qu, and Y. F. Gao, “Effects of machine stiffness on the loading-displacement curve during spherical nano-indentation,” *J. Mater. Res.* **28**, 1903–1911 (2013).

N. S. McIntyre, R. I. Barabash, J. Qin, M. Kunz, N. Tamura, and H. Bei, “Acquisition, sharing, and processing of large data sets for strain imaging: an example of an indented NiAl/Mo composite,” *JOM* **65**, 29–34 (2013).

F. Otto, A. Dlouhy, C. Somsen, H. Bei, G. Eggeler, and E. P. George, “The influences of temperature and microstructure on the tensile properties of a CoCrFeMnNi high-entropy alloy,” *Acta Mater.* **61**, 5743–5755 (2013).

F. Otto, Y. Yang, H. Bei, and E. P. George, “Relative effects of enthalpy and entropy on the phase stability of equiatomic high-entropy alloys,” *Acta Mater.* **61**, 2628–2638 (2013).

P. S. Phani, K. E. Johanns, E. P. George, and G. M. Pharr, “A simple stochastic model for yielding in specimens with limited number of dislocations,” *Acta Mater.* **61**, 2489–2499 (2013).

P. S. Phani, K. E. Johanns, E. P. George, and G. M. Pharr, “A stochastic model for the size dependence of spherical indentation pop-in,” *J. Mater. Res.* **28**, 2728–2739 (2013).

C. Su, E. G. Herbert, S. Sohn, J. A. Lamanna, W. C. Oliver, and G. M. Pharr, “Measurement of Power-law Creep Parameters by Instrumented Indentation Methods,” *J. Mech. Phys. Solids* **61**, 517–536 (2013).

D. Wu, J. Y. Zhang, J. C. Huang, H. Bei, and T. G. Nieh, “Grain-boundary strengthening in nanocrystalline chromium and the Hall-Petch coefficient of body-centered cubic metals,” *Scr. Mater.* **68**, 118–121 (2013).

X. Wu, I. Baker, M. K. Miller, K. L. More, H. Bei, and H. Wu, “Microstructure and mechanical behavior of directionally solidified Fe<sub>35</sub>Ni<sub>15</sub>Mn<sub>25</sub>Al<sub>25</sub>,” *Intermetallics* **32**, 413–422 (2013).

### 2014

B. Gludovatz, A. Hohenwarter, D. Catoor, E. H. Chang, E. P. George, and R. O. Ritchie, “A fracture resistant high-entropy alloy for cryogenic applications,” *Science* **345**, 1153–1158 (2014).

G. Hasemann, J. H. Schneibel, M. Krüger, E. P. George, "Vacancy strengthening in Fe<sub>3</sub>Al iron aluminides," *Intermetallics* **54**, 95–103 (2014).

P. E. Loya, Y. Z. Xia, C. Peng, H. Bei, P. Zhang, J. Zhang, E. P. George, Y. F. Gao, and J. Lou, "Yield strength dependence on strain rate of molybdenum-alloy nanofibers," *Appl. Phys. Lett.* **104**, 251909 (2014).

J. R. Morris, V. R. Cooper, and F. W. Averill, "Theoretical studies of Ir<sub>5</sub>Th and Ir<sub>5</sub>Ce nanoscale precipitates in Ir," *Philos. Mag.* **94**, 991 (2014).

F. Otto, N. L. Hanold, E. P. George, "Microstructural evolution after thermomechanical processing in an equiatomic, single-phase CoCrFeMnNi high-entropy alloy with special focus on twin boundaries," *Intermetallics* **54**, 39–48 (2014).

Z. Wu, H. Bei, F. Otto, G. M. Pharr, and E. P. George, "Recovery, recrystallization, grain growth and phase stability of a family of FCC-structured multi-component equiatomic solid solution alloys," *Intermetallics* **46**, 131–140 (2014).

Z. Wu, H. Bei, G. M. Pharr, and E. P. George, "Temperature dependence of the mechanical properties of equiatomic solid solution alloys with face-centered cubic crystal structures," *Acta Mater.* **81**, 428–441 (2014).

Y. Z. Xia, T. L. Li, F. Ren, Y. F. Gao, and H. Wang, "Failure analysis of pinch-torsion tests as a thermal runaway risk evaluation method of Li-ion cells," *J. Power Sources* **265**, 356–362 (2014).

Y. H. Zhang, Y. F. Gao, and L. Nicola, "Lattice rotation caused by wedge indentation of a single crystal: dislocation dynamics compared to crystal plasticity simulations," *J. Mech. Phys. Sol.* **68**, 267–279 (2014).

## 2015

Y. F. Gao, B. C. Larson, J. H. Lee, L. Nicola, J. Z. Tischler, and G. M. Pharr, "Lattice Rotation Patterns and Strain Gradient Effects in Face-Centered-Cubic Single Crystals Under Spherical Indentation," *Trans. of ASME, Journal of Applied Mechanics* **82**, iss. 6, 061007:1-10 (2015).

A. Haglund, M. Koehler, D. Catoor, E. P. George, V. Keppens, "Polycrystalline elastic moduli of a high-entropy alloy at cryogenic temperatures," *Intermetallics* **58**, 62–64 (2015).

J. Kwon, M. L. Bowers, M. C. Brandes, V. McCreary, I. M. Robertson, P. Sudharshan Phani, H. Bei, Y. F. Gao, G. M. Pharr, E. P. George, and M. J. Mills, "Characterization of Dislocation Structures and Deformation Mechanisms in As-Grown and Deformed Directionally Solidified NiAl-Mo Composites," *Acta Materialia* **89**, 315–326 (2015).



- G. Laplanche, P. Gadaud, O. Horst, F. Otto, G. Eggeler, E. P. George, "Temperature dependencies of the elastic moduli and thermal expansion coefficient of an equiatomic, single-phase CoCrFeMnNi high-entropy alloy," *J. Alloys Compd.* **623**, 348–353 (2015).
- C. Pu and Y. F. Gao, "Crystal plasticity analysis of stress partitioning mechanisms and their microstructural dependence in advanced steels," *Trans. of ASME, Journal of Applied Mechanics* **82**, iss. 3, 031003 (2015).
- M. Claudia Tropaevsky, James R. Morris, Paul R. C. Kent, Andrew R. Lupini, and G. Malcolm Stocks, "Criteria for predicting the formation of single-phase high-entropy alloys," *Phys. Rev. X* **5**, 011041 (2015).
- D. Wu, J. R. Morris and T. G. Nieh, "Effect of tip radius on the incipient plasticity of chromium studied by nanoindentation," *Scripta Mat.* **94**, 52–55 (2015).
- J. B. Yang, Z. F. Zhang, Y. N. Osetsky, and R. E. Stoller, "Using a scalar parameter to trace dislocation evolution in atomistic modeling," *Comput. Mater. Sci.* **96**, 85–89 (2015).

## Electric Field and Temperature Induced Defect Catastrophe and Related Phenomena

Rishi Raj  
University of Colorado Boulder  
Boulder, CO 80302

### Program Scope

We have discovered that electric fields of intermediate strengths, in the range of about  $100 \text{ V cm}^{-1}$  to  $1000 \text{ V cm}^{-1}$ , applied at elevated temperatures, from approximately  $500 \text{ }^\circ\text{C}$  to  $1200 \text{ }^\circ\text{C}$  produce *highly non-linear effects* in ceramics. The effects are observed in oxides that are semiconductors, ionic conductors, electronic conductors and insulators. Remarkably, they include (i) a transition to ultrahigh electrical conductivity, (ii) massive self-diffusion, (iii) a “green glow” of electroluminescence, (iv) formation of non-equilibrium phases, and (v) accelerated kinetics of chemical reactions. The objective of this program is to elucidate the fundamental mechanism(s) that can unfold the underlying science of these remarkable effects. This field of research emerged with the discovery of ultrafast sintering in 2010 [1] as shown in Fig. 1; it was given the name flash sintering. There is a need, now, to give it a broader context in view of the other effects in this list, which have been identified in this program.

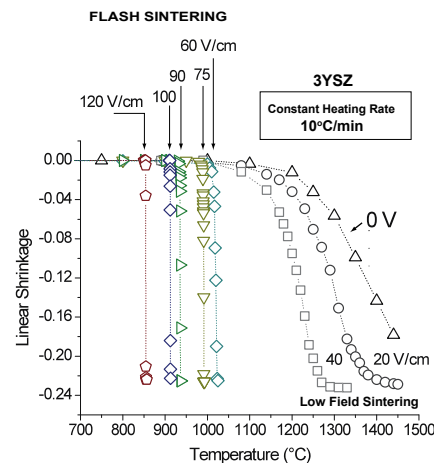


Fig. 1. The discovery of flash sintering in 2010 [1].

Most likely, these effects are controlled by different kinds of defects. For example mass transport, which is needed for sintering, occurs by stoichiometric diffusion, which depends on the slowest moving charged species. On the other hand electrical conductivity depends on the fast moving charge. Electroluminescence requires electron-hole recombination. Formation of unusual phases under electric field suggests a role for electrical potential in the thermodynamic description of phases. Kinetics of chemical reactions can depend on the defects present at interfaces. That so many different types of defects are apparently involved in this non-linear behavior is startling. We hypothesize the non-linearity is produced by catastrophic generation of defects. We visualize the production of charge neutral vacancies and interstitials as well as electrons and holes by ionization of Frenkel pairs. The increase in conductivity produces Joule heating. The role of Joule heating in defect generation is unclear at the present time, and remains a key question in full understanding of this phenomenon. Analysis of results for many different ceramics, discussed in a manuscript under review (available on request), suggests that Joule heating is likely to be necessary, but cannot be a sufficient condition for instigating these catastrophes. The role of electrical fields on defect chemistry of grain boundaries, as well as than of single crystals, is a profound question in this scientific enquiry, which is planned in the future.

The objective of this research program is to develop a fundamental understanding of the defect catastrophe which is manifested in different ways. We will perform well defined experiments that seek to answer critically posed issues, closed from modeling of thermodynamics and kinetics which includes the electrical potential, and eventually first

principles calculations of well focused problems that mesh with the analytical models. Experiments at the Advanced Photon Source at the Argonne Laboratory, which have already yielded valuable information, as described in the following section, are of great significance in this pursuit of scientific enquiry in this program.

## Recent Progress

Over the last two years flash experiments in real time performed *in-situ* at the APS at the Argonne National Laboratory (and in one case at the Pohang Light Source II) have provided valuable results. These experiments began with the objective of measuring the specimen temperature by thermal expansion of the lattice in order to better understand the role of Joule heating in the flash phenomena. By happenstance these experiments have revealed new effects of electrical fields under flash conditions. We have measured unusual phase transformations, and vastly accelerated chemical kinetics as if beyond equilibrium. Some of these results are described below.

The intense optical luminescence during the flash experiments had been in the back of our minds since the early days [1], but we had (mistakenly) ascribed it to Joule heating\*. Spectral analysis of the emission showed it to lie in the 400 nm to 2500 nm wavelength range. These results were coupled with the measurements of specimen temperature made at APS, to determine if the emission could be explained by black body radiation. It was definitively shown that the “green glow” of the emission was from the recombination of electron-hole pairs. These findings have underpinned the hypothesis that the non-linear rise in conductivity is also instigated by the generation of electrons and holes. The concept now emerging in our work is that while the electrons and holes can serve both functions, they may either emit photons or impart electrical conductivity within the constraints of their total population. Indeed, we are discovering that materials that are more electronically conducting glow less intensely.

It is important to understand the design of the electrical cycle which powers the flash phenomena. The experiments at APS are done at isothermal furnace temperature (not in constant heating rate experiments shown in Fig. 1). The typical protocol for these experiments is shown in Fig. 2. The specimen is brought up to the furnace temperature, and an electric field is applied as a step function. After an incubation time, which lengthens as the strength of the field is lowered, the conductivity rises abruptly; we call this Stage I. The power dissipation is controlled by switching the power supply to current control; this short lived transient of about 2 – 5 seconds is called Stage II. Under current control the specimen settles into a steady state condition of flash, which is Stage III. Powder specimens sinter during Stage II. Thus the measurements in Stage III are always on dense specimens. We also conduct experiments with pre-sintered specimens, which flash and show the same effects as the powder samples. In the future we will conduct flash

---

\* Very recently two papers have been published [2,3] which have sought to show, from numerical analysis that the Arrhenius rise in conductivity, in special cases, can lead to the non-linear rise in temperature which can explain flash sintering. We have recently submitted a manuscript which gives a closed-form analysis which can be applied generally to all ceramics, and compared it to results from many experiments on flash sintering. This analysis shows that while Joule heating may be necessary to instigate the flash, it is not sufficient to explain the diversity of results that continue to emerge in the study of this effect. Because of a constraint on space this analysis is not presented here but the PI will be happy to send it if requested. The title is “On the Power Density at the Onset of Non-Linearity in Experiments Related to Flash Sintering”; submitted for publication in August 2015.

experiments on single crystals to understand and to distinguish between the role of grain matrices and grain boundaries in flash sintering.

We now describe the two particular effects which have been discovered recently. They occur during Stage III in Fig. 2. They are: (i) measurement of specimen temperature at APS and electroluminescence, and (ii) the emergence of a new phase in 3YSZ during Stage III which turns on and off with the electric field. In order to conserve space a complete explanation of these discoveries are given in the figure captions. Please read them with care.

There are several other results which have been published or in process which cannot be described here due to space; for example the measurement of the power at which the temperature in the sample transitions from being uniform to non-uniform, determined from *in-situ* experiments of peak broadening at APS, and the development of a processing map from these measurements since temperature localization also creates non-uniform microstructure [in review], and a model for the incubation time – as in Stage I – in terms of the nucleation of a polar phase [4], where the interface between the polar nature of the embryo and the non-polar matrix can create a metallic interface that spreads throughout the specimen to create the catastrophe that we seek to understand [5].

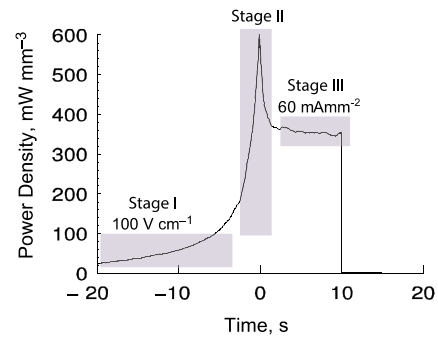


Fig. 2. Three Stages of a flash experiment. It applied to porous as well as to dense specimens.

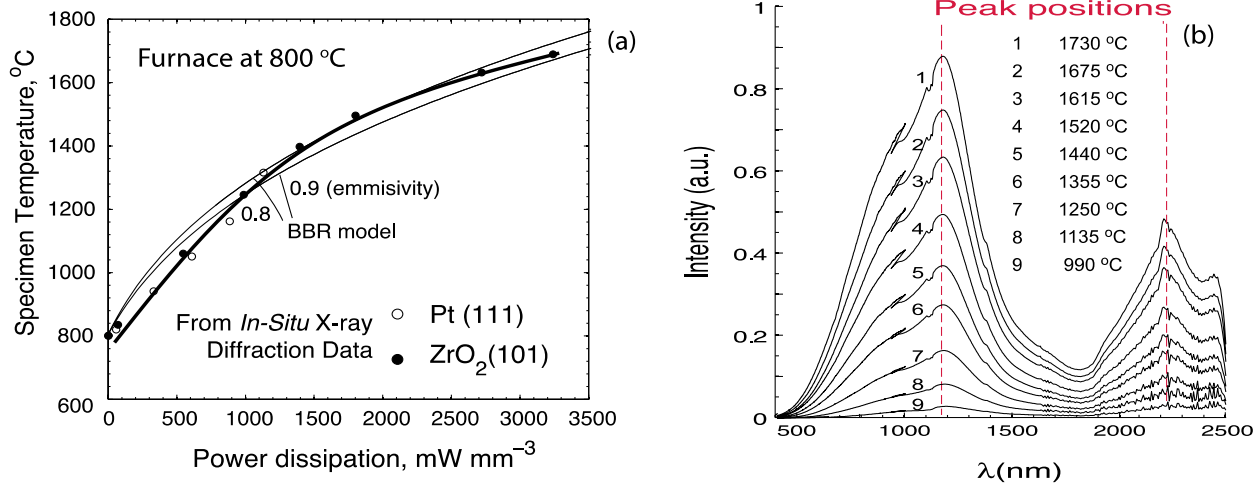


Fig. 3. Measurements of specimen temperature and accompanying electroluminescence in Stage III. (a) Determination of the specimen temperature from *in-situ* measurements of lattice expansion during the flash. The shifts of the zirconia peaks with temperature were calibrated against a platinum standard. Note that the black body radiation model [6] agrees well with the measurements. (b) The electroluminescence spectra measured at different specimen temperatures when the specimen is in the state of flash. The specimen temperature is increased by increasing the current flowing through the specimen. Note that the peaks remain at the same wavelength but increase in intensity. If the optical luminescence had been from black body radiation then the peak would shift to shorter wavelengths at higher temperatures, and the emission wavelengths would have been much more toward the infrared. We conclude from these experiments that electron-hole recombination is producing the electroluminescence. It is further inferred that the same electrons and holes produce the catastrophic rise in conductivity. Thus conductivity and luminescence compete for the e/h that are produced by the defect avalanche in the flash experiments.

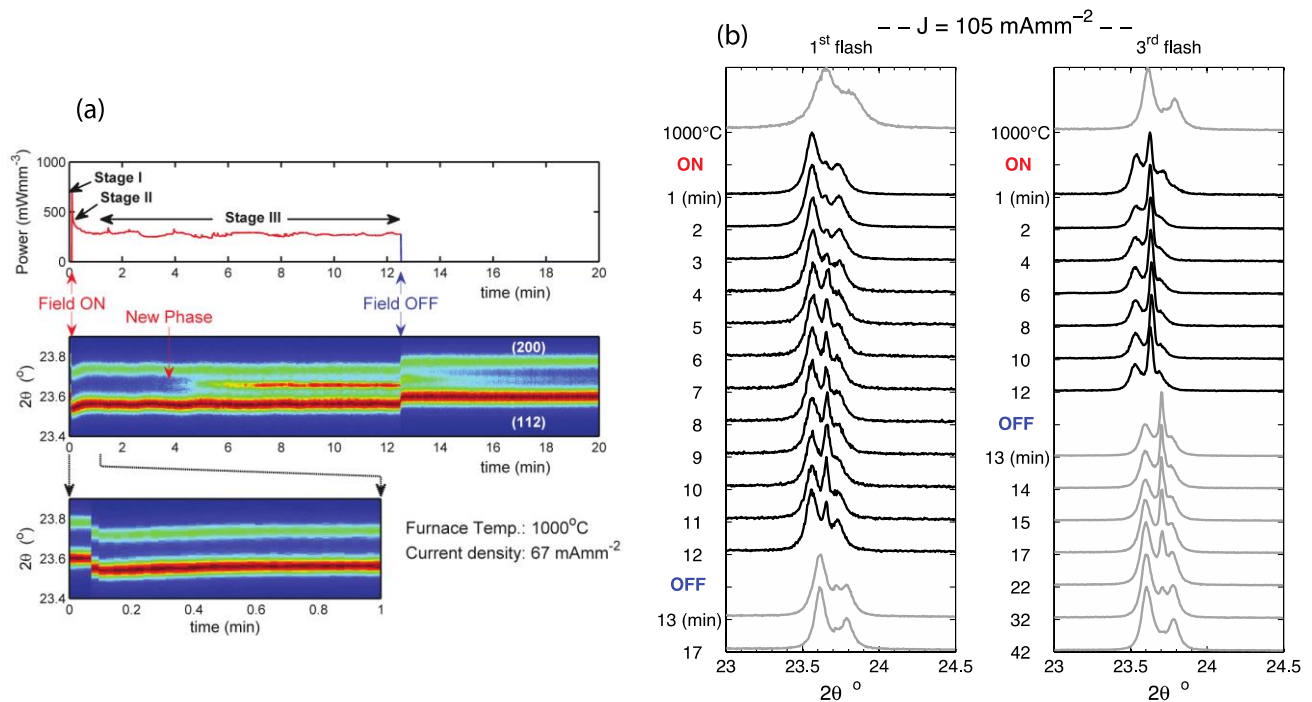


Fig. 4. Emergence and dissolution of a new phase during flash experiments with 3YSZ. (a) *In-situ* scans of (200) and (112) peaks showing the gradual development of a third peak lying midway between the parent peaks. This third peak gradually strengthens with time but then gradually dissolves when the field is turned off. The sudden shift in the peaks arises with the field being turned on and off due to Joule heating. (b) The emergence and extinction of the new peak with time with two sequential flashes in the same experiment. Note that the peak from the new phase gains in strength in the second flash, which is attributed to the presence of nuclei from the first flash. Note the complete extinction of the peak when the field is turned off. Experiments without the field but at the same specimen temperature as estimated from peak shifts do not show this third peak. Full scans of the diffraction pattern suggest that the new phase is a pseudo cubic form of yttria-stabilized zirconia.

## Future Plans

We are completely committed to the discovery of the underlying science of the defect avalanche induced by modest electrical fields at elevated temperature. The approach has three aspects, (i) measuring effects that further underpin the presence of a surge in defects including superplasticity and perhaps swelling as in radiation damage, (ii) continuation of *in-situ* experiments at APS especially concentrating on Stage II behavior, and (iii) creating models and ultimately first principles calculations that provide the underpinning for the defect physics.

**References:** [1.](#) Cologna, M., Rashkova, B., & Raj, R. (2010). Flash Sintering of Nanograin Zirconia in < 5 s at 850 C. *Journal of the American Ceramic Society*, 93(11), 3556-3559. [2.](#) Todd, R. I., Zapata-Solvas, E., Bonilla, R. S., Sneddon, T., & Wilshaw, P. R. (2015). Electrical characteristics of flash sintering: thermal runaway of Joule heating. *Journal of the European Ceramic Society*, 35(6), 1865-1877. [3.](#) Dong, Y., & Chen, I. (2015). Predicting the Onset of Flash Sintering. *Journal of the American Ceramic Society*, 98(8), 2333-2335. [4.](#) Naik, K. S., Sglavo, V. M., & Raj, R. (2014). Flash sintering as a nucleation phenomenon and a model thereof. *Journal of the European Ceramic Society*, 34(15), 4063-4067. [5.](#) Yu, L., & Zunger, A. (2014). A polarity-induced defect mechanism for conductivity and magnetism at polar-nonpolar oxide interfaces. *Nature communications*, 5. [6.](#) Raj, R. (2012). Joule heating during flash-sintering. *Journal of the European Ceramic Society*, 32(10), 2293-2301.

## Publications from January 01, 2014 to August 21, 2015

Pereira da Silva, J. G., Lebrun, J. M., Al-Qureshi, H. A., Janssen, R., & Raj, R. (2015). Temperature Distributions During Flash Sintering of 8% Yttria-Stabilized Zirconia. *Journal of the American Ceramic Society*.

Lebrun, J. M., & Raj, R. (2014). A first report of photoemission in experiments related to flash sintering. *Journal of the American Ceramic Society*, 97(8), 2427-2430.

Lebrun, J. M., Morrissey, T. G., Francis, J. S., Seymour, K. C., Kriven, W. M., & Raj, R. (2015). Emergence and Extinction of a New Phase During On–Off Experiments Related to Flash Sintering of 3YSZ. *Journal of the American Ceramic Society*.

Jha, S. K., & Raj, R. (2014). The effect of electric field on sintering and electrical conductivity of titania. *Journal of the American Ceramic Society*, 97(2), 527-534.

Jha, S. K., & Raj, R. (2014). Electric Fields Obviate Constrained Sintering. *Journal of the American Ceramic Society*, 97(10), 3103-3109.

Terauds, K., Lebrun, J. M., Lee, H. H., Jeon, T. Y., Lee, S. H., Je, J. H., & Raj, R. (2015). Electroluminescence and the measurement of temperature during Stage III of flash sintering experiments. *Journal of the European Ceramic Society*, 35(11), 3195-3199.

Naik, K. S., Sglavo, V. M., & Raj, R. (2014). Flash sintering as a nucleation phenomenon and a model thereof. *Journal of the European Ceramic Society*, 34(15), 4063-4067.

Raj, R., Cologna, M., Prette, A. L. G., Sglavo, V. M., & Francis, J. (2015). *U.S. Patent No. 8,940,220*. Washington, DC: U.S. Patent and Trademark Office.

Naik, K. S., Sglavo, V. M., & Raj, R. (2014). Field assisted sintering of ceramic constituted by alumina and yttria stabilized zirconia. *Journal of the European Ceramic Society*, 34(10), 2435-2442.

## Mechanical Behavior in Ceramics with Unusual Thermal-Mechanical Properties

Ivar Reimanis and Cristian Ciobanu  
Colorado School of Mines  
Golden, CO 80401

### Program Scope

The study of ceramics with unusual properties offers new insight into structure-property relations as well as promise for the design of novel composites. In this spirit, the PIs seek to

(i) understand fundamental mechanical phenomena in ceramics that exhibit pressure-induced phase transitions, negative coefficient of thermal expansion (CTE), and negative compressibility, and

(ii) explore the effect of these phenomena on the mechanical behavior of composites designed with such ceramics.

Focus is placed on framework silicates, for example  $\beta$ -eucryptite ( $\text{LiAlSiO}_4$ , Figure 1), where there has been significant interest recently to understand thermo-mechanical behavior [1-4]. The picture that has been emerging is that many properties, including thermal expansion, elastic behavior, pressure-induced response, and irradiation-induced amorphization, are controlled by the coordinated movement of the tetrahedral units making up the structure [5-11]. The studies have direct relevance to many applications ranging from transformation toughening to solid-state memory technology [12-14]. The broad and long-term goal is to utilize this insight to obtain desired mechanical responses.

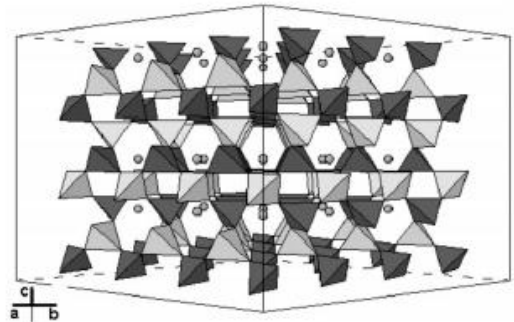


Figure 1. The crystal structure of  $\beta$ -eucryptite. The dark tetrahedra represent  $\text{SiO}_4$  and the light ones represent  $\text{AlO}_4$ . Li cations are represented by the small spheres. The view is parallel to  $[110]$ . [1]

Objectives include the following. (1) Perform fundamental physical property measurements on silicates that exhibit unusual thermal-mechanical properties, including eucryptite and orthopyroxene. (2) Develop atomistic level models that may be used to describe the above properties with the purpose of correlating structure and thermal and/or mechanical behavior. (3) Utilize the above results to develop models that may be used to predict the response of the above ceramics under mechanical and thermal stimulus and under irradiation conditions. These models are inherently multi-scale and incorporate cooperative effects of individual phenomena. Specifically, a descriptive model for utilizing a pressure induced phase transformation for toughness enhancement in ceramics is sought. (4) Verify experimentally the theoretical prediction that toughening is possible utilizing a pressure-induced phase transformation.

## Recent Progress

*In situ* x-ray diffraction experiments were performed at the Cornell High Energy Synchrotron Source (CHESS) to determine the crystal structure of the high pressure phase ( $\epsilon$ -eucryptite) that has been extensively characterized with indentation methods [7-9]. These results (Figure 2) were used to guide atomistic simulations, leading to the determination of the detailed crystal structure and space group of the high pressure phase  $\epsilon$ -eucryptite ( $\text{LiAlSiO}_4$ ), as well as the pathway of the pressure-induced phase transformation. The simulations were performed via a combination of path-search algorithms and metadynamics calculations. The phase transformation is best viewed by examining the relative motions of  $\text{SiO}_4$  and  $\text{AlO}_4$  tetrahedra (Figure 3).

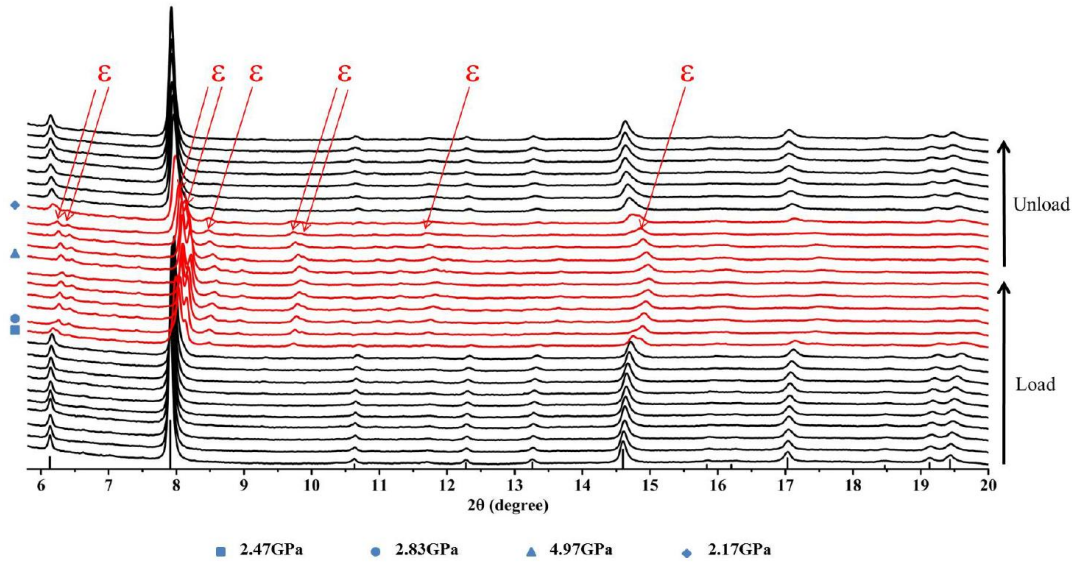


Figure 2. *In situ* diamond anvil cell x-ray diffraction results for eucryptite loaded and unloaded in a diamond anvil cell. The high pressure phase  $\epsilon$ -eucryptite is first observed at around 2.5 GPa. The crystal structure, lattice parameters, and space group were determined: these results will supersede the previous literature on structure determination of the high pressure phase.

The activation volume of the pressure-induced phase transformation has been shown to be on the order of the volume of a tetrahedral unit [9,10], and the present simulations (Figure 3) reveal the specific type of atomic-scale motion involved in effecting the transformation. The detailed structural information for the high-pressure phase along with an understanding of the transformation pathway enables the development of strategies to modify the tetrahedral movements during physical, thermal or electrical stimulation. Such alterations could be achieved by doping and are expected to manifest themselves in measurable properties such as the coefficient of thermal expansion or lithium ion conductivity.



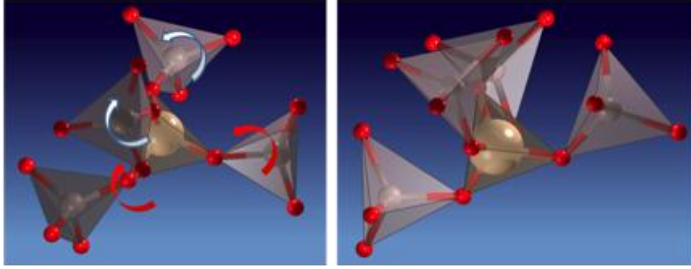


Figure 3. Partial structural units for  $\beta$ -eucryptite (left) and  $\epsilon$ -eucryptite (right), viewed along the  $c$ -axis. The purple tetrahedra are only guides to the eyes, to show the position and coordination of the Li ions that are "harbored" at their centers. The other tetrahedra are Si-centered (ball bulging through) or Al-centered. The high-pressure phase ( $\epsilon$ ) has a density 9.5% higher than that of the low-pressure phase ( $\beta$ ).

conductivity as a function of temperature (Figure 4) show that the activation energy (slope of the curve) depends on the specific temperature regime. It is hypothesized that the tetrahedral configurations which dictate the ion hopping within the one-dimensional,  $c$ -axis channels in the structure (Figure 1) exhibit distinct transitions that depend on temperature. Molecular dynamics simulations based the reactive force field developed in the group [15] are in progress to verify this.

### Future Plans

The results generated so far have inspired plans to pursue the design of silicate layered structures where the layer wavelength is on the order of a few tetrahedral structural units. Two general approaches that enable "knobs" for tuning material behavior are apparent: 1. ones that retain the structure, but modify slightly the dynamics of tetrahedral movement; and 2. ones that trigger phase transitions and therefore lead to dramatic behavior changes. Doping constitutes a direct approach for controlling properties: for example, preliminary simulations show that doping can open up Li diffusion pathways between  $c$ -axis channels, and leading to transition from anisotropic to isotropic Li transport. Research will focus on the uncovering the relationships between various thermo-physical-electrical behaviors and the movement of tetrahedral units in silicate structures, since a deeper understanding such relationships can lead to predictions and observations of novel phenomena that can appear in many other crystalline framework ceramics made of rigid-body units.

The detailed structural information for the high pressure phase and an understanding of the transformation pathway enables the development of strategies to modify the tetrahedral movements during physical, thermal or electrical stimulation. Such alterations could be achieved by doping and are expected to manifest themselves in measurable properties, such as the coefficient of thermal expansion and lithium ion conductivity.

Recent results on lithium ion

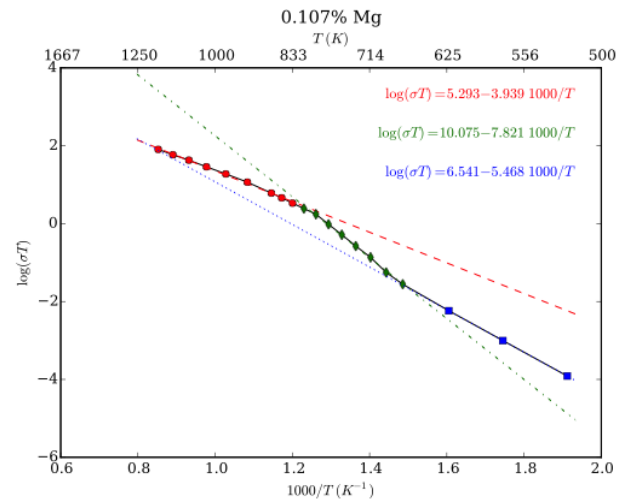


Figure 4. Lithium ion conductivity (measured by impedance spectroscopy) in  $\beta$ -eucryptite doped with a small amount of Mg. Three regimes, corresponding to three activation energies for Li diffusion are shown. Three different tetrahedral configurations are responsible for the change in activation energy.

## References

1. R. Sprengard, K. Binder, M. Brandle, U. Fotheringham, J. Sauer and W. Pannhorst, "On the Interpretation of the Experimental Raman Spectrum of  $\beta$ -Eucryptite  $\text{LiAlSiO}_4$  from Atomistic Computer Modeling", *J. Non-Cryst. Solids* 274, 264-270 (2000).
2. J. Zhang, Y. Zhao, H. Xu, M. V. Zelinskas, L. Wang, Y. Wang and T. Uchida, "Pressured-Induced Amorphization and Phase Transformations in  $\beta$ - $\text{LiAlSiO}_4$ ", *Chem. Mater.*, 17, 2817-2824 (2005).
3. B. Narayanan, I. E. Reimanis, E. R. Fuller Jr., C. V. Ciobanu, "Elastic constants of  $\beta$ -eucryptite : A density functional theory study", *Phys. Rev. B* 81, 104106 (2010).
4. I. E. Reimanis, C. Seick, K. Fitzpatrick, E. R. Fuller, and S. Landin, "Spontaneous Ejecta from  $\beta$ -Eucryptite Composites", *J. Am. Ceram. Soc.*, **90**[8] 2497-2501(2007).
5. H. Xu, P. J. Heaney, D. M. Yates, R. B. Von Dreele and M. A. Bourke, "Structural Mechanisms Underlying Near-Zero Thermal Expansion in  $\beta$ -Eucryptite: A Combined Synchrotron X-Ray and Neutron Rietveld Analysis", *J. Mater. Res.*, Vol. 14, No. 7 3138-3151 (1999).
6. S. Ramalingam and I. E. Reimanis, "Effect of Doping on the Thermal Expansion of  $\beta$ -eucryptite Prepared by Sol-Gel Methods", *Journal of the American Ceramic Society* . 95[9] 2939-2943, (2012).
7. T. Jochum, I. E. Reimanis, M. Lance and E. R. Fuller, "In-Situ Raman Indentation of Eucryptite: Characterization of the Pressure-Induced Phase Transformation", *J. Am. Ceram. Soc.* **92**[4] 857-863, (2009).
8. S. Ramalingam, I. E. Reimanis and C. Packard, "Determining Activation Volume for the Pressure-Induced Phase Transformation in  $\beta$ -Eucryptite Through Nanoindentation", *J. Am. Ceram. Soc.*, 95 [6] 2051-2058 (2012).
9. S. Ramalingam, C. Packard, and I. E. Reimanis, "In-situ Diamond Anvil Cell–Raman Spectroscopy and Nanoindentation Study of the Pressure-Induced Phase Transformation in Pure and Zinc-Doped  $\beta$ -eucryptite", *Journal of American Ceramic Society* 96[6] 1909-1915 (2013).
10. B. Narayanan, I. E. Reimanis, and C. V. Ciobanu, "Atomic-scale Mechanism for Pressure-induced Amorphization of  $\beta$ -eucryptite", *Journal of Applied Physics* 114, 083520 (2013). URL: <http://dx.doi.org/10.1063/1.4819452>
11. B. Narayanan, I. E. Reimanis, H. Huang, and C. V. Ciobanu, "Radiation Effects and Tolerance Mechanism in  $\beta$ -eucryptite", *Journal of Applied Physics* 113, 033504 (2013). URL: <http://link.aip.org/link/?JAP/113/033504>; DOI: 10.1063/1.4775838
12. Q. Williams and R. Jeanloz, "Spectroscopic Evidence for Pressure-Induced Coordination Changes in Silicate Glasses and Melts", *Science* 239, 902 (1988).
13. E. M. Stolper and T. J. Ahrens, "On the Nature of Pressure-Induced Coordination Changes in Silicate Melts and Glasses" *Geophysical Research Letters* 14, 1231 (1987).
14. R. J. Hemley, A. P. Jephcoat, H. K. Mao, L. C. Ming, and M. H. Manghnani, "Pressure-induced amorphization of crystalline silica", *Nature* (1988).
15. B. Narayanan, A. C. T. van Duin, B. B. Kappes, I. E. Reimanis and C. V. Ciobanu, "Reactive force field for lithium-aluminum silicates with applications to eucryptite phases", *Modelling and Simulation in Materials Science and Engineering*, 20, 1, 14 pages, (2012).

## Publications (2012-present)

1. S. Ramalingam, I. E. Reimanis, and C. Packard, "Determining Activation Volume for the Pressure-Induced Phase Transformation in  $\beta$ -eucryptite through Nanoindentation", *J. Amer. Ceram. Soc* 95[6] 2051-2058, (2012).
2. B. Narayanan, A. C. T. van Duin, B. B. Kappes, I. E. Reimanis and C. V. Ciobanu, "Reactive force field for lithium-aluminum silicates with applications to eucryptite phases", *Modelling and Simulation in Materials Science and Engineering*, 20, 1, 14 pages, (2012).
3. B. Narayanan, Y. Zhao, and C. V. Ciobanu, "Migration Mechanism for Atomic Hydrogen in Porous Materials", *Appl. Phys. Lett.* 100, 203901 (2012).
4. S. Ramalingam and I. E. Reimanis, "Effect of Doping on the Thermal Expansion of  $\beta$ -eucryptite Prepared by Sol-Gel Methods", *J. Am. Ceram. Soc.* 95[9] 2939-2943, (2012).
5. C. E. Packard, S. Ramalingam, I. E. Reimanis, "Indentation Study of the Pressure-Induced Phase Transformation in Beta-Eucryptite: a Candidate Material for New Transformation-Toughened Ceramics", International Symposium on Plasticity 2012 and its Current Applications Jan 3-8, 2012, San Juan, Puerto Rico.
6. B. Narayanan, I. E. Reimanis, H. Huang, and C. V. Ciobanu, "Radiation Effects and Tolerance Mechanism in  $\beta$ -eucryptite", *Journal of Applied Physics* 113, 033504 (2013). URL: <http://link.aip.org/link/?JAP/113/033504>; DOI: 10.1063/1.4775838
7. S. Ramalingam, C. Packard, and I. E. Reimanis, "In-situ Diamond Anvil Cell-Raman Spectroscopy and Nanoindentation Study of the Pressure-Induced Phase Transformation in Pure and Zinc-Doped  $\beta$ -eucryptite", *Journal of American Ceramic Society* 96[6] 1909-1915 (2013).
8. B. Narayanan, S.L. Weeks, B.N. Jariwala, B.Macco, J.W. Weber, S. Rathi, M.C.M. van de Sanden, P. Sutter, S. Agarwal, and C.V. Ciobanu, "Carbon monoxide-induced reduction and healing of graphene oxide" *Journal of Vacuum Science and Technology A (Letters)* 31, 040601 (2013).
9. B. Narayanan, I. E. Reimanis, and C. V. Ciobanu, "Atomic-scale Mechanism for Pressure-induced Amorphization of  $\beta$ -eucryptite", *Journal of Applied Physics* 114, 083520 (2013). URL: <http://dx.doi.org/10.1063/1.4819452>
10. Ivar E. Reimanis and Subra Ramalingam, "Near Zero Coefficient of Thermal Expansion Beta-Eucryptite Without Microcracking", U.S. Patent, 2013/0281282, (2013).1
11. B. B. Kappes and C. V. Ciobanu, "Materials Screening Through GPU Accelerated Topological Mapping", *Materials and Manufacturing Processes*, 30: 529:537 (2015).

<http://dx.doi.org/10.1080/10426914.2014.984215> DOI: 10.1080/10426914.2014.984215

12. D. Marhsall, R. F. Cook, N. P. Pature, M. L. Oyen, A. Pajares, J. E. Bradby, I. E. Reimanis, R. Tandon, T. F. Page, G. M. Pharr, and B. R. Lawn, "The Compelling Case for Indentation as a Functional Exploratory and Characterization Tool", in press in *Journal of American Ceramic Society* 98 (2015). DOI: 10.1111/jace.13729

# NanoMechanics: Elasticity and Friction in Nano-Objects

## Principal Investigator: Elisa Riedo

Advanced Science Research Center (ASRC) and City College New York, City University of New York, 85 St Nicholas Terrace, New York, New York 10031, USA

School of Physics, Georgia Institute of Technology, Atlanta, Georgia 30332-0430

## Program Scope

The scope of this research program is to understand, predict and manipulate the relationship between mechanical properties and size, chemistry and structure of matter with reduced dimensions, such as 1D and 2D materials.

## Recent Progress

### 2D Materials: Structure and Perpendicular Elasticity

Two-dimensional (2D) materials, such as graphene and MoS<sub>2</sub>, are few-atomic-layer thick films with strong in-plane bonds and weak interactions between the layers. The in-plane elasticity has been widely studied in bending experiments where a suspended film is deformed substantially; however, little is known about the films' elastic modulus perpendicular to the planes, as the measurement of the out-of-plane elasticity of supported 2D films requires indentation depths smaller than the films' interlayer distance. Here, we report on sub-Å-resolution indentation measurements of the perpendicular-to-the-plane elasticity of 2D materials. Our indentation data, combined with semi-analytical models and density functional theory are then used to study the perpendicular elasticity of a few-layers thick graphene and graphene oxide films. We find that the perpendicular Young's modulus of graphene oxide films reaches a maximum when one complete water layer is intercalated between the graphitic planes. This non-destructive methodology can map interlayer coupling and intercalation in 2D films. Recently, a large scientific and technological effort is underway to understand and control the properties of 2D materials because of their potential technological applications. The most studied 2D material is graphene, existing as a single layer of graphite or a few-layer thick epitaxial graphene film.

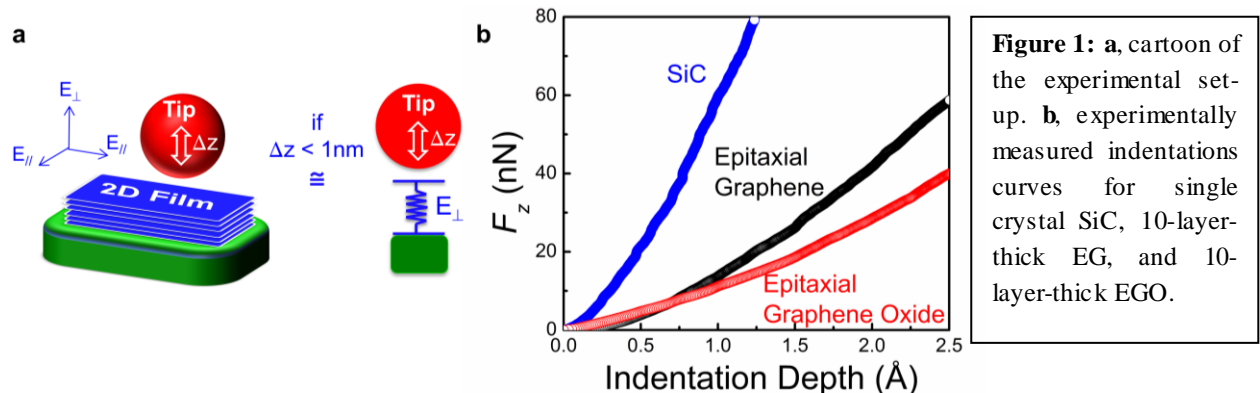


**Figure 1:** **a**, cartoon of the experimental setup. **b**, experimentally measured indentations curves for single crystal SiC, 10-layer-thick EG, and 10-layer-thick EGO.

Graphene possesses a large in-plane Young's modulus ( $\sim 1$  TPa) as well as high intrinsic carrier mobility and high in-plane thermal conductivity. Besides graphene, also 2D films of graphene oxide (GO), hexagonal Boron Nitride (h-BN) and transition metal dichalcogenides such as MoS<sub>2</sub> exhibit unique and excellent properties and hold great promise for nanotechnology applications. One of the main characteristics of 2D materials is the high anisotropy between the in-plane and perpendicular-to-the-plane properties. For example, in graphite due to the strong covalent bonds between atoms in the plane, and the weak Van der Waals interlayer interaction, the in-plane Young's modulus is  $E_{//} = 1$  TPa, while the interlayer perpendicular-to-the-plane Young's modulus is only  $E_{\perp} = 36$  GPa.

Recent studies have suggested that the mechanical properties of 2D materials are strongly correlated to their structure, and properties. The in-plane Young's modulus of exfoliated graphene and MoS<sub>2</sub> has been widely studied in bending experiments where a film is suspended on trenches or holes, and an AFM tip is used to bend the suspended film with deformations of tens and hundreds of nanometers. On the other hand, very little is known about the elasticity perpendicular to the planes, hereafter called perpendicular or interlayer elasticity, of 2D materials composed of very few atomic layers. Recent calculations have investigated the out-of-plane shear and Young's modulus of carbon nanotubes and graphene. Experimentally, resonance ultrasound spectroscopy was used to study the elastic constants and the anisotropy between the in-plane and perpendicular-to-the-plane directions of thin films. Investigations of the perpendicular-to-the-plane elasticity of a-few-layer-thick 2D films have not been reported, at the best of our knowledge, and remain an experimental challenge because they require to perform indentations on supported—as opposed to suspended—2D films where the indentation should remain smaller than the films interlayer distance, i.e., less than a few Angstroms. Nevertheless, the interlayer elastic coupling is particularly important since it is related to the thermal,

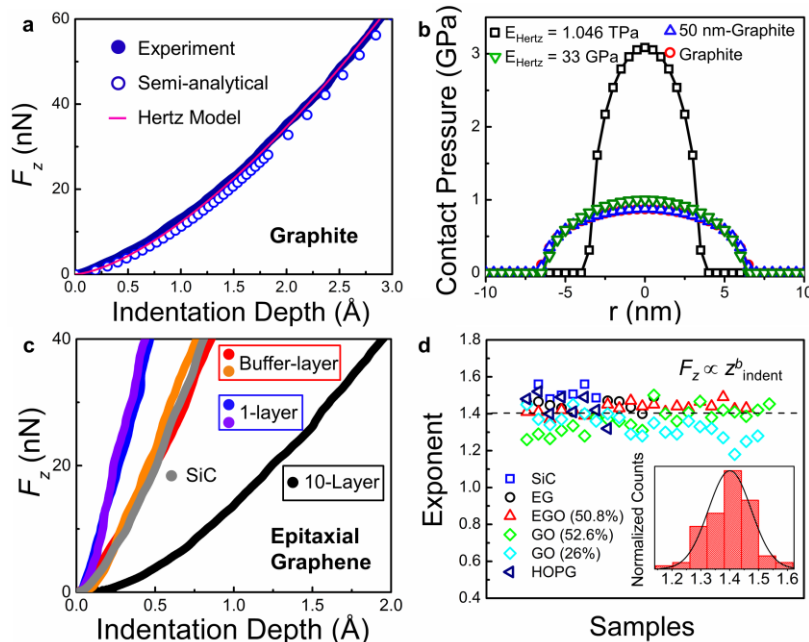


**Figure 3:** **a**, experimentally measured indentation curves in HOPG (full circles), semi-analytical model simulations of indentation in Graphite (open circles), and Hertzian fitting (continuum line) of the indentation curves on HOPG. **b**, contact pressure distribution profiles for Hertz contacts and SAM simulations. **c**, experimental indentation curves on 10-layer-thick Epitaxial Graphene (EG), 1-layer-thick EG, buffer layer EG, and SiC. **d**, statistical analysis of exponent number  $b$  in the fitting function  $F_z = C * z^b * \text{indent}^b$ .

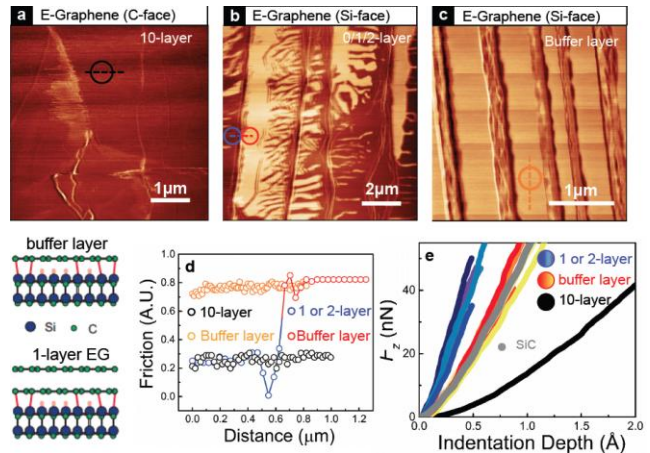


electronic, tribological, and optical properties of 2D films. The perpendicular elasticity is expected to be affected by the structure and chemistry of the layers, the presence of stacking and intrinsic defects, and intercalation, which is a critical process for doping and tuning mechanical and electronic properties in 2D films. Mapping the interlayer elastic coupling in 2D films is therefore an important technological and scientific advancement.

Here, an unconventional atomic force microscopy (AFM) based method allowing for sub-Å-resolution indentations coupled with a semi-analytical method (SAM) is used to measure the elasticity of 2D films in the direction perpendicular to the layers, for a number of layers as small as two (see Fig.1 and 2). This AFM based method is capable of maintaining an indentation depth smaller than the interlayer distance, with a resolution of 0.1 Å. We report on AFM-SAM investigations of the perpendicular elastic modulus of epitaxial graphene, epitaxial graphene oxide, and conventional graphene oxide films at varying ambient humidity. These studies, together with DFT calculations, highlight how the interlayer elastic coupling in graphene and graphene oxide films is affected by the films chemistry, structure, water intercalation, and number of layers. Interestingly, the perpendicular Young's modulus of graphene oxide increases by increasing the amount of water trapped in between the layers until a full monolayer is produced. Then, when the second water layer is forming the modulus decreases (Fig. 2). Finally, our studies show that when using sub-interlayer distance indentations in 2D films thicker than a few layers, the AFM indentation curves are very sensitive to the elastic modulus perpendicular to the layers,  $E_{\perp}$ , and almost independent of the value of the in-plane Young's modulus,  $E_{//}$  (see Fig. 3). As a consequence, the indentation force curves can be fitted with a simple modified Hertz model as if the film is an isotropic material, where the Young's modulus of the film is indeed the perpendicular modulus  $E_{\perp}$ . This work is therefore offering a new experimental and theoretical framework to investigate the interlayer elastic coupling in 2D films.

## Future Plans

In future we plan to continue our work on 2D materials. In particular we are working on single layer graphene and 1L MoS<sub>2</sub> grown epitaxially or by CVD on different substrates. Very interestingly (see Figure below here) we observe that 1L graphene has a stiffness much larger than SiC or the buffer layer, and quite astonishingly it is larger than the stiffness of diamond. Also, we have initiated a collaboration with Prof. David Cahill to study the relationship between thermal transport and elastic constants along the direction perpendicular to the planes of 2D films.



## Publications (period 2014-2015, DoE supported)

1. E. Albisetti, D. Petti, M. Bologna, P. Vavassori, E. Riedo and R. Bertacco “Designing unconventional magnetic meta-materials at the nanoscale”, submitted (2015)
2. "Imaging thermal conductivity with nanoscale resolution using a scanning spin probe", submitted (2015)
3. Yang Gao, Si Zhou, Suenne Kim, Hsian-Chih Chiu, Daniel Nélias, Claire Berger, Walt de Heer, Laura Polloni, Roman Sordan, Angelo Bongiorno and Elisa Riedo, “Elastic coupling between layers in two-dimensional materials”, **Nature Materials** 14, 714–721 (2015), DOI: 10.1038/nmat4322
4. Kyung Duk Koh, Hsian-Chih Chiu, Elisa Riedo and Francesca Storici “Measuring the elasticity of ribonucleotide(s)-containing DNA molecules using AFM”, book chapter in *Methods in Molecular Biology with the topic of RNA nanotechnology*, Springer Protocols, (2015)
5. Si Zhou, Suenne Kim, Emiliano Di Gennaro, Yike Hu, Cheng Gong, Chien-Yuan Chang, Xi Lu, Hsian-Chih Chiu, Claire Berger, Walt de Heer, Elisa Riedo, Yves J. Chabal, Carmela Aruta, and Angelo Bongiorno “Film Structure of Epitaxial Graphene Oxide on SiC: Insight on the Relationship Between Interlayer Spacing, Water Content, and Intralayer Structure”, **Advanced Materials Interfaces**, DOI: 10.1002/admi.201300106 (2014).
6. Ricardo Garcia, Armin Knoll, and Elisa Riedo “Advanced Scanning Probe Lithography”, **Nature Nanotechnology**, 9, 577 (2014) DOI: 10.1038/NNANO.2014.157.
7. Robert Szoszkiewicz and Elisa Riedo “Sliding Charges” *News & Views*, **Nature Materials**, 13, 666–668 (2014) DOI: 10.1038/nmat4020.
8. Hsian-Chih Chiu, Deborah Ortiz-Young, Elisa Riedo, “Nanorheology by atomic force microscopy”, **Review of Scientific Instruments**, 85 (12), 123707 (2014)
9. Hsian-Chih Chiu, Kyung Duk Koh, Marina Evich, Annie L. Lesiak, Markus W. Germann, Angelo Bongiorno, Elisa Riedo and Francesca Storici “How RNA intrusions change DNA structure and elastic properties”, **Nanoscale** 6 (17), 10009-10017 (2014) DOI: 10.1039/C4NR01794C.
10. Keith M. Carroll, Maitri Desai, Anthony J. Giordano, Jan Scrimgeour, William P. King, Elisa Riedo, and Jennifer E. Curtis “Speed Dependence of Thermochemical Nanolithography for Gray-Scale Patterning”, in press in **ChemPhysChem**, (2014) DOI: 10.1002/cphc.201402168.
11. Keith M. Carroll, Xi Lu, Suenne Kim, Yang Gao, Hoe-Joon Kim, Suhas Somnath, Laura Polloni, Roman Sordan, William P. King, Jennifer E. Curtis, Elisa Riedo “Parallelization of Thermochemical Nanolithography”, **Nanoscale** 6 (3), 1299 – 1304, (2014).



# Damage-Tolerant Structural Materials

Robert O. Ritchie, Mark Asta, Antoni P. Tomsia

Materials Sciences Division, Lawrence Berkeley National Laboratory, Berkeley, CA 94720

## Program Scope

The attainment of strength and toughness is a vital requirement for structural materials; unfortunately these properties are generally mutually exclusive. It is the lower strength, and hence tougher, materials that find use for most safety-critical applications where premature, or worse still catastrophic, fracture is unacceptable. Accordingly, the development of strong and tough materials has traditionally been a compromise between hardness *vs.* ductility. Using advanced metallic alloys, natural materials and biomimetic ceramics, we examine strategies to solve this “conflict”. We focus on the interplay between the individual mechanisms that contribute to strength and toughness, that of plasticity and crack-tip shielding, noting that these phenomena originate at very different structural length-scales. The lessons from Nature are particularly relevant here, as natural materials such as sea shells display unique combinations of mechanical properties that derive from architectures that span nano- to macro-scale dimensions with precisely engineered interfaces. Metallic glasses and single-phase high-entropy alloys can also display superb damage tolerance, but now seemingly with little structure. By focusing on mechanisms that permit *stable* cracking, we examine how the strength *vs.* toughness conflict can be solved to achieve unprecedented levels of damage-tolerance.

## Recent Progress

Our research is focused on experimental/theoretical efforts to probe the mechanics/mechanisms of deformation and fracture at multiple dimensions in structural materials. We look at materials modeled on natural hierarchical designs, but also at materials which have limited recognizable structure over most length-scales, specifically metallic glasses and high-entropy alloys. Our aim is to create new materials with unprecedented mechanical properties, specifically with damage tolerance.

An ability to undergo *limited* deformation is crucial for toughness as this enables the local dissipation of stresses which would otherwise cause fracture (Fig. 1a). Deformation mechanisms can be diverse; though dislocation plasticity in crystalline solids is most quoted, inelastic deformation can occur by the sliding of collagen fibrils in bone, frictional motion between mineral bricks in seashells, and by such mechanisms as microcracking in rocks and shear banding in glasses. The operative word here is *limited*; with too much deformability, toughness is lost. Toughness is thus a compromise, often of strength *vs.* ductility - two properties that are generally mutually exclusive – but it can be created without ductility<sup>13</sup>, as ceramics are not toughened by plasticity. Indeed, fracture is a mutual competition of intrinsic damage operating ahead of an incipient crack to promote its advance and extrinsic “shielding” mechanisms mostly behind the crack tip to inhibit it (Fig. 1b). *Intrinsic toughening* involves plasticity; *extrinsic toughening* involves mechanisms acting mainly in the crack wake to reduce the crack-tip stresses/strains, which results in R-curves where the crack-driving force must increase to maintain crack extension – a key to designing strong and tough materials.

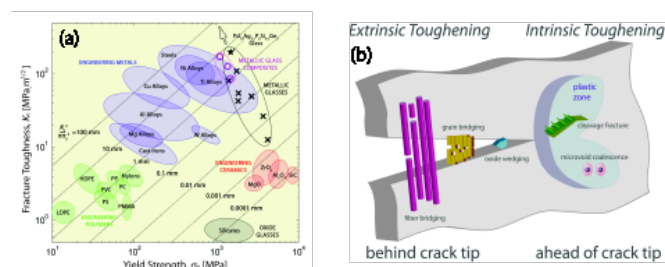


**Fig. 1.** (a) Ashby-plot showing strength-toughness relationships for various classes of materials. Diagonal lines show the plastic-zone size,  $K_c^2/\pi\sigma_y^2$ , where  $K_c$  is the fracture toughness,  $\sigma_y$  the yield strength. (b) Schematic illustration showing how fracture behavior can be considered in terms of intrinsic (plasticity) *vs.* extrinsic (shielding) toughening mechanisms associated with crack extension.

**Nature-inspired hierarchical materials:** Seashells are a prime example of Nature’s design for damage-tolerance, e.g., nacre which has a brick-and-mortar structure, with aragonite “bricks” separated by a biopolymer “mortar”. The mineral provides strength; limited slip in the compliant mortar dissipates high stresses, thereby conferring toughness. In early work, by freeze-casting  $\text{Al}_2\text{O}_3$  powders and infiltrating the resulting scaffolds with compliant PMMA, we made bulk, “brick-and-mortar”  $\text{Al}_2\text{O}_3$  in the image of nacre with remarkable toughness -  $K_c$  values exceeding  $30 \text{ MPa}\sqrt{\text{m}}$ .<sup>14</sup> Toughening involves crack deflection and crack bridging from brick “pull-out”, but with a myriad of other toughening mechanisms at play. Our theoretical efforts,<sup>10</sup> however, suggest that the strength and toughness properties of such nacre-like structures could be further enhanced through the use of higher strength mortars; accordingly, we have attempted to replace the polymeric compliant phase with a metallic mortar. Processing is now far more complex as metals do not readily wet ceramics, but we have been partially successful in developing lamellar alumina structures containing either a Zr-based metallic glass (BMG) or with Al-Si. Resulting toughness properties originate from a similar suite of toughening mechanisms but are higher than those of the equivalent ceramics structures with a polymeric compliant phase (Fig. 2). Unlike  $\text{Al}_2\text{O}_3/\text{PMMA}$ , however, we have yet to attain such materials with a high (>75-80%) volume fraction of the ceramic phase.

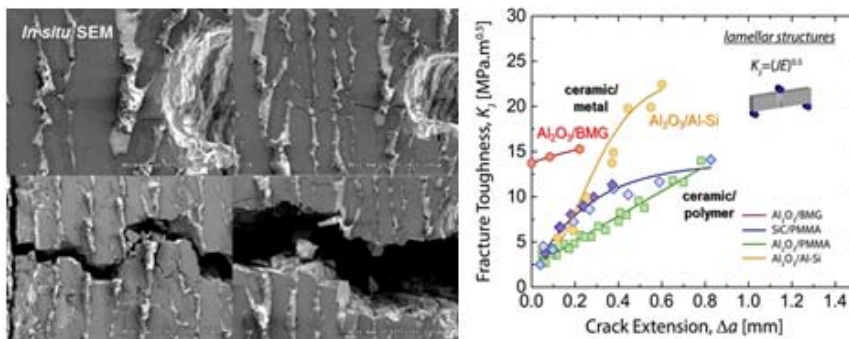


**Fig. 2.**  $\text{Al}_2\text{O}_3$  ceramics with a freeze-cast lamellar structure with metallic compliant phases. (left) Microstructures and crack paths for  $\text{Al}_2\text{O}_3$  with a Zr-based BMG, (right) resulting R-curves for  $\text{Al}_2\text{O}_3$ -BMG and for  $\text{Al}_2\text{O}_3$ -Al-Si, as compared to ceramics with a PMMA compliant phase.

We have also created freeze-cast SiC ceramics with a compliant phase,<sup>1,17</sup> and examined the influence of structural features, ceramic/polymer ratio, layer thickness, and presence of bridges between ceramic lamellae, on their mechanical performance. Our SiC/PMMA layered composites all showed increasing toughness with crack extension due to such extrinsic toughening mechanisms as crack bridging, inelastic deformation of ductile layers, lamellae pull out and ceramic bridge fracture. Resulting R-curves revealed  $K_c > 12 \text{ MPa}\sqrt{\text{m}}$  with stable crack growth at  $K > 18 \text{ MPa}\sqrt{\text{m}}$ , making these the toughest SiC ceramics to date; strength levels though were lower than in commercial SiC.

**Bulk metallic glasses:** BMGs are nominally brittle with  $\sim 1\text{-}2 \text{ GPa}$  strengths, yet by inducing multiple shear banding, we achieved a toughness of  $\sim 200 \text{ MPa}\sqrt{\text{m}}$  in a Pd-glass. Theoretical work has been initiated to probe structure-property relations in BMGs, with the goal of seeking how unique combinations of properties, such as those in Pd glass, may be understood by atomic-level structure. We have started atomistic computer simulation studies of the atomic order within second nearest-neighbor shells in BMGs, derived from atomic cluster connection schemes between linked coordination polyhedra.<sup>22</sup> Analyses show that cluster connections by face-sharing yield the stiffest elastic response during shear deformation, and are favored when changing from the liquid to glassy state. We have also examined the effect of hydrostatic pressure on glass formation,<sup>25</sup> and have found that  $\text{Cu}_{50}\text{Zr}_{50}$  glasses exhibit an anomalous structure-property relationship after removal of the pressure at room temperature; the glasses are less stable and display a lower shear modulus, despite having a denser packing structure, and a significant increase in full icosahedra short-range order.

**High-entropy alloys:** High-entropy alloys are an intriguing new class of metallic materials that derive their properties from multi-element systems that can crystallize as a single phase, despite

containing high concentrations of five or so elements with different crystal structures. We have examined high-entropy CrMnFeCoNi<sup>12</sup> and medium-entropy CrCoNi<sup>20</sup> single-phase fcc alloys and found exceptional strength/toughness properties which can further improve at cryogenic temperatures.

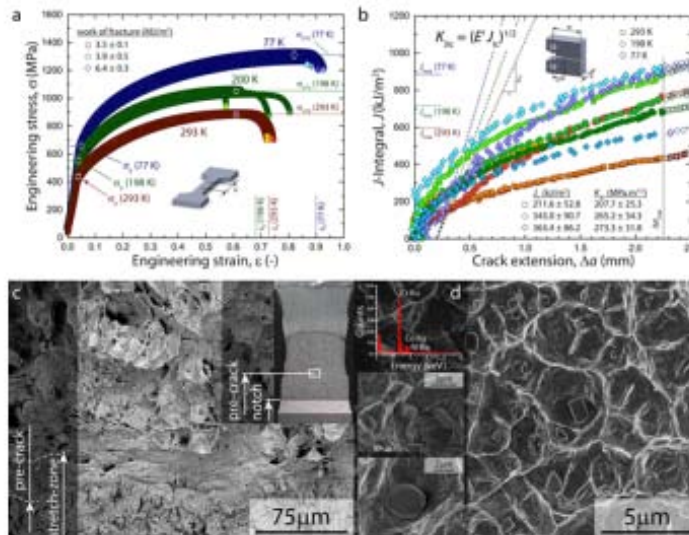


**Fig. 3.** Mechanical properties of CrCoNi medium-entropy alloy. (a) Tensile tests show a significant increase in yield strength,  $\sigma_y$ , tensile strength,  $\sigma_{UTS}$ , and strain to failure,  $\epsilon_f$ , with decreasing temperature from room temperature to cryogenic temperatures (200K & 77K). (b) Fracture toughness tests show an increasing fracture resistance with crack extension giving  $K_{Ic}$ , values of 208, 265 and 273 MPa $\sqrt{m}$  at 293, 198 and 77K, respectively. (c) Stereo microscopy and SEM images show a pronounced stretch-zone between the pre-crack and the fully ductile fracture region. (d) The fracture surface shows ductile dimpled fracture and Cr-rich particles that act as void initiation sites. (Data points shown are mean  $\pm$  SD; see Supplementary Information for exact values.)

To discern the salient atomistic to micro-scale mechanisms underlying these excellent properties, we used *in situ* mechanical loading in an aberration-corrected TEM to identify a unique synergy among multiple deformation mechanisms related to the low stacking fault energy and high friction stress of these alloys which we believe are rarely achieved in conventional alloys.<sup>24</sup> In particular, we find that cracking is impeded by the formation of twinned, nano-scale, fiber-like bridges which span the crack faces and act to delay fracture by shielding the crack tip, a mechanism that to our knowledge has not been reported before for a metallic alloy at the nano-scale. This synergism between plasticity-related intrinsic toughening and shielding-related extrinsic toughening provides a unique and effective means to enhance damage tolerance that is quite different from traditional strategies where secondary phases and hetero-interfaces are added to optimize strength and toughness of metallic alloys.

## Future Plans

Our approach will continue to focus on the development of materials with exceptional damage tolerance and with seeking the scientific mechanisms underlying such behavior at multiple (atomistic to macro) length-scales. With respect to **bioinspired hierarchical materials**, our future plans will be on the use of hard ceramics specifically now with compliant metallic additions to enhance high-temperature properties, which we will examine with *in situ* high-temperature x-ray microtomography. In the topic area of **bulk metallic glasses**, in addition to examining new alloys, including the corrosion fatigue properties of a new Ni-based glass, we intend to place an increasing emphasis on atomic-scale simulation studies to discern whether relationships can be deduced between the atomistic-scale short-range order in BMGs and specific macroscale properties, especially strength and toughness. Similarly, with **entropy alloys** we plan to search for new compositions which can provide excellent damage-tolerant properties, but more importantly to discern their mechanistic basis at nano- to micro-scales. In this regard, our recent work<sup>27</sup> has demonstrated the particular utility of *in situ* ultrahigh resolution TEM studies of crack-tip behavior, and our intent is now to expand the use of this technique to understanding fracture in a wider range of materials, including 2D materials such as graphene. To this end, we hope in the near future to be able to include Andy Minor as a co-PI in the program.

## Publications/References

1. V. Naglieri, H.A. Bale, B. Gludovatz, **A.P. Tomsia, R.O. Ritchie**, On the development of ice-templated silicon carbide scaffolds for nature-inspired structural materials, *Acta Mater.* 61; 2013: 6948-57.
2. W. Yang, I.H. Chen, B. Gludovatz, E.A. Zimmermann, **R.O. Ritchie**, M.A. Meyers, Natural flexible dermal armor, *Advanced Materials* 25; 2013: 31-48.
3. W. Yang, B. Gludovatz, E.A. Zimmermann, H.A. Bale, **R.O. Ritchie**, M.A. Meyers, Structure and fracture resistance of alligator gar (*tractosteus spatula*) armored fish scales, *Acta Biomater.* 9; 2013: 5876-89.
4. S.N. Raja, A.C.K. Olson, K. Thorkelsson, A.J. Luong, L. Hsueh, B. Gludovatz, G. Chang, J.J. Huang, J. Zhang, D. Jang, A.Y. Lu, **T. Xu, L. Lin, R.O. Ritchie, A.P. Ali visatos**, Tetrapod nanocrystals as fluorescent stress probes of electrospun nanocomposites, *Nano Letters* 13; 2013: 3915-22.
5. E.A. Zimmermann, B. Gludovatz, E. Schaible, N.K.N. Dave, W. Yang, M.A. Meyers, **R.O. Ritchie**, Mechanical adaptability of the Bouligand-type structure in natural dermal armor, *Nature Commu.* 4; 2013: 2634.
6. B. Gludovatz, M.D. Demetriou, M. Floyd, A. Hohenwarter, W. **R.O. Ritchie**, Enhanced fatigue endurance of metallic glasses through a “staircase-like” fracture mechanism, *PNAS* 110; 2013: 18419-24.
7. S.E. Naleway, R.B. Greene, B. Gludovatz, N.K.N. Dave, **R.O. Ritchie**, J.J. Kruzic, A highly fatigue resistant Zr-based bulk metallic glass, *Metall. Mater. Trans. A* 44A; 2013: 5688-93.
8. B. Delattre, H. Bai, **R.O. Ritchie**, J. De Coninck, **A.P. Tomsia**, Unidirectional freezing of ceramics suspensions: *In Situ* x-ray investigation of the effects of additives, *ACS Appl. Mater. Interfaces* 6; 2014: 159-66.
9. B. Gludovatz, S.E. Naleway, **R.O. Ritchie**, J.J. Kruzic, Size-dependent fracture toughness of bulk-metallic glasses, *Acta Mater.* 70; 2014: 198-207.
10. M. Genet, G. Couégnat, **A.P. Tomsia, R.O. Ritchie**, Scaling strength distributions in quasi-brittle materials from micro to macro scales: A computational approach to modeling nature-inspired structural ceramics, *J. Mech. Phys. Sol.* 68; 2014: 93-106.
11. W. Yang, V. Sherman, B. Gludovatz, M. Mackey, E.A. Zimmermann, E.H. Chang, E. Schaible, Z. Qin, M.J. Buehler, **R.O. Ritchie**, M.A. Meyers, Protective role of arapaima gigas fish scales: Structure and mechanical behavior, *Acta Biomater.* 10; 2014: 3599-614.
12. B. Gludovatz, A. Hohenwarter, D. Cartoor, E.H. Chang, **E.P. George, R.O. Ritchie**. A fracture resistant high-entropy alloy for cryogenic applications, *Science* 345 (6201); 2014: 1153-58.
13. **R.O. Ritchie**, In pursuit of damage tolerance in engineering & biological materials, *MRS Bull.* 39; 2014: 880-90.
14. U.G.K. Wegst, H. Bai, E. Saiz, **A.P. Tomsia, R.O. Ritchie**, Bioinspired structural materials, *Nature Mater.* 14; 2015: 23-36.
15. S.N. Raja, S. Basu, A.M. Limaye, T.J. Anderson, C.H. Hyland, L. Lin, **A.P. Ali visatos, R.O. Ritchie**, Strain-dependent dynamic mechanical properties of Kevlar to failure: Structural correlations and comparisons to other polymers, *Materials Today Comm.* 2; 2015: e33-37.
16. S.N. Raja, A.C.K. Olson, A.M. Limaye, K. Thorkelsson, A.J. Luong, L. Lin, **R.O. Ritchie, T. Xu, A.P. Ali visatos**, Influence of nanoparticle branching on the Young’s modulus of nanocomposites: Effect of interface orientation, *PNAS* 112; 2015: 6533-38.
17. V. Naglieri, B. Gludovatz, **A.P. Tomsia, R.O. Ritchie**, Developing strength and toughness in bio-inspired silicon carbide hybrid materials containing a compliant phase, *Acta Mater.* 98; 2015: 141-51.
18. B. Gludovatz, **E.P. George** and **R.O. Ritchie**, Processing, microstructure and mechanical properties of the CrMnFeCoNi high-entropy alloy, *J. Materials (JOM)* 67 (10); 2015.
19. H. Bai, Y. Chen, B. Delattre, **A.P. Tomsia, R.O. Ritchie**, Bioinspired large-scale aligned porous materials assembled with dual temperature gradients, *Science Advances*, in review June 2015.
20. B. Gludovatz, A. Hohenwarter, K.V.S. Thurston, H. Bei, Z. Wu, **E.P. George, R.O. Ritchie**, Exceptional damage-tolerance of a medium-entropy alloy CrCoNi at cryogenic temperatures, *Nature Commu.*, in review July 2015.
21. S.N. Raja, A.M. Limaye, A.J. Luong, K. Thorkelsson, W. Zhang, L. Lin, **R.O. Ritchie, A.P. Ali visatos**, Cavitation-induced stiffness reductions in quantum dot polymer nanocomposites, *Chemistry Mater.*, submitted July 2015.
22. J. Ding, E. Ma, **M. Asta, R.O. Ritchie**, Atomic order within the second nearest-neighbor shell in metallic glasses and liquids, *Scientific Reports*, in review July 2015.
23. A. Shekhawat, **R.O. Ritchie**, Strength and toughness of nanocrystalline graphene, *Nature*, submitted Aug. 2015.
24. Z.-J. Zhang, M.M. Mao, H. Tian, B. Gludovatz, Z. Zhang, S.X. Mao, **E.P. George, R.O. Ritchie**, Q. Yu, Nanoscale origins of the damage tolerance of the high-entropy alloy CrMnFeCoNi, *Nature Mater.*, in review Aug. 2015.
25. J. Ding, **M. Asta, R.O. Ritchie**, Anomalous structure-property relationships in metallic glasses through pressure-mediated glass formation, *Phys. Rev. Lett.*, submitted Aug. 2015.

**Doping Metallic Grain Boundaries to Control Atomic Structure and Damage Tolerance  
(DE-SC0014232, Project Period 07/2015 – 07/2020)**

**Timothy J. Rupert  
Department of Mechanical and Aerospace Engineering  
Department of Chemical Engineering and Materials Science  
University of California, Irvine**

**Program Scope**

Grain boundaries and other interfaces often act as nucleation sites for cracks and voids that lead to failure during plastic deformation of metallic materials. While it is known that interface character and structural state can greatly influence this damage nucleation process, the current level of understanding and control over such details is relatively limited. The objective of this research is to obtain a fundamental understanding of how grain boundary structure can be controlled by locally and selectively adding other elements, with the idea of inducing planned grain boundary phases or *complexions* for desired behavior. The effect of complexion structure on dislocation accommodation mechanisms will also be studied, to improve the field's understanding of damage nucleation at interfaces and identify materials design strategies for extremely tough materials. This research will use a combination of cutting-edge computational, experimental, and characterization techniques to isolate and understand the importance of atomic grain boundary structure as well as interfacial chemistry. The fundamental insights provided by this research will enable the creation of advanced engineering metals with improved damage tolerance.

**Recent Progress**

This project is very new, starting July 15, 2015, but significant progress has been made towards the computational tasks. A main goal of this project is to uncover the processing conditions that will allow materials scientists to access a variety of grain boundary structures. We need to explore a wide range of alloy chemistries, temperatures, and boundary characters, but collection of this vast dataset experimentally would be restrictively time consuming. Therefore, in the spirit of recent integrated computational materials engineering (ICME) efforts, we have been using high throughput atomistic modeling techniques to identify processing conditions which are promising for the formation of interesting transitions in grain boundary structure.

We began by exploring interfacial complexion transitions in Cu-Zr, a system chosen because it should be able to access amorphous complexions based on theoretical considerations and our preliminary observations in nanocrystalline alloys. Atomistic simulation with molecular dynamics (MD) alone is not appropriate for modeling how grain boundary structure changes with doping and temperature, because diffusion is dramatically limited in MD due to the short time scales which can be accessed. Therefore, we are using a hybrid Monte Carlo (MC)/MD

technique recently developed by Sadigh et al. [1] to simulate structural transformation in different grain boundaries. Among our primary concerns is understanding how grain boundary character affects complexion transition behavior, in addition to observing general trends in the formation of various complexions. Six bicrystals of pure Cu were used as starting configurations, to access a range of different misorientation angles, grain boundary planes, and thus grain boundary energies. For each boundary, global composition and temperature were varied and equilibrium grain boundary structure was calculated. Figure 1 shows an example for a  $\Sigma 5$  (013) grain boundary, where a transition from single layer doping to nanoscale amorphous intergranular films (AIFs) occurs through a gradual transition region, where some sections of the interface remain ordered while others are amorphous. Such plots for different boundaries allow the thermodynamics of complexion transitions to be analyzed in detail.

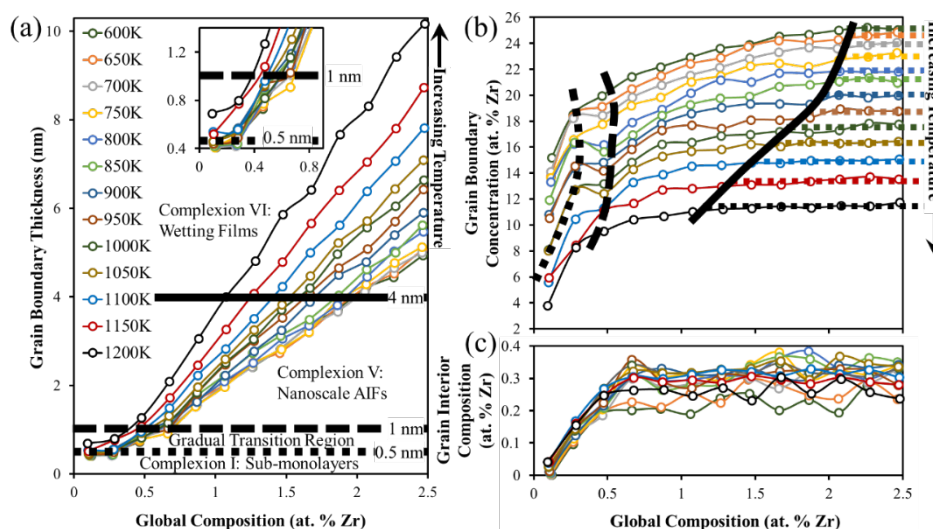


Figure 1. (a) Grain boundary thickness, (b) grain boundary concentration, and (c) grain interior composition for the sample containing  $\Sigma 5$  (013) grain boundaries as a function of global composition for different doping temperatures, indicating a gradual disordering transition. The thick dotted, dashed, and solid lines (b) mark the boundaries between ordered grain boundary, gradual transition region, nanoscale amorphous intergranular film, and wetting film. The corresponding thick lines in (a) mark the approximate grain boundary thickness at the boundaries. Horizontal dotted lines in (b) mark the equilibrium grain boundary concentration of the wetting film formed at respective temperatures.

One important, unexpected finding has been that the ordered complexion a boundary first sees (single layer, bilayer, or multilayer) depends strongly on the starting grain boundary structure. For example, while a  $\Sigma 5$  (013) boundary forms single segregation layers due to the presence of high energy atomic sites in the repeating structural units, a  $\Sigma 11$  (113) boundary has a multilayer segregation pattern due to its local structure. This variety is shown in Figure 2(a), where Zr dopants are shown as blue atoms. This concept fits with a very recent paper from Frolov et al, who reported that a  $\Sigma 5$  boundary in Cu-Ag can experience either single layer or bilayer segregation based on whether a single or double kite structure exists prior to doping [2]. Another important finding is that not all boundary types can form nanoscale AIFs, the type of disordered complexion that is in thermodynamic equilibrium. Some interfaces skip this and transform directly to wetting films, a bulk phase. Finally, we observe that grain boundary energy is not a



perfect indicator of a boundary's tendency to disorder, as was previously thought. Instead, the tendency to disorder is more closely connected to the relative solute excess, as shown in Figure 2(b). This work has been detailed in a manuscript that is under review.

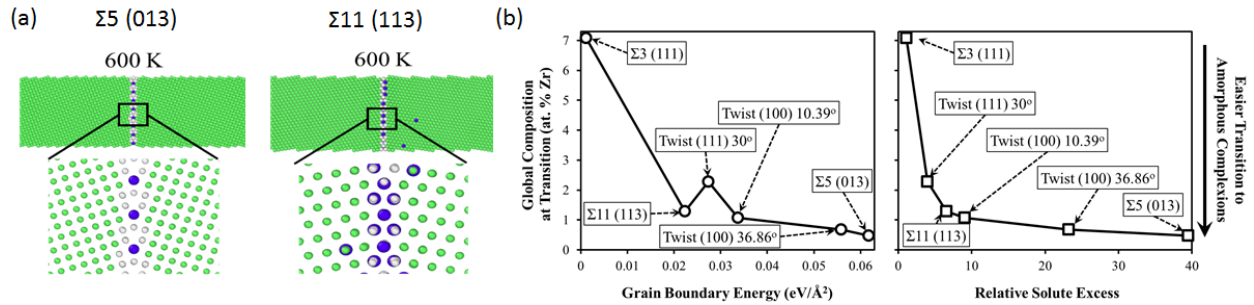


Figure 2. (a) Ordered complexes in two different grain boundaries at 600 K show that starting structure is important for doping configuration. (b) Global composition at transition at 1200 K as a function of grain boundary energy and relative solute excess (the ratio of grain boundary concentration over grain interior composition) which gives a more consistent behavior and is more indicative of the propensity of segregation-induced disordering transitions.

While the main focus of this project is mechanical behavior, we believe that certain complexes may also be beneficial for increasing the radiation tolerance of materials. MD simulations were used to explore the effect of interfacial structure on residual radiation damage. An ordered grain boundary was compared to a disordered amorphous intergranular film, to investigate how interface thickness and free volume impacts point defect recombination. The collision cascades induced by ion bombardment were simulated and residual point defect populations analyzed as a function of boundary type and primary knock on atom energy. While ordered grain boundaries easily absorb interstitials, these interfaces are inefficient vacancy sinks. Alternatively, amorphous intergranular films act as ultra-efficient, unbiased defect sinks, providing a path for the creation of radiation-tolerant materials. Figure 3 shows a tabulation of data from these simulations.

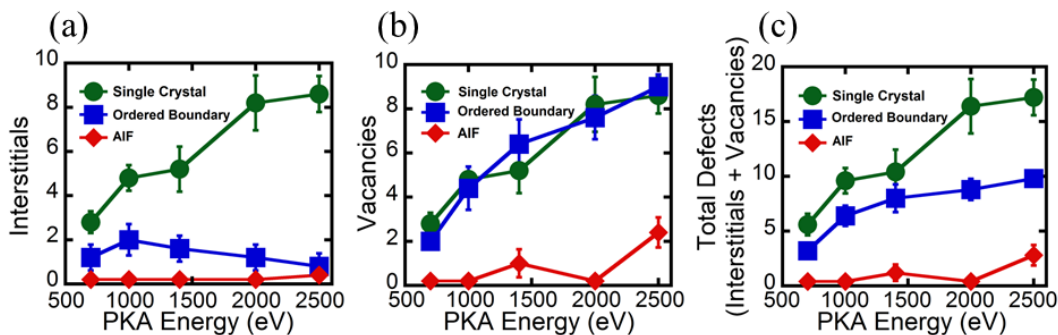


Figure 3. The number of residual (a) interstitials, (b) vacancies, and (c) total defects as a function of PKA energy. The  $\Sigma 5$  (310) boundary preferentially absorbs interstitials, but the AIF acts as a superior, unbiased sink.

### Future Plans

The atomistic simulations mentioned above are providing guidelines for the creation of real materials with different grain boundary complexion states. Co-sputtering is being used to create Cu-Zr, Cu-Nb, and Cu-Ta alloys with various chemical compositions and low impurity levels.

Deposition will be carried out at elevated temperature to promote the formation of large columnar grains with diameters of at least a few hundred nanometers with well-defined GBs, to aid characterization and mechanical testing. For each alloy, we will explore a range of compositions, but strongly focus on the solvent-rich end of the spectrum. Site-specific transmission electron microscopy (TEM) specimens will be taken from promising boundaries for detailed characterization of atomic structure, local chemistry, complexion type, etc. Nanoindentation will then be used to probe damage resistance. During nanoindentation, “pop-ins,” or large load-displacement excursions, are a signature of the transmission of dislocation activity. We will tabulate such activity and quantify the effect of different boundaries on the load required for pop-ins. However, since we are mainly interested in the atomic details of grain boundary-dislocation interactions in this project, we will also follow nanoindentation near a boundary with additional TEM investigation from site-specific samples. We will capture both the dislocation network associated with the indentation deformation and the structural details of the grain boundary.

Additional computational tasks will also be pursued. Although we have promising results from the Cu-Zr, we will continue to extend the MC/MD work to the Cu-Nb and Cu-Ta systems. These alloys are less likely to be able to sustain amorphous intergranular films, so we expect them to be insightful for lower level complexions that are more ordered. In addition, we will study dislocation absorption and crack nucleation, using a technique developed in two of our recent papers [3, 4]. Metrics we are interested in include the number of dislocations that can be accommodated before crack nucleation, the evolution of local stress over time, and the details of slip transfer into the second grain. Our results will then be rationalized with atomistic measurements of structure (grain boundary thickness, boundary energy, free volume, local stress, etc.) as well as continuum theories that predict damage (boundary misorientation, line tension theory, fracture initiation parameter, etc.) to gain a more clear understanding of what grain boundary features are most important for damage resistance.

## References

- [1] Sadigh B, Erhart P, Stukowski A, Caro A, Martinez E, Zepeda-Ruiz L. Scalable parallel Monte Carlo algorithm for atomistic simulations of precipitation in alloys. *Phys. Rev. B* 2012;85.
- [2] Frolov T, Asta M, Mishin Y. Segregation-induced phase transformations in grain boundaries. *Phys. Rev. B* 2015;92:020103.
- [3] Pan Z, Rupert TJ. Damage nucleation from repeated dislocation absorption at a grain boundary. *Computational Materials Science* 2014;93:206.
- [4] Pan Z, Rupert TJ. Amorphous intergranular films as toughening structural features. *Acta Mater.* 2015;89:205.

## Publications

- Ludy JE, Rupert TJ. “Amorphous intergranular films act as ultra-efficient point defect sinks during collision cascades,” *Scripta Materialia*, (2015) In Press.



- Pan Z, Rupert TJ. “Effect of grain boundary character on segregation-induced interface structural transitions,” *Submitted*.

## **Deformation Mechanisms at Grain Boundaries in Polycrystals**

**Michael D. Sangid, Purdue University**

**Samantha Daly, University of Michigan**

### **Program Scope**

The objective of this research is to characterize the role of dislocation slip and grain boundary sliding in polycrystalline deformation, which is known to be centrally important but is not fully understood. Mechanisms of deformation in a polycrystalline aggregate include slip within grains, transfer of slip across grains, twinning, and sliding of the grain boundaries; however, little is known about the interactions between these mechanisms during plastic deformation. Without accounting for the coupling between these mechanisms, predictions of mechanical behavior can be largely inaccurate compared with experiment. This predictive uncertainty results in the overdesign of components, posing a major barrier to lightweighting and energy efficiency. There is a critical need to investigate the interactions between multiple deformation mechanisms and their effect on macroscopic material behavior; this is particularly true in the context of dislocation slip at/across grain boundaries (GBs) and in grain boundary sliding. It is known that GBs play a complex and important role in polycrystalline deformation, as they store a large amount of strain/energy/damage. Coupled deformation mechanisms (synergistic and competing) that occur at GBs are a primary source of the fundamental strain incompatibilities that occur during plastic deformation, and play a large role in material response. By viewing deformation mechanisms as coupled processes, rather than independent, this research will significantly extend our understanding of polycrystalline deformation at the mesoscale and improve predictive modeling.

Typically, constitutive theories for hardening and plastic flow during deformation in alloys account for slip and GB sliding as isolated phenomena, whereas here we will determine their coupling through an integrated modeling/experimental approach. We will address fundamental theories of plasticity in polycrystalline materials at ambient and elevated temperatures during monotonic and low cycle fatigue loading at the mesoscale. The central hypothesis under examination is that slip at/near GBs and grain boundary sliding are coupled, synergistic processes. The rationale for this premise is that an increase in the shear stress on a GB (necessary for GB sliding to occur) decreases the energy barrier for slip transmission through the GB. To test this central hypothesis, the following specific scientific aims will be targeted:

- I. Identify the interactions of slip/sliding deformation mechanisms based on local stress states.
- II. Relate stress state and associated slip/sliding deformation mechanisms to damage and crack formation.

### III. Correlate slip/sliding mechanisms and damage/cracking to microstructural attributes.

The collaborative effort is a close integration between microstructure-based modeling and high resolution, microscale experiments that uniquely capture full-field deformations at the same length scale as the model. The outcome of this work will be an understanding of the interactions between slip and GB sliding as competitive or synergistic processes, depending on the complex 3D stress state of the system and on the local microstructural features. Coupled deformation mechanisms will be related to the propensity to form damage and cracks within the material. The results will lead to a more accurate description of deformation characteristics and the ability to predict material behavior with higher confidence. The fundamental relationships discovered in this research will be leveraged in analytical tools to reduce component overdesign and new material design frameworks, which will have far reaching implications for lightweighting and other energy applications.

#### Recent Progress

Since the project start date was July 15 2015, research is in the ramp up phase. Fortunately, the Sangid and Daly groups both have established graduate researchers on this project and anticipate significant strides in the research within the first year.

For the crystal plasticity modeling efforts, the graduate student is becoming familiar with existing crystal plasticity models developed within the Sangid group. Simplifications are taken by using existing 3D microstructures (random texture with an assumed grain size distribution - Fig. 1) as the model input and accounting for only crystallographic slip, on the 12 FCC slip systems, as governed by the following constitutive relationship:

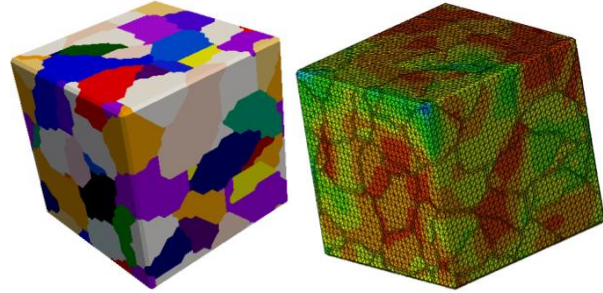


Figure 1. Example microstructure realization as an input into the crystal plasticity model and view of strain accumulation after loading.

$$\dot{\epsilon}_{slip}^{pl}(\mathbf{x}) = \dot{\gamma}_{slip}^0 \sum_{\alpha=1}^N \mathbf{M}^{\alpha}(\mathbf{x}) \left[ \frac{|\mathbf{M}^{\alpha}(\mathbf{x}) : \boldsymbol{\sigma}(\mathbf{x})| - \chi^{\alpha}(\mathbf{x})}{\tau_{0,slip}^{\alpha}(\mathbf{x})} \right]^n \text{sgn}(\mathbf{M}^{\alpha}(\mathbf{x}) : \boldsymbol{\sigma}(\mathbf{x}) - \chi^{\alpha}(\mathbf{x}))$$

where  $N$  is the number of slip systems;  $\tau_{0,slip}^{\alpha}(\mathbf{x})$ ,  $\chi^{\alpha}(\mathbf{x})$ , and  $\mathbf{M}^{\alpha}(\mathbf{x})$  are the critical resolved shear stress (CRSS), backstress, and the symmetric Schmid tensor associated with the slip system  $\alpha$  at each spatial point,  $\mathbf{x}$  (representing a 3D space);  $\dot{\epsilon}_{slip}^{pl}(\mathbf{x})$  and  $\boldsymbol{\sigma}(\mathbf{x})$  are the strain-rate and stress tensors at each spatial position;  $\dot{\gamma}_{slip}^0$  is a normalization factor; and  $n$  is the rate-sensitivity exponent. For the simulation results shown in Fig. 1, the material is loaded to 2% strain and the effective strain is plotted.

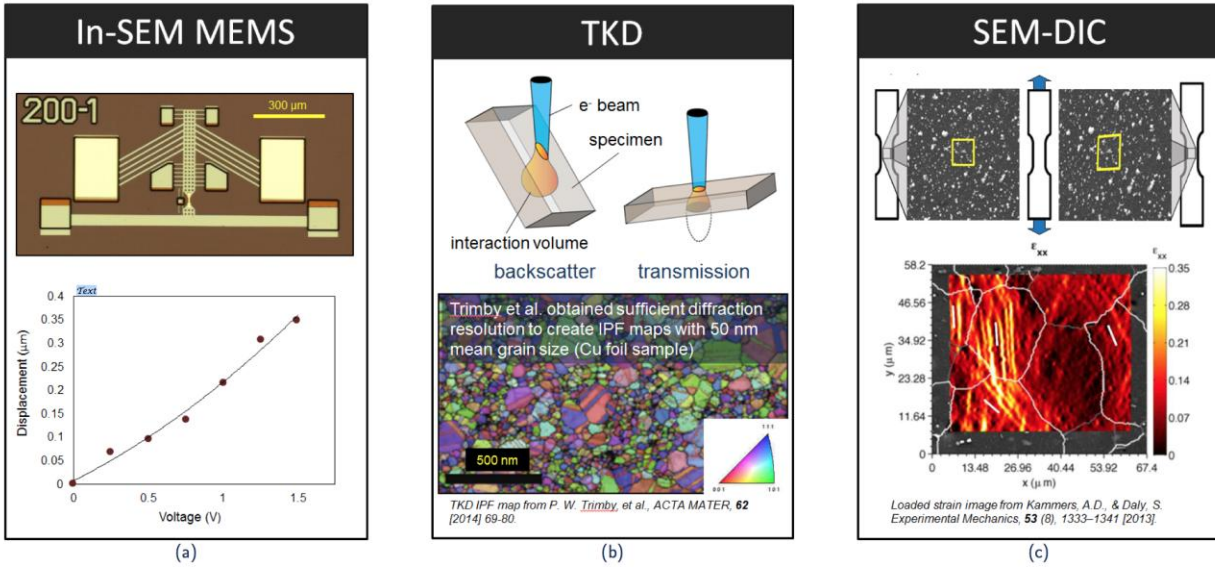


Figure 2. (a) (top) Thermal actuator used for applying tensile load to specimen. Chevron beams are joule heated when voltage is applied and the shuttle is pushed forward due to beam geometry and thermal expansion. Actuator displacement linearly increases with voltage (bottom). (b) TKD is similar to EBSD; the sample is held at an opposite angle with respect to the CCD to collect transmitted  $e^-$ s. Transmitted electrons are diffracted from a much smaller interaction volume than backscattered  $e^-$ s (top), making TKD better suited for thinner ( $\sim 10$ -300 nm) specimens. (c) A speckle pattern (top) is created on the sample surface by chemically attaching Au nanoparticles. A series of SEM micrographs of the sample surface are obtained during loading. By tracking the movement of speckle subsets with DIC, a full-field strain map (bottom) can be captured with high spatial resolution.

The experimental approach uses the novel integration of three distinct techniques in order to create a new and comprehensive approach towards thin film material characterization. Here, (1) in-SEM MEMS using thermal actuator-based sample loading is combined with (2) Transmission Kikuchi Diffraction (TKD) to collect through thickness grain orientation and (3) distortion-corrected SEM-DIC in order to map full-field strains on the length scale of the microstructure. The first revision of the MEMS device (Figure 2a - top) has been designed and fabricated, and is currently being improved upon for the second revision. The device was shown to be active and working, and we have been able to characterize and demonstrate linear change in actuator displacement with voltage (Figure 2a - bottom). Currently, we are working on combining Transmission Kikuchi Diffraction (TKD) with the in-SEM MEMS actuation – TKD was chosen because transmitted electrons are diffracted from a much smaller interaction volume than backscattered, making it better suited for thinner ( $\sim 10$ -300 nm) samples (Figure 2b). Finally, a combination of distortion-corrected digital image correlation (DIC) and scanning electron microscopy (SEM), here termed SEM-DIC, will be utilized by tracking nanoparticles that are self-assembled on the sample surface using a chemical functionalization developed by the Daly group (Figure 2c - top) (Kammers and Daly, Exp Mech, 2013). By tracking the movement of

speckle subsets with DIC and correcting for distortions inherent in SEM imaging, a full-field strain map (Figure 2c – bottom) can be captured with high spatial resolution.

### Future Plans

This project is in its initial stages, and therefore future plans are in line with the project objectives. On the modeling side, initial plans are threefold. First, with an existing user material subroutine (UMAT) for crystal plasticity within a finite element framework, we will calibrate the model for Al (as the microstructure and stress-strain response is characterized and measured from the Daly group), taking

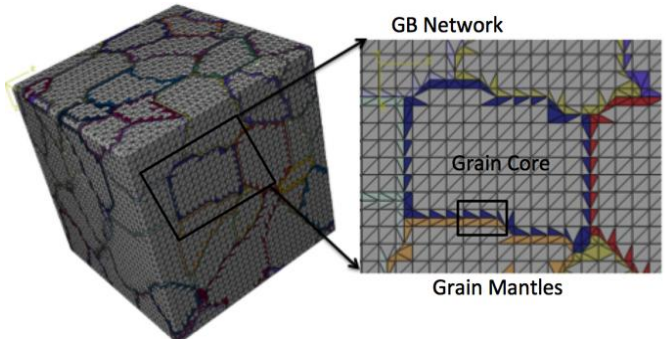


Figure 3. The microstructure is split into core and mantle regions, each displaying their own constitutive relationships.

into account crystal slip as the only deformation mechanism accommodating plastic strain. Next, we build a generic workflow to automate the creation of representative volume elements separating regions in grain cores and grain boundary mantles, defining separate material types (i.e. flow rules and hardening laws) to each of these regions, as shown in Fig. 3. Third, the existing UMAT will be generalized to include deformation of GB sliding at the mantle regions.

For the experimental aspects, near future plans focus on the successful integration of the three experimental techniques described above. Specific focus is currently on upgrading the MEMS device, integrating TKD with the in-SEM MEMS testing, and determining the correct parameters for deposition and annealing of thin films with sufficiently large through-thickness grains. We are making solid progress on these fronts. When these have been achieved, the next step will be to capture full-field deformations and underlying (through-thickness) crystallographic information of these thin films under a range of testing conditions and work in tandem with the modeling efforts. Additional analysis of experimental results will be performed using unsupervised learning methods currently being developed by the Daly group, in order to identify critical features of microstructural neighborhoods that cause similarities in the way in which strain clusters.

### References

Kammers AD, Daly S. Self-assembled nanoparticle surface patterning for digital image correlation in a scanning electron microscope. *Experimental Mechanics* 53(8): 1333-1341, 2013.

### Publications

None yet; the project started July 15 2015.

# Using Artificial Microstructures to Measure Fracture Toughness in Metallic Glasses and their Cellular Structures and Composites

Jan Schroers, Yale University

## Program Scope

The research activity of this proposal is based on a unique materials characterization strategy which we have developed during the previous project. This so-called Artificial Microstructures (AM) strategy allows us to overcome aspects of the grand challenge in Materials Science, to study microstructure-property relationships. Typically microstructural features are interdependent, and hence prevent or make a systematic study of microstructure-property relationship very difficult. Through AM we can completely manipulate those features separately and characterize the effect on properties. AM fabrication is based on a two-step method (Fig.1). In the first step, the mold is fabricated which is subsequently replicated in the second step through thermoplastic forming (TPF) into a bulk metallic glass (BMG).

Within the previous funded DOE project, we have developed this technique and used it as a toolbox to characterize microstructure-property relationships in cellular materials [1]. The focus of this funding period is to use AM to study fracture toughness of metallic glasses. Within the current project, our focus is on understanding the microstructure-property in monolithic materials such as BMGs. Here, most sensitive to processing conditions is fracture toughness.

Understanding this relationship is critical for a fundamental understanding of glasses in their vast range of structures, and how those different structural states mechanically behave and how these states can be experimentally realized through processing. From a technological point of view, this project identifies conditions under which metallic glasses can be processed without deteriorating their properties.

## Recent Progress

Precise measurements of BMGs' toughness have been proven to be challenging with concerning scatter [2]. For example, toughness values ranging from  $\sim 16$  to  $\sim 130 \text{ MPa} \sqrt{\text{m}}$  have been reported for  $\text{Zr}_{41.2}\text{Ti}_{12.5}\text{Cu}_{10}\text{Ni}_{10}\text{Be}_{22.5}$  BMG [3-7]. Our AM method can potentially reduce

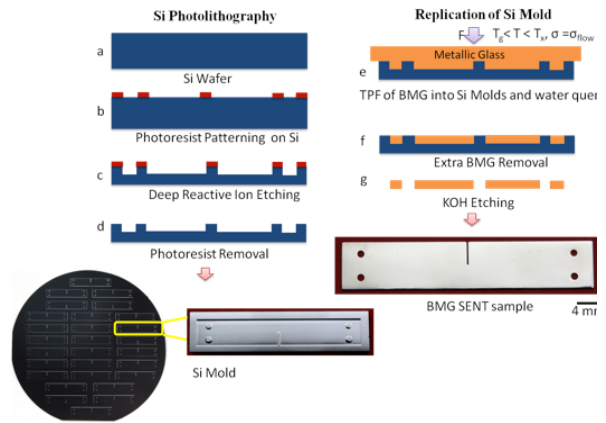


Figure 1: Schematic illustration of the fabrication method of Artificial Microstructures, here BMG single edge notched tension (SENT) samples. Using Si lithography and deep reactive ion etching, Si molds are fabricated (a - d). Thermoplastic molding is employed to replicate the mold into the BMG (e - g).



difficulties in fabricating precise notches, different cooling rates, casting defects, and compositional fluctuations during vitrification [2], and hence eliminate extrinsic contributions to reveal intrinsic behavior of BMGs. In order to test the potential of AM to eliminate or at least drastically reduce the extrinsic contributions we fabricated 20 “identical” BMG single edge notched tension (SENT) samples. We considered a representative, medium-tough and well studied Zr-based BMG,  $Zr_{44}Ti_{11}Cu_{10}Ni_{10}Be_{25}$ . Through our approach, we repeatedly prepared 20 SENT samples under the same processing conditions, and conducted fracture toughness test for each specimen to evaluate the scatter.

A representative  $\sigma - \varepsilon$  curve associated with the corresponding plastic zone development events are shown in Fig. 2. The measured notch toughness  $K_Q$  of all tested 20 specimens are summarized in Fig. 3. Overall,  $K_Q$  ranges from 105 to 114  $MPa \sqrt{m}$ , with an average value of  $(K_Q)_{avg} = 109 MPa \sqrt{m}$ , and a standard deviation of  $\sigma(K_Q) = 3 MPa \sqrt{m}$ . The scatter in  $K_Q$  is comparable to the behavior in conventional crystalline metals such as a 1200 °C Austenitized AISI 4340 steel that exhibited  $K_{Ic} \approx 67 \sim 73 MPa \sqrt{m}$  [8]. Our measured toughness scatter is two orders of magnitude lower than the previously reported scatter for BMGs [2]. We attribute the observed minute scatter of  $K_Q$  in this work as an intrinsic behavior of BMGs which in the past has been overshadowed by extrinsic sample preparation methods.

We also explored this AM technology to investigate the flaw tolerance behavior of BMGs. Mechanistically, flaw tolerance has been associated with an intrinsic length scale set by the microstructure. A representative material class that is microstructurally featureless are bulk metallic glasses (BMGs). Therefore, it has been generally accepted that apparent toughness continuously decreases with increasing crack acuity in BMGs. Surprisingly we found that notch toughness in BMGs decreases apparently with decreasing  $\rho$  until a critical value,  $\rho_c$  (Fig. 4). Below  $\rho_c$ , notch toughness is independent of  $\rho$ , suggesting a flaw tolerance behavior of BMGs. We explain such flaw tolerance by a critical stress controlled fracture where  $\rho_c$  is defined by a

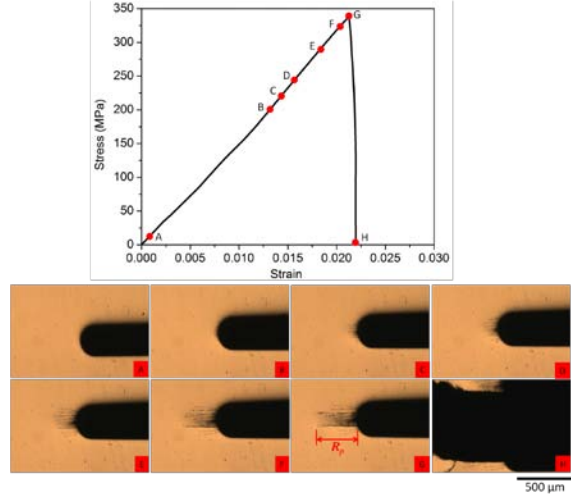


Figure 2: A representative  $\sigma - \varepsilon$  curve associated with the sequential plastic process zone development.

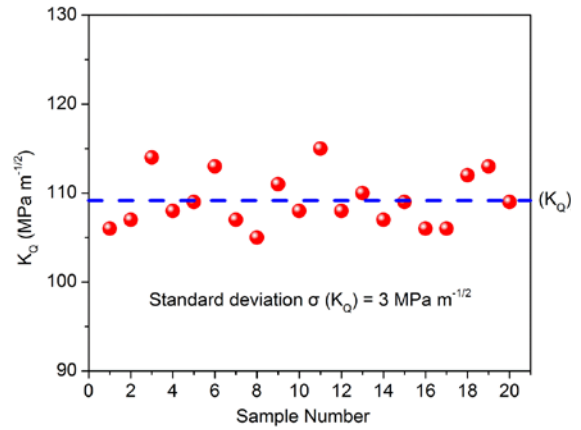


Figure 3: Measured notch toughness  $K_Q$  and plastic zone size  $R_p$  of all the tested 20 specimens. An average notch toughness of  $(K_Q)_{avg} = 109 MPa \sqrt{m}$  with a standard deviation of  $\sigma(K_Q) = 3 MPa \sqrt{m}$  is measured.

critical plastic zone associated with the BMGs' inherent crack tip blunting capability. The specific characteristic distance and ability to blunt cracks up to the specific  $\rho_c$  vary widely among BMGs which rationalizes the vast variety in their fracture behavior and suggest specific flaw tolerance. Our finding is encouraging for BMGs' structural applications since flaws smaller than  $\rho_c$  are increasingly difficult to avoid but are “indistinguishable” in their influence to the fracture toughness.

### Future Plans

Uncontrolled partial crystallization has been identified as a mechanism which can drastically deteriorate BMGs' mechanical properties. Due to the metastable nature of BMGs, crystallization can occur during liquid cooling or thermoplastic forming (TPF), and complete avoidance has been proven difficult [9-12]. For the majority of BMG forming alloys, partially crystallization has been shown to degrade properties [13-16]. To date, a quantitative understanding of the effect of partial crystallization of metallic glass forming alloys on the fracture toughness and hence a mechanistic understanding is lacking.

Within this project, we propose to study the effect of the crystallized volume fraction (crystallinity) formed during devitrification on the fracture toughness and aim to develop a mechanistic model that can describe this mechanism. For representative BMGs we will consider  $Zr_{44}Ti_{11}Cu_{10}Ni_{10}Be_{25}$  (Zr-BMG) and  $Pd_{43}Cu_{27}Ni_{10}P_{20}$  (Pd-BMG) as BMGs with a high (Zr-BMG) and low (Pd-BMG) critical fictive temperature [17]. We aim to precisely introduce crystallization and determine its effect on the fracture toughness.

### References

1. Chen, W., et al., *Flaw tolerance vs. performance: A tradeoff in metallic glass cellular structures*. Acta Materialia, 2014. **73**: p. 259-274.
2. Xu, J., U. Ramamurty, and E. Ma, *The fracture toughness of bulk metallic glasses*. Jom, 2010. **62**(4): p. 10-18.
3. Conner, R.D., et al., *Fracture toughness determination for a beryllium-bearing bulk metallic glass*. Scripta Materialia, 1997. **37**(9): p. 1373-1378.
4. Flores, K.M. and R.H. Dauskardt, *Enhanced toughness due to stable crack tip damage zones in bulk metallic glass*. Scripta Materialia, 1999. **41**(9): p. 937-943.
5. Gilbert, C., V. Schroeder, and R. Ritchie, *Mechanisms for fracture and fatigue-crack propagation in a bulk metallic glass*. Metallurgical and Materials Transactions A, 1999. **30**(7): p. 1739-1753.
6. Lowhaphandu, P. and J.J. Lewandowski, *Fracture toughness and notched toughness of bulk amorphous alloy: Zr-Ti-Ni-Cu-Be*. Scripta Materialia, 1998. **38**(12): p. 1811-1817.

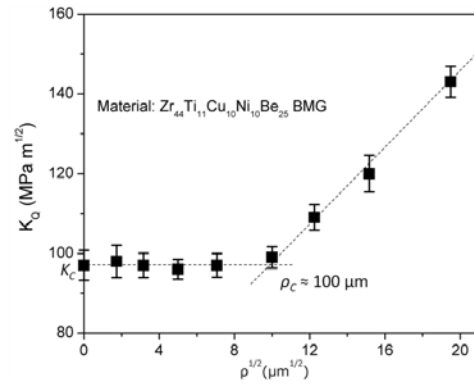


Figure 4: Notch radius dependence of notch toughness ( $K_Q$ ) of  $Zr_{44}Ti_{11}Cu_{10}Ni_{10}Be_{25}$  BMGs. A specific critical radius of  $\rho_c \approx 100 \mu\text{m}$  is found for  $Zr_{44}Ti_{11}Cu_{10}Ni_{10}Be_{25}$ . Above  $\rho_c$ ,  $K_Q$  scales linearly with  $\rho^{1/2}$ . Below  $\rho_c$ ,  $K_Q$  is independent of  $\rho$ .



7. Suh, D. and R.H. Dauskardt, *Effects of open-volume regions on relaxation time scales and fracture behavior of a Zr–Ti–Ni–Cu–Be bulk metallic glass*. Journal of non-crystalline solids, 2003. **317**(1): p. 181-186.
8. Ritchie, R.O., B. Francis, and W.L. Server, *Evaluation of toughness in AISI 4340 alloy steel austenitized at low and high temperatures*. Metallurgical Transactions A, 1976. **7**(6): p. 831-838.
9. Johnson, W.L., *Bulk Glass-Forming Metallic Alloys: Science and Technology*. MRS Bulletin, 1999. **24**(10): p. 42-56.
10. Schroers, J., *Processing of bulk metallic glass*. Adv Mater, 2010. **22**(14): p. 1566-97.
11. Shen, Y.T., L.Q. Xing, and K.F. Kelton, *Formation and crystallization of ZrCuTi metallic glasses*. Philosophical Magazine, 2005. **85**(31): p. 3673-3682.
12. Kelton, K.F., et al., *Mechanisms for nanocrystal formation in metallic glasses*. Journal of Non-Crystalline Solids, 2003. **317**(1–2): p. 71-77.
13. Gilbert, C.J., R.O. Ritchie, and W.L. Johnson, *Fracture toughness and fatigue-crack propagation in a Zr–Ti–Ni–Cu–Be bulk metallic glass*. Applied Physics Letters, 1997. **71**(4): p. 476.
14. Song, M., et al., *The effect of annealing on the mechanical properties of a ZrAlNiCu metallic glass*. Journal of Non-Crystalline Solids, 2011. **357**(3): p. 1239-1241.
15. Lund, A.C. and C.A. Schuh, *Critical length scales for the deformation of amorphous metals containing nanocrystals*. Philosophical Magazine Letters, 2007. **87**(8): p. 603-611.
16. Fan, C.L., Chunfei; Inoue, Akihisa; Haas, Volker, *Deformation behavior of Zr-based bulk nanocrystalline amorphous alloys*. Physical Review B, 2000. **61**(6).
17. Kumar, G., et al., *Critical Fictive Temperature for ductility in metallic glasses*. Nature Communications, 2013. **4**: p. 1536.

## **Publications**

1. W. Chen, Z. Liu, J. Schroers, *Joining of bulk metallic glasses in air*. Acta Materialia 62, 49-57 (2014).
2. W. Chen, Z. Liu, H.M. Robinson, J. Schroers, *Flaw tolerance vs. performance: A tradeoff in metallic glass cellular structures*. Acta Materialia 73, 259-274 (2014).
3. W. Chen, J. Ketkaew, Z. Liu, R.M.O. Mota, K. O'Brien, C.S. da Silva, J. Schroers, *Does the fracture toughness of bulk metallic glasses scatter?* Scripta Materialia 107, 1-4 (2015).
4. P. Bordeenithikasem, S. Sohn, Z. Liu, J. Schroers, *Protocols for multi-step thermoplastic processing of metallic glasses*. Scripta Materialia 104, 56-59 (2015).

## Deformed Materials: Towards a Theory of Materials Morphology Dynamics

James P. Sethna, Physics Department, Cornell University

### Program Scope

Our program's traditional focus has been on statistical models of fracture and on cell boundary structure in plastically deformed metals. Our fracture work has culminated [1,3] in a quantitative scaling theory of precursor events in disordered systems. The power-law fracture precursors observed in materials like bone and seashells are seen to be crossover effects in finite-size systems between a strong-disordered percolation fixed point and nucleated fracture events (Figure 1). Our work on continuum plasticity, resting on sophisticated simulations of a shock-forming PDE for the Nye dislocation density tensor, manifests a scaling morphology that reproduces the experimental behavior analyzed both by fractal [R1] and non-fractal [R2] methods, and has been analyzed within a renormalization-group framework [2]. Our recent continuum dislocation work has focused on idiosyncrasies in the numerical methods available for solving such PDEs [5], which frustrate efforts to incorporate material-specific laws for boundary migration.

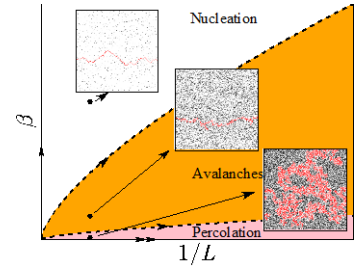


Figure 1. Phase diagram for disordered, brittle material

### Recent Progress

The complex cell boundary microstructures [2,R1,R2] and the striking dislocation avalanche scaling behavior seen in ice and micropillars [R3] inspire us to broadening our efforts to understand plastic deformation microstructure, both with direct theoretical efforts and in collaborations with experimental colleagues (attendee Papanikolaou and Dimiduk [R3], and Julia Greer and Karin Dahmen on micropillars, and Itai Cohen on colloids (Figure 2). We have been invited by Richard LeSar to write a review article on analogies between plastic yield and deformation in other systems (jamming, self-organized critical behavior, etc.) Even more broadly, we have recently developed a simulation of the evolution of one-dimensional crystals (smectic liquid crystals), whose focal conic microstructure has hitherto escaped computational scrutiny (Figure 3).

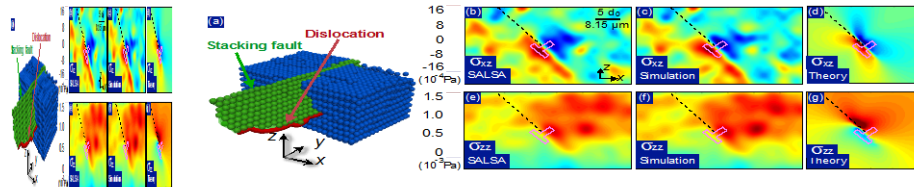


Figure 2. SALSA evaluation of stress fields around a colloidal dislocation.

### Future Plans

We intend to leverage our work on the review article to build bridges between three communities: those engaged in the engineering of plastic deformation of crystalline materials (slip systems, dislocation dynamics, etc.), physicists using renormalization-group and scaling methods to study scale-invariant microstructure and dynamics other materials (crackling noise in

magnets [R4], jamming of granular materials and glassy systems [R5]), and mathematical engineers using minimizing sequences to study martensitic and other microstructures. In particular, our recent simulations of smectic liquids (with attendee Danilo Liarte) have inspired a wonderful generalization of the theory of martensites – with crystalline variants becoming cyclides of Dupin parameterized by the relativistic Lorentz group, and conical ruled surfaces replacing twin boundaries (Figure 3).

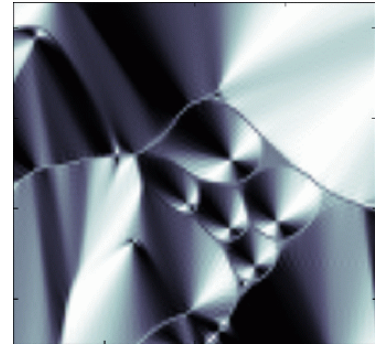


Figure 3. Simulated focal conic microstructure of smectic liquid

## References

- [R1] D.A. Hughes, Q. Liu, D.C. Chrzan, N. Hansen, *Scaling of microstructural parameters: misorientations of deformation induced boundaries*, Acta Mater., 45 (1997), pp. 105–112.
- [R2] M. Zaiser, K. Bay, P. Hähner, *Fractal analysis of deformation-induced dislocation patterns*, Acta Mater., 47 (1999), pp. 2463–2476.
- [R3] *Quasi-periodic events in crystal plasticity and the self-organized avalanche oscillator*, Stefanos Papanikolaou, Dennis M. Dimiduk, Woosong Choi, James P. Sethna, Michael D. Uchic, Christopher F. Woodward, and Stefano Zapperi, Nature **490**, 517-521 (2012).

## Publications

- [1] *From damage percolation to crack nucleation through finite size criticality*, Ashivni Shekhawat, Stefano Zapperi, and James P. Sethna, Physical Review Letters **110**, 185505 (2013). (Editor's choice for a viewpoint, The Breaking of Brittle Materials by Elisabeth Bouchaud.)
- [2] *Scaling theory of continuum dislocation dynamics: Self-organized critical pattern formation*, Yong S. Chen, Woosong Choi, Stefanos Papanikolaou, and James P. Sethna, International Journal of Plasticity **46**, 94-129 (2013).
- [3] *Fracture strength: Stress concentration, extreme value statistics and the fate of the Weibull distribution*, Zolt Bertalan, Ashivni Shekhawat, James P. Sethna, and Stefano Zapperi, Phys. Rev. Applied, 09/2014, Volume 2, p.034008, (2014).
- [4] *Visualization, coarsening and flow dynamics of focal conic domains in simulated Smectic-A liquid crystals*, Liarte, Danilo B., Bierbaum Matthew, Zhang Muxin, Leahy Brian D., Cohen Itai, and Sethna James P. , (submitted 2014).
- [5] *"Irregularization" of Systems of Conservation Laws*, Hunter Swan, Woosong Choi, Stefanos Papanikolaou, Matthew Bierbaum, Yong S. Chen, James P. Sethna (submitted).

## Radiation Response of Low Dimensional Carbon Systems

Lin Shao

Department of Nuclear Engineering and Department of Materials Science and Engineering  
Texas A&M University  
College Station, TX 777843

### Program Scope

The project is aimed at understanding the fundamentals of radiation response of low dimensional carbon systems and irradiation-induced property changes, with a focus on the unique phenomena caused by their geometry, boundary, and quantum size effects. Materials of key interest include graphene, carbon nanotubes (CNTs), CNT films, and CNT embedded composites.

### Recent Progress

We applied quantum mechanics calculations to understand atomic scale details of C atom displacement creation under electron and ion irradiation. In addition to the stress and curvature effect on displacing atoms, we considered Mott scattering, charge screening effects, thermal vibration of target atoms, and interactions with nearest neighboring atoms. The mechanism for atom displacement is complicated: thermal vibration can greatly reduce the displacement threshold energy ( $T_d$ ). Furthermore,  $T_d$  is very sensitive to neighboring atom configurations. For the middle wall of a multi-walled carbon nanotube (MWCNTs), both inward and outward displacements are influenced by the presence of the inner and outer tube walls. For the outermost and innermost tubes, the lack of atom interactions make their displacement creation and sputtering much easier.

The above modeling considerations find good agreement with experimental observations. For example, we studied radiation tolerance of individual graphene layers in self-suspended few-layer graphene (Fig. 1) and found the outermost and innermost layers are more easily damaged under electron beam irradiation. Fig. 1a illustrates the atomic configurations of the graphene edge after rolling. The rolled graphene layers result in strong electronic potentials lines, with a line separation distance equal to the closest distance between rolled graphene planes. This results in increased scattering contrast, enabling imaging of graphene planes. Fig. 1b is the simulated TEM image, showing that the rolled edge contributes to visible parallel lines after interference. Fig. 1c is the same structure after introducing damage cascades, which clearly shows the distortion of the lines of atoms due to displacements.

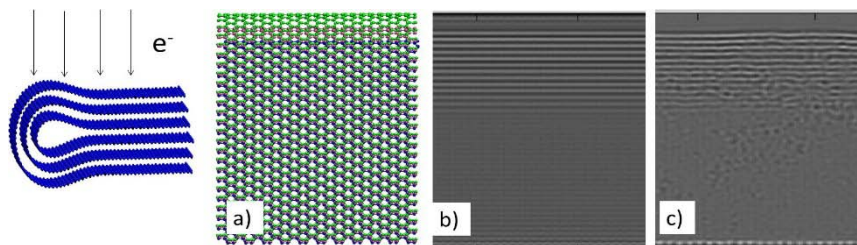


Fig. 1 (a) Atomic configurations of few-layer graphene with a rolled edge, (b) simulated TEM images without radiation damage, and (c) with radiation damage.

Fig. 2A(a-c) shows the bright-field TEM images and corresponding diffraction patterns of graphene edges as a function of 200 keV electron irradiation fluences. Fig. 2B is the corresponding two dimensional intensity mapping. With increasing electron fluence, the diffraction patterns evolve from a matrix of sharp white spots into diffusive rings, caused by

transition of ordered structures to amorphous-like, disordered structures. Fig. 2B(a) shows the intensity changes of major diffraction spots as a function of electron fluences. The intensity drops and saturates to a constant value at high fluences. Fig. 2B(b) shows the spot size changes. The original sharp spots become wider (black line) and evolve into flattened signals (red line). The transition point represents threshold fluence for amorphization.

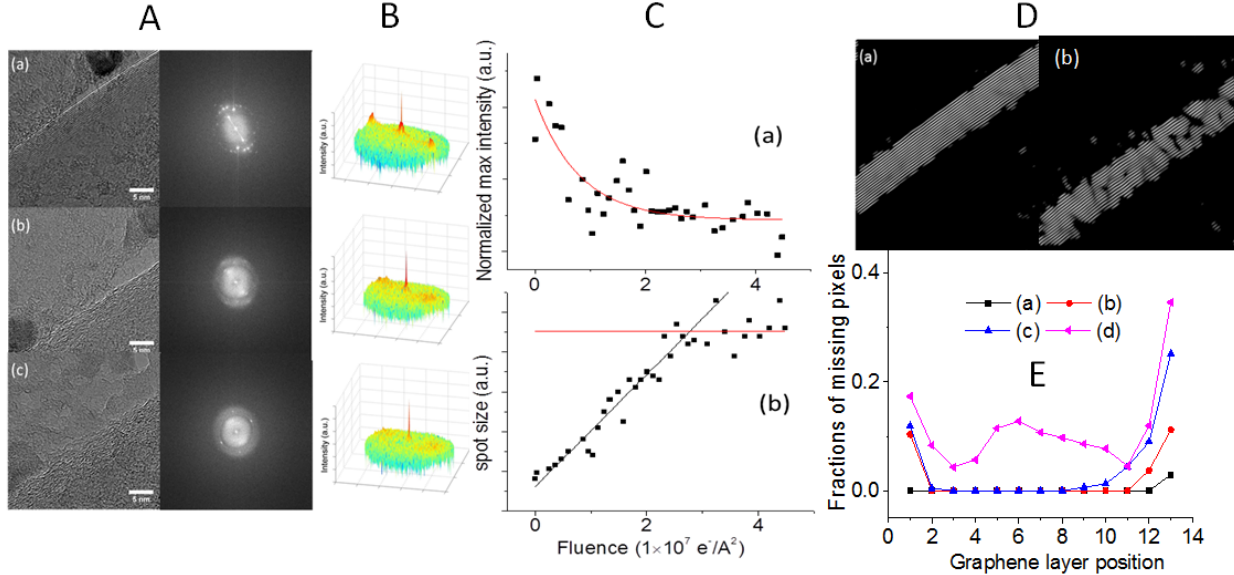


Fig. 2 (A) Experimental TEM images of folded graphene edge as a function of electron fluence and the corresponding localized diffraction patterns for the rolled edges, (B) mapping of diffraction pattern intensity, (C) the height and spot size changes of the major diffraction peaks in the diffraction patterns, (D) reconstructed high-resolution TEM images after Fourier mask filtering, and (E) fractions of missing pixels in Fourier transformed TEM images as a function of electron fluences and layer positions. Layers 1 and 13 represent the outmost edges.

We further obtained experimental evidence showing that the top and bottom layers of graphene have lower radiation tolerance, which agrees with our modeling prediction that graphene atoms have a strong anisotropic recoiling-direction-dependence of displacement energies. Fig. 2D(a-b) are high resolution TEM images after Fourier mask filtering at low and intermediate ion fluences. With radiation damage, lines are first distorted, then broken, and eventually rendered into short segments. We found that atom displacement creation is more efficient for the outermost graphene planes. As shown in Fig. 2E, fractions of missing lines (obtained by analyzing Fig. 2D) are the highest for two edged lines. As a function of electron fluence, edges are first distorted and lose line continuity quickly, in a way much more significant than central regions. Fundamentally, this is caused by the fact that threshold displacement energies are lower for the graphene edges, due to the lack of atom confinement from the vacuum side. This agrees with our MD simulation results.

For studies on CNT embedded composites, we synthesized, irradiated, and characterized CNT-dispersion-strengthened metals. By combining spark plasma sintering and extrusion techniques, aligned CNTs are incorporated into aluminum for obtaining strong but ductile CNT-metal composite. After helium ion irradiation or Al self-ion irradiation, we found that CNT-dispersed Al has significantly enhanced radiation tolerance: the presence of CNTs suppress large void swelling. CNT-matrix interfaces act as strong defect sinks to remove radiation damage.

Although CNTs are heavily damaged under irradiation to high displacements per atom (dpa), the interface effects sustain.

As shown in Fig. 3A, the fabrication process includes the following key steps: (1) A CNT declustering process on Al particle surfaces; (2) spark plasma sintering to consolidate dispersed CNTs and Al particles; and (3) extrusion of CNT-metal composites to align CNTs

The surface mechanical properties were characterized by Knoop hardness. Fig. 3B shows that the hardness increases with CNT volume percentages, while their ductility sustains. As shown by a high resolution TEM image in Fig. 3C, a majority of the CNTs are embedded inside Al grains, and a small fraction of them are found to decorate and immobilize grain boundaries.

Extruded 2.5 mm of Al specimens with and without CNTs were irradiated at the room temperature with 100 keV helium ions, up to  $2 \times 10^{18}$  ions/cm<sup>2</sup>. Fig. 4 compares their very different radiation tolerance. Figs. 4A and 4B show TEM images of pristine multi-walled CNTs and CNTs embedded inside an Al grain, respectively. Fig. 4C shows tight bonding of CNTs with Al matrix after sintering and extrusion. As shown in Figs. 4D and 4E, large voids are formed in the control Al specimens, with void sizes ranging from a few nanometers to a few hundred nanometers. By comparison, CNT-embedded Al exhibits enhanced radiation tolerance. As shown in Fig. 4F and 4G, no voids are observed up to the highest helium ion fluences.

## Future Plans

(1) A larger sample matrix consisting of CNTs incorporated into Zr, Ti, and Ni are currently under preparation. Ion irradiation will be extended to self-ion irradiations at elevated temperature and up to higher fluences, to study CNT-matrix interfacial sink properties; (2) Aberration corrected TEM is currently in use to characterize graphene with a grain boundary in order to study whether a two-dimensional grain boundary on a graphene can absorb point defects; (3) Understanding the effects of stress on defect morphology by using aberration corrected TEM is currently underway. Our MD simulations predict that a stress can change isolated vacancies to vacancy clusters, and control the size of nanometer pores formed in the graphene.

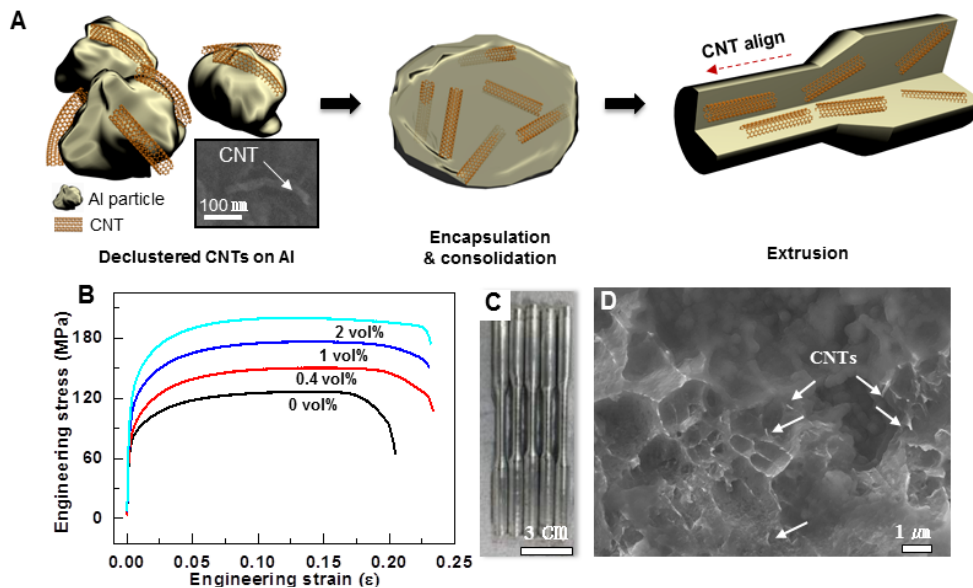


Fig. 3 (A) schematic representation of the Al/CNT composite, (B) The stress and strain curve, (C) ASTM E8 tensile specimen and (D) fractured area at CNT 2 vol%.



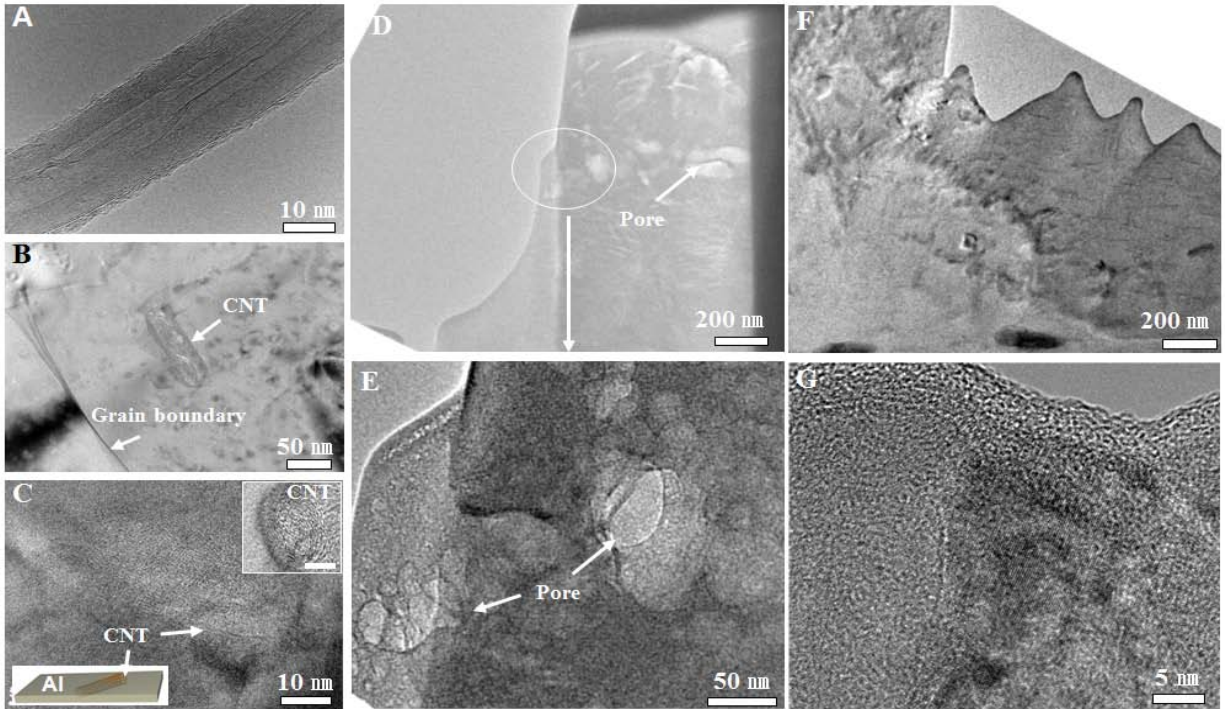


Fig. 4. Structural evolution of Al/CNTs composite under He ion irradiation. Brightfield TEM images of (A) pristine CNT, (B) CNT inside Al grain and (C) intact wall structure of CNT (inset: the scale is 5 nm). Pore generation observation in control Al (D and E) and Al/CNTs 0.5 wt% (F and G) after irradiation to 3.6 dpa.

#### Publications for 2013-2015

- [1] J. Wallace, L. Shao, "Defect-induced carbon nanoscroll formation", *Carbon* 91, 96 (2015).
- [2] Q. Yan, J. Wang, D. Chen, J. Gigax, L. Shao, "Displacement cross sections of electron irradiated graphene and carbon nanotubes", *Nucl. Instru. Methods Phys. Res. B* 350, 20 (2015)
- [3] Jing Wang, Di Chen, Joseph Wallace, Jonathan Gigax, Xuemei Wang, Lin Shao, "Introducing thermally stable inter-tube defects to assist off-axial phonon transport in carbon nanotube films", *Applied Physics Letters* 104, 191902 (2014).
- [4] Assel Aitkaliyeva, Michael S Martin, Tres A Harriman, Daniel S Hildebrand, Don A Lucca, Jing Wang, Di Chen, Lin Shao, "Radiation effects on the D to G Raman intensities of carbon nanotubes", *Phys. Rev. B* 89, 235437 (2014).
- [5] Jing Wang, Di Chen, Julia S. Bykova, Anvar A. Zakhidov, J. Gigax, Xuemei Wang, Lin Shao, "Thermal property tuning in aligned carbon nanotube films and random entangled carbon nanotube films by ion irradiation", *Applied Physics Letters*, accepted and in press
- [6] Jing Wang, Di Chen, Lin Shao, "The edge effect on structural stability of individual graphene layers in few-layer graphene under electron irradiation", *Phys. Rev. B*, submitted.
- [7] Assel Aitkaliyeva\* and Lin Shao, "Phonon transport assisted by inter-tube carbon displacements in carbon nanotube mats", *Scientific Reports* 3, 2774 (2013).
- [8] A. Aitkaliyeva, L. Shao, "The change of microstructure and thermal properties in ion irradiated carbon nanotube mats as a function of ion penetration depth", *Appl. Phys. Lett.* 102, 063109 (2013).
- [9] K.P. So, et al, "Improvement of the He<sup>+</sup> ion irradiation tolerance via the incorporation of carbon nanotube", *Nano Lett.*, in press
- [10] J. Wallace, D. Chen, L. Shao, "Carbon displacement induced single carbon atomic chain formation and its effects on sliding of SiC fibers in SiC/graphene/SiC composite, *Mat. Res. Lett.*, in press

## “Understanding and Controlling Toughening Mechanisms in Nanotube Reinforced Ceramic Coatings”

Brian W. Sheldon and Nitin Padture, Brown University, Providence, Rhode Island  
Jun Lou, Rice University, Houston, Texas

### Program Scope

Research in this program is designed to understand mechanical behavior, particularly fracture toughness, in ceramics that are reinforced with carbon nanotubes (CNTs). In the past year, emphasis was placed on:

- Synthesizing nanocomposite materials reinforced with both multiwall carbon nanotubes (MWNTs) and single wall nanotubes (SWNTs).
- Implementation and analysis of *in situ* mechanical testing methods.

### Recent Progress

#### A. Mechanical Behavior of MWNT Reinforced Ceramics (directed by B.W. Sheldon)

##### *Nanoindentation of Micromachined Cantilevers*

Measuring the fracture toughness of nanocomposite coatings is a substantial challenge. The method we are developing uses Focused Ion Beam (FIB) milling to produce microcantilever beams, with a sharp notch on the beam cut close to the point of support. Nanoindentation of these beams is then used to obtain load deflection curves to investigate fracture of the material. The materials investigated in this work consist of CVD grown vertically aligned carbon nanotubes, with an amorphous silicon nitride matrix produced by vapor infiltration.

In a majority of the composite beams tested to date, slow crack growth occurs (rather than brittle fracture). In several cases nanoindentation was halted (i.e., stop-start testing), to increase the displacement in successive experiments. This was followed by monitoring the crack position in between experiments (see Figure 1). These measurements make it possible to correlate crack

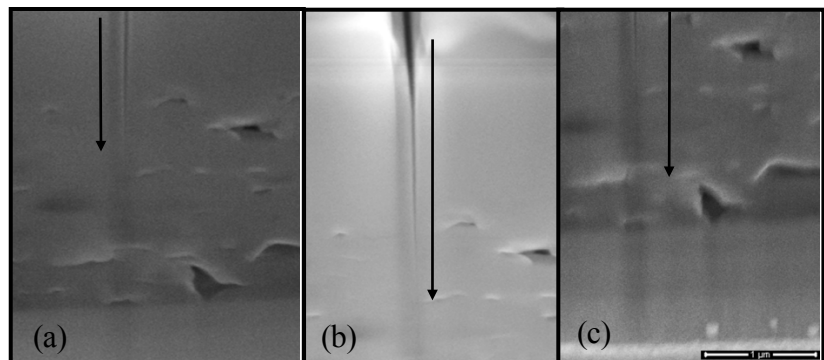


Figure 1: Micrographs of the crack front in cantilever beam milled from MWCNT reinforced silicon nitride. Measured crack length increases with each successive nanoindentation. Images for beam deflections of: (a) 100 nm; (b) 150 nm; (c) 250 nm.



growth with load-displacement data obtained during nanoindentation. The slow crack growth observed is indicative of progressive damage that is typical of R curve behavior during fracture. The corresponding load displacement curves obtained from the nanoindenter show an unexpected increase in stiffness (and not observed in beams that undergo simple brittle fracture). Finite element modeling of the beam configuration is currently being used to evaluate the data obtained from these measurements. Preliminary analysis confirms  $K_{Ic}$  values that exceed  $5 \text{ MPa m}^{0.5}$  (compared to the unreinforced matrix, where  $K_{Ic} < 1 \text{ MPa m}^{0.5}$ ).

#### *Synthesis and Testing MWCNT Reinforced Polymer-Derived Ceramic Coatings*

Additional work is being conducted with ceramic matrix nanocomposites fabricated with a polymer-derived ceramic matrix, using several different types of multiwalled carbon nanotubes (MWCNTs) that exhibit relatively long pull-out lengths. These materials are being used in several different efforts, including fracture toughness improvements via interface modifications. Here, very thin oxide interface coatings are being produced with atomic layer deposition (ALD). Complementary single fiber *in situ* pull-out tests with these fibers are also being conducted by Prof. Lou's group at Rice (described in the next section).

#### **B. Quantification and Promotion of Interfacial Interactions between Carbon Nanotubes and Polymer Derived Ceramics** (directed by J. Lou)

The work at Rice is focused on *in situ* electron microscopy studies with the same MWCNT reinforced ceramics that are being studied at Brown. The measured IFSS values for this type of failure were much higher than  $\tau_i$  for ideal MWCNT interwall sliding, and also higher than the IFSS for the same fibers in a polymer matrix. Following last year's successful effort to quantitatively assess the localized interfacial properties between an individual CNT and ceramic matrix, the two research teams from Rice and Brown have worked closely to implement a new design strategy to improve such interfacial interactions. Figure 3 shows the TEM images of pristine CNTs and CNTs/ $\text{Al}_2\text{O}_3$  nanostructures. The surface of pristine CNTs in Figs. 3a and 3b is quite smooth. The outer and inner diameters of CNT are  $75.9 \pm 6.7 \text{ nm}$  and  $3.0 \pm 1.6 \text{ nm}$ , respectively. All tested CNTs debonded either from PDC or epoxy, with no CNT fractures observed during pull-out test. The CNTs coated with  $\text{Al}_2\text{O}_3$  are shown in Figs 3c

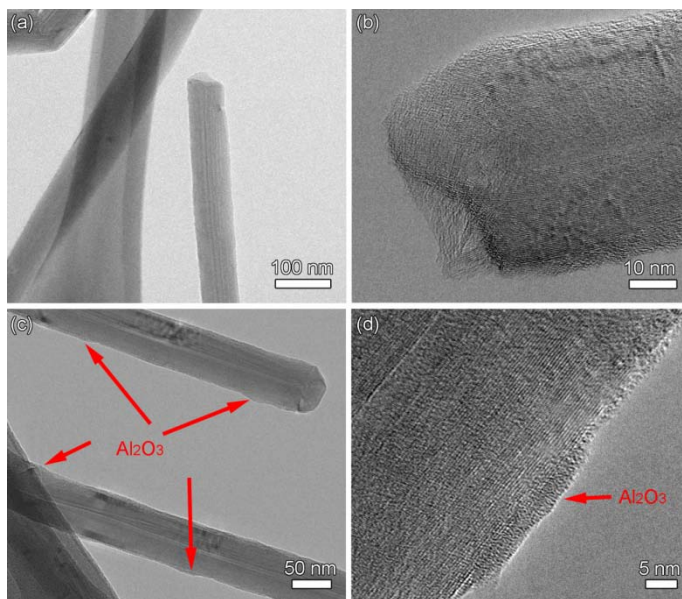


Fig 2. TEM images of CNTs and CNT/ $\text{Al}_2\text{O}_3$ . (a),(b) low- and high-magnification images of CNTs. (c),(d) low- and high-magnification images

and 3d. The  $\text{Al}_2\text{O}_3$  islands can be clearly seen and are highlighted by arrows. The average thickness of  $\text{Al}_2\text{O}_3$  in Fig. 3d is  $2.4 \pm 1.2$  nm. No lattice structures could be found in the  $\text{Al}_2\text{O}_3$  islands, indicating the amorphousness of the obtained ALD  $\text{Al}_2\text{O}_3$ . The  $\text{Al}_2\text{O}_3$  islands are well attached to the CNT surface with no apparent interfacial cracks or delaminations found. Additionally, the discontinuous  $\text{Al}_2\text{O}_3$  islands resemble the schematic features of “enlarged ends” or “dumbbell-shapes”, which modify load transfer between the matrix and the CNT/ $\text{Al}_2\text{O}_3$ .

We then carried out *in-situ* pull-out experiments of both pristine CNTs and CNTs coated with these ALD  $\text{Al}_2\text{O}_3$  coatings, embedded in PDC matrices. This was conducted in micro-fabricated devices in a scanning electron microscope. This carefully designed comparative study provides direct measurements of the interfacial interactions between CNTs and PDC matrices. The interfacial shear strength (IFSS) of CNT-PDC is  $10.0 \pm 2.8$  MPa, while the IFSS of CNT/ $\text{Al}_2\text{O}_3$ -PDC with  $\sim 3$  nm  $\text{Al}_2\text{O}_3$  coating thickness is  $14.5 \pm 2.7$  MPa, demonstrating a 45% improvement. The IFSS increase in CNT/ $\text{Al}_2\text{O}_3$ -PDC is believed to originate from the surface roughness.

### C. ***Composite Synthesis with Spark Plasma Sintering and Mechanical Behavior of SWNT Reinforced Ceramics*** (directed by N. Padture)

Studies claiming noticeable toughening in CNT reinforced ceramics have primarily used simple indentation tests, which are an indirect and unreliable method for the accurate measurement of the  $K_{IC}$  of CNTs-ceramic composites. Single edge notched beam (SENB) tests that provide more reliable and accurate toughness-measurements show either no toughening or marginal toughening results in different composites. These existing techniques are well established for measuring macroscopic mechanical properties of structural ceramics at microscale levels. The validity of any of these technologies in investigating the toughening effect of nanoscale CNTs has been strongly questioned. In addition, the current mechanisms used to explain the toughening effect of CNTs borrows heavily from those used in conventional ceramic composites. However, these concepts may not be fully applicable to CNT-ceramic composites, because their microstructures with the nanoscale, flexible CNTs differ vastly from those of conventional composites. In light of these considerations, the goals of our efforts are:

- To obtain dense, homogeneously dispersed CNTs- $\text{Al}_2\text{O}_3$  matrix nanocomposites by colloidal mixing processes and spark plasma sintering (SPS).
- To systematically study the ability of CNTs to toughen structural ceramics with direct and convincing evidence.
- To understand the load bearing effect of CNTs during the rupture process and properly demonstrate the toughening mechanisms in these nanocomposites at both nanoscale and macroscale levels.

The first of these has been achieved. Progress towards the other two goals is summarized below.

### Direct Observation of CNTs in Controlled Cracks

Toughness measurement with the Vickers indentation method is not valid in these materials. However, the distributed damage around the indent in the received nanocomposites indicates their weakness in shear, which causes significant redistribution of stresses under the indenter, and prevents the formation of long cracks. The results show that MWCNTs are stronger in shear resistance than SWCNTs as a second phase. This is because SWCNTs cannot be dispersed individually with direct interfaces with the matrix, but exists mainly in bundled form.

### In-Situ Observation of the CNTs' Behavior during Crack Propagation under Controlled Load.

These observations of bridging CNTs in cracks were conducted with modified double cantilever beam specimens. A notch with an indentation crack at the tip was made at the short edge of the specimen. Subsequent crack extension could be controlled by inserting a metal wedge into the notch via a micrometer drive system. The whole system was attached to the stage of SEM to allow for continuous monitoring of the crack evolution along its entire length while the driving force is applied. The load-displacement curves of the wedge against the notch of pure  $\text{Al}_2\text{O}_3$  and several CNTs- $\text{Al}_2\text{O}_3$  nanocomposites are shown in Fig. 3. The addition of SDS stabilized SWCNTs, shows subtle improvement of crack resistance of the nanocomposites while acid treated SWCNTs made it worse. In contrast, the load bearing ability of C- $\text{Al}_2\text{O}_3$ -10MWCNTs nanocomposite is remarkably superior, with the fracture load of three times of the formers. This result together with the observations of CNTs bridging in the indentation cracks suggest the contribution of CNTs bridging in bearing the applied load and energy dissipation.

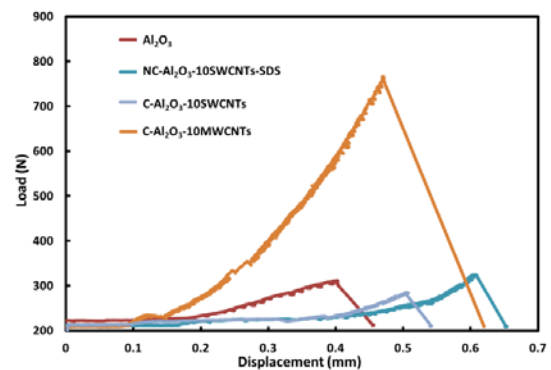


Fig. 3. Load-displacement curves of the wedge against the notch of pure  $\text{Al}_2\text{O}_3$  and CNT- $\text{Al}_2\text{O}_3$  nanocomposites during *in-situ* observation of crack propagation.

### Future Plans

A variety of *in situ* testing methods have been successfully implemented. Most of the results obtained to date are preliminary, and more detailed research will be conducted over the next year. Collaborations on detailed modeling with Prof. Bill Curtin (EPFL, Lausanne) are continuing. A new collaboration has been initiated with Prof. Izabela Szulfarska (U. Wisconsin), where radiation exposures are being used to systematically introduce defects in the MWCNTs (this will eventually be extended to the matrix as well). Previous atomistic modeling at Brown predicts that internal defects can be used to improve MWCNT toughening, however, experiments with high defect density tubes have not confirmed this. The controlled experiments at Wisconsin

are designed to provide a systematic investigation of these effects (ultimately in collaboration with Prof. Szulfarska's modeling efforts, currently supported by DOE-BES).

# Dynamic Fracture in Dealloying Induced Stress Corrosion Cracking

Karl Sie radzki, PI  
Xiy ing Chen, Nilesh Badwe, Shaofeng Sun  
Arizona State University  
Tempe, Arizona 85287-6106

## Program Scope

When metallic alloys are exposed to a corrosive environment that selectively leaches one or more of the alloy components, porous nanoscale morphologies spontaneously form that can adversely affect the mechanical integrity of engineered structures<sup>1,2</sup>. This form of stress-corrosion cracking (SCC) is responsible for the well-known “season cracking” of brass as well as cracking of noble metal alloys and stainless steel components in nuclear power generating stations<sup>3,4</sup>. This form of SCC is characterized by the formation of a thin dealloyed nanoporous layer on the surface of an alloy undergoing corrosion while simultaneously subjected to tensile loading. We hypothesize that a high-speed crack is nucleated within this layer that subsequently is injected for a short distance (of order microns in the case of transgranular cracking) into the un-corroded parent phase alloy prior to coming to arrest by plastic processes<sup>5-9</sup>. This process is discontinuous: a nanoporous layer forms by dealloying corrosion, then the crack propagates exposing more parent-phase to the electrolyte which in-turn corrodes and the cycle repeats. Importantly, the measured rate of cracking is incompatible with a purely electrochemical process<sup>10-12</sup>. In some cases the crack growth velocity has been reported to be factors of 20-100 times that which would be predicted from the measured current density<sup>6,11,12</sup>.

In order to examine these issues we perform experiments on Ag-Au alloys for which hydrogen effects can be ruled out on thermodynamic grounds. There are two major types of experiments we have pursued. One set of experiments examines dynamic fracture in crack-free monolithic nanoporous gold (NPG) as a function of electrochemical potential. The second set of experiments is aimed at separating the mechanical component of cracking from any corrosion or stress-corrosion component. These crack injection experiments involve forming a dealloyed layer of prescribed thickness and ligament size on the surface of a sample under zero applied stress, removing the sample from the electrolyte and subsequently rapidly loading the sample in bending. We examine both intergranular and transgranular crack injection phenomena using polycrystalline and single crystal samples respectively. Post mortem fractography, EBSD, EDS, APT and aberration-corrected STEM are used in characterization.

## Recent Progress

*Potential dependent dynamic fracture*

In order to make further progress in our understanding of dynamic fracture in NPG<sup>13</sup> we have adopted a new experimental protocol and sample configuration. Instead of using miniature (15 mm long x 5 mm wide x 0.125 mm thick) single edge-notched (SEN) samples, we are using an experimental realization of an “infinite strip” (IS) geometry<sup>14</sup>. The IS geometry allows for gathering reliable data over a larger portion of the sample than the SEN sample. For the SEN sample, we could only obtain data over ~2.5 mm of crack growth (reliable sample compliance) while in the IS configuration we should be able to get reliable data over 5-6 mm of growth. In collaboration with J. Ostwald (ASU), we are in the process of examining this using this using finite element analysis.

### *Polycrystalline crack injection experiments*

Most of our crack injection experiments employed the following experimental protocol: (1) A fully annealed (900 C 24 hr) polycrystalline Ag<sub>0.70</sub>Au<sub>0.30</sub> alloy sample is dealloyed (typically at 1.25 V for 15-30 s) under zero applied stress forming a nanoporous layer of thickness (350-750 nm). (2) The sample is disconnected from the potentiostat, removed from the electrolyte, and placed in DI water for delay times ranging from 10-60 s. (3) The

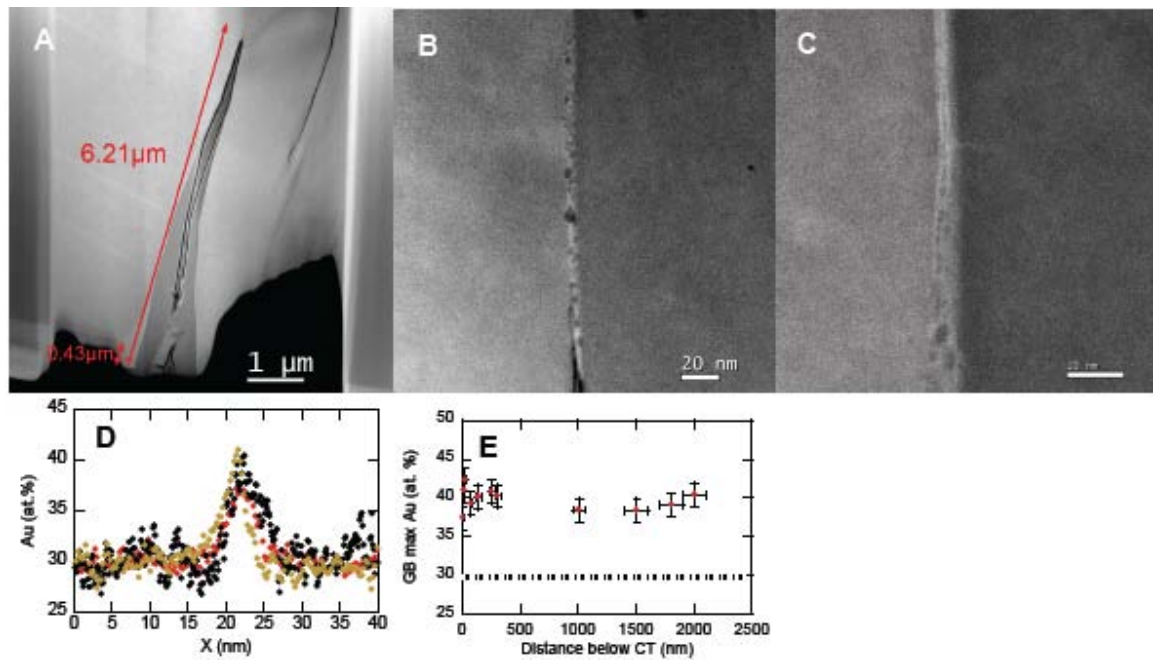


**Figure 1| Analysis of an injected GB crack.** **A**, Full view of the injected crack that has a 430 nm thick NPG layer, a “V” extending 1360 nm below the surface and a 6210 nm long injected GB crack. **B**, HAADF image showing porosity within the grain boundary below the crack. **C**, HAADF image at the end of the 300 nm long porous GB region showing the cascade in pore size reminiscent of a Rayleigh-like instability. **D**, EDS line scans across the GB at the crack tip (red points), 10 nm below the crack tip within a GB pore (gold points) and 2000 nm below the crack tip within a region of the GB that is not porous (black points). **E**, Summary plot of the EDS line scans below the crack tip along the GB. The average Au concentration within the GB along this line scan was 40 at.%. The dotted line shows the parent-phase composition.

sample is removed from the DI water and loaded quickly by hand bending. For each variation of test protocol we ran no-load control experiments. Figure 1 shows representative results obtained.

### *Single crystal crack injection experiments*

Samples (9 mm x 3mm x 0.1 mm thick) were cut in various orientations from a  $\text{Ag}_{0.77}\text{Au}_{0.23}$  single crystal and annealed. A  $\sim 1\ \mu\text{m}$ -thick dealloyed layer was produced on the surface of the samples by immersion in 1M  $\text{HClO}_4$  at 1.26 V NHE for 10 s. Following this protocol, the sample was disconnected from the potentiostat, removed from the electrolyte and subjected to bending. Remarkably these samples underwent through-thickness fracture. Representative results are shown in Figure 2.

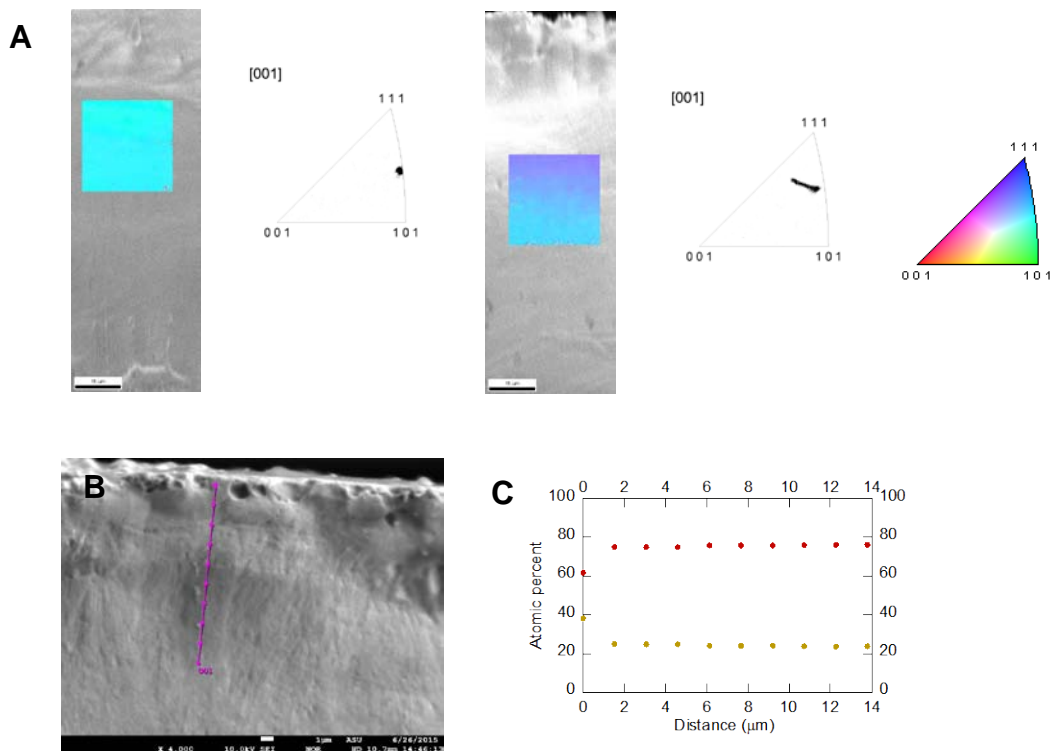


**Figure 2| Fracture surface analysis of a single crystal sample that underwent crack injection and through-thickness fracture. A, EBSD result showing fracture surface orientation. B, SEM showing a portion of the fracture surface. C, EDS analysis of the composition of the fracture surface along the violet line in B.**

### **Future Plans**

- Potential dependent mechanical property and dynamic fracture experiments in 5-10 nm NPG.
- Crack injection experiments in poly and single crystalline NPG.

## Publications

Shaofeng Sun, Xiyang Chen, Nilesh Badwe, Karl Sieradzki; Potential-dependent dynamic fracture of nanoporous gold, *Nature Materials*, **14**, 894-898 (2015)/ doi:10.1038/nmat4335.

## References

1. Erlebacher, J., Aziz, M.J., Karma, A., Dimitrov, N., & Sieradzki, K. Evolution of nanoporosity in dealloying, *Nature* **410**, 450-453 (2001).
2. Sieradzki, K., & Newman, R.C. Stress-corrosion cracking, *J. Phys. Chem. Solids* **48**, 1101-1113 (1987).
3. Ford, F.P., & Andresen, P.L. Development and use of a predictive model of crack propagation in 304/316L, A533B/A508 and Inconel 600/182 alloys in 288 °C water, In *Proceedings Of The Third International Symposium On Environmental Degradation Of Materials In Nuclear Power Systems*, 789-800 (1988).
4. Nisbet, W.J., Lorimer, G.W., & Newman, R.C. A transmission electron microscopy study of stress corrosion cracking in stainless steels, *Corros. Sci.* **35**, 457-469 (1993).
5. Sieradzki, K., & Newman, R.C. Brittle behavior of ductile metals during stress-corrosion cracking, *Philos. Mag.* **A51**, 95-132 (1985).
6. Cassagne, T.B., Flanagan, W.F., & Lichter, B.D. On the failure mechanism of chemically embrittled Cu<sub>3</sub>Au single crystals, *Metall. Trans. A* **17**, 703-710 (1986).
7. Chen, J.S., Salmeron, M., & Devine, T.M. Intergranular and transgranular stress corrosion cracking of Cu-30Au, *Corros. Sci.* **34**, 2071-2097 (1993).
8. Friedersdorf, F. & Sieradzki, K. Film-induced brittle intergranular cracking of silver-gold alloys, *Corrosion* **52**, 331-336 (1996).
9. Barnes, A., Senior, N.A., & Newman, R.C. Film-induced cleavage of Ag-Au alloys, *Metall. Mater. Trans. A* **40**, 58-68 (2009).
10. Sieradzki, K., Kim, J.S., Cole, A.T., & Newman R.C. The relationship between dealloying and transgranular stress-corrosion cracking of CuZn and CuAl alloys, *J. Electrochem. Soc.* **134**, 1635-1639 (1987).
11. Serebrinsky, S.A., & Galvele, J.R. Effect of the strain rate on stress corrosion crack velocities in face-centered cubic alloys. A mechanistic interpretation, *Corros. Sci.* **46**, 591-612 (2004).
12. Newman, R.C., & Senior, N.A. A revised interpretation of ultra-fast stress corrosion cracking experiment by Serebrinsky and Galvele, *Corros. Sci.* **52**, 1541-1544 (2010).
13. Sun, S., Chen, X., Badwe, N., Sieradzki, K. Potential-dependent dynamic fracture of nanoporous gold, *Nat. Mater.*, **14**, 894-898 (2015).
14. Goldman, T., Livne, A., & Fineberg, J. Acquisition of inertia by a moving crack, *Phys. Rev. Lett.* **104**, 114301 (2010).



# Understanding, controlling and creating martensitic phase transformations in nanostructured polycrystals and metamaterials

Alejandro Strachan

School of Materials Engineering, Purdue University

## Program Scope

Martensitic phase transformations are exploited to enhance the performance and to achieve otherwise inaccessible functionalities in a wide range of advanced materials. Examples range from TRIP steels [1] to shape memory alloys (SMAs) [2] used for environmental-friendly energy conversion [3] and refrigeration, [4] as well as sensors and actuators for medicine and vibration damping. Despite many decades of research and a host of successful applications, recent advances indicate that this class of materials possesses a significant untapped potential. Nano-engineered composites and metamaterials with at least one component capable of undergoing martensitic transformation can open the door to remarkable mechanical properties. Examples include composites that combine ultra-high elastic limit with high-strength [5] and our group's work on shape memory metamaterials (SMMs) with tunable transformation hysteresis and temperature.[6] In addition, our preliminary research shows unexpected behavior in ultra-fine grained SMAs that could enable the design of SMAs that combine high-strength with pseudoelasticity or shape memory. However, engineering architectures that fully exploit the potential of this class of materials requires significant advances in basic materials science including a mechanistic understanding of the atomic-level processes that govern the performance of these complex materials. Most of the key, open science questions in the field stem from a poor understanding of the interplay between the complex microstructure in nanostructured SMAs and their martensitic transformation, the resulting martensite microstructure, and the relative importance of reversible and irreversible plastic deformation mechanisms. Our work in this area and that of others show that atomistic simulations can provide answers to these fundamental questions, can enable the discovery of new phenomena, and be used to optimize formulations. Thus, the objectives of this project are to characterize the mechanisms that control the thermo-mechanical response of nanocrystalline SMAs and nanostructured SMMs and to use this knowledge to computationally

Understanding, controlling and creating martensitic phase transformations

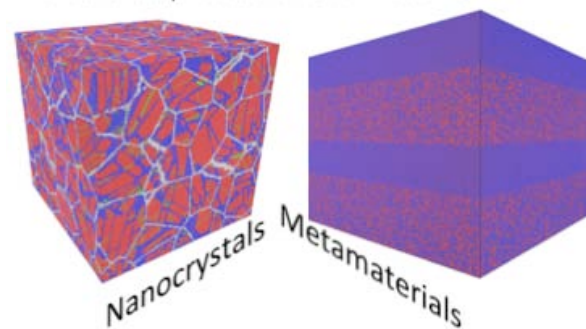


Figure 1. Schematic representation of the two thrusts of the effort aimed at characterizing and exploiting nanostructured martensitic materials.

optimize their nanostructure to achieve desired properties, including SMMs with ultra-low and tunable stiffness and thermal conductivity, as well as SMMs made with non-martensitic materials. As shown schematically in Figure 1, the proposed effort is organized along two complementary thrusts:

**Thrust 1: Shape-memory and pseudoelasticity in nanocrystalline alloys.** We propose to characterize the effect of microstructure (grain size, texture, and defect densities) on the thermo-mechanical response of nanocrystalline SMAs via large-scale molecular dynamics (MD) simulations. The proposed studies on the effect of microstructure on the temperature- and stress-induced martensitic transformation have been designed to quantify the relative importance of the various competing mechanisms that govern the process; including nucleation around defects, mechanical constraints and autocatalytic effects. Mechanical deformation studies will enable the quantification of the mechanisms of plastic deformation in the martensite and austenite phases; we will focus on the relative importance of reversible processes (phase transformation and domain wall motion) and irreversible ones (grain boundary sliding and dislocation glide). It is generally accepted that grain refinement hinders the martensitic transformation and this effort will shed light into such size effects and explore intriguing results from our preliminary studies in ultra-fine-grained materials. The knowledge gained will be used to establish fundamental limits in grain refinement of SMAs and to optimize microstructure to achieve shape memory and pseudoelasticity in fine-grained materials.

**Thrust 2: phase transforming metamaterials with novel properties.** Our ongoing research on epitaxial metamaterials containing phase-transforming phases, supported by DoE-BES, showed that these materials can be designed to exhibit remarkable tunability in their transformation characteristics and mechanical response via nanostructure optimization. Error! Bookmark not defined. Furthermore, our work and that of others showed that phase transforming materials provide significantly flexibility in epitaxial integration due to their non-convex energy landscape and afford the possibility of using materials in thermodynamically unstable states (negative stiffness) that are stabilized by atomic-level constraints by the other phases. We propose to build on this progress on *energy landscape engineering* to computationally design and test metamaterials with novel properties including: i) ultra-low and tunable stiffness and thermal conductivity; ii) optimized shape memory metamaterials (SMMs) from non-transforming constituents with desirable transformation characteristics. Promising metamaterials identified by the simulations will be fabricated and tested experimentally by an unfunded collaboration, see letters of collaboration from Drs. Amit Misra and Nathan Mara.

## Recent Progress

**Martensitic transformations in nanocrystalline SMAs.** We used multi-million-atom molecular dynamics (MD) simulations with an embedded atom model potential parameterized for NiAl to study temperature- and stress-induced martensitic phase transformations in nanocrystalline shape memory alloys.[7] The simulations show that nucleation of the martensite phase occurs in the

grain interiors and grows outwards up to the point where further transformation is hindered by the constraints imposed by neighboring grains. Decreasing grain size inhibits the transformation process and the temperature-induced transformation is completely suppressed for samples with average grain sizes of 7.5 nm and less.

Interestingly, mechanical loads can induce the martensitic transformation in samples with ultra-fine grains and, quite surprisingly, the sample with 7.5 nm grain size exhibits improved, ultra-fast, superelasticity as compared with its coarser grain counterparts, see Figure 2. The simulations provide a picture of the processes that govern the performance and fundamental limits of nanocrystalline shape memory alloys with atomistic resolution.

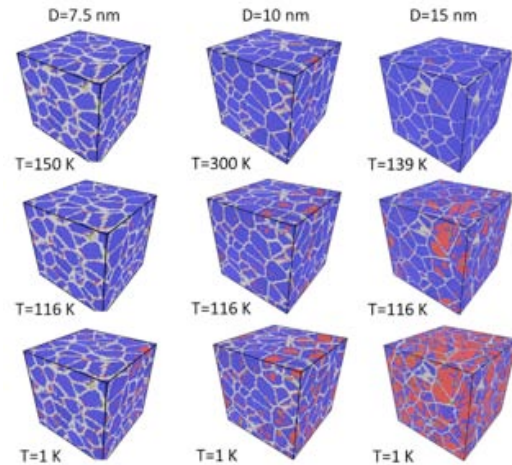


Figure 1. Martensitic transformation under cooling for three grain sizes. Red spheres denote martensite and blue austenite.

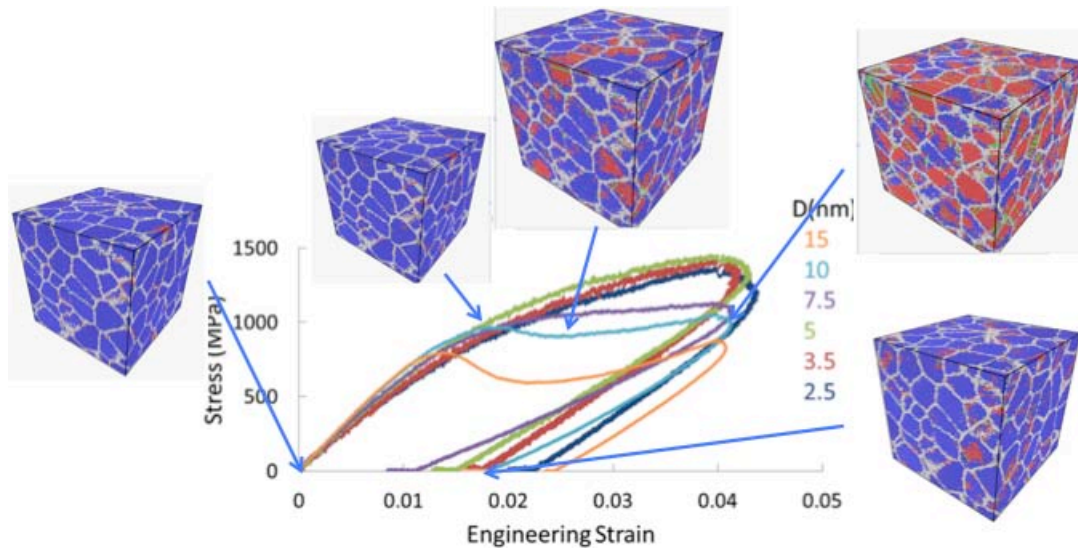


Figure 2. Stress-strain curves for nanocrystalline alloys of different grain size. The snapshots show atomic snapshots for a specimen with average grain size of 10 nm, red spheres denote martensite and blue austenite.

**Phase transforming materials with novel properties.** We had previously demonstrated the ability to tune the phase transformation properties of shape memory materials via epitaxial integration of dissimilar materials to engineer the energy landscape that governs the phase transformation.[6] We extended this work with the objective of engineering novel properties in metallic alloys via energy landscape engineering. We used large-scale MD to study core/shell nanowires consisting of NiAl (a non-transforming alloys with the B2 phase) and Ni<sub>63</sub>Al<sub>37</sub> phase

transformation materials. This choice is motivated by an analysis of the energy vs. lattice parameter of the combined metamaterial that indicates that their epitaxial integration can result in ultra-low stiffness metallic systems. Explicit MD simulations on the mechanical deformation of the core/shell nanowires reveal a variety of interesting properties including ultra-low stiffness (<3GPa) while maintaining strength. The simulations reveal the nucleation and propagation of martensitic transformation in the metamaterials and show that it is possible to stabilize the spatial coexistence of austenite and martensite phases resulting in ultra-low stiffness. Once the material is fully transformed it becomes stiffer and additional plastic deformation requires nucleating defects in the martensite phase, leading to high strength.

### **Future Plans**

We will continue to focus on the computational design of phase transforming materials with novel properties. To this end we will construct a database of energy landscapes for a range of metals using density functional theory electronic structure calculations that will be used to explore possible combinations. At the same time we will finalize the characterization of the NiAl/Ni<sub>x</sub>Al<sub>1-x</sub> metamaterials to fully explore their potential, this includes shape memory and superelasticity for laminates, nanowires and nano-precipitates in bulk samples as well as the thermal transport properties of these materials.

### **References**

1. Grässel, O., L. Krüger, G. Frommeyer, and L. W. Meyer. *International Journal of Plasticity* 16, no. 10 (2000): 1391-1409.
2. T. Waitz, K. Tsuchiya, T. Antretter, and F.D. Fischer, *MRS Bulletin*, 34, 814 (2009).
3. Srivastava, Vijay, Yintao Song, Kanwal Bhatti, and R. D. James. *Advanced Energy Materials* 1, no. 1 (2011): 97-104.
4. Liu, Jian, Tino Gottschall, Konstantin P. Skokov, James D. Moore, and Oliver Gutfleisch. *Nature materials* 11, no. 7 (2012): 620-626.
5. Hao, Shijie, et al. *Science* 339.6124 (2013): 1191-1194.
6. Vishnu, Karthik Guda, and Alejandro Strachan. *Journal of Applied Physics* 113.10 (2013): 103503.
7. "Role of grain size on the martensitic transformation and ultra-fast superelasticity in shape memory alloys", R. Morrison, Mathew J. Cherukara, Hojin Kim, Alejandro Strachan, *Acta Materialia* 95, 37-43 (2015).

### **Publications (2013-2015)**

1. "Role of grain size on the martensitic transformation and ultra-fast superelasticity in shape memory alloys", R. Morrison, Mathew J. Cherukara, Hojin Kim, Alejandro Strachan, *Acta Materialia* 95, 37-43 (2015).
2. "Role of atomic variability and mechanical constraints on the martensitic phase transformation of a model disordered shape memory alloy via molecular dynamics", Keith Morrison, Mathew Cherukara, and Alejandro Strachan, *Acta Materialia* 69 30–36 (2014).
3. "Shape memory metamaterials with tunable thermo-mechanical response via hetero-epitaxial integration", K. Guda Vishnu and A. Strachan, *Journal of Applied Physics*, 113, 103503 (2013).

## Interfacial Effects in Radiation Phenomena of Ceramics

**PI: Izabela Szlufarska, Unfunded collaborators: Dane Morgan, Paul Voyles**  
**Department of Materials Science & Engineering, University of Wisconsin – Madison**

### Program Scope

We use an integrated approach that includes multi-scale simulations and state of the art experimental characterization techniques to develop understanding and atomistically informed models of radiation phenomena in SiC. This understanding and these models will provide design principles for future synthesis or radiation-tolerant covalent ceramics. The main themes of this project are: (i) discover the role of interfaces (e.g. grain boundaries, GBs) in defect annihilation and radiation-induced amorphization; (ii) understand and control how interfaces themselves evolve under radiation; (iii) explore new types of interfaces (e.g., carbon nanotube / SiC composites) to control radiation effects on mechanical properties; (iv) provide atomic-level understanding of complex radiation-induced defects in SiC using state of the art experimental characterization techniques.

### Recent Progress

*Coupling of irradiation species and grain boundaries in radiation-induced amorphization:* Our previous studies have shown that the effects of grain refinement can be coupled to the effect of irradiation species on radiation-induced amorphization. We hypothesized that the reason for this coupling is that amorphization mechanisms depend on the irradiation species and these amorphization mechanisms can be non-trivially coupled to the GB effects. To investigate this hypothesis, a partially amorphous polycrystalline 3C-SiC sample was analyzed *post mortem* using high-resolution electron microscope (HRTEM). In all the obtained HRTEM images, we observed an unusual morphology of highly curved crystalline/amorphous (c/a) boundaries (Fig. 1a), which is surprising since the c/a boundaries contribute excess interfacial energy to the system so their total area should be minimized.

Based on our coarse-grained model informed by atomistic simulations, the unique features of the morphology have been reproduced and explained. Specifically,



**Figure 1** Comparison of (a) the original HRTEM image with hand-drawn c/a boundaries; (b) simulated c/a morphology by coarse-grained modeling ;(c) the experimental image (a) after processing. In (a) the c/a boundaries are shown as white dashed lines, in (b) and (c) white and black colors represent crystalline and amorphous regions, respectively.

we demonstrated that the morphology is due to cascade overlap (Fig. 1b), which governs the amorphization process under heavy ion (e.g.,  $\text{Kr}^{2+}$ ) irradiation. The amorphization mechanism for heavy ions revealed in our study can help understand the reduced radiation resistance of nc SiC under heavy ion irradiation. Unlike light particles, heavy ions generate a substantial amount of defect clusters in the collision cascade, in addition to point defects. These defect clusters are much less mobile than point defects, which makes it difficult for the clusters to be annihilated at GBs. Therefore the presence of larger volume fraction of GBs (due to grain refinement) is not as beneficial to defect annealing as in the case of lighter ions. An interesting question is whether the GBs play any role in increasing radiation resistance of SiC. We found that they do and that GBs can reduce resistance of SiC to amorphization under heavy ion irradiation. To demonstrate this effect, we developed a new analysis technique that quantifies the c/a fractions near and far from boundaries in HRTEM images, without introducing a bias from the observer. The processed c/a morphology (Fig. 1c) agrees well with the c/a morphology determined directly by eye (Fig. 1a). Using this method, we found that the local amorphization fraction is the largest at a GB and gradually decreases as a function of distance from the GB, implying that GBs actually increase the local amorphization rate (Fig. 2). We concluded that this phenomenon is due to interstitial starvation mechanism, which has been previously proposed in our rate theory simulations [1] (also funded by this BES project). To the best of our knowledge, this is the first time that interstitial starvation is demonstrated experimentally in SiC. As a competing effect to defect sinks, interstitial starvation actually degrades the radiation resistance of nc SiC. A balance of these two effects of GBs may also lead to an optimum intermediate grain size that maximizes the radiation resistance of nanocrystalline SiC.

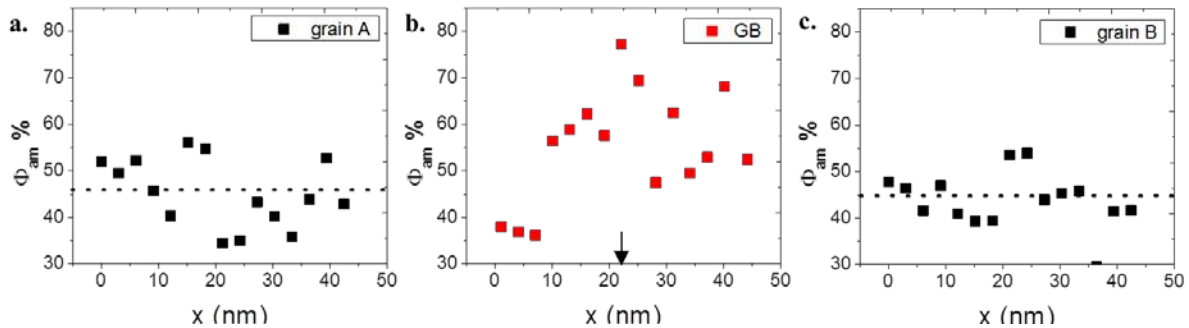


**Figure 2** Local amorphous area fraction ( $\Phi_{am}$ ) in 3 nm strips as a function of the strip position ( $x$ ) in HRTEM images. The position of the GB in (b) is marked by an arrow. Horizontal dotted lines in (a) and (c) indicate the average amorphization ratio in HRTEM images of grain A and B.

**Radiation-induced mobility of black spot defects in SiC:** Black spot defects (BSD) are defects that have been difficult to identify in traditional TEM. These defects are believed to contribute to radiation-induced swelling and radiation-induced creep of SiC. The focus of the current BES project is to understand the nature and fundamental properties of these defects, both in the bulk



and in GBs of SiC. It is likely that BSDs are formed by small interstitial clusters, although the true atomic structure is currently unknown. BSDs identified in HRSTEM experiments are shown in Fig. 3a (circled). Typically defect clusters in covalent-ionic ceramics are expected to be immobile. In this project we have determined, using accelerated molecular simulations, that the migration barrier of small interstitial clusters in SiC is very high (above 4 eV). Consequently, we do not expect any thermally-induced diffusion of these clusters in SiC, consistently with assumptions of classical defect evolution models for this material. However, our experiments revealed that these clusters can become mobile due to interactions with electron beam (Figs. 3b and 3c).

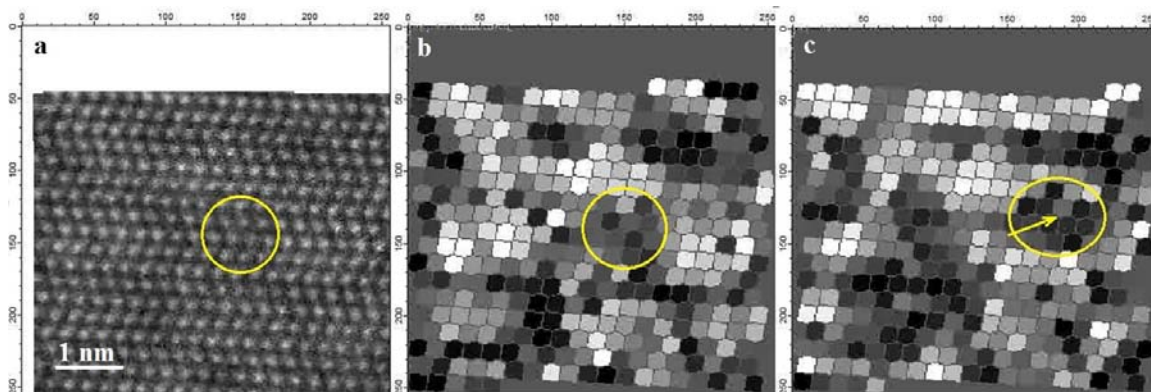


**Figure 3** (a) STEM image of irradiated SiC; (b) coarse grained view of (a), BSDs are easier to be seen in this image; (c) coarse grained view of one frame captured 8 s later than (b), where the circle shows one BSD and the arrow points its trajectory from frame b to frame c.

To understand the origin of this mobility, we considered a number of hypotheses, including ionization, electron-hole excitation, and ballistic motion. We concluded that the most likely reason for the radiation-induced mobility of clusters in SiC is a ballistic interaction of the incoming species (here: electrons) with atoms in the interstitial clusters. We developed a model for such radiation-induced mobility and demonstrated that the diffusion coefficients predicted by the model are in a very good agreement with the values determined experimentally based on the mean squared displacement. Our study changes the way one should view defect clusters in SiC (and perhaps also in other ceramics). Although these clusters are immobile under equilibrium conditions, they can become mobile in non-equilibrium radiation environments. This mobility of defect clusters under irradiation should be taken into account when modeling defect annealing processes and the resulting microstructural evolution. A manuscript on this topic is being prepared for publication.

Genetic algorithms: We have previously discovered the atomic structure of stable small C interstitial clusters that form in SiC under radiation. These earlier results were obtained by combining high-temperature molecular dynamics simulations and Monte Carlo basin-hopping algorithms. These approaches were necessary to explore the complex energy landscape of defect



clusters in ceramics, although there is no guarantee that they lead to identification of the ground states for all the defects. Since then we have also developed a new method based on genetic algorithms (GA) to accelerate the structure identification. This method has been integrated with the LAMMPS software package for classical molecular dynamics simulations and it has been validated against clusters identified in our earlier studies on SiC. We are currently integrating this method with the VASP software package, which will enable density functional theory (DFT) calculations of cluster energies and structures. The use of DFT will allow circumventing limitations of classical empirical potentials used in LAMMPS.

## Future Plans

The following research is either being currently pursued or will be pursued in the near future:

- Identify structure of small defect clusters induced by irradiation in SiC using high resolution scanning tunneling microscopy (HRSTEM). State of the art HRSTEM is now capable of identifying individual interstitials in materials, which provides an unprecedented opportunity to discover defect structures formed in SiC under radiation (until now they have been described as black spot defects because of the way they appear in traditional TEM). Understanding the properties of these defects is critical for predicting performance of SiC under irradiation with respect to its thermo-mechanical properties.
- Discover how defects are accommodated at grain boundaries and consequently how GB sink strength depends on the GB type and irradiation conditions. Traditionally, GBs have been treated as continuous sinks with little consideration given to their atomic structure and chemistry. This is a challenging but important problem because understanding of the atomic-nature of sinks can provide guidelines to engineering of materials with superior ability to annihilate radiation-induced defects. In SiC there is a biased flux of C atoms to GBs and it is unknown whether this effect leads to saturation of sinks, GB graphitization or radiation-induced segregation. We are using a combination of atomistic simulations and EELS experiments to determine the evolution of GBs under irradiation.
- As discussed in the earlier sections, we are integrating our newly developed genetic algorithm (GA) methods with DFT calculations in VASP. This will allow us to determine how defect structure and stoichiometry changes as a function of defect size. For instance, large Frank's loops in SiC are known to be stoichiometric whereas small clusters are often non-stoichiometric and have a complex 3D morphology. Understanding the transition from small off-stoichiometric 3D clusters to large stoichiometric 2D loops is important for building predictive models of defect evolution in SiC and for prediction of swelling. Understanding of defect chemistry is also important for predicting how evolution of SiC self-interstitials, vacancies and antisites will be affected by the presence of impurities (e.g., transmutation products).

## References

- [1] *Role of recombination kinetics and grain size in radiation-induced amorphization*, N. Swaminathan, D. Morgan, I. Szlufarska, Phys. Rev. B **86**, 214110 (2012)

## Publications (2014-2015)

1. *Genetic Algorithm Optimization of Defect Clusters in Crystalline Materials*, A. Kaczmarowski, S. Yang, I. Szlufarska, D. Morgan, *Computational Materials Science* **98**, 234-244 (2015)
2. *Evidence for cascade overlap and grain boundary enhanced amorphization in silicon carbide irradiated with Kr ions*, X. Wang, L. Jamison, K. Sridharan, D. Morgan, P. M. Voyles, I. Szlufarska, *Acta Materialia* **99**, 7-15 (2015)
3. *Temperature and Irradiating Species Dependence of Radiation Response of Nanocrystalline Silicon Carbide*, L. Jamison, K. Sridharan, S. Shannon, I. Szlufarska, *J. Mater. Science* **29**, 2871-2880 (2014)
4. *Accelerated atomistic simulation study on the stability and mobility of carbon tri-interstitial cluster in cubic SiC*, H. Jiang, C. Jiang, D. Morgan, I. Szlufarska, *Computational Materials Science*, **89** 182-188 (2014)
5. *Effect of grain boundary stresses on sink strength*, C. Jiang, N. Swaminathan, D. Morgan, I. Szlufarska, *Materials Research Letters*, **2**, 100-106 (2014)
6. *Experimental and ab initio study of enhanced resistance to amorphization of nanocrystalline silicon carbide under electron irradiation*, L. Jamison, M-J. Zheng, S. Shannon, T. Allen, D. Morgan, I. Szlufarska, *J. Nucl. Mater.* **445**, 181-189 (2014)
7. *Structure and stability of small carbon interstitial clusters in 3C-SiC*, C. Jiang, D. Morgan, I. Szlufarska, *Acta Materialia* **62**, 162-172 (2014)

# Linking the Correlated Dependence of Grain Boundary Structure and Density to Defect Evolution Mechanisms during Radiation Damage

Mitra Taheri (Department of Materials Science & Engineering, Drexel University, Philadelphia, PA 19104)

## Program Scope

This work aims to define a framework for understanding the origin of radiation damage mechanisms in model BCC and FCC nanocrystalline materials, on which a foundation of radiation tolerant material development can be built. The key questions that will be addressed by this work are:

1. What is the influence of GB density and GB character (GBC) on radiation damage accumulation near grain boundaries in model nanocrystalline FCC and BCC alloys; how are these two effects connected?
2. In the context of radiation induced segregation (RIS), what effect does species dependent interstitial diffusion have on the GB chemistry in light of these two dependencies?

In situ and analytical transmission electron microscopy techniques are used to study both pure and alloy nanocrystalline materials under irradiation. TEM samples prepared from thin films will be irradiated *in-situ*, allowing for dynamic observation of the behavior of the alloy under ion irradiation.

## Recent Progress

### *Probing the “Immunity” of Grain Boundaries*

Advancement in the understanding of denuded zone development has shown that there exists a competition between local and global behavior in nanocrystalline materials under irradiation. Specifically, grain boundaries act like sinks no matter what their character, and as such, having a higher density of them results in smaller amounts of loops and/or loop diameters. The concept of a constant denuded zone, or even that a denuded zone is produced in the same way/by the same mechanisms, all the time is not true. This is evident in our results from irradiation of nanocrystalline iron in that the scatter of the defect density as a function of grain size does not show a clear trend of decreasing density like that reported by Rose et al. and others [1-4]. The size of the defect loops is affected in all of the samples observed with grain sizes below about 500nm, but defect density appears to be unaffected in grains where there is no prominent denuded zone. A number of grain boundaries in iron contain a very well defined denuded zone, such as the examples of boundaries in polycrystalline, ultrafine grain, and nanocrystalline iron. As the grain size is decreased the denuded zone comprises a larger portion of the grain and the

average defect density is greatly reduced. Clearly the efficiency of the grain boundaries as defect sinks play a significant role in the ability of a nanocrystalline material to reduce radiation damage.

The variations along GBs are likely due to structural effects at the misfit level. To probe the relationship between denuded zone development, grain boundary efficiency, and dislocation behavior, we coupled a recently developed algorithm [5] to determine dislocation density based on data obtained using precession electron diffraction, with in situ irradiation to determine any connection between denuded zones and this interpreted “strain.” The precession diffraction-based method was developed to estimate local dislocation densities from orientation data acquired in TEM using the Nye tensor. This spatially resolved orientation data is used to estimate the dislocation density by assuming that defects must be present to accommodate the contortion of the lattice. Using this approach local dislocation densities can be resolved with a spatial resolution on the order of 1-10 nm without the need to specify the crystal orientation or do any manual counting.

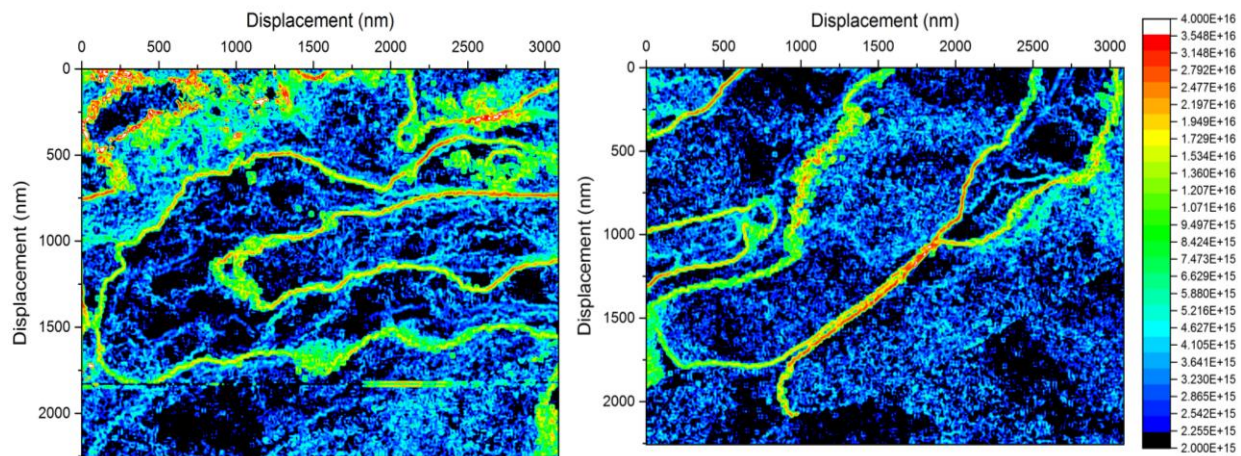


**Figure 1. Dislocation cells in rolled Cu (left) evolve into clearly defined sub-grain boundaries (right) after recovery during annealing *in situ* in TEM. Units =  $\text{m}^{-2}$ .**

In-situ irradiation was performed in a transmission electron microscope (TEM) on freestanding nanocrystalline Fe samples using the i3TEM facility in the Department of Radiation Solid Interactions at Sandia National Laboratories. Automated crystallographic orientation mapping (ACOM) was also performed via NanoMEGAS ASTAR precession diffraction. Irradiations were performed with 10 keV Helium (He) ions at 300°C with a dose rate of  $0.004 \text{ dpa}\cdot\text{s}^{-1}$  to a final dose of the irradiated samples (found using SRIM) of 18.3 dpa. Quantification of loop density and loop size (vs dpa) was then performed on specific grains of reliable diffraction contrast.

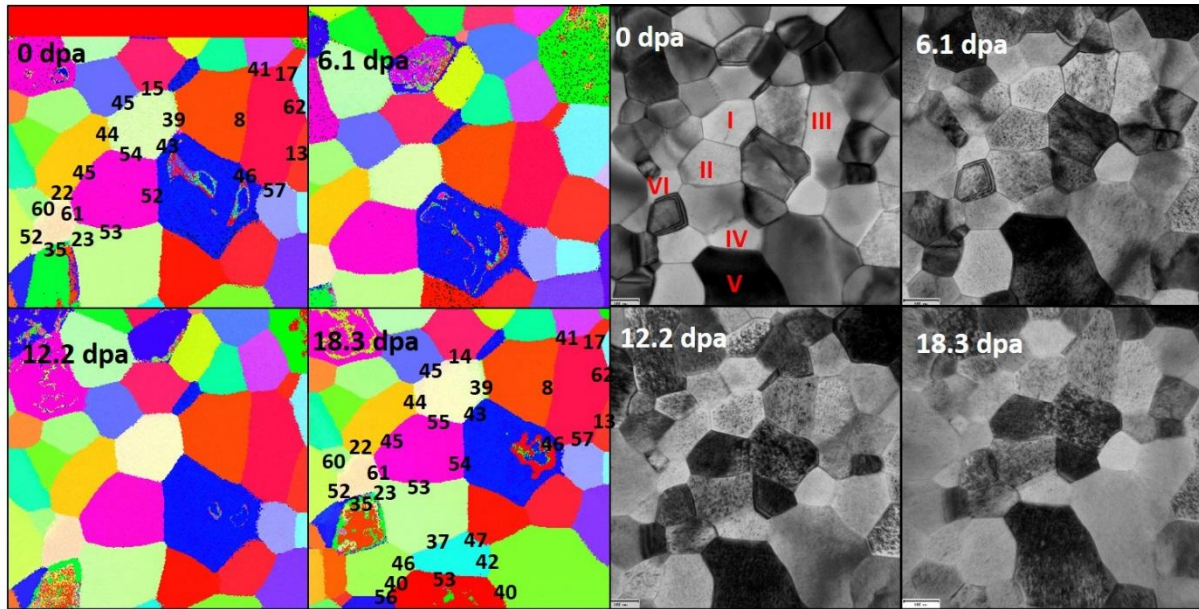


**Figure 2. Bright field TEM images and the corresponding crystallographic orientation maps of nanocrystalline Fe film before and after irradiation to different doses**

Comparing loop area and density within individual grains demonstrated different defect absorption and grain boundary interaction behavior between different grain sizes (figure 3). For example, grains with ~ 60 nm in diameter showed no change in loop density with increasing dpa, suggesting high efficiency of defect absorption by the grain boundaries. On the other hand, grains of ~270 nm exhibited an increase in loop area and a decrease in loop density with increasing dpa, demonstrating loop coalescence. Grains between 100 and 150 nm, however, showed decrease in loop density while the loop area stayed the same, which suggests loop absorption by the boundaries.

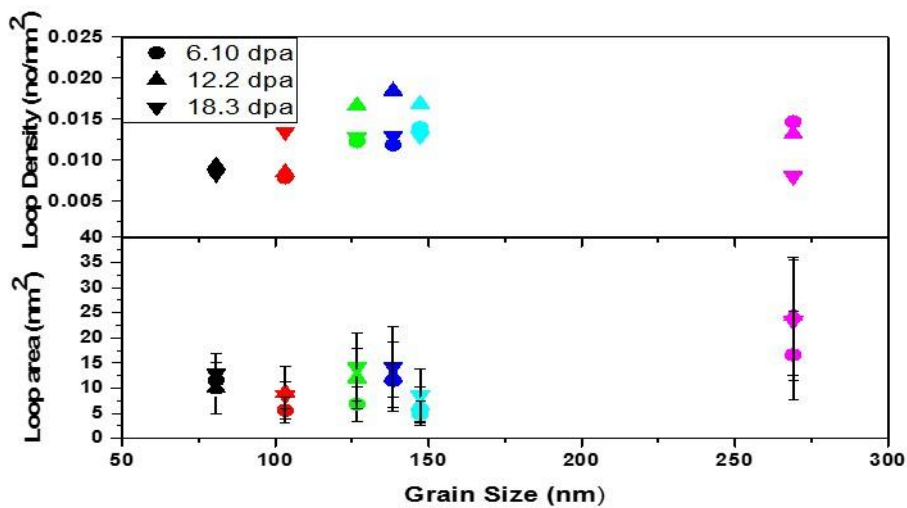


**Figure 3: Loop area and density of the six different grains (shown in Figure 2)**



To analyze this behavior further, denuded zones were assessed in great detail. Grains that appeared to have denuded zones at low dpa started to collapse after 6.1 dpa. At high dpa (~18.3 dpa), many denuded zones were completely vanished (Figure 4-top). Grain boundary analysis, using the Nye tensor method described above, demonstrated high an increase in defect densities near the boundary with increasing dose, correlating with denuded zone collapse. The breakdown of denuded zones corresponded with an increase in geometrically necessary dislocations at the boundary (Figure 4-bottom), indicating that the boundary defect structure had been changed by the absorption of radiation defects. No correlation, however, was seen between denuded zone formation and grain boundary misorientation angle

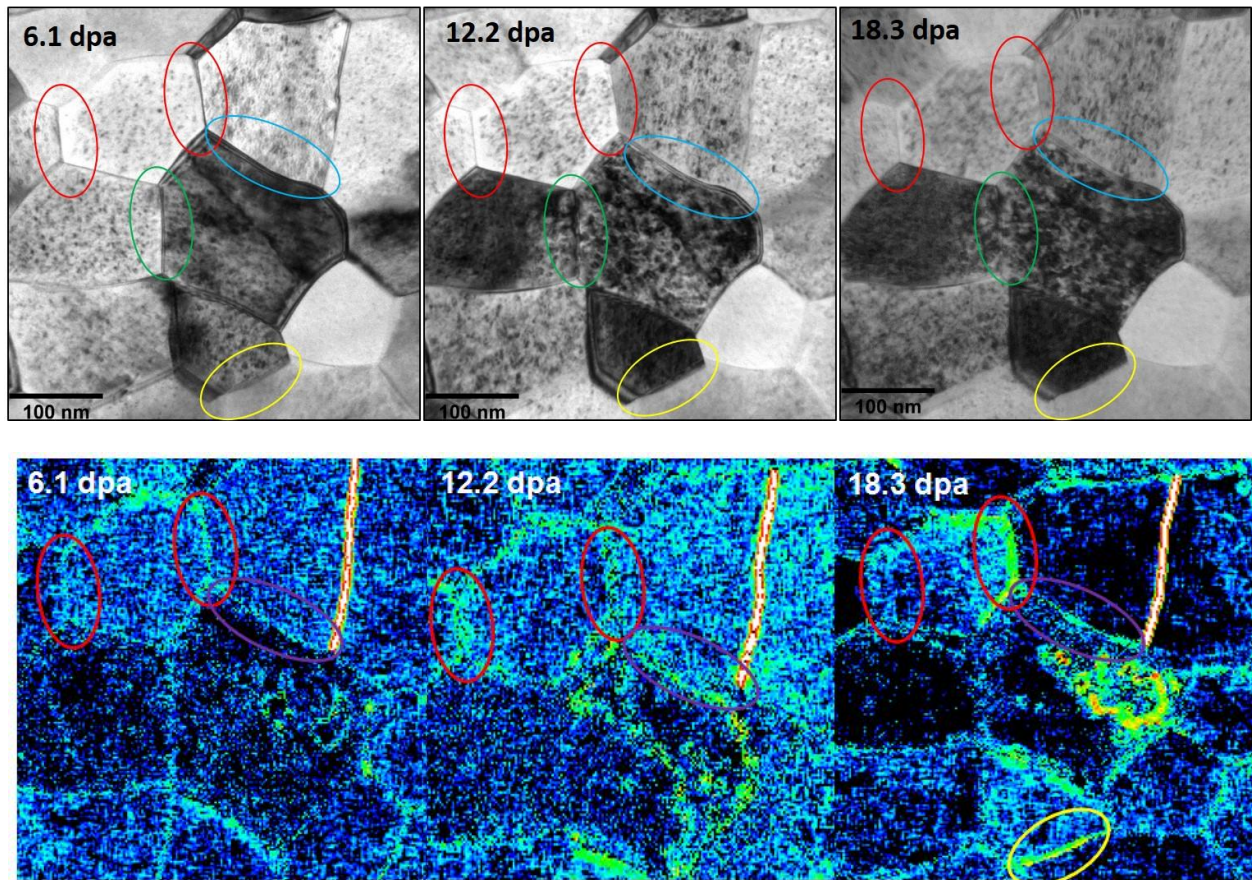


**Figure 4: Bright field TEM images of irradiated nanocrystalline iron at different dpa values demonstrating denuded zone collapse (top) and corresponding Nye tensor GND density maps of irradiated nanocrystalline iron at different dpa values demonstrating denuded zone collapse (bottom).**

In conclusion, our results indicate that in some cases, there is no clear trend of loop formation vs grain size. Comparison between different grain sizes at a particular dose can be misleading. At high doses, large grains or other grains of particular grain boundary character can show low defect density due to coalescence than small grains. Grains of similar size can have different defect densities due to different grain boundary character or other mechanisms such as local

grain boundary strain. Our results indicate that denuded zone formation is not a measure of grain boundary resistance to defect accumulation and loop formation.

### Future Plans

Our future plans include honing in on the role of grain boundary strain with respect to defect absorption. We plan to also develop a metric by which denuded zones can be defined that includes more information about grain boundaries. Finally, we are currently studying the differences in behavior between BCC and FCC nanocrystalline materials, and will continue with additional work in FCC systems (primarily Ni-based alloys).

### References

1. Rose et al, *Nuclear Instruments and Methods in Physics Research B* 127/128 (1997) 119- 122
2. T.D. Shen et al., *Nuclear Instruments and Methods in Physics Research B* 266 (2008) 921–925
3. C. Sun, K.Y. Yu, J.H. Lee, Y. Liu, H. Wang, L. Shao, S.A. Maloy, K.T. Hartwig, X. Zhang, *Journal of Nuclear Materials*, 420 (2012) 235–240
4. C. Sun, M. Song, K.Y. Yu, Y. Chen, M. Kirk, M. Li, H. Wang, X. Zhang, *Metallurgical and Materials Transactions A* 44 (2013) 1969-1974.
5. A.C. Leff, C.R. Weinberger, and M.L. Taheri, *Ultramicroscopy*, 153 (2015) 9–21.

### Publications

1. G Vetterick, JK Baldwin, A Misra, ML Taheri, “Texture evolution in nanocrystalline iron films deposited using biased magnetron sputtering,” *Journal of Applied Physics* (2014) 116 (23), 233503
2. Christopher M Barr, Leland Barnard, James E Nathaniel, Khalid Hattar, Kinga A Unocic, Izabela Szlurfarska, Dane Morgan, Mitra L Taheri, “Grain boundary character dependence of radiation-induced segregation in a model Ni–Cr alloy,” *Journal of Materials Research* (2015) 30 (09), 1290-1299
3. A.C. Leff, C.R. Weinberger, and M.L. Taheri, “Estimation of dislocation density from precession electron diffraction data using the Nye tensor,” *Ultramicroscopy*, 153 (2015) 9–21.

# Multi-Scale Study of the Role of Microstructure in the Deformation Behavior of Hexagonal Materials

**PI:** Carlos N Tomé<sup>1</sup>; **Co-PIs:** Irene J Beyerlein<sup>2</sup>, Rodney M McCabe<sup>1</sup>, Jian Wang<sup>1</sup>

**Postdocs:** Anil Kumar, Arul Kumar, Yue Liu, Huamiao Wang

<sup>1</sup> Materials Science and Technology Division – Los Alamos National Laboratory

<sup>2</sup> Theoretical Division – Los Alamos National Laboratory

## Program Scope

The complexity of plastic deformation in Hexagonal Close Packed (HCP) materials originates on dislocation glide taking place in a few restricted planes, with different threshold stress of activation, and the stress induced twinning transformations that contribute to accommodate shear. In this Program we pursue a comprehensive study of the shear mechanisms of twinning in HCP. We link these transformations with the macroscopic plastic response of metallic aggregates. The systems studied are the HCP metals Mg, Zr, Be. This comprehensive research links modeling with experimental studies, at length scales spanning from the atomistic to the continuum. The overarching goals are: a) to improve our understanding of the basic crystallographic mechanisms of shear localization and their role in deformation; b) to develop a predictive multi-scale modeling capability based on such mechanisms. **The deliverables of this project are:** state-of-the-art material models at atomistic (micro), grain (meso), and polycrystalline (macro) length scales; mechanism-based constitutive laws for HCP; new experimental characterization techniques. The numerical and experimental tools developed through this program are shared with other LANL programs and with the Materials Science community.

## Recent Progress (FY 2015)

During FY 2015 we used TEM, EBSD and MD to characterize the ‘lateral’ (as opposed to ‘forward’ and ‘thickness’) growth of twins, and the configuration of the ‘lateral’ facet of the twin, which we call the ‘dark side’ (Fig 1) [Liu et al, 2015]. We believe that understanding this feature - curiously not accounted for in any

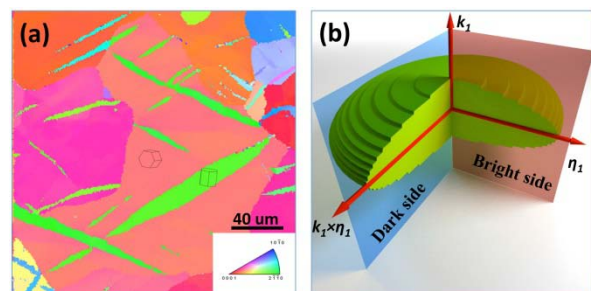


Figure 1: Usual appearance of twins (bright side) and schematic representation of twin showing the bright and dark sides



previous study - is necessary to fully understand twin properties, interactions, and mobility. In addition, we used microscopy to investigate twin-twin junctions that form on cycled Mg, and that are responsible for increased hardening behavior (Fig 2), with the ultimate purpose of developing a constitutive law that accounts for such microstructural evolution [Yu et al, 2015]. The ‘dark side’ of twins and the characterization of twin-twin junctions will be addressed in our Project’s poster, titled **“Low scale characterization of twins in HCP using microscopy and modeling”**.

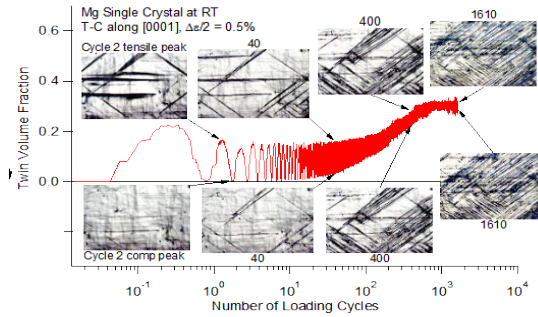


Figure 2: Increasing twin-twin junctions during cycling of Mg single crystal

The subject of the oral presentation is **“Introducing probabilistic distributions at the mesoscale for the modeling of hexagonal materials”** and focuses on a new paradigm that we started developing in our Project more than two years ago. The paradigm is based on recognizing that the macroscopic mechanical response of polycrystals is the average manifestation of local behavior and states inside the grains. Such local behavior and states (i.e.: stress distributions, plus dislocation, twin and grain boundary structures) are usually very inhomogeneous. And, while macroscopic models describe the mechanical response in terms of effective average magnitudes (such as average dislocation density or average twin fraction), the aforementioned intra-granular inhomogeneity adds to the inter-granular inhomogeneity (grain orientation) to affect the macroscopic response, especially when strain-path-changes are involved.

In our DOE-BES Program on HCP materials we introduce the experimental statistical characterization of micro-structure and stress distributions into the development of grain-scale models. The latter are in turn implemented probabilistically into the polycrystal plasticity simulation models VPSC and E-VPSC, in what constitutes a paradigm for linking length scales.

**In this talk we present three examples of such approach, namely: twin nucleation and twin growth treated as stochastic events, and stress relaxation treated as shifts in internal stress distributions.**

Twin nucleation is driven by local stresses and atomistic configurations at grain boundaries. Both are stochastic entities and we introduce them in a micro-scale model that predicts which twin variant

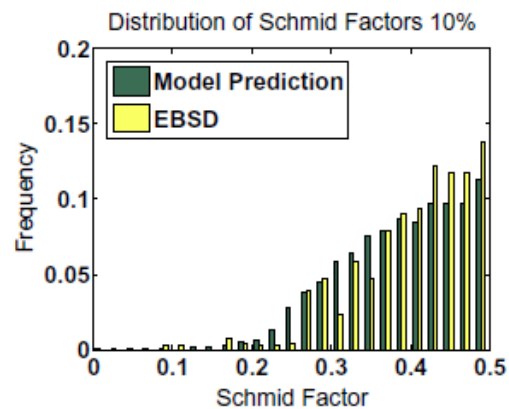


Figure 3: Predicted and measured distribution of twins after 10% compression of Zr according to their Schmid Factor (orientation)

will nucleate and from which grain boundary. Nucleation of the right fraction of variants determines which variants will be able to propagate and contribute to strain in each grain, which in turn determines the stress-strain hardening response of the polycrystal and the texture evolution observed. We have implemented this nucleation model in the polycrystal code VPSC and the predictions are consistent with our experimental characterization. Figure 3 shows a comparison of measured and predicted tensile twins as a function of their Schmid factor (0.5 is best oriented, 0 is worst oriented) obtained as part of our research in deformation of Zr [Niezgoda et al, 2014]

Twin growth is affected by back stresses induced by the twin shear transformation and by the reaction to it exerted by neighboring grains, as experimentally documented in our Project [Balogh et al, 2013; Arul Kumar et al, 2015]. As a consequence of the back stress the propagation of a twin in a grain will be conditioned by the grain size and by the orientation of its neighbors, which are stochastic entities. We use local crystal calculations to find how those variables affect the threshold stress for twin propagation. We account for such dependence of the threshold stress used to propagate twins in the polycrystal code VPSC by introducing the (measured) distribution of grain size and neighbor orientations in a statistical fashion. Preliminary results show that the new approach predicts a decrease in twin contribution in those orientations most favorably oriented for twinning, in agreement with our EBSD statistical evidence (see Fig 4).

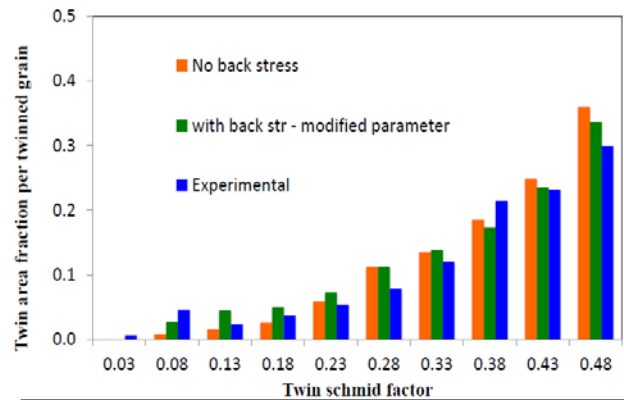


Figure 4: Predicted and measured distribution of twins after 10% compression of Mg according to their Schmid Factor (orientation indicator). Simulations were done with and without the back stress effect on twins

Finally, neutron diffraction shows that there is substantial relaxation of internal stress during mechanical tests followed by strain holds. A rapid drop of stress takes place when the test is stopped, followed by an asymptotically slower decrease. The stress relaxation and its time dependence can be explained in terms of shifts in the intra-granular stress distributions inside grains [Wang et al, 2015]. Specifically, as the distribution of resolved shear acting on dislocation

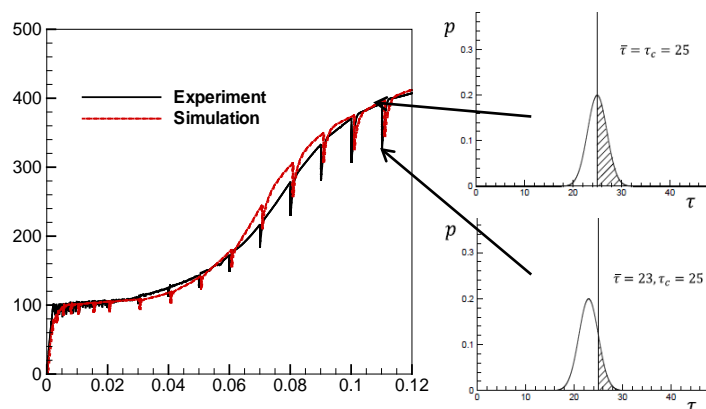


Figure 5: Predicted and measured stress-strain response of Mg AZ31 during strain holds required for neutron measurements. Schematic of distribution of resolved shear stress acting on dislocation segments, showing its evolution with time.

segments shifts left (see Fig 5), less and less segments can be mobilized. In addition, and this is a major breakthrough in linking experiments and theory at the meso length scale, the ‘width’ of those distributions can be connected to measured peak width and to dislocation densities.

## Future Plans

The future research lines build-upon the research described above and represent its logic continuation.

1- We will continue with the experimental and atomistic characterization of the ‘dark side’ of twins in HCP, in order to elucidate their lateral (screw) motion, how the dark side mobility conditions the forward propagation of the twin, and how the ‘dark side’ atomistic configuration affects the twin-grain-boundary and twin-twin interactions.

2- We will continue the experimental and atomistic characterization of twin-twin junctions, determine their strength, and introduce such knowledge into a statistical model of hardening at the grain level. We will combine such contribution of twin junctions with the other research on twin interaction with grain boundaries and will develop a model of hardening of HCP polycrystals which can explain the behavior during cyclic deformation

3- We will continue with our statistical study of how the distributions of : internal stress, dislocation density, grain size, and grain boundary misorientation determine the mechanical behavior of HCP materials deforming by slip and twinning

## References

- M. Arul Kumar, A.K. Kanjarla, S.R. Niezgoda, R.A. Lebensohn, C.N. Tomé, “Numerical study of the stress state of a deformation twin in magnesium”, *Acta Materialia* **84** (2015) 349-358
- L. Balogh, S.R. Niezgoda, A.K. Kanjarla, D.W. Brown, B. Clausen, W. Liu, C.N. Tomé, “Spatially resolved in-situ strain measurements from an interior twinned grain in bulk polycrystalline AZ31 alloy”, *Acta Materialia* 61 (2013) 3612-20
- Y. Liu, N. Li, S. Shao, J. Wang, R.J. McCabe, Y. Jiang, C.N. Tomé, “Characterizing the ‘dark side’ of  $\{10\bar{1}2\}$  deformation twins in Mg”, Submitted to *Science Materials*, August 2015
- S.R. Niezgoda, A.K. Kanjarla, I.J. Beyerlein, C.N. Tomé, “Stochastic model of twin nucleation in polycrystals: an application to hexagonal close packed metals”, *Intl J of Plasticity* 56 (2014) 119-138
- H. Wang, B. Clausen, L. Capolungo, I.J. Beyerlein, J. Wang, C.N. Tomé, “Stress and strain relaxation in magnesium AZ31 rolled plate: in-situ neutron measurement and elastic viscoplastic polycrystal modeling”, *International Journal of Plasticity* (2015, accepted)
- Q Yu, J Wang, Y Jiang, RJ McCabe, N Li, CN Tomé, “Twin–twin interactions in magnesium”, *Acta Materialia* 77 (2015) 28-42

## **Publications 2014-2015 Intellectually Led by this FWP**

1. N. Bertin, C. N. Tomé, I. J. Beyerlein, M. R. Barnett, L. Capolungo, “On the strength of dislocation interactions and their effect on latent hardening in pure Magnesium”, *International Journal of Plasticity* 62 (2014) 72-92
2. P.A. Juan, S. Berbenni, M.R. Barnett, C.N. Tomé, L. Capolungo, “A double inclusion homogenization scheme for polycrystals with hierarchical topologies: application to twinning in Mg alloys”, *Intl J of Plasticity* 60 (2014) 182-196
3. B.M. Morrow, E.K. Cerreta, R.J. McCabe, C.N. Tomé, “Toward understanding twin-twin interactions in hcp metals: utilizing multiscale techniques to characterize deformation mechanisms in Mg”, *Mats Science & Eng A613* (2014) 365-371
4. S.R. Niezgod, A.K. Kanjarla, I.J. Beyerlein, C.N. Tomé, “Stochastic model of twin nucleation in polycrystals: an application to hexagonal close packed metals”, *Intl J of Plasticity* 56 (2014) 119-138
5. J. Wang, I.J. Beyerlein, C.N. Tomé, “Reactions of lattice dislocations with grain boundaries in Mg: implications on the micro scale from atomic-scale calculations”, *Intl J of Plasticity* 56 (2014) 156-172
6. J. Wang, Q. Yu, Y. Jiang, I. J. Beyerlein, “Several twinning-associated boundaries in hexagonal-close-packed metals”, *JOM* 66 (2014) 95-101
7. Q. Yu, J. Wang, Y. Jiang, R.J. McCabe, N. Li, C.N. Tomé, “Twin-twin interactions in Magnesium”, *Acta Mater* 77 (2014) 28-42
8. Q. Yu, J. Wang, Y. Jiang, R. McCabe, C.N. Tomé, “Co-zone {10-12} twin interaction in Magnesium single crystal”, *Materials Research Letters* 2(2) (2014) 182-188
9. Q. Yu, Y Jiang, J Wang, “Tension-compression-tension tertiary twins in coarse-grained polycrystalline pure magnesium at room temperature”, *Philosophical Magazine Letters*, (2015), DOI:10.1080/09500839.2015.1022621
10. H. Wang, PD Wu, SY Lee, J Wang, KW Neale, “Numerical study of the effects of shear deformation and superimposed hydrostatic pressure on the formability of AZ31B sheet at room temperature”, *International Journal of Mechanical Sciences* 92 (2015) 70-79
11. H. El Kadiri, CD Barrett, J Wang, CN Tomé, “Why are twins profuse in magnesium?” *Acta Materialia* 85 (2015) 354-361
12. A. Kumar, J Wang, CN Tomé, “First-principles study of energy and atomic solubility of twinning-associated boundaries in hexagonal metals”, *Acta Materialia* 85 (2015) 144-154

13. Q. Yu, Y Jiang, J Wang, "Cyclic deformation and fatigue damage in single-crystal magnesium under fully reversed strain-controlled tension-compression in the [10-10] direction", *Scripta Materialia* 96 (2015) 41-44
14. H. Wang, PD Wu, J Wang, "Modelling the role of slips and twins in magnesium alloys under cyclic shear", *Computational Materials Science* 96 (2015) 214-218
15. B.Y. Liu, L Wan, J Wang, E Ma, ZW Shan, "Terrace-like morphology of the boundary created through basal-prismatic transformation in magnesium", *Scripta Materialia* 96 (2015) 86-89
16. H. Wang, P Wu, J Wang, "Numerical assessment of the role of slip and twinning in Magnesium alloy AZ31 B during loading path reversal", *Metallurgical and Materials Transactions A46* (2015) 3079-3090
17. Q. Yu, J Wang, Y Jiang, RJ McCabe, N Li, CN Tomé, "Twin-twin interactions in magnesium", *Acta Materialia* 77 (2015) 28-42
18. B.M. Morrow, E.K. Cerreta, R.J. McCabe, C.N. Tomé, "Toward understanding twin-twin interactions in hcp metals: utilizing multiscale techniques to characterize deformation mechanisms in Mg", *Mats Science & Eng A613* (2014) 365-371
19. N. Bertin, C. N. Tomé, I. J. Beyerlein, M. R. Barnett, L. Capolungo, "On the strength of dislocation interactions and their effect on latent hardening in pure Magnesium", *International J of Plasticity* 62 (2014) 72-92
20. B.M. Morrow, R.J. McCabe, E.K. Cerreta, C.N. Tomé, "Observations of the atomic structure of tensile and compressive twin boundaries and twin-twin interactions in Zr", *Metall Mater Transactions* 45A (2014) 5891-97
21. M. Arul Kumar, A.K. Kanjarla, S.R. Niezgod, R.A. Lebensohn, C.N. Tomé, "Numerical study of the stress state of a deformation twin in magnesium", *Acta Materialia* 84 (2015) 349-358
22. P.A. Juan, C. Pradalier, S. Berbenni, R. McCabe, C.N. Tomé, L. Capolungo, "A statistical analysis of the influence of microstructure and twin-twin junctions on twin nucleation and twin growth in Zr", *Acta Mater* 95 (2015) 399-410
23. H. Wang, B. Clausen, L. Capolungo, I.J. Beyerlein, J. Wang, C.N. Tomé, "Stress and strain relaxation in magnesium AZ31 rolled plate: in-situ neutron measurement and elastic viscoplastic polycrystal modeling", *International Journal of Plasticity* (accepted)

## Chemomechanics of Far-From-Equilibrium Interfaces (COFFEI)

Harry L. Tuller, Krystyn J. Van Vliet, W. Craig Carter, Yet-Ming Chiang, and Bilge Yildiz, Departments of Materials Science and Engineering; and Nuclear Science and Engineering

Massachusetts Institute of Technology, Cambridge, MA 02139

### Program Scope

Brittle oxide functional materials, such as those utilized in solid oxide fuel cells, permeation membranes and lithium-ion batteries, exhibit significant operational stresses induced via chemical and electrochemical diffusion across material interfaces. Virtually all functional materials in battery electrodes undergo considerable mechanical strain during Li flux at solid-liquid and solid-solid interfaces, which can promote fracture and decrease charge capacity. Likewise, electrode materials in fuel cell components and permeation membranes operate under steep oxygen activity gradients, and often suffer from chemically induced strains and highly variable energy conversion efficiencies. At the same time, exciting new evidence suggests that certain types of highly defective ionic compounds can relieve stresses by defect redistribution or phase changes, and thereby tolerate larger deformations and/or induce enhanced charge and mass transport near interfaces. The discovery of highly active electrode materials for reliable energy storage in portable batteries, and for oxygen reduction in solid oxide fuel cells at intermediate temperatures, remain important challenges for improved materials stability and decreased system cost. Overcoming this challenge in energy storage electrodes requires improved understanding of electrochemical fatigue during redox cycles, to minimize mechanical fracture via material and device design. Surmounting this challenge in energy conversion electrodes requires understanding of the mechanisms correlating the oxygen reduction reaction (ORR) kinetics and the inherent surface structure of the electrode materials. In-situ measurements and strain-manipulated interfaces present new opportunities for advances in both energy storage and conversion materials. Tailoring the surface chemistry, atomic and electronic structure of

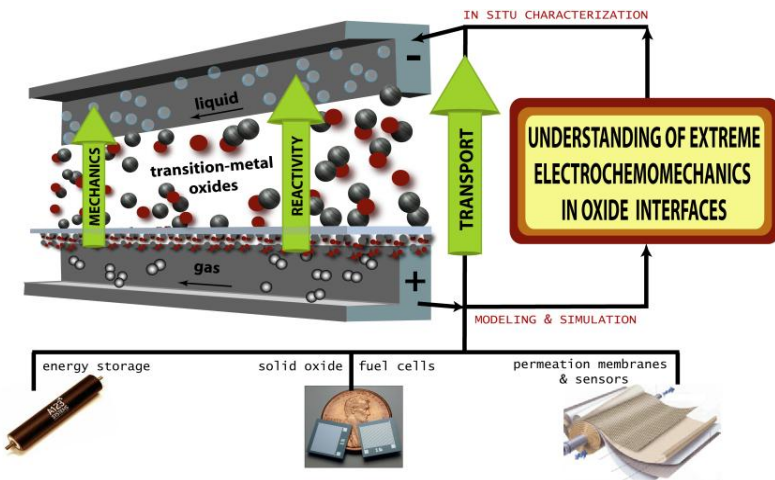


**Figure 1.** COFFEI Group research focuses on fundamental understanding of the coupling between electrochemical ion transport and mechanical stress in transition/rare earth metal oxides key to energy applications.

nonstoichiometric transition metal oxides (TMOs) and rare earth oxides (REOs) for faster oxygen reduction kinetics under harsh conditions of high temperature, reactive gas pressure and material strain state is critical, and requires fundamental understanding of the coupling among the historically important subfields of solid-state electrochemistry, transport kinetics, and mechanical deformation for nonstoichiometric TMOs. In particular, the **chemomechanical coupling** of defect concentrations, ionic transport, electro-catalytic activity and stored elastic energy is particularly acute in the far-from-equilibrium conditions typical of energy device applications (Figure 1).

## Recent Progress

The interdisciplinary group of MIT faculty from *Materials Sc. & Eng. (H.L. Tuller - Lead PI, W.C. Carter, Y.M. Chiang, K.J. Van Vliet and Nuclear Sc. & Eng. (B. Yildiz)* addresses these important issues by (a) applying advanced *in-situ* and *ex-situ* characterization tools to characterize model materials and interfaces synthesized with molecular-level control, under both laboratory-controlled and extreme environments representative of energy device operation; and (b) employing computational modeling and simulation frameworks to predict transport mechanisms, reactivity and stability of these model materials and interfaces under significant chemical strains typical of energy device operation. This program includes two tightly integrated thrusts. Thrust I focuses on chemomechanics due to cation transport and interactions with solid electrolytes in battery TMOs, while Thrust II focuses on chemomechanics of anion transport at fuel cell TMO and REO interfaces. We provide only one example for each of Thrusts I and II, among many recent integrated experimental and computational efforts.

### **Thrust I, Example I.1. Identifying effects of electrochemical cycling on electrode mechanical properties**

Our interdisciplinary COFFEI collaborations enabled us to propose and quantify the phenomenon of “electrochemical shock.” This is fracture of LIB cathode particles arising from the chemomechanical stress that evolves in Li-ion intercalation materials during battery charging and discharging, leading to mechanical fracture of the cathode particles.<sup>i,ii,iii</sup> Correlations between these fracture events and impedance growth, a primary mode of battery degradation, have been suggested, but causal mechanisms remain unestablished. *Van Vliet, Chiang, and Carter* have now shown that key mechanical properties depend strongly on prior electrochemical history of cathode materials such as LCO, as measured via *in-situ* nanoindentation and chemical analysis. ***Charging of LCO for even a single cycle can reduce the fracture toughness  $K_{Ic}$  of this compound (Fig. 2a) by nearly an order of magnitude (Fig. 2b)<sup>iii</sup>.*** We found such degradation of mechanical properties due to battery charging and discharging to correlate with accumulated inter- and intragranular cracking associated with massive  $\text{Li}^+$  ion flux. ***This marked change in fracture toughness holds significant implications for our prediction of the particle diameters resistant to catastrophic fracture, as this critical particle size depends directly on  $K_{Ic}$  in our electrochemical shock maps (Fig. 2c).*** This chemomechanical coupling suggests that: (i) fracture properties of existing and new cathode particles should be verified experimentally and

in-situ; and (ii) mechanisms by which fracture within LIB cathode materials and at cathode-electrolyte interfaces must be better understood to increase LIB mechanical durability and battery lifetime.

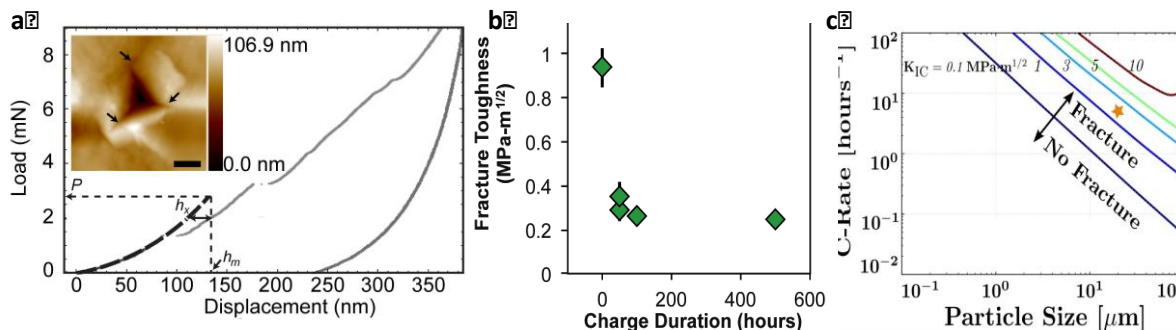


**Figure 2.** (a) Fracture toughness quantified via in-situ nanoindentation of LCO particles. (b) Fracture toughness decreases nearly ten fold upon electrochemical cycling; (c) The magnitude of this fracture toughness directly correlates with the cathode particle size for which the electrode is mechanically robust at specific charge- or C-rates of the battery. Adapted from COFFEI-sponsored publications (refs. ii, iii).

### Thrust II, Example II.1. Identifying and controlling factors responsible for chemical expansion

Using molecular dynamics (MD), density functional theory, and empirical analysis, Yildiz, Tuller, and Bishop showed that chemical expansion in ceria arises from two opposing mechanisms associated with oxygen loss, i.e., lattice dilation upon reduction of cations (e.g.,  $\text{Ce}^{4+} \rightarrow \text{Ce}^{3+}$ ) and shrinkage upon oxygen vacancy formation<sup>iv</sup>. We recently demonstrated that for several fluorite oxides, the oxygen vacancy radius shows a maximum around the lattice parameter for  $\text{CeO}_2$  (see Fig. 4a)<sup>v</sup>. This suggested a new strategy for *engineering* chemical expansion in these oxides by substituting Zr (with a smaller vacancy radius) for Ce in acceptor doped cerium oxide. As shown by Fig. 4b, the solid solution resulted in a > 50% reduction in chemical expansion coefficient over acceptor doped ceria without Zr<sup>vi</sup>. This approach creates the opportunity to *engineer and optimize materials towards achieving a near zero coefficient of chemical expansion* by more effectively compensating the two opposite trends.

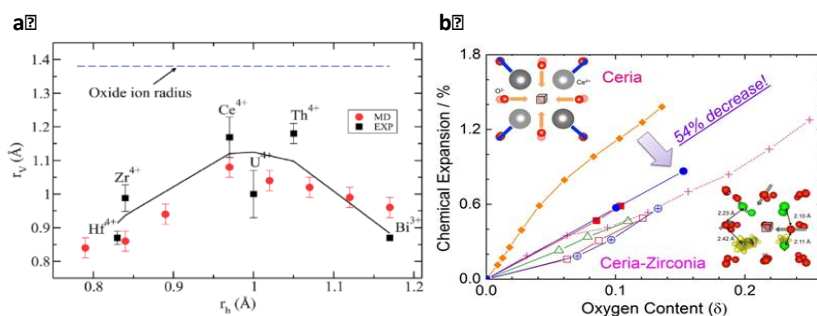


**Figure 6.** (a) Oxygen vacancy radius ( $r_v$ ) versus the host cation radius ( $r_h$ ) for fluorite oxides. (b) Large decrease in chemical expansion coefficient upon partial substitution of Zr for Ce in  $\text{Pr}_{0.1}\text{Zr}_{0.4}\text{Ce}_{0.5}\text{O}_{1.95-\delta}$ , (+) are computational data, others measured via dilatometry or HTXRD over 700 - 900°C.

We then predicted, with the aid of a computational study, that more de-localized charges associated with reduced cations lead to decreased chemical expansion coefficients<sup>vii</sup>. In order to



experimentally validate this result, *Tuller, Van Vliet, and Bishop* investigated two model systems with controllable degrees of charge localization. In both cases, a multivalent element is partially substituted for one of the host cations. Upon reduction of the material, electrons are highly localized on the multivalent element for low concentrations. In  $\text{La}_{0.9}\text{Sr}_{0.1}(\text{Ga},\text{Ni})\text{O}_{2.95-\delta}$  (LSGN), with increasing Ni content, the chemical expansion coefficient showed a decrease consistent with charge de-localization<sup>viii</sup>. *In situ* high temperature X-ray diffraction (HTXRD) measurements showed slight distortions in the symmetry for LSGN, highlighting the more complex relationship between non-stoichiometry parameter  $\delta$  and chemical expansion in these perovskite systems.

## Future Plans

Ongoing and planned studies in Thrust I focus on three main questions with *attendant design challenges for energy storage via lithium ion batteries (LIBs)*, specifically for cathodes and solid electrolyte materials, via *in situ* chemomechanical experiments and models:

(a) **Increase *operando* mechanical integrity:** How and why do the mechanical properties of candidate cathode oxides & solid electrolyte materials vary with electrochemical history? *Which cathode compositions and microstructures maximize fracture toughness?*

(b) **Explore coupled strain-transport mechanisms:** Are interfaces between cathode oxide & solid electrolyte materials chemically stable under electro-chemo-mechanical cycling of the cathode material? *How can the cathode-electrolyte microstructure be optimized to maximize ion transport under cycling-induced strains?*

(c) **Control interface reactivity via strain:** Does electrochemical fatigue – the extension of electrochemical shock to repeated charge-discharge cycles – correlate with impedance growth? *If so, which microstructural attributes of the cathode oxide and the cathode-electrolyte interface reduce failure probability and minimize capacity fade over many electrochemical cycles?*

Ongoing and planned studies in Thrust II focus on three main questions, with *attendant scientific underpinnings for energy conversion in solid oxide fuel cells (SOFCs) with extension to electrolyzers and gas permeation membranes*, via *in situ* experiments and models:

(a) **Increase *operando* mechanical integrity:** Can strain-to-failure of SOFC cathode materials be increased to extend the durable lifetime of SOFCs? *What are the roles of crystal structure, cation substitution, oxidation state and defect ordering in influencing chemical dilation and mechanical strength.*

(b) **Explore coupled strain-transport mechanisms:** Can strain in SOFC cathodes be engineered to increase ionic conductivity? *How can we elucidate and control stability of hetero-nanostructures under electrochemical driving forces?*

(c) **Control interface reactivity via strain:** Can strain in SOFC cathodes be engineered to increase the oxygen reduction reaction (ORR)? *What are the roles of crystal structure, cation type, and in-plane strain at hetero-interfaces in influencing electronic structure and point defect physics and their impact on pathways and barriers for oxygen reduction and diffusion?*

## References

- <sup>i</sup> Zhang, X., Shyy, W. & Sastry, A. M. Numerical Simulation of Intercalation-Induced Stress in Li-Ion Battery Electrode Particles. *J. Electrochem. Soc.* 154, A910–A916 (2007).
- <sup>ii</sup> Woodford, W. H.; Chiang, Y.-M.; Carter, W. C. "Electrochemical Shock" of Intercalation Electrodes: A Fracture Mechanics Analysis, *J. Electrochem. Soc.* 157 A1052-A1059 (2010).
- <sup>iii</sup> Swallow, J.G., Woodford, W.H., McGrogan, F.P., Ferralis, N., Chiang, Y.-M., and Van Vliet, K.J., *Effect Of Electrochemical Charging On Elastoplastic Properties And Fracture Toughness Of LixCoO<sub>2</sub>*, *Journal of the Electrochemical Society* 161 F3084-F3090, 2014
- <sup>iv</sup> D. Marrocchelli, S. R. Bishop, H. L. Tuller and B. Yildiz, *Understanding Chemical Expansion in Non-stoichiometric Oxides: Ceria and Zirconia Case Studies*, *Advanced Functional Materials*, 22 [9] 1958-1965 (2012).
- <sup>v</sup> D. Marrocchelli, S. R. Bishop, and J. Kilner, *Chemical expansion and its dependence on the host cation radius*, *J. Mater. Chem. A*, 1, 7673-7680 (2013).
- <sup>vi</sup> S. R. Bishop, D. Marrocchelli, F. Wang, K. Amezawa, K. Yashiro, and G. Watson, *Reducing the chemical expansion coefficient in ceria by addition of zirconia*, *Energy Environ. Sci.*, 6, 1142-1146 (2013).
- <sup>vii</sup> D. Marrocchelli, S. R. Bishop, H. L. Tuller, G. W. Watson and B. Yildiz, *The Effect of Charge Localization on Chemical Expansion in Cerium Oxide*, *Phys. Chem. Chem. Phys.*, 14, 12070-12074 (2012).
- <sup>viii</sup> N. Perry, S.R. Bishop, H.L. Tuller, *Tailoring Chemical Expansion by Controlling Charge Localization: In Situ X-ray Diffraction and Dilatometric Study of (La,Sr)(Ga,Ni)O<sub>3-δ</sub> Perovskite*, *Journal of Materials Chemistry A*, 2, 18906-18916 (2014).

## Publications

- Swallow, J., ;W. Woodford, Y. Chen, Q. Lu, J.J. Kim, D. Chen, Y.M.Chiang, W.C. Carter, B. Yildiz, H. Tuller, and K. J. Van Vliet, *Chemomechanics of Ionically Conductive Ceramics for Electrical Energy Conversion and Storage*, *J. Electroceram.*, 32, 3-27 (2014).
- Bishop, S.R.; D. Marrocchelli, C. Chatzichristodoulou, M. Mogensen, N. H. Perry, H. L. Tuller, and E. D. Wachsman, *Chemical Expansion: Implications for Electrochemical Energy Storage and Conversion Devices*, *Annual Review of Materials Research*, 44, 205-239 (2014).
- Swallow, J.G., Woodford, W.H., McGrogan, F.P., Ferralis, N., Chiang, Y.-M., and Van Vliet, K.J., *Effect Of Electrochemical Charging On Elastoplastic Properties And Fracture Toughness Of LixCoO<sub>2</sub>*, *Journal of the Electrochemical Society* 161 F3084-F3090 (2014)
- Woodford, W.H.; Y.-M. Chiang, W.C. Carter. *Quantifying Reliability Statistics For Electrochemical Shock Of Brittle Materials*, *J. Mech. Phys. Sol.* 70, 71-83 (2014).

- 
- Marrocchelli, D.; C. Chatzichristodoulou, and S. R. Bishop, *Defining chemical expansion: the choice of units for the stoichiometric expansion coefficient*, Phys. Chem. Chem. Phys., 16, 9229-9232 (2014).
- Perry, N.H.; S.R. Bishop, H.L. Tuller, *Tailoring Chemical Expansion by Controlling Charge Localization: In Situ X-ray Diffraction and Dilatometric Study of (La,Sr)(Ga,Ni)O<sub>3-δ</sub> Perovskite*, Journal of Materials Chemistry A, 2, 18906-18916 (2014).
- Perry, N.H.; J. Kim, S. R. Bishop, and H. L. Tuller, *Strongly Coupled Thermal and Chemical Expansion of SrTi<sub>0.65</sub>Fe<sub>0.35</sub>O<sub>3-α</sub>*, J. Mat. Chem. A, 3, 3602-3611 (2015).
- Perry, N.H.; D. Pergolesi, S. R. Bishop, and H. L. Tuller, *Defect Chemistry and Surface Oxygen Exchange Kinetics of La-Doped Sr(Ti,Fe)O<sub>3-α</sub> in Oxygen-Rich Atmospheres*, Solid State Ionics (2014).
- Chen, D.; Y. Cao, D. Weng, H. L. Tuller, *Defect and Transport Model of Ceria-zirconia Solid Solutions: Ce<sub>0.8</sub>Zr<sub>0.2</sub>O<sub>2-δ</sub> - an Electrical Conductivity Study*, Chem. Mater., 26 (17), 5143–5150 (2014)
- Chen, D.; S. R. Bishop, and H. L. Tuller, *Nonstoichiometry in Oxide Films Operating Under Anodic Conditions: A Chemical Capacitance Study of the Praseodymium-Cerium Oxide System*, Chem. Mat., 26, 6622-6627 (2014).
- Chen, D.; H. L. Tuller, *Voltage Controlled Nonstoichiometry in Oxide Thin Films: Pr<sub>0.1</sub>Ce<sub>0.9</sub>O<sub>2-δ</sub> Case Study*, Adv. Funct. Mater., (2014).
- Kim, J.J.; S.R. Bishop; N. J. Thompson, D. Chen, and H. L. Tuller, *Investigation of Nonstoichiometry in Oxide Thin Films by Simultaneous In Situ Optical Absorption and Chemical Capacitance Measurements: Pr Doped Ceria - Case Study*, Chem. Mat., 26 [3], 1374-1379 (2014).
- Engel, J.; S. R. Bishop, H. L. Tuller, L. Vayssieres, *In-Situ Characterization of Anatase TiO<sub>2</sub> Q-dots*, Adv. Funct. Mater., 24, 4952-4958 (2014).
- Knauth, P.; J. Engel, S. R. Bishop, H. L. Tuller, *Study of Compaction and Sintering of Nanosized Oxide Powders by In Situ Electrical Measurements and Dilatometry: Nano CeO<sub>2</sub> – Case Study*, J. Electroceram., (2015).
- Swallow, J.G.; J. J. Kim, D. Chen, S. Bishop, J. F. Smith, H. Tuller, and K. J Van Vliet, *Facile method to quantify dynamic chemical expansion of non-stoichiometric oxides in situ*, ECS Conference on Electrochemical Energy and Storage, SOFC XIV, Glasgow, Scotland (2015).
- Swallow J.G.; J. J. Kim, Sean Bishop, J. F. Smith, M. Kabir<sup>4</sup>, H. L. Tuller, and K. J. Van Vliet, *Elastic properties of (Pr, Ce)O<sub>2-δ</sub> thin film electrodes under in operando conditions of solid oxide fuel cells*, ECS Conference on Electrochemical Energy and Storage, SOFC XIV, Glasgow, Scotland (2015).
- Bishop, S.R.; D. Chen, J. Sheth, S. Misture, B. Sheldon, J. J. Kim, and H. L. Tuller, *Impact of size scale on electro-chemo-mechanical coupling properties in MIECs: Bulk and thin film (Pr,Ce)O<sub>2-δ</sub>*, ECS Transactions, 61 (1) 31-36 (2014) .
- Sun, L.; D. Marrocchelli, & B. Yildiz, *Edge dislocation slows down oxide ion diffusion in doped CeO<sub>2</sub> by segregation of charged defects*. Nat Commun. 6 6294 (2015).

- 
- Marrocchelli., D.; S. Lixin, & B. Yildiz, *Dislocations in SrTiO<sub>3</sub>: Easy To Reduce But Not So Fast For Oxygen Transport. Journal of the American Chemical Society* (2015).
- Chen, Y.; Z. Cai, Y. Kuru, W. Ma, H. L. Tuller and B. Yildiz, *Electronic Activation of Cathode Superlattices at Elevated Temperatures – Source of Markedly Accelerated Oxygen Reduction Kinetics*, *Adv. Energy Mater.* 3, 1221-1229 (2013).
- Ma, Y.; J. J. Kim, N. Tsvetkov, Y. Kuru, Z. Cai; Y. Chen, H. L. Tuller; B. Yildiz, *Vertically Aligned Nanocomposite La<sub>0.8</sub>Sr<sub>0.2</sub>CoO<sub>3</sub>/(La<sub>0.5</sub>Sr<sub>0.5</sub>)<sub>2</sub>CoO<sub>4</sub> Cathodes – Electronic Structure, Surface Chemistry and Oxygen Reduction Kinetics*, *J Mat. Chem. A*, 3, 207-219 (2015).

# Disorder & diffusion in complex oxides: towards prediction & control

Blas Pedro Uberuaga, Los Alamos National Laboratory

## Program Scope

Mass transport is the defining property for a number of technologically important complex oxides, with numerous applications, from fuel cells to nuclear materials. Thus, there is great incentive for both predicting and controlling mass transport. Intrinsic site disorder, in which cation species of different types exchange position, is one key mechanism for controlling transport. In addition, site disorder can itself be controlled with irradiation. Not only is site disorder a controlling factor in the radiation tolerance of complex oxides, it also greatly influences mass transport. There is great potential in both predicting and controlling diffusion as it relates to site disorder in complex oxides. Further, given that site disorder greatly influences radiation damage evolution in complex oxides, there is a need for understanding not only anion but also cation transport – how both depend on site disorder in the material and how that site disorder depends on crystal structure and chemistry. Conversely, radiation damage can be used as a tool to induce site disorder. We use a combination of state-of-the-art atomistic modeling methods with advanced experimental characterization to determine how the atomic scale mechanisms governing mass transport depend on the local site disorder as a function of the chemistry and structure of the material.

## Recent Progress

Over the last two years, we have had two major foci. The first involves applying molecular dynamics (MD) and accelerated molecular dynamics methods to study the kinetic behavior of complex oxides. The second focus has been on developing experimental capability to examine defect mobilities in a variety of environments.

Our simulation efforts have examined two aspects of defect kinetics in complex oxides. First, in both pyrochlores ( $A_2B_2O_7$ ) and double perovskites ( $AA'BB'O_6$ ), we have studied the migration of oxygen as a function of cation ordering. In the case of pyrochlores, we examined how cation disorder – mixing between the A and B sublattices – influences oxygen transport. Pyrochlores have been widely studied in the past as fast ion conductors where it has been shown that oxygen ionic conductivity increases significantly as the chemistry changes from  $B=Ti$  to  $B=Zr$  [1]. However, experimentally, it is difficult to separate the roles of chemistry and disorder. Using MD [2], we separated these effects, showing that the increase in conductivity as  $Ti \rightarrow Zr$  is

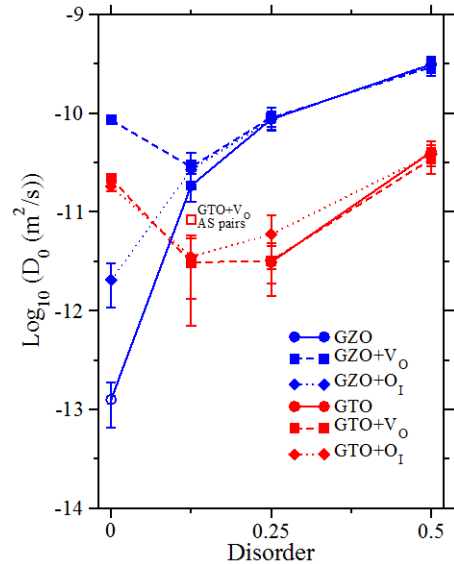


Figure 1: Oxygen diffusivity as a function of disorder and stoichiometry (oxygen vacancies or interstitials) in GZO ( $Gd_2Zr_2O_7$ ) and GTO ( $Gd_2Ti_2O_7$ ) as found with molecular dynamics.

consequence of *both* the changing chemistry and cation disorder, see Fig. 1. Zr pyrochlores exhibit higher ionic conductivities than Ti pyrochlores for the same level of cation disorder. However, in both pyrochlores, ionic conductivity increases with A/B cation mixing. When excess oxygen defects are introduced, we find that the change in conductivity with cation disorder is non-monotonic, with small amounts of cation disorder slowing oxygen diffusion down.

We also simulated how oxygen vacancies diffuse in double perovskites as a function of cation ordering [3]. The cations in double perovskites can order in several different ways. On each sublattice, they can be ordered in a columnar, layered or rocksalt manner. When the two sublattices are combined, this leads to nine distinct ordered structures. Using temperature accelerated dynamics (TAD), we determined the pathway and activation energy for oxygen vacancies in each of these orderings. Both the activation energy and the fundamental nature (one-dimensional versus three-dimensional) of migration are sensitive to the cation ordering. Surprisingly, mobility can be faster in double perovskites than in either of the single perovskite end members, as highlighted in Fig. 2.

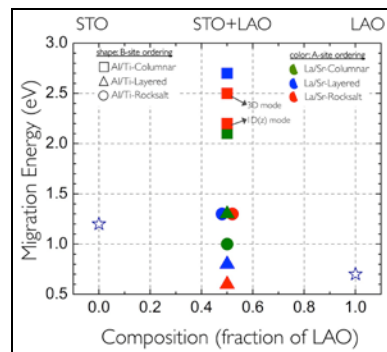


Figure 2: Migration energies for oxygen vacancies in double perovskites as a function of cation ordering.

On the other front, we have been studying cation dynamics, which are critical for understanding not only radiation damage evolution but also fundamental processes associated with sintering. Two examples highlight our efforts in this area. First, in a paper recently accepted in *Phys. Chem. Chem. Phys.* [4], we simulated, using TAD, the evolution of cation defects within pyrochlore. We found complex behavior in which the two cation sublattices are not always independent. Defects created on one sublattice can decay into antisites and defects on the other sublattice (Fig. 3). Further, this behavior is sensitive to the chemistry of the pyrochlore, with pyrochlores having cations with more dissimilar ionic radii exhibit pure diffusion on the B sublattice while those with more similar radii displaying this more complex behavior.

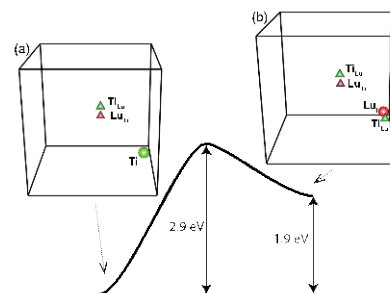


Figure 3: Pathway, as found from TAD simulations, for the decay of a Ti interstitial into a Lu interstitial and Ti antisite in  $\text{Lu}_2\text{Ti}_2\text{O}_7$ .

Past work has shown that, in pyrochlores, amorphization resistance correlates with the ease of cation disordering [5]. That is, pyrochlores in which the cations easily disorder are more amorphization resistant. In a paper currently under review at *Nature Communications* [6], we used experiment and theory to examine whether this behavior holds in another class of complex oxides, spinels ( $\text{AB}_2\text{O}_4$ ). Surprisingly, transmission electron microscopy (TEM) and x-ray diffraction on three irradiated spinels reveal exactly the opposite behavior: those spinels in which cation disordering is the most difficult were the *hardest* to amorphize. Density functional theory (DFT) finds that the observed tendencies to amorphize are anti-correlated with the

disordering energy while TAD simulations show that the harder it is to disorder the spinel, the faster it recovers (Fig. 4). Together, these results reveal that the structural cation vacancies that are present in spinel lead to recovery pathways that are not present in pyrochlore. The fundamental difference is due to cation kinetics.

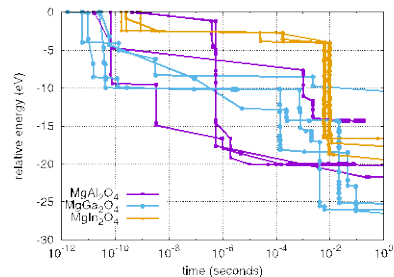


Figure 4: Kinetic recovery of spinels when placed in the rocksalt structure:  $\text{MgAl}_2\text{O}_4$  recovers faster than  $\text{MgIn}_2\text{O}_4$ .

Finally, we are developing experimental capability to probe the kinetics associated with irradiated complex oxides. We have purchased a microprobe test station to enhance our capabilities to measure ionic conductivity, a hot stage for our x-ray diffractometer (XRD), and a hot stage holder for *in situ* TEM. The microprobe has been installed and is providing data, as reported below. The hot stage for XRD had some issues as delivered from the vendor and is being replaced. Finally, the hot stage for TEM was just ordered and we expect delivery by the end of this fiscal year. Together, these capabilities will provide enhanced abilities to interrogate the kinetics associated with damaged oxides.

Concurrently, our experimental efforts have focused on two thrusts. First, we have been developing a procedure to grow thin films of pyrochlores. This is to ensure that, upon irradiation, a uniform level of damage is introduced across the pyrochlore, providing less ambiguity regarding the damage profile and thus interpretation of the measured conductivity. This has proved challenging – all reports in the literature of attempts to grow thin films of pyrochlore have led to disordered fluorite. However, we have recently had a breakthrough in which we did produce a pyrochlore film, though with higher levels of porosity than ideal. We are currently refining the process to provide a denser film suitable for conductivity measurements.

In parallel, we have implanted bulk pyrochlores and measured ionic conductivity as a function of damage. While these have the disadvantage of non-uniform damage profiles, they provide us with samples to understand the relationship between damage and oxygen transport. We have performed two sets of implants, one using He to produce minimal damage, to introduce cation disorder gradually. The second set of implants used Kr to heavily damage the samples (~100 dpa) to understand the high-damage regime. Both  $\text{Gd}_2\text{Ti}_2\text{O}_7$  (GTO) and  $\text{Gd}_2\text{Zr}_2\text{O}_7$  were implanted under both conditions. Our preliminary results for GTO are highlighted in Fig. 5. We are currently working to both validate and understand these measurements, but they reveal some surprising behavior. Ionic conductivity in the pristine sample is in reasonable agreement with literature results [1]. Upon implantation with He, we find an increase in the ionic conductivity. XRD confirms that, after this implant, the pyrochlore has disordered to fluorite; thus this result is consistent with our MD simulations as described above. However, upon implantation with a heavy dose of Kr, the ionic conductivity increases dramatically, especially at lower temperatures. We are currently characterizing this material, but initial indications are that the material first amorphized and then recrystallized during the first temperature cycle. However, clearly, it did not recover to perfect pyrochlore.

## Future Plans

Over the next year, our focus will be on experimentally interrogating the kinetics of damaged complex oxides. This will include irradiating and characterizing pyrochlore thin films. Once we have optimized the growth parameters to provide dense films with the pyrochlore structure, we will irradiate these such that the implanting ion is deep into the substrate, providing a uniformly damaged pyrochlore without the influence of the implanted species. Ionic conductivity will be measured in these films to better connect cation disorder with ionic conductivity. In parallel, we will continue to characterize our bulk samples. We have intriguing results on the highly-damaged GTO and GZO. In contrast to GTO in which we saw large increases in conductivity (Fig. 5), in GZO we see large decreases in conductivity under the same irradiation conditions. We will characterize (TEM and XRD) these samples to identify the origins of the differing changes in ionic conductivity. These will be compared with the He implanted samples to form a complete picture of the relationship between cation disorder and ionic conductivity.

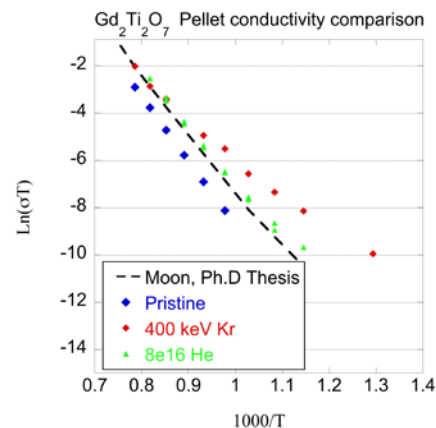


Figure 5: Ionic conductivity in GTO versus irradiation conditions. The literature data is from Ref. [1]. He was implanted at 200 keV to a fluence of  $8 \times 10^{16}$  ions/m<sup>2</sup> while the Kr was 400 keV to a fluence of  $5 \times 10^{16}$  ions/m<sup>2</sup>.

At the same time, we will begin *in situ* TEM high temperature annealing studies to identify the mechanisms responsible for damage recovery on the cation sublattices in pyrochlore. By identifying the temperature at which different kinetic regimes activate (annealing of amorphous phases, growth of dislocation loops, etc), we can correlate those temperatures with activation energies determined from simulations to identify rate-limiting steps and thus atomistic mechanisms that are responsible for these different kinetic regimes.

Our modeling will be integrated into these experimental studies to provide the connection to fundamental mechanisms. In addition, we are closely working with Art Voter and his team at LANL to extend the accelerated molecular dynamics methods to treat the types of disordered systems we are examining here in which there are multiple and very different time scales.

## References

- [1] H. L. Tuller, *J. Phys. Chem. Solids* **55**, 1393 (1994); P.K. Moon, PhD thesis, MIT, Cambridge, MA, 1988.
- [2] R. Perriot and B. P. Uberuaga, *J. Mater. Chem. A* **3**, 11554 (2015).
- [3] B. P. Uberuaga and G. Pilania, *Chemistry of Materials* **27**, 5020 (2015).
- [4] B. P. Uberuaga and R. Perriot, *Phys. Chem. Chem. Phys.*, in press.
- [5] K. E. Sickafus, et al., *Science* **289**, 748 (2000); *Nature Materials* **6**, 217 (2007).
- [6] B. P. Uberuaga, M. Tang, C. Jiang, J. A. Valdez, R. Smith and K. E. Sickafus, submitted to *Nature Communications*.



## Publications

### Publications with primary BES support

#### 2015

- R Perriot and BP Uberuaga, Structural vs. intrinsic carriers: contrasting effects of cation chemistry and disorder on ionic conductivity in pyrochlores, *J. Mater. Chem. A* **3**, 11554 (2015).
- BP Uberuaga, M Tang, C Jiang, JA Valdez, R Smith and KE Sickafus, Opposite correlations between cation disordering and amorphization resistance in spinels versus pyrochlores, submitted to *Nature Communications*.
- BP Uberuaga and R Perriot, Insights into dynamic processes of cations in pyrochlores and other complex oxides, *Phys. Chem. Chem. Phys.*, in press.
- BP Uberuaga and G Pilania, Effect of cation ordering on oxygen vacancy diffusion pathways in double perovskites, *Chemistry of Materials* **27**, 5020 (2015).
- BP Uberuaga and KE Sickafus, Interpreting oxygen vacancy migration mechanisms in oxides using the layered structure motif, *Comp. Mater. Sci.* **103**, 216 (2015).

#### 2014

- BP Uberuaga, C Jiang, CR Stanek, KE Sickafus, C Scott and R Smith, Prediction of Irradiation Spectrum Effects in Pyrochlores, *JOM* **66**, 2578 (2014).

### Publications with partial BES support

#### 2015

- C Sun, BP Uberuaga, L Yin, C Yu, Y Chen, MA Kirk, M Li, SA Maloy, H Wang, and X Zhang, Resilient ZnO nanowires in a harsh radiation environment: an in situ study, *Acta Mater.* **95**, 156 (2015).
- D Perez, BP Uberuaga and AF Voter, The parallel replica dynamics method – coming of age, *Comp. Mater. Sci.* **100B**, 90 (2015).
- PP Dholabhai, JA Aguiar, L Wu, TG Holesinger, T Aoki, RHR Castro, and BP Uberuaga, Structure and segregation of dopant-defect complexes at grain boundaries in nanocrystalline doped ceria, *Phys. Chem. Chem. Phys.* **17**, 15375 (2015).
- G Pilania and BP Uberuaga, Cation Ordering and Effect of Biaxial Strain in Double Perovskite CsRbCaZnCl<sub>6</sub>, *J. Appl. Phys.* **117**, 114103 (2015).

- S Dey, JW Drazin, YQ Wang, JA Valdez, TG Holesinger, BP Uberuaga, and RH Castro, Radiation tolerance of nanocrystalline ceramics: insights from yttria stabilized zirconia, *Scientific Reports* **5**, 7746 (2015)
- J Zhang, M Patel, YQ Wang, M Tang, J Won, JA Valdez, and KE Sickafus, Strong irradiation tolerance to amorphization in delta-Sc<sub>4</sub>Ti<sub>3</sub>O<sub>12</sub>, *J. Nucl. Mater.* **459**, 265 (2015).
- J Wen, YH Li, M Tang, JA Valdez, YQ Wang, M Patel, and KE Sickafus, Heavy and light ion irradiation damage effects in  $\alpha$ -phase Sc<sub>4</sub>Hf<sub>3</sub>O<sub>12</sub>, *NIMB*, DOI: 10.1016/j.nimb.2015.04.011.
- SK Yadav, BP Uberuaga, M Nikl, C Jiang, and CR Stanek, Band-gap and band-edge engineering of multicomponent garnet scintillators: a first-principles study, submitted to *Phys. Rev. Applied*.
- J Zhu, L Yang, C Jiang, CR Stanek, H Xu, BP Uberuaga, and Y Zhao, Formation of an Unconventional BaCl Phase at High Pressure and Temperature, submitted to *Scientific Reports*.

## 2014

- MK Patel, DJ Tallman, JA Valdez, JA Aguiar, O Anderoglu, M Tang, J Griggs, E Fu, Y Wang, and MW Barsoum, Effect of helium irradiation on Ti<sub>3</sub>AlC<sub>2</sub> at 500 degrees C. *Scripta Materialia* **77**, 1 (2014)

## 2013

- BP Uberuaga, DA Andersson and CR Stanek, Defect behavior in oxides: Insights from modern atomistic simulation methods, *Current Opinion in Solid State & Materials Science* **17**, 249 (2013).

# ATOMISTIC AND MESOSCOPIC STUDY OF PLASTIC DEFORMATION OF ALLOYS OF BODY-CENTERED-CUBIC TRANSITION METALS AND MAGNETIC IRON

V. VITEK

Department of Materials Science and Engineering,  
University of Pennsylvania, Philadelphia, PA 19104

## Program Scope

The overarching goal of this project is to advance our atomic and electronic level understanding of the plastic deformation and other mechanical properties of body-centered-cubic (BCC) transition metals and alloys, including effects of irradiation. This is carried out by atomistic computer simulations of relevant lattice defects (dislocations, point defects, interfaces) and their behavior when mechanically loading the corresponding material. The impetus for this study is two-fold. From the engineering point of view BCC transition metals and their alloys are the central materials employed in technologies associated with energy production and conversion. From the point of view of the basic science the major challenge in their modeling is that bonding in these metals is a mixed covalent and nearly free electron and cannot be treated adequately using common central-force schemes such as EAM. In principle, a full inclusion of complex bonding mediated by electrons could be achieved by calculations based on the density-functional theory (DFT) but in such calculations studies of phenomena, such as dislocation glide, are very restricted owing to the rather small size of the atomic block and periodic boundary conditions. Hence, a description of atomic interactions in these materials in terms of interatomic potentials is essential for extensive atomistic modeling of their mechanical properties. Such approach represents a coarse-graining that removes the electronic degrees of freedom [1, 2].

In our research the potentials developed and used are bond-order-potentials in which the cohesive energy is the sum of the attractive contribution,  $E^{\text{cov}}$ , and the repulsive contribution  $E^{\text{rep}}$ .  $E^{\text{cov}}$  is written as a sum of contributions from bonds between individual atoms  $i$  and  $j$

$$E^{\text{cov}} = \sum_{i \neq j} \sum_{\delta, \gamma} H_{i\delta, j\gamma} \Theta_{j\gamma, i\delta}$$

where  $H_{i\delta, j\gamma}$  are the matrix elements of the two-center tight-binding (TB) Hamiltonian that may be written in terms of the Slater–Koster bond integrals and direction cosines of the bond vector [3].  $\Theta_{j\gamma, i\delta}$  are the matrix elements of the bond order corresponding to twice the density matrix. The indices  $\delta$  and  $\gamma$  relate to orbitals included. The scheme for evaluation of the bond order is implemented in the Oxford order-N package (OXON) that has been used in all our calculations. Only d-bonds are included in the Hamiltonian but the effect of s-electrons is comprised via screening of the corresponding d bonds by s electrons at neighboring atoms [4]. The local charge neutrality is imposed in the calculations self-consistently and the repulsion is represented by a physically justified functional form described in detail in [5]. Moreover, the BCC iron is mechanically stable owing to the ferromagnetism [6] and thus this aspect of bonding has to be incorporated into the interatomic potentials for iron. This is done by including into the energy the magnetic contribution via the model of the itinerant magnetism [7] with the magnetic moments adjusted self-consistently together with the charge neutrality [8].

## Recent Progress

### Bond-order potentials (BOPs)

The bond order potentials were fully developed for BCC metals of group 5 (V, Ta, Nb), group

6 (Cr, Mo, W) and Fe. The transferability of these potentials to environments that differ significantly from the ideal BCC lattice, in particular those that are very distorted locally was thoroughly investigated. These tests, the results of which were compared either with DFT calculations or experiments, involved evaluation of energies of several alternate structures (FCC, HCP, A15 and simple cubic), vacancy formation energies, transformation paths that connect the BCC lattice with FCC, HCP, BCT and SC via continuously distorted configurations, phonon dispersion dependences and interstitial configurations. In the latter case some adjustments of the total number of d electrons is needed in some cases in order to achieve agreement with DFT calculations. In the case of Fe different magnetic states (ferromagnetic, anti-ferromagnetic and non magnetic) were studied showing the BCC ferromagnetic state to be the most favored.

As examples of these tests the Table 1 summarizes the results of the study of vacancy formation energies and Figure 1 shows examples of phonon dispersions for Nb and Fe. The quality of the results for other metals studied is very much the same as those shown here as examples.

	V	Nb	Ta	Cr	Mo	W	Fe
BOP	2.33	3.22	3.32	2.43	2.53	3.93	1.91
DFT	2.51	2.99	3.14	2.64	2.96	3.56	2.15
Experiment	2.1 — 2.2	2.6 — 3.1	2.8 — 3.1	2.0 — 2.4	2.6 — 3.2	3.5 — 4.1	1.6 — 2.2

Table 1. Vacancy formation energies (eV) calculated using BOP, DFT and measured experimentally

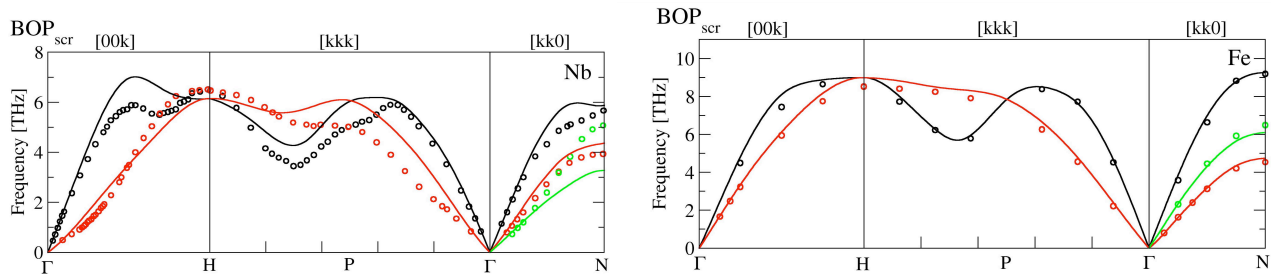


Figure 1. Phonon dispersion curves for Nb and Fe. Lines are results of BOP calculations and dots are experimental data. The black color corresponds to the longitudinal mode L, red to the transversal modes T and T1, and green to the transversal mode T2.

The tests of the transferability of the developed BOPs demonstrate unambiguously that they are appropriate for modeling of defective structures, such as various crystal defects and their properties. It is essential that these potentials reflect fully the most important aspects of bonding in the metals studied, in particular mixed covalent and nearly free electron bonding and the many-body character of the repulsion between the atoms. In this way they capture the most important aspects of bonding that is fully included in any DFT study but allow us to carry out the calculations for much larger blocks of atoms without the requirement of periodic boundary conditions.

### Structure and motion of $1/2\langle 111 \rangle$ screw dislocations – Anomalous slip

It is now well established that the mechanical behavior in BCC metals is controlled by  $1/2\langle 111 \rangle$  screw dislocations that possess non-planar cores (for a recent review see [9]). The core structure of these dislocations in all metals studied was calculated using the BOPs developed. In all cases the non-degenerate core structure, invariant to both the  $[111]$  screw axis and the  $[\bar{1}01]$  diad (reflection in the  $(111)$  plane followed by reflection in the  $(\bar{1}2\bar{1})$  plane), was found for the  $1/2[111]$  screw dislocation. This was also found in all available DFT calculations (e.g. [10, 11]). The screw components of the relative displacements of neighboring atoms within the core were found to be practically the same for all the metals studied. This could suggest that the cores of screw dislocations and thus their behavior is the same in all transition metals, depending only on the geometry of the BCC lattice. However, it is well known that there are significant differences in the

plastic properties of different transition metals, in particular in their slip geometry. Indeed, important differences were found in the core displacements perpendicular to the Burgers vector, called edge displacements. Examples are shown in Figure 2 for Nb, Mo and Fe. While these displacements are much smaller than the screw displacements, they are, apparently, responsible for different aspects of the dislocation glide in different transition metals.

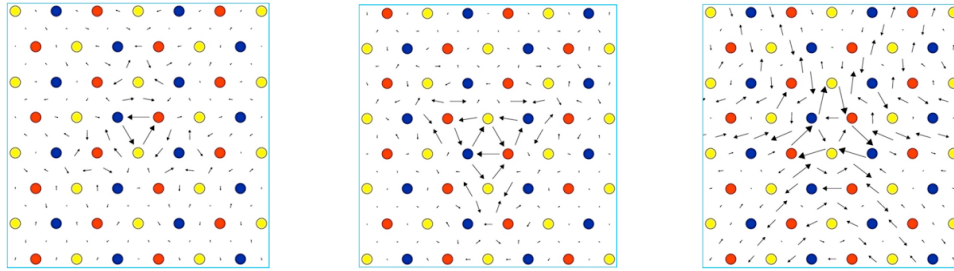


Figure 2. Edge components of the core displacements in Nb, Mo and Fe. The arrows represent relative displacements of atoms perpendicular to the Burgers vector in the direction of these arrows.

Using molecular statics the glide of the  $\frac{1}{2}[111]$  screw dislocation (at 0K) was studied for loading in pure shear parallel to the Burgers vector and in tension/compression for a number of orientations of the loading axes within the standard triangle. In all cases the shear stress parallel to the Burgers vector that drives the dislocation glide was highest in the  $(\bar{1}01)$  plane. While the slip was in all cases confined to a  $\{101\}$  plane, the glide was not necessarily in the plane with the highest shear stress parallel to the Burgers vector. For example, in Nb loaded in tension along various loading axes the slip plane was always  $(0\bar{1}1)$  that is inclined by  $60^\circ$  with respect to the most highly stressed  $\{101\}$  plane,  $(\bar{1}01)$ . In Mo the most active  $\{101\}$  plane was also inclined with respect to the most highly stressed  $(\bar{1}01)$  plane by  $60^\circ$  but for loading in compression. At the same time in Fe the slip plane was always the  $(\bar{1}01)$  plane and for some special orientations of loading a combination of  $(\bar{1}01)$  and  $(0\bar{1}1)$  planes. This suggests an explanation of the anomalous slip observed in some pure BCC metals at low temperatures, in particular those of group 5. This phenomenon, which has never been fully explained, is that in some bcc transition metals the dominant slip system may have the Schmid factor significantly lower than several other more highly stressed systems. Meanwhile, these more highly stressed slip systems may be considerably less active and even absent. The pronounced example is the deformation of Nb in tension with the loading axis in the center of the standard triangle [12]. The most active slip that carries about 70% of the strain is the  $(0\bar{1}1)[111]$  that is fifth in the order of Schmid factors. This agrees excellently with results of our simulations. Similarly, observation of the anomalous slip in compressed Mo [13] also shows the slip on the same type of the slip system but in this case carrying only about 10% of the strain. This again agrees with our modeling that shows that while the anomalous system is a possible slip system, the most highly stressed  $(\bar{1}01)[111]$  system may operate more significantly. At the same time, the anomalous slip has never been observed in Fe, again in agreement with our modeling. Thus the most important finding based on our simulations of the dislocation glide is that the anomalous slip arises from the structure of the core of  $\frac{1}{2}\langle 111 \rangle$  screw dislocations as many other plastic properties of BCC metals do. The differences between different metals relate to their different details of bonding and are reflected in different edge components of core displacements.

## Substitutional random alloys composed of several transition metals

The approach adopted introduces the alloying effect in the spirit of the regular solution by considering individual atoms of the system as ‘pseudo-atoms’ whose properties are ‘mixtures’ of properties of the two types of atoms. The assumption is that the mixing of the two materials is homogeneous and no ordering occurs. The mixing is introduced on the level of bond integrals for the attractive part while repulsion is a direct mixing of individual repulsions. This approach was applied to the study of the Ta-W alloy. The calculated dependence of the lattice parameter on the concentration of Ta follows quantitatively the deviation from the Vegards law found in DFT calculations in [14]. The same was found for the concentration dependence of the bulk modulus. The related dislocation study demonstrated that the anomalous slip in Ta decreases with increasing concentration of W in agreement with experiments.

### Future Plans

As explained above, atomistic studies of the dislocation glide at 0K lead to an explanation of the anomalous slip based on the special properties of the cores of  $\frac{1}{2}\langle 111 \rangle$  screw dislocations. In order to include the effect of temperature used in experiments, we expand the study to calculating relevant Peierls barriers. The essential part of this study is the full inclusion of the effect of the applied stress tensor on these barriers needed for investigation of the thermally activated dislocation glide [15]. This will allow us to assess accurately in which materials the anomalous slip dominates and in which it is shared with the slip on the most highly stressed  $\{101\}$  planes. When completed, we believe it will solve the long-standing puzzle of the anomalous slip.

In collaboration with the group of Prof. Drautz at the University of Bochum, we shall participate in the development of analytical BOPs that will allow us to employ BOPs in molecular dynamics studies and may be included into the codes such as LAMMPS simulator.

Another development is investigation of the interaction of dislocations and grain boundaries with point defects, specifically vacancies and self-interstitials. This is an important step in studying the effect of the radiation damage on the mechanical properties of transition metals and iron.

The most important future direction of our research will be development of BOPs for substitutional alloys, following the approach described above and employed for Ta-W alloys. A long-term plan is that this development will lead towards modeling of the mechanical behavior of the compositionally complex, also called high-entropy, alloys that contain multiple principal elements while crystalizing in relatively simple structures (FCC and BCC). When such potentials are developed they will be used first to investigate structural stabilities of these complex alloys and later in studies of dislocations and other crystal defects that control the mechanical properties of these materials.

### References

1. D. G. Pettifor, *Acta Mater.* **51**, 5649, 2003.
2. M. W. Finnis, *Interatomic Forces in Condensed Matter* (Oxford University Press, 2003).
3. J. C. Slater and G. F. Koster, *Phys. Rev.* **94**, 1498, 1954.
4. D. Nguyen-Manh, D. G. Pettifor and V. Vitek, *Phys. Rev. Lett.* **85**, 4136, 2000.
5. Yi-Shen Lin, M. Mrovec and V. Vitek, *Modelling Simul. Mater. Sci. Eng.* **22**, 034002, 2014.
6. H. Hasegawa and D. G. Pettifor, *Phys. Rev. Lett.* **50**, 130, 1983.
7. E. C. Stoner, *Proc. R. Soc. Lond. A*, **169**, 339, 1939.
8. M. Mrovec, D. NguyenManh, C. Elsasser and P. Gumbsch, *Phys. Rev. Lett.* **106**, 6402, 2011.
9. V. Vitek and V. Paidar, *Dislocations in Solids* **14**, p. 439, 2008.
10. C. Woodward and S. I. Rao, *Phys. Rev. Lett.* **88**, 216402, 2002.
11. L. Dezerald, L. Ventelon, E. Clouet, C. Denoual, D. Rodney, and F. Willaime, *Phys. Rev. B*, **89** 024104, 2014.

12. C. J. Bolton and G. Taylor, *Philos. Mag.* **26**, 1359, 1972.
13. P. J. Jeffcoat, B. L. Mordike and K. D. Rogausch, *Philos. Mag.* **34**, 583, 1976.
14. P. E. A. Turchi, V. Drchal, J. Kudrnovsky, C. Colinet, L. Kaufman and Z. K. Liu, *Phys. Rev. B* **7109**, 4206, 2005.
15. R. Gröger and V. Vitek, *Acta Mater.* **56**, 5426, 2008.

### **Publications 2013-2015**

1. R. Gröger and V. Vitek: *Stress dependence of the Peierls barrier of  $\frac{1}{2}$   $\langle 111 \rangle$  screw dislocations in bcc metals*, *Acta Materialia* **61**, 6362, 2013.
2. Yi-Shen Lin, M. Mrovec, and V. Vitek: *A new method for development of bond-order potentials for transition bcc metals*, *Modelling Simul. Mater. Sci. Eng.* **22**, 034002, 2014.
3. M. Cak, T. Hammerschmid, J. Rogal, V. Vitek and R. Drautz: *Analytic bond-order potentials for the bcc refractory metals Nb, Ta, Mo and W*, *J. Phys.: Condensed Matter* **26**, 195501, 2014.
4. R. Gröger and V. Vitek: *Determination of positions and curved transition pathways of screw dislocations in bcc crystals from atomic displacements*, *Mater. Sci. Eng. A* **643**, 203, 2015.
5. Yi-Shen Lin: *Development of bond-order potentials for body-centered-cubic transition metals and their application in atomistic studies of plastic properties mediated by dislocations*, PhD Thesis, University of Pennsylvania, July 2015.

## **Localized Deformation and Intergranular Fracture of Irradiated Alloys under Extreme Environmental Conditions**

**Gary S. Was**

**2355 Bonisteel Blvd., University of Michigan, Ann Arbor, MI 48109 [gsw@umich.edu](mailto:gsw@umich.edu)**

**Ian M. Robertson**

**1415 Engineering Drive, University of Wisconsin-Madison, Madison WI 53706  
[ian.robertson@wisc.edu](mailto:ian.robertson@wisc.edu)**

**Diana Farkas**

**201A Holden Hall, Virginia Tech, Blacksburg, VA 24061, [diana@vt.edu](mailto:diana@vt.edu)**

### **Program Scope**

The overall objective of this project is to determine the basic processes by which localized deformation in irradiated materials leads to intergranular cracking in alloys in aggressive environments at high temperature. We will utilize a mesoscale science approach that provides linkage from atomistic simulations of dislocation responses to the accommodation and emission of dislocations from grain boundaries, through direct observation of dislocations with irradiation defects and grain boundaries, to macroscale experiments. The consequence of this combined effort will be the identification of the factors most likely responsible for establishing not only the local stress state at grain boundaries prone to failure but also their location with respect to the macroscopic applied stress. The grain boundaries and local conditions at which disruption of the surface oxide and hence, exposure to the water environment is most probable, have been identified. Having isolated these conditions, we are poised to address why this failure does not occur at every grain boundary that is favorably oriented, why it remains isolated at one channel over others along the same grain boundary, and what is the role of environment in inducing the cracking. With these questions in mind, we will focus on the following sub-objectives that are designed to bring us closer to determining the mechanism of irradiation assisted stress corrosion cracking, IASCC.

- Since all DC-GB intersections do not result in cracking, what is the distinguishing factor or condition? That is, what conditions or properties determine the weakest link that initiates grain boundary failure at a specific site on a particular boundary? If a threshold in stress for initiation of IASCC exists, can it be determined?
- Can the variability in cracking propensity between different alloys be explained by specific material properties such as stacking fault energy, grain boundary structure, or the constraints imposed by the surrounding grains?
- A characteristic of IASCC is that while cracking readily occurs in high temperature water, straining at the same temperature and strain rate in an inert environment does not result in cracking. So the water environment plays a critical role on the cracking process. The corrosion reaction between high temperature water and the base metal results in the formation of an oxide, the generation of hydrogen and the generation of vacancies. Which of these factors, either separately or in combination work in concert with a highly localized stress state to explain the susceptibility to IASCC?



## Recent Progress

As a precursor to quantitative measurement of localized stresses in irradiated samples, a method was developed for measuring the stress ahead of a blocked slip band in unirradiated material utilizing high-resolution electron backscatter diffraction (HREBSD) patterns and a cross correlation software, Cross Court 3 (CC3), for data analysis. For this study, a Fe-21Cr-32Ni tensile bar was electropolished for EBSD analysis. A constant extension rate tensile (CERT) test was performed in an argon environment at 288°C to 0.7% total plastic strain. EBSD was then performed using a Philips XL30FEG SEM and TSL 6 software.

Several scans were made in areas that showed prominent slip bands in one grain, with no sign of localized deformation in the adjacent grain. This should correspond to the highest stress state since transmission of the slip band would relax some of the stress. The stress state calculated by the CC3 software, using the process outlined above, for one particular scan area is shown in Fig. 1. Visible here is a plume of elevated stress leading from the head of the slip band into the adjacent grain. This stress distribution is representative of many scans that have been taken using this technique. The highest magnitude of stress occurred at the intersection point, and dropped significantly with distance from the grain boundary. Stress values deviated from the matrix stress values significantly over the first couple microns, reaching 20% of the maximum value at a distance of 3.1 microns from the intersection site. The data is fit to a function of the form  $\sigma = A + K/(X + B)^{1/2}$  where  $A$  is the stress just outside the affected zone,  $K$  is the stress intensity factor caused by the intersection of a slip system and a grain boundary,  $X$  is the distance from the grain boundary and  $B$  is a correction for the uncertainty of the grain boundary position. For the case shown in Fig. 2, the value of  $K$  is 0.807 MPa m<sup>1/2</sup>. It follows a similar decay in magnitude as observed by Britton and Wilkinson, who showed an 80% stress reduction in 3.2 microns [2], with a  $K$  value of 0.477 MPa m<sup>1/2</sup> for commercial purity titanium. Given the distribution of stress and the magnitude of measured values, HREBSD has been shown to be a plausible technique for analyzing unirradiated austenitic stainless steel.

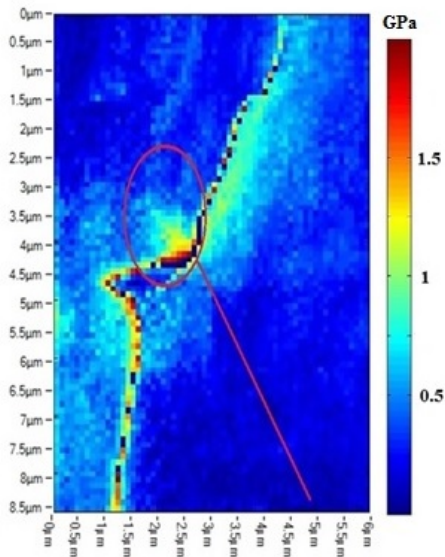


Figure 1. Stress map near a slip band-grain boundary intersection as determined from Cross Court 3 [1].

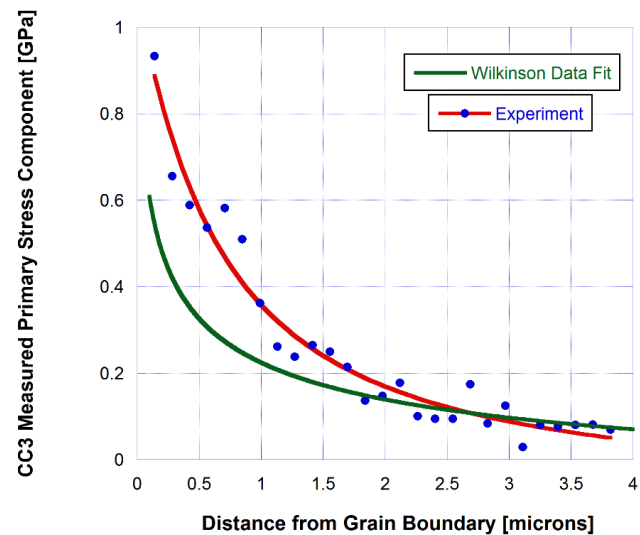


Figure 2. Stress as a function of distance from the slip band-grain boundary intersection and that from Wilkinson et al. on commercial purity Ti [2].

The localized stresses near the dislocation-grain boundary intersections were also studied using atomistic computer simulations in polycrystalline digital samples. The samples were subject to virtual tensile testing using a model EAM interatomic potential and a temperature of 300K. The molecular dynamics simulations yielded information on the local stress state of every atom in the sample and 30 atom averages were calculated to study the stress localization in the intersection region. An example is shown in Fig. 3 for an overall sample deformation level of 3.5%. The snapshot in this figure corresponds to the arrival of the dislocation at the grain boundary. The stresses are plotted using a color map up to 2 GPa, for a direct comparison with experimental results of Figure 1. Figure 4 shows the corresponding stress values as a function of the distance to the boundary in the grain adjacent to the one where the dislocation has just arrived. As expected, the individual atom data show a large scatter, particularly in the region near the grain boundary. The calculated 30 atom averages show a stress concentration near the

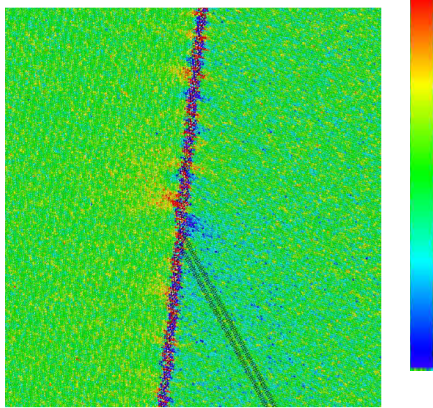


Figure 3. Stress map near a dislocation-grain boundary intersection as determined from the atomistic simulations. The color map goes from compressive 2GPa(blue) to tensile 2GPa (red)

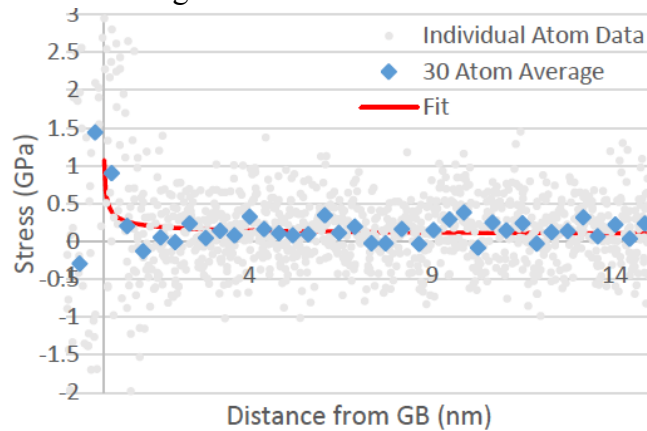


Figure 4. Stress as a function of the distance from the dislocation-grain boundary intersection. The data are fit to the same equation used in the experiments

boundary at levels of about 1 GPa. This peak value is similar to that observed in the experiment. The data in the simulations also decay with distance from the grain boundary, but the decay is more pronounced than the experimental observations. In order to make a quantitative comparison the simulation data were fit to the same equation as the experiments. The value of the constant  $K$  obtained for the case of Figure 5 is  $0.005 \text{MPa m}^{1/2}$ . This value is much smaller than the corresponding experimental result. The difference could be due to the much smaller grain sizes utilized in the simulations. The experimental result corresponds to the intersection of a slip band that possibly contains many more dislocations than the simulation. The agreement in the general values of maximum stress observed is an important result. The simulation work can now study the conditions for dislocation transmission.

Recent work has also focused on the correlation between composition of grain boundaries (GBs) and their susceptibility to irradiation-assisted stress corrosion cracking (IASCC). Tensile bars of a Fe-13Cr-15Ni austenitic stainless steel were irradiated with 3.2 MeV protons to a dose of 5 dpa, and then strained in a simulated boiling water reactor environment to a plastic strain of 3%. Cross-sectional specimens were extracted inside focused-ion beam (FIB) machined from regions of interest where dislocation channels intersected with GBs but no slip transfer occurred. Characterization of GB microstructure and composition was then carried out using (scanning) transmission electron microscope (S/TEM).

Figure 5(a) shows a representative dark-field STEM image of a GB and the surface oxides. Diffraction analysis suggests this GB to be close to a  $\Sigma 39$  (111)/ $32.2^\circ$  twist boundary, and no intergranular cracking was observed. A slight depletion of Cr and segregation of Ni were noticed near this GB (see Fig. 5(b)), while no detectable change of composition was found near some other  $\Sigma 3$  (111)/ $60^\circ$  twin boundaries (not shown here). The GB depletion of Cr (and Fe) and enrichment of Ni was more significant near the metal/oxide interface, which led to the formation of a Cr-rich protective oxide layer right above the GB (see Fig. 5(c)). Therefore, the susceptibility of a local site of GB would be reasonably correlated with a) the initial level of GB depletion of Cr that depends on the GB character, and b) the localized deformation at a GB that keeps rupturing the Cr-rich oxides and driving the Cr from GB to surface. Ultimately, a cracked GB would be exhausted of Cr.

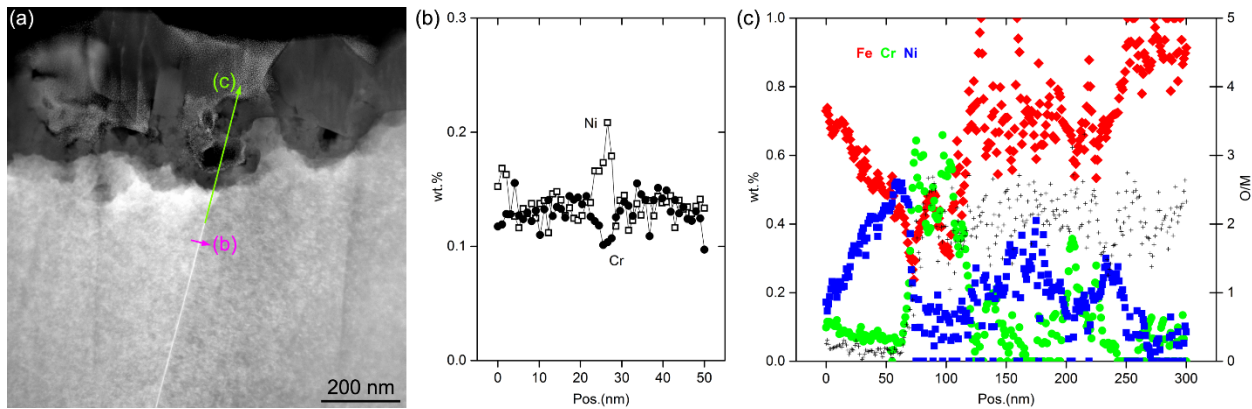


Figure 5. TEM characterization of GB microchemistry. (a) STEM image. (b) Composition profile across the GB as measured by energy dispersive spectroscopy (EDS). (c) Composition profile measured along the GB from base metal to surface oxide layer.

## Future Plans

With the successful characterization of slip lines at grain boundaries and a method for reducing the height of the dislocation channel steps on the surface, our immediate future plans are to characterize the stress distribution ahead of the DC-GB intersection in irradiated samples.

The simulation work will study the effects of grain size on the stress near the intersections. The simulations will also allow the study of the time evolution of these stresses as the dislocation is arriving at the boundary and the critical transmission event is reached.

Microscopic work will focus on obtaining more cross-sectional specimens from cracked grain boundaries and on the evolution of composition along GB (from base metal to oxides inside crack) to correlate with susceptibility to IASCC. Efforts will be made to capture the evidence of dislocation channels intersecting with GBs, to shed light on the local stress at GBs. In-situ TEM straining tests will also be performed to understand the effect of alloy composition on the mechanism of slip transfer at GBs in irradiated systems.

## References

1. T.B. Britton, J. Jiang, P.S. Karamched, A.J. Wilkinson, "Probing Deformation and Revealing Microstructural Mechanisms with Cross-Correlation-Based, High-Resolution Electron Backscatter Diffraction," *JOM* 65 (2013) 1245.
2. T.B. Britton and A.J. Wilkinson, "Stress fields and geometrically necessary dislocation density distributions near the head of a blocked slip band," *Acta Materialia* 60 (2012) 5773.

## Publications

1. M. D. McMurtrey, B. Cui, I. Robertson, D. Farkas, G. S. Was, "Mechanism of dislocation Channel-Induced Irradiation Assisted Stress Corrosion Crack Initiation in Austenitic Stainless Steel," Current Opinion in Solid State and Materials Science, accepted, in press.
2. M. D. McMurtrey, G. S. Was, B. Cui, I. M. Robertson, L. Patrick and D. Farkas, "Strain Localization at Dislocation Channel - Grain Boundary Intersections in Irradiated Stainless Steel," Int'l J. Plasticity 56 (2014) 219-231.
3. B. Cui, M. D. McMurtrey, G. S. Was, I. M. Robertson, "Micromechanistic Origin of Irradiation-Assisted Stress Corrosion Cracking," Phil. Mag. 94, No. 36 (2014) 4197-4218.
4. B. Cui, J. Kacher, M. D. McMurtrey, G. Was, I. M. Robertson, "Influence of Irradiation Damage on Slip Transfer across Grain Boundaries," Acta. Mater. 65 (2014) 150-160.
5. L. Smith, D. Farkas, "Non-planar grain boundary structures in fcc metals and their role in nano-scale deformation mechanisms," Philosophical Magazine 94 (2014) 152-173.
6. J. Kacher, B. Eftink, B. Cui, I. M. Robertson, "Dislocation interactions with grain boundary interactions," Current Opinion in Solid State and Materials Science 18 (2014) 227-243.

## Electronic and Atomic Response of Ceramic Structures to Irradiation

William J. Weber, Oak Ridge National Laboratory and University of Tennessee

Yanwen Zhang, Oak Ridge National Laboratory

Matthew F. Chisholm, Oak Ridge National Laboratory

### Program Scope

The overarching goal of this research is to understand, predictively model, and ultimately control the dynamic response of ceramic structures to energy deposition from irradiation at the level of electrons and atoms. The design of radiation tolerant materials and creation of new functional materials by ion beam modification demand a comprehensive understanding and predictive models of energy transfer and exchange processes between the electronic and atomic structures. To achieve this goal, this research is currently focused on applying integrated experimental and computational approaches to investigate the additive, competitive and synergistic effects of energy deposition and dissipation to electrons and atomic nuclei on the response of model ceramics to single ion events and the collective effects of multiple ion events. The separate and coupled dynamics of electronic and atomic processes are investigated over a range of irradiation conditions to elucidate the underlying mechanisms. Scientific advances from the work will not only lead to new design principles for self-healing and radiation tolerant materials in extreme radiation environments, but will also provide the foundation for the design and control of material properties to enable broad advances in sustainable energy technologies and national security.

### Recent Progress

The interaction of energetic ions with solids results in energy loss to both atomic nuclei and electrons in the solid, as illustrated in Fig. 1. In an invited article, recent advances in understanding and modeling the additive and competitive effects of nuclear and electronic energy loss on the response of materials to ion beam modification were reviewed. The results provide conclusive evidence that energy loss by energetic ions to electrons (ionization) can contribute additively to radiation damage production or lead to competitive self-

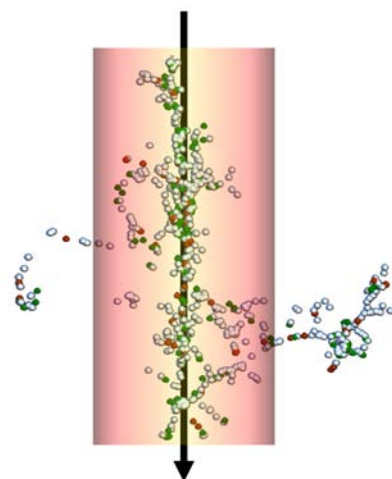


Fig. 1. Combined effects of energy loss to electrons and atomic nuclei by an ion. Electronic energy loss results in a concentric thermal spike along the ion path (depicted by arrow), while energy loss to atomic nuclei results in atomic collisions that displace atoms creating damage [1].

healing of radiation damage created by atomic collisions [1]. Hybrid computational methods that model the effects of energy transfer from electrons to atomic nuclei are experimentally validated. These findings have significant implications because of the evolving use of ion beams to synthesize and functionalize materials or mimic the response of materials to extreme radiation environments. Ionization-induced self-healing provides a novel approach to: (1) improve the quality of epitaxial films for devices and surface barrier coatings for harsh environments; (2) non-thermally heal ion-implantation damage during chip manufacturing; and (3) develop radiation-tolerant materials for nuclear, high-energy accelerator and space applications. Ionization-induced damage production can be exploited over a wide range of energies to create: novel defect states and structures far from equilibrium; nanopores; unique nanostructures; and new functionalities in materials.

Understanding of ionization-induced recovery has been advanced by the discovery of substantial annealing of pre-existing defects and restoration of structural order in SiC from energy transferred to electrons, via inelastic ionization processes, by ions with large ratios of electronic to nuclear energy loss [2]. This discovery was validated experimentally by substantial reduction of structural disorder measured macroscopically by ion channeling methods and at the atomic level by scanning transmission electron microscopy, and the results were confirmed by atomistic simulations based on the two-temperature model. Cross sections for defect recovery, derived from the experiments, increase linearly with electronic energy loss, as shown in Fig. 2, and decrease with increasing level of relative structural disorder,  $f_0$ . Energy transfer to electrons of 1.4 keV/nm causes sufficient ionization to activate this recovery process. These results identify a significant mechanism for self-healing of radiation damage in SiC for nuclear and space applications, and demonstrate the important effects of energy transfer to electrons for repair of ion implantation damage in advanced electronics and for predicting material performance in extreme radiation environments where ionization and defect production occur simultaneously.

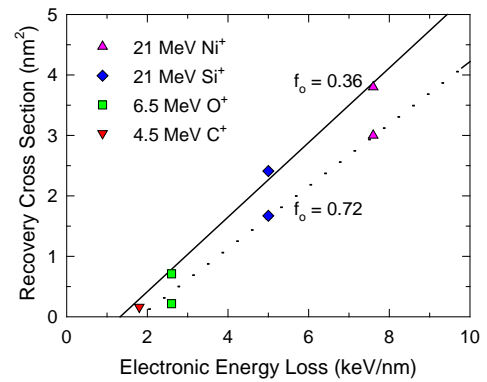


Fig. 2. Normalized recovery cross sections in SiC as function of electronic energy loss and initial level of relative disorder,  $f_0$  [2].

A colossal synergy, orders of magnitude larger than anything previously reported, has been discovered to occur between electronic energy loss by ions and pre-existing atomic defects created by elastic energy loss in single-crystal SrTiO<sub>3</sub> [3]. This synergy results in the formation of nanometer-sized amorphous tracks, but only in the region with pre-existing defects. These defects decrease the electronic and atomic thermal conductivities and increase the electron-phonon coupling, which highly localizes the thermal spike for each ion, resulting in the formation of an amorphous track that is observed experimentally and confirmed in atomistic



simulations based on the two-temperature model, as shown in Fig. 3. This work identifies a major gap in fundamental understanding on the role of defects in electronic energy dissipation and electron-lattice coupling. As  $\text{SrTiO}_3$  is a foundational material in functional microelectronics, the work also provides new insights for creating novel interfaces and nanostructures to functionalize thin-film structures, including tunable electronic, magnetic and optical properties.

*Ab initio* molecular dynamics calculations have revealed that electronic excitations induce a structural instability that transforms  $\text{Y}_2\text{Ti}_2\text{O}_7$ ,  $\text{Gd}_2\text{Ti}_2\text{O}_7$  and  $\text{Sm}_2\text{Ti}_2\text{O}_7$  with the pyrochlore crystal structure to an amorphous state [4]. Normally, radiation-induced amorphization is a high-energy process caused by local melting due to thermal spikes created by atomic collision cascades or extreme ionization; however, this work demonstrates that localized electronic excitations make the transformation to an amorphous state easier. In these pyrochlore structures, excitation of the oxygen 2p electrons creates an instability of the structure, as illustrated in Fig. 4, that decreases the temperature for the crystalline-to-amorphous transformation as the concentration of electronic excitations increases: from the melt temperature for no electronic excitations to room temperature for electronic excitation concentrations of 1.4% for  $\text{Gd}_2\text{Ti}_2\text{O}_7$  and  $\text{Sm}_2\text{Ti}_2\text{O}_7$  and 1.6% for  $\text{Y}_2\text{Ti}_2\text{O}_7$ . The results demonstrate the critical role local electronic excitations have on the structural stability of ceramics, and improved understanding will lead to more radiation-tolerant materials and novel approaches using lasers, electrons and ions to modifying the structures and properties of ceramic surfaces, films and coatings for nuclear, electronic, magnetic, optical, catalytic and thermal-barrier applications.

### Future Plans

Any significant synergistic effects are expected to come primarily from the interaction of the electronic energy loss with the defects that accumulate and evolve from previous ion trajectories. Based on the colossal synergistic effect observed in  $\text{SrTiO}_3$  [2], experimental and

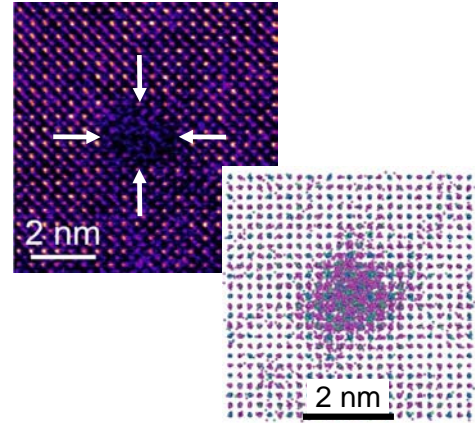


Fig. 3. Upper left, a high angle annular dark field image is shown of an amorphous track produced by a 21 MeV Ni ion in  $\text{SrTiO}_3$  with pre-existing defects. Lower right, an atomistic simulation depicts the amorphous track formed by a 21 MeV Ni ion in  $\text{SrTiO}_3$  with defects [3].

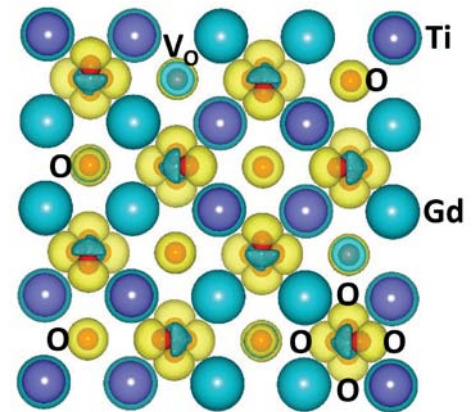


Fig. 4. Electron-spin density distribution for crystalline  $\text{Gd}_2\text{Ti}_2\text{O}_7$  with 1.6% electronic excitations prior to amorphous transformation [4]. Electronic excitations lead to charge redistributions, indicated by yellow spheres/ellipsoids, located primarily on oxygen atoms (small orange spheres). Large spheres are Gd & Ti atoms; O vacancies,  $\text{V}_o$ , are small spheres with blue cores.

computational studies are planned to investigate this effect as functions of electronic energy loss, pre-existing defect concentration, and temperature. Based on atomistic simulations, a similar synergistic effect is predicted to occur in  $\text{KTaO}_3$ , and experimental studies are planned to validate these predictions. To understand how broadly this new phenomena may occur, similar studies are planned for  $\text{LiTaO}_3$ .

While much of our current and planned research is focused on separate effects studies using heavy ions that have high ratios of electronic to nuclear energy loss, studies on the effects of simultaneous electronic and nuclear energy loss for single ion trajectories are planned for SiC using ions with comparable electronic and nuclear energy loss. In these studies, the thermal spike from the primary ion will overlap much of the recoil trajectories, and the energy of the thermal spike is supplemented to some extent by the electronic energy loss of the secondary recoils.

A primary focus over the next 3 years will be on materials, ions and energy regimes where the two temperature model is applicable and can be utilized to reveal underlying mechanisms. The computation effort will focus on molecular dynamics simulations, based on the two-temperature model and simultaneous effects of electronic and nuclear energy losses, which support the parallel experimental effort. By exploring a wide range of experimental conditions for a few model ceramics, the fidelity of the two-temperature model will be evaluated and constraints on some of the parameters will be determined. We will work toward separately measuring (or even calculating) some of the parameters, such as electron-phonon coupling and thermal conductivity, for pristine and pre-damaged model  $\text{ABO}_3$  oxides to improve the predictive power and accuracy.

Most of the model ceramics of interest have strong luminescence signatures for vacancy defects, and *in situ* luminescence measurements at cryogenic temperatures (down to 20 K) will be used to study the production and recovery of vacancy defects from the energy loss to electrons and atomic nuclei by energetic ions. The outcome from these studies will be essential to advance our understanding on electronic and atomic response of ceramic structures to irradiation.

## References

1. W. J. Weber, D. M. Duffy, L. Thomé, Y. Zhang, “The role of electronic energy loss in ion beam modification of materials,” *Curr. Opin. Solid State Mater. Sci.* **19**, 1 (2015).
2. Y. Zhang, R. Sachan, O. H. Pakarinen, M. F. Chisholm, P. Liu, H. Xue, W. J. Weber, “Ionization-induced annealing of pre-existing defects in silicon carbide,” *Nature Commun.* **6**, 8049 (2015).
3. W. J. Weber, E. Zarkadoula, O. H. Pakarinen, R. Sachan, M. F. Chisholm, P. Liu, H. Xue, K. Jin, Y. Zhang, “Synergy of elastic and inelastic energy loss on ion track formation in  $\text{SrTiO}_3$ ,” *Scientific Reports* **5**, 7726 (2015).
4. H. Y. Xiao, W. J. Weber, Y. Zhang, X. T. Zu, S. Li, “Electronic excitation induced amorphization in titanate pyrochlores: an *ab initio* molecular dynamics study,” *Scientific Reports* **5**, 8265 (2015).



## Publications

- Y. Zhang, R. Sachan, O. H. Pakarinen, M. F. Chisholm, P. Liu, H. Xue, W. J. Weber, "Ionization-induced annealing of pre-existing defects in silicon carbide," *Nature Commun.* **6**, 8049 (2015).
- S. Moll, Y. Zhang, A. Debelle, L. Thomé, J. P. Crocombette, Z. Zihua, J. Jagielski, W. J. Weber, "Damage processes in MgO irradiated with medium-energy heavy ions," *Acta Mater.* **88**: 314-322 (2015).
- E. Zarkadoula, D. M. Duffy, K. Nordlund, M. A. Seaton, I. T. Todorov, W. J. Weber, K. Trachenko, "Electronic effects in high-energy radiation damage in tungsten," *J. Phys.: Condens. Matter* **27** [13]: 135401 (2015).
- R. Sachan, O. H. Pakarinen, P. Liu, M. K. Patel, M. F. Chisholm, Y. Zhang, X. L. Wang, W. J. Weber, "Structure and band gap determination on irradiation-induced amorphous nano-channels in LiNbO<sub>3</sub>," *J. Appl. Phys.* **117** [13]: 135902 (2015).
- B. Liu, V. R. Cooper, Y. Zhang, W. J. Weber, "Segregation and trapping of oxygen vacancies near the SrTiO<sub>3</sub> Σ3 (1 1 2) [1 1 1] tilt grain boundary," *Acta Mater.* **90**: 394-399 (2015).
- F. Yuan, Y. Zhang, W. J. Weber, "Vacancy-Vacancy Interaction Induced Oxygen Diffusivity Enhancement in Undoped Nonstoichiometric Ceria," *J. Phys. Chem. C* **119** [23]: 13153-13159 (2015).
- W. J. Weber, E. Zarkadoula, O. H. Pakarinen, R. Sachan, M. F. Chisholm, P. Liu, H. Xue, K. Jin, Y. Zhang, "Synergy of elastic and inelastic energy loss on ion track formation in SrTiO<sub>3</sub>," *Scientific Reports* **5**: 7726 (2015).
- H. Y. Xiao, W. J. Weber, Y. Zhang, X. T. Zu, "Ab initio molecular dynamics simulations of ion-solid interactions in zirconate pyrochlores," *Acta Mater.* **87**: 273-282 (2015).
- W. J. Weber, D. M. Duffy, L. Thomé, Y. Zhang, "The role of electronic energy loss in ion beam modification of materials," *Curr. Opin. Solid State Mater. Sci.* **19** [1]: 1-11 (2015).
- Y. Zhang, A. Debelle, A. Boule, P. Kluth, and F. Tuomisto, "Advanced techniques for characterization of ion beam modified materials," *Curr. Opin. Solid State Mater. Sci.* **19** [1]: 19-28 (2015).
- D. S. Aidhy, Y. Zhang, W. J. Weber, "Radiation damage in cubic ZrO<sub>2</sub> and yttria-stabilized zirconia from molecular dynamics simulations," *Scripta Mater.* **98**: 16-19 (2015).
- H. Y. Xiao, W. J. Weber, Y. Zhang, X. T. Zu, and S. Li, "Electronic excitation induced amorphization in titanate pyrochlores: an ab initio molecular dynamics study," *Scientific Reports* **5**: 8265 (2015).
- D. S. Aidhy, B. Liu, Y. Zhang, W. J. Weber, "Chemical expansion of affected oxygen vacancy stability in different oxide structures from first principles calculations," *Comp. Mater. Sci.* **99**: 298-305 (2015).
- D. S. Aidhy, B. Liu, Y. Zhang, W. J. Weber, "Strain-Induced Phase and Oxygen-Vacancy Stability in Ionic Interfaces from First-Principles Calculations," *J. Phys. Chem. C* **118** [51]: 30139-30144 (2014).

A. Debelle, A. Boulle, A. Chartier, F. Gao, W. J. Weber, "Interplay between atomic disorder, lattice swelling, and defect energy in ion-irradiation-induced amorphization of SiC," *Phys. Rev. B* **90** [17]: 174112 (2014).

B. Liu, H. Y. Xiao, Y. Zhang, D. S. Aidhy, W. J. Weber, "Investigation of oxygen point defects in cubic ZrO<sub>2</sub> by density functional theory," *Comp. Mater. Sci.* **92**: 22-27 (2014).

Y. Zhang, M. L. Crespillo, H. Xue, K. Jin, C.-H. Chen, C. L. Fontana, J. T. Graham, W. J. Weber, "New ion beam materials laboratory for effective investigation of materials modification and irradiation effects," *Nucl. Instrum. Meth. B* **338**: 19-30 (2014).

B. Liu, V. R. Cooper, H. Xu, H. Y. Xiao, Y. Zhang, W. J. Weber, "Composition dependent intrinsic defect structures in SrTiO<sub>3</sub>," *Phys. Chem. Chem. Phys.* **16** [29]: 15590-15596 (2014).

D. S. Aidhy, Y. Zhang, W. J. Weber, "(001) SrTiO<sub>3</sub>|MgO interface and oxygen-vacancy stability from first-principles calculations," *ACS Appl. Mater. Interfaces* **6** [17]: 15536-15541 (2014).

K. Jin, H. Y. Xiao, Y. Zhang, W. J. Weber, "Effects of boron-nitride substrates on Stone-Wales defect formation in graphene: An *ab initio* molecular dynamics study," *Appl. Phys. Lett.* **104** [20]: 203106 (2014).

P. Liu, Y. Zhang, H. Y. Xiao, X. Xiang, X. Wang, W. J. Weber, "Nonlinear luminescence response of CaF<sub>2</sub>:Eu and YAlO<sub>3</sub>:Ce to single ion excitation," *J. Appl. Phys.* **115** [3]: 033108 (2014).

K. Jin, Y. Zhang, Z. Zhu, D. A. Grove, H. Xue, J. Xue, W. J. Weber, "Electronic stopping powers for heavy ions in SiC and SiO<sub>2</sub>," *J. Appl. Phys.* **115** [4]: 044903 (2014).

E. Zarkadoula, R. Devanathan, W. J. Weber, M. A. Seaton, I. T. Todorov, K. Nordlund, M. T. Dove, K. Trachenko, "High-energy radiation damage in zirconia: Modeling results," *J. Appl. Phys.* **115** [8]: 083507 (2014).

A. Debelle, M. Backman, L. Thomé, K. Nordlund, F. Djurabekova, W. J. Weber, I. Monnet, O. H. Pakarinen, F. Garrido, F. Paumier, "Swift heavy ion induced recrystallization in cubic silicon carbide: New insights from designed experiments and MD simulations," *Nucl. Instrum. Meth. B* **326**: 326-331 (2014).

J.-M Costantini, F. Beuneu, W. J. Weber, "Annealing of Paramagnetic centres in electron- and ion-irradiated yttria-stabilized zirconia: effect of yttria content," *Philos. Mag.* **94** [20]: 2281-2296 (2014).

K. Jin, Z. Zhu, S. Manandhar, J. Liu, C. H. Chen, V. Shutthanandan, S. Thevuthasan, W. J. Weber, Y. Zhang, "Angular distribution and recoil effect for 1 MeV Au<sup>+</sup> ions through a Si<sub>3</sub>N<sub>4</sub> thin film," *Nucl. Instrum. Meth. B* **332**: 346-350 (2014).

B. Liu, H. Y. Xiao, Y. Zhang, D. S. Aidhy, W. J. Weber, “*Ab initio* molecular dynamics simulations of threshold displacement events in SrTiO<sub>3</sub>,” *J. Phys.: Condens. Matter* **25** [48]: 485003 (2013).

P. Liu, Y. Zhang, X. Wang, X. Xiang, W. J. Weber, “Response properties of YAlO<sub>3</sub>:Ce scintillation crystal under ion irradiation,” *Nucl. Instrum. Meth. B* **307**: 49-54 (2013).

T. Oda, Y. Zhang, and W. J. Weber, “Optimization of a hybrid exchange-correlation functional for silicon carbides,” *Chem. Phys. Lett.* **579**: 58-63 (2013) 58-63.

J.-M. Costantini, F. Beuneu, W. J. Weber, “Radiation damage in cubic-stabilized zirconia,” *J. Nucl. Mater.* **440**: 508-514 (2013).

T. Oda, Y. Zhang, W. J. Weber, “Study of intrinsic defects in 3C-SiC using first principles calculation with a hybrid functional,” *J. Chemical Physics* **139** : 124707(2013).

## Deformation mechanisms of nanotwinned Al

Xinghang Zhang, Dept. Mechanical Engineering, Dept. Materials Science and Engineering, Texas A&M University, College Station, TX 77843-3123

Phone: (979) 845-2143; Email: [zhangx@tamue.edu](mailto:zhangx@tamue.edu)

### Program Scope

The objective of this proposal is to investigate the role of different types of layer interfaces on the formation of high density stacking fault (SF) in Al in Al/fcc multilayers, and understand the corresponding deformation mechanisms of the films. Stacking faults or twins can be intentionally introduced (via growth) into certain fcc metals with low stacking fault energy (such as Cu, Ag and 330 stainless steels) to achieve high strength, high ductility, superior thermal stability and good electrical conductivity. However it is still a major challenge to synthesize these types of defects into metals with high stacking fault energy, such as Al. Although deformation twins have been observed in some nanocrystalline Al powders by low temperature, high strain rate cryomilling or in Al at the edge of crack tip or indentation (with the assistance of high stress intensity factor), these deformation techniques typically introduce twins sporadically and the control of deformation twin density in Al is still not feasible.

This proposal will test the following **hypotheses**: (1) *Certain type of layer interfaces may assist the formation of SF in Al*, (2) *Al with high density SF may have deformation mechanisms drastically different from those of coarse-grained Al and nanotwinned Cu*. To test these hypotheses, we will perform **the following tasks**: (i) Investigate the influence of layer interfaces, stresses and deposition parameters on the formation and density of SF in Al. (ii) *Understand the role of SF on the deformation behavior of Al. In situ nanoindentation experiments will be performed to probe deformation mechanisms in Al.*

### Recent Progress

During 2014-2015, we have performed in-depth studies on several projects: (1) *apply in situ nanoindentation technique to study the plasticity and working hardening of nt Al*; (2) *reveal the detwinning process and interaction between dislocations and coherent twin boundaries (CTBs) of nanotwinned (nt) metals under in-situ nanoindentation*; (3) *investigate fatigue resistance of nanotwinned metals*; (4) *explore the formation of growth twins in nanocrystalline Al films*

**(1) In situ nanoindentation study on plasticity and work hardening in Al with incoherent twin boundaries (ITBs)** (Nature Communications, 2014)

The plasticity of twinned high stacking-fault energy metal, such as Al with ITBs, has not been investigated. We report on high work hardening capacity and plasticity in highly twinned aluminum containing abundant  $\Sigma 3 \{112\}$  ITBs based on *in-situ* nanoindentation studies in a transmission electron microscope and corresponding molecular dynamics (MD) simulations. The simulations also reveal major differences in deformation mechanisms between nt Cu and Al ascribed to stacking-fault energy controlled dislocation-incoherent twin boundary interactions.

Multiple indentation cycles were performed near ITB (in nt Al) which is parallel to the loading direction. During the first and second indentation cycles, the dislocations are nucleated and confined by the ITB<sup>49</sup>. During the third cycle, the indentation stress-displacement curve in Fig. 1a shows apparent work hardening behavior (Fig. 1). In particular we observed extensive

dislocation pile-ups against the ITB during this indentation. Furthermore the originally flat ITB becomes distorted as evidenced by the formation of steps shown by the red dotted line in Fig. 1f.

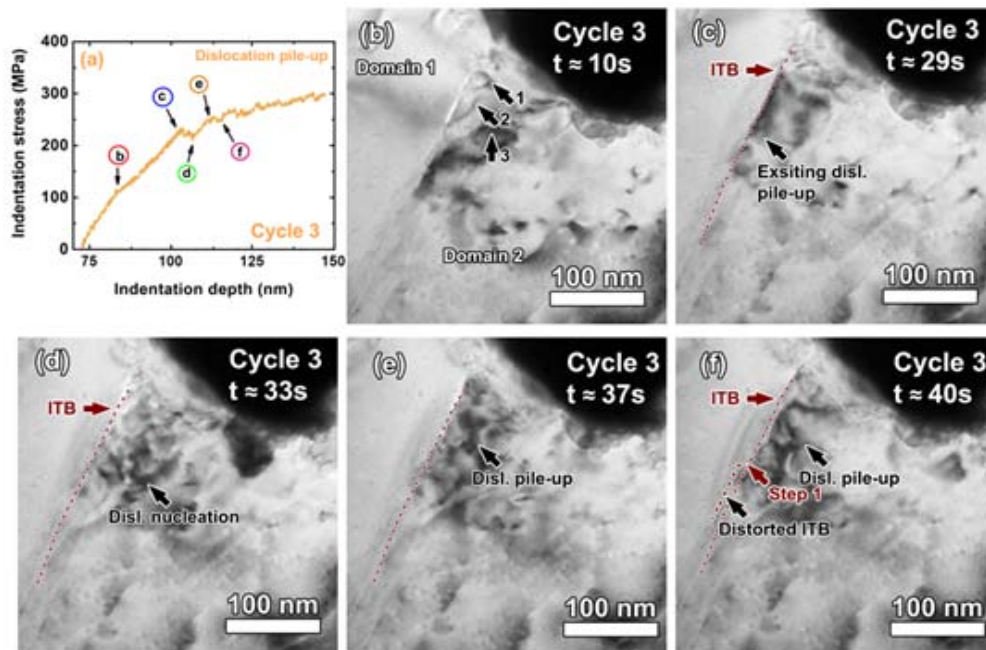


Figure 1. Dislocation pile-ups against ITBs and work hardening in nanotwinned Al. (a) The indentation stress–displacement curve during the indentation cycle 3 shows work hardening behavior. Multiple arrows placed on each side of the curve and the adjacent letters correspond to the following TEM micrographs. (b) During elastic deformation up to 10 s, several pre-existing dislocations started to migrate toward the ITB. The domain 2 underneath the indenter remained its low dislocation density. Scale bar here and in subsequent panels is 100 nm. (c) By 29 s, right before the onset of load drop (shown in e), the pre-existing dislocations formed a network and piled up at the ITB, the position of which was outlined by a red dotted line. (d) At 33 s, instantaneous nucleation of numerous dislocations occurred, and a distinctive load drop accompanied the nucleation event. (e) At 37 s, these new dislocations propagated left toward the ITB whereat they were blocked. (f) By 40 s, the continuous pile-up of dislocations appeared to distort a small portion of the ITB as indicated by a red dotted line labeled as step 1.

Molecular dynamics (MD) simulations (in collaboration with Jian Wang at Los Alamos National Lab) were applied to investigate the influence of SFE on deformation mechanisms in twinned metals. The major findings from simulations include the followings. (a) ITBs are stable when lattice dislocations are nucleated during indentation in nt Al, while in nt Cu, ITBs dissociate into two tilt walls bounding a volume of 9R phase before absorbing lattice dislocations. (b) In nt Al, lattice dislocations interact with ITBs and then dissociate into interface disconnections. In comparison in nt Cu, the 9R regions can accommodate plastic deformation by allowing frequent transmission of lattice dislocations. Therefore, the ITB barrier resistance for lattice dislocations in nt Cu is much lower than that in nt Al. Correspondingly ITBs in high SFE nt metals could induce significant work hardening and plasticity.

**(2) Plasticity and ultra-low stress induced twin boundary migration in nanotwinned Cu by *in situ* nanoindentation studies** (Applied Physics Letters, 2014)

*In situ* nanoindentation was performed on sputtered epitaxial nt Cu films. Fig. 2a shows a typical indentation stress vs. displacement plot captured during indentation. At 12s, a clear stress plateau has been observed at ~ 0.1 GPa. The corresponding snapshots in Fig. 2b reveal that a fine

twin (T2) with 5 nm in thickness migrates by  $\sim 15$  nm. At 30s, a transition from linear to non-linear behavior has been recorded in the stress-displacement plot at  $\sim 0.5$  GPa. The snapshots in Fig. 2c-c' show an avalanche of nucleated dislocations, corresponding to the onsite of non-linear deviation of stress. After nucleation, the dislocations form a network and propagate downward until they are blocked by a TB T3 (Fig. 2d). At 46 s the dislocation network transmits across T3 (Fig. 2d') manifested by a prominent stress drop.

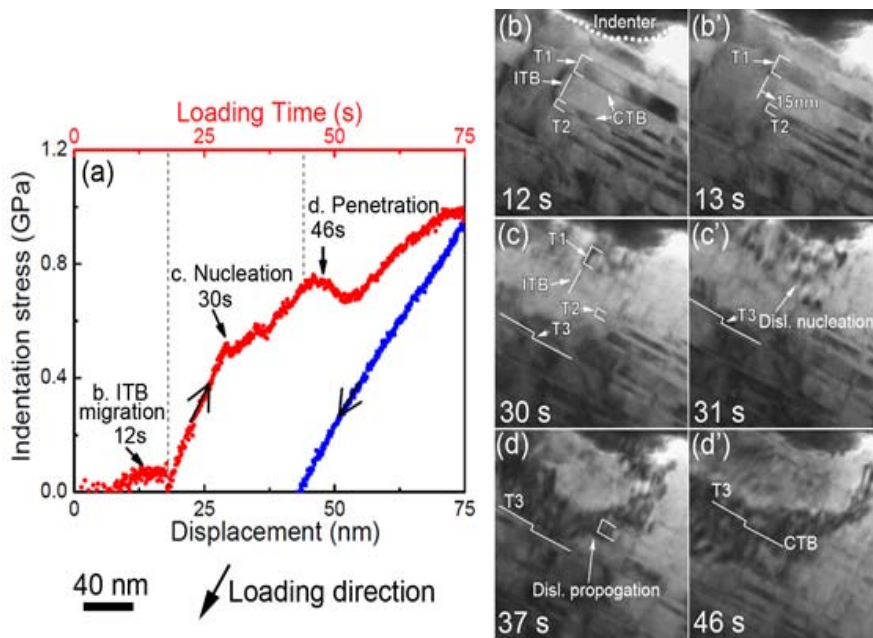


Figure 2. *In situ* nanoindentation on nanotwinned Cu. (a) Indentation stress vs. displacement (time) plot during loading (red) and unloading (blue) process. A clear stress plateau along with the stress drop was observed at around 12s, corresponding to the migration of ITB of fine twins ( $\sim 5$  nm thickness) as shown in (b). (c) Dislocation nucleation (microscopic yielding) occurred at 30s. (d') A large load drop event at 46s, corresponds to dislocation transmission or penetration to twin boundary, T3, (macroscopic yielding).

The ITB migration (detwinning), dislocation nucleation, and dislocation penetration across CTBs are three distinct stages revealed in nt Cu. First, the fine twins start detwinning at an ultra-low stress ( $\sim 0.1$  GPa), well before the dislocation nucleation ( $\sim 0.5$  GPa), while the thick twins remain little changed during test. Second, the dislocation nucleation captured at lower stress levels ( $\sim 0.5$  GPa) during *in situ* nanoindentation study can be described as a microscopic yielding event, which is difficult to detect via conventional (*ex situ*) mechanical testing techniques. Finally the stress necessary for the dislocation penetration event ( $\sim 0.8$  GPa) compares well to macroscopic yielding measured by conventional (*ex situ*) tension or nanoindentation tests. Therefore, this *in situ* nanoindentation study validates the general perception between dislocation penetration across TBs and macroscopic yielding.

### (3) Quantitative detwinning analysis of nt Cu under cyclic loading (Acta Mater, 2015)

High-purity nt Cu foils with median spacing of about 25 nm were subjected to tension-compression cyclic loading by a high-throughput cyclic testing method. The methodology utilizes gradients in surface strain amplitude of a vibrating cantilever. Systematic microstructural investigations indicate that nanotwins are not stable under cyclic loading and that the applied strain amplitude has a strong influence on the resulting twin structure. In the highly stressed regions the detwinning process produces a twin free microstructure, allowing for subsequent extrusion and crack formation and introduces fatal defects into structural parts.

### (4) The formation mechanisms of growth twins in polycrystalline Al with high stacking fault energy

Growth twins are scarcely observed in metals with high stacking fault energy, such as pure Al. In this study, however, we report the observation of growth twins in sputtered



polycrystalline Al films on amorphous substrates and a majority of these growth twins are inclined to the growth direction (inclined twins). Although the fraction of twinned grains is low in general, it increases monotonically with increasing film thickness, reaches a maximum at

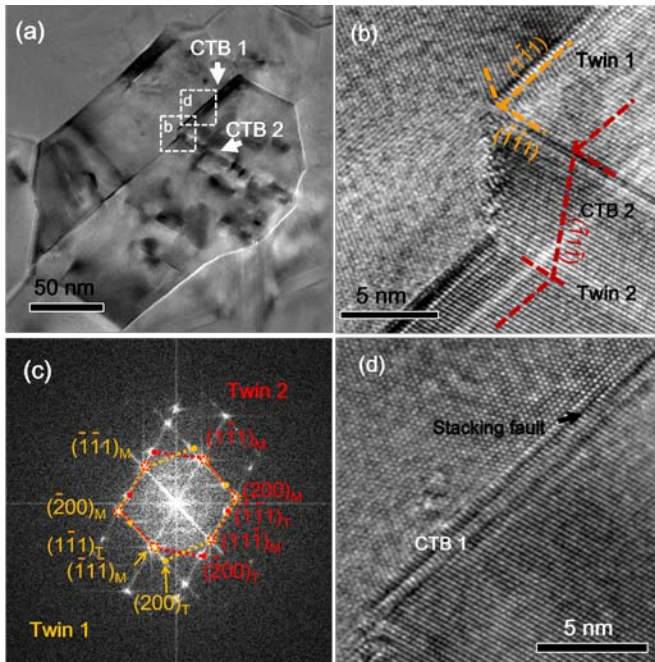


Figure 3. Microstructure of long CTBs in twinned Al films. (a) Low magnification TEM micrograph of the CTB multi-junction in Al film,  $h = 40$  nm. (b) HRTEM micrograph showing the intersection of CTBs at the junctions. (c) The fast Fourier transform (FFT) of the CTB junctions confirmation the formation of two sets of twins. (d) HRTEM micrograph showing the CTB1 decorated with stacking faults.

certain film thickness, and decreases gradually thereafter. The nucleation mechanism for the inclined twins is compared with that of the parallel growth twins in Al. Different twin formation mechanisms are discussed.

### Future Plans

In the next fiscal year, we plan to undertake the following tasks:

- 1) Explore the mechanisms for formation of growth twins in Al with various crystal orientation.
- 2) Examine mechanical strength of Al/Ag multilayers with different texture.
- 3) Explore the thermal stability of nanotwins in Al. TBs or SFs are anticipated to be very difficult to form in Al, but once formed, little is known about their thermal stability.
- 4) Investigate the tensile properties of nt Al films

### Publications-patent through this program, 2014-2015

1. Irene J. Beyerlein, Xinghang Zhang, and Amit Misra, Growth Twins and Deformation Twins in Metals, *Ann. Rev. Mater. Res.* 2014, 44:15.1–15.35.
2. KY Yu, D Bufford, Y Chen, Y Liu, H Wang, X Zhang, Basic criteria for formation of growth twins in high stacking fault energy metals, *Applied Physics Letters* 103 (18), 181903, 2014.
3. Y. Liu, J. Hay, H. Wang, and X. Zhang, “A new method for reliable determination of strain-rate sensitivity of low-dimensional metallic materials by using nanoindentation”, *Scripta Mater.*, 77 (2014) 5.
4. Y. Liu, J. Jian, Y. Chen, H. Wang and X. Zhang, Plasticity and ultra-low stress induced twin boundary migration in nanotwinned Cu by *in situ* nanoindentation studies, *Appl. Phys. Lett.* 104, 231910 (2014).
5. D. Bufford, Y. Liu, J. Wang, H. Wang and X. Zhang, *In situ* nanoindentation study on

- plasticity and work hardening in aluminium with incoherent twin boundaries, *Nature Communications* 5, 4864 (2014)
6. BG Yoo, ST. Boles, Y. Liu, X. Zhang, R. Schwaiger, C. Eberl, O. Kraft, Quantitative damage and detwinning analysis of nanotwinned copper foil under cyclic loading, *Acta Mater.*, 81 (2014) 184-193.
  7. Y. Liu, N. Li, D. Bufford, J. Wang, J.H. Lee, H. Wang, and X. Zhang, *In situ* nanoindentation studies on detwinning and work hardening in nanotwinned monolithic metals”, *JOM* (invited review article), 2015.
  8. J. Li, K. Y. Yu, Y. Chen, M. Song, H. Wang, M.A. Kirk, M. Li, and X. Zhang, *In situ* Study of Defect Migration Kinetics and Self-Healing of Twin Boundaries in Heavy Ion Irradiated Nanotwinned Metals, *Nano Letters*, 2015.
  9. Y. Chen, Y. Liu, S. Shao, H. Wang, M.A. Kirk, J. Wang and X. Zhang, Damage tolerant nanotwinned metals with nanovoids under radiation environments, *Nature Communications*, 6, 7036, 2015.
  10. Xinghang Zhang, Daniel Bufford, Yue Liu and Haiyan Wang, Method for producing high stacking fault energy metal films and coatings with high density nanotwins, US patent filed in spring 2015.



# ***Author Index***



## Author Index

Allison, John.....	5	Lienert, Ulrich .....	90
Anderson, Peter M.....	95	Lou, Jun .....	156
Asta, Mark .....	133	Ma, Dong.....	105
Averback, Robert S. ....	14	McCabe, Rodney M.....	180
Badwe, Nilesh.....	161	Mendelev, Mikhail .....	85
Baker, Ian .....	10	Miller, Matthew .....	90
Bei, Hongbin.....	3, 111	Miller, Michael K. ....	105
Bellon, Pascal .....	14	Mills, Michael J. ....	59, 95, 105
Beyerlein, Irene J.....	180	Morgan, Dane .....	170
Bieler, T. R. ....	19	Morris, James R.....	111
Boehlert, C. J. ....	19	Obstalecki, Mark .....	90
Boyce, Brad L.....	24	Olszta, M. J.....	34
Brinson, L. Catherine .....	30	Osetskiy, Yuri N.....	105, 111
Bruemmer, S. M. ....	34	Ott, Ryan.....	85
Cai, Wei.....	40	Padture, Nitin.....	156
Caro, Alfredo.....	3	Papanikolaou, S. ....	101
Caro, Magdalena.....	3	Parish, Chad M. ....	105
Carson, Robert.....	90	Pharr, George M. ....	111
Carter, W. Craig .....	186	Raj, Rishi .....	118
Castro, Ricardo .....	42	Reimanis, Ivar.....	123
Chen, Xiyang.....	161	Riedo, Elisa.....	129
Chiang, Yet-Ming.....	186	Ritchie, Robert O.....	133
Chisholm, Matthew F. ....	209	Robertson, Ian M. ....	204
Ciobanu, Cristian.....	123	Rosso, K. M. ....	34
Collins, Peter .....	85	Rupert, Timothy J.....	137
Crimp, M. A. ....	19	Samolyuk, German .....	3, 105
Daly, Samantha.....	142	Sangid, Michael D. ....	142
Dauskardt, Reinhold H. ....	47	Schreiber, D. K.....	34
Dawson, Paul.....	90	Schroers, Jan.....	146
Demkowicz, Michael J. ....	51	Sethna, James P. ....	150
Dillon, Shen J. ....	14	Shao, Lin.....	152
Dunand, David C.....	30	Sheldon, Brian W. ....	156
Eisenlohr, P.....	19	Sieradzki, Karl.....	161
Farkas, Diana.....	204	Stocks, G. Malcolm .....	3
Fullwood, David.....	55	Stoller, Roger E. ....	3
Gao, Yanfei.....	111	Strachan, Alejandro .....	165
Ghazisaeidi, Maryam.....	59	Sun, Shaofeng.....	161
Gianola, Daniel S.....	63	Sushko, M. L. ....	34
Greer, Julia R.....	68	Szlufarska, Izabela.....	170
Hemker, Kevin .....	81, 101	Taheri, Mitra.....	175
Homer, Eric .....	55	Tomé, Carlos N. ....	180
King, Alex .....	85	Tomsia, Antoni P.....	133
King, William P.....	14	Trinkle, Dallas R. ....	14
LeSar, Richard.....	85	Tuller, Harry L.....	186

Uberuaga, Blas Pedro .....	193
Van Vliet, Krystyn J.....	186
Vitek, V. ....	199
Voyles, Paul.....	170
Wagoner, Robert.....	55
Wang, C.....	34
Wang, Jian .....	180
Wang, Lumin.....	3
Wang, Yunzhi.....	95
Was, Gary S.....	204
Weber, William J.....	3, 209
Williams, Jim.....	90
Yildiz, Bilge .....	186
Zhang, Xinghang.....	216
Zhang, Yanwen.....	3, 209

# ***Participant List***



<b>Name</b>	<b>Organization</b>	<b>E-mail</b>
Allison, John	University of Michigan	johnea@umich.edu
Anderson, Peter	Ohio State University	anderson.1@osu.edu
Asta, Mark	University of California, Berkeley	mdasta@berkeley.edu
Baker, Ian	Dartmouth College	ian.baker@dartmouth.edu
Bellon, Pascal	University of Illinois	bellon@illinois.edu
Beyerlein, Irene	Los Alamos National Laboratory	irene@lanl.gov
Boyce, Brad	Sandia National Laboratories	blboyce@sandia.gov
Brinson, Catherine	Northwestern University	cbrinson@northwestern.edu
Bruemmer, Stephen	Pacific Northwest National Laboratory	stephen.bruemmer@pnnl.gov
Byun, Thak Sang	Pacific Northwest National Laboratory	thaksang.byun@pnnl.gov
Cai, Wei	Stanford University	caiwei@stanford.edu
Castro, Ricardo	University of California, Davis	rhrcaastro@ucdavis.edu
Chen, Wen	Yale University	chen.wen@yale.edu
Chen, Xiying	Arizona State University	xchen128@asu.edu
Ciobanu, Cristian	Colorado School of Mines	cciobanu@mines.edu
Collins, Peter	Iowa State University	pcollins@iastate.edu
Crimp, Martin	Michigan State University	crimp@egr.msu.edu
Daly, Samantha	University of Michigan	samanthadaly@gmail.com
Dauskardt, Reinhold	Stanford University	dauskardt@stanford.edu
Dawson, Paul	Cornell University	paul.dawson@cornell.edu
Demkowicz, Michael	Massachusetts Institute of Technology	demkowicz@mit.edu
El-Atwani, Osman	Drexel University	oe36@drexel.edu
Fischer, Peter	Lawrence Berkeley National Laboratory	PJFischer@lbl.gov
Fullwood, David	Brigham Young University	dfullwood@byu.edu
Ganesan, Sriram	University of Michigan-Ann Arbor	sriramg@umich.edu
Gao, Yanfei	Univ. of Tennessee/Oak Ridge National Lab	ygao7@utk.edu
Ghazisaeidi, Maryam	Ohio State University	ghazisaeidi.1@osu.edu
Gianola, Daniel	University of Pennsylvania	gianola@seas.upenn.edu
Graf, Matthias	U.S. Department of Energy	matthias.graf@science.doe.gov
Greer, Julia	Caltech	jrgreer@caltech.edu
Hattar, Khalid	Sandia National Laboratories	khattar@sandia.gov
Hemker, Kevin	Johns Hopkins University	hemker@jhu.edu
Khademi, Vahid	Michigan State University	khademiv@egr.msu.edu
LeSar, Richard	Ames Laboratory	lesar@iastate.edu
Liarte, Danilo	Cornell University	danilo@if.usp.br
Liu, Yue	Los Alamos National Laboratory	yueliu@lanl.gov
Lou, Jun	Rice University	jlou@rice.edu
Mara, Nathan	Los Alamos National Laboratory	namara@lanl.gov
Miller, Matthew	Cornell University	mpm4@cornell.edu
Mills, Michael	The Ohio State University	mills.108@osu.edu
Morgan, Dane	University of Wisconsin	ddmorgan@wisc.edu
Papanikolaou, Stefanos	Johns Hopkins University	spapanikolaou@jhu.edu

Paranjape, Harshad	Northwestern Univ./Colorado School of Mines	harshad.paranjape@northwestern.edu
Parish, Chad	Oak Ridge National Laboratory	parishcm@ornl.gov
Paul, Partha	Northwestern University	parthapaul2018@u.northwestern.edu
Perry, Kelly	U.S. Department of Energy	kelly.perry@science.doe.gov
Pharr, George	Oak Ridge National Laboratory	pharr@utk.edu
Raj, Rishi	University of Colorado at Boulder	rishi.raj@colorado.edu
Reimanis, Ivar	Colorado School of Mines	reimanis@mines.edu
Riedo, Elisa	City University of New York - ASRC	elisa.riedo@asrc.cuny.edu
Ritchie, Robert	Lawrence Berkeley National Laboratory	roritchie@lbl.gov
Rottmann, Paul	Johns Hopkins University	paul.rottmann@jhu.edu
Rudraraju, Krishna Siva	University of Michigan, Ann Arbor	rudraa@umich.edu
Rupert, Timothy	University of California, Irvine	trupert@uci.edu
Schreiber, Daniel	Pacific Northwest National Laboratory	daniel.schreiber@pnl.gov
Schroers, Jan	Yale University	jan.schroers@yale.edu
Sethna, James	Cornell University	sethna@lassp.cornell.edu
Severs, Linda	ORISE	linda.severs@orau.org
Shao, Lin	Texas A&M University	lshao@tamu.edu
Sheldon, Brian	Brown University	Brian_Sheldon@brown.edu
Sieradzki, Karl	Arizona State University	Karl.Sieradzki@asu.edu
Strachan, Alejandro	Purdue University	strachan@purdue.edu
Swallow, Jessica	Massachusetts Institute of Technology	jswallow@mit.edu
Taheri, Mitra	Drexel University	mtaheri@coe.drexel.edu
Thiyagarajan, Pappannan	U.S. Department of Energy	p.thiyagarajan@science.doe.gov
Tome, Carlos	Los Alamos National Laboratory	TOME@LANL.GOV
Uberuaga, Blas	Los Alamos National Laboratory	blas@lanl.gov
Van Vliet, Krystyn	Massachusetts Institute of Technology	krystyn@mit.edu
Vetrano, John	U.S. Department of Energy	john.vetrano@science.doe.gov
Vitek, Vaclav	University of Pennsylvania	vitek@seas.upenn.edu
Was, Gary	University of Michigan	gsw@umich.edu
Weber, William	Oak Ridge National Laboratory	weberwj@ornl.gov
Zarkadoula, Eva	Oak Ridge National Laboratory	zarkadoulae@ornl.gov
Zhang, Chen	Michigan State University	zhangc43@msu.edu
Zhang, Xinghang	Texas A&M University	zhangx@tamu.edu
Zhang, Yanwen	Oak Ridge National Laboratory	Zhangy1@ornl.gov